Superlattice Band Structure Engineering of Graphene

Dissertation

zur Erlangung des Doktorgrades
der Naturwissenschaften (Dr. rer. nat.)
der Fakultät für Physik
der Universität Regensburg

vorgelegt von
Robin Tobias Huber
aus Kötzting

im Jahr 2021

Promotionsgesuch eingereicht am: 04.11.2020

Die Arbeit wurde angeleitet von:
PD Dr. Jonathan Eroms
Prof. Dr. Dieter Weiss

Prüfungsausschuss:
Vorsitzender: Prof. Dr. Klaus Richter
1. Gutachter: PD Dr. Jonathan Eroms
2. Gutachter: Prof. Dr. Dominique Bougeard
weiterer Prüfer: Prof. Dr. Sergey Ganichev

CONTENTS

CHAPTER 1

INTRODUCTION

Since the dawn of modern science, physics has always endeavoured not only to unravel the mysteries of the fundamental laws and properties of our universe, but also to modify and utilize nature in order to develop new and useful technologies. One fruitful branch of physics with huge impact on our society is undoubtedly condensed matter physics with achievements like computers, smartphones, solar cells, and many more, which have shaped our world in a way never before imaginable. One recent field of research in condensed matter physics deals with graphene and other two-dimensional materials. These novel materials are of great interest for fundamental research and also have the potential to be used in a variety of technological applications like transistors, sensors, displays, batteries, and more.

This work investigates graphene − a one-atom-thick crystal consisting of a single layer of carbon atoms and containing relativistic charge carriers [1, 2] − by means of electrical transport measurements. The focus lies on techniques that can be used to engineer the electronic band structure and, consequently, the electronic properties of this extraordinary material, eventually producing graphene devices with tailor-made properties. One way to achieve this goal is given by nanostructuring graphene into an antidot lattice [3]. In such a perforated graphene layer the emergence of a magnetically tunable band gap is possible [4–6], transforming the initially gapless graphene into a gapped semiconductor and enabling in principle its use as a field-effect transistor.

Another technique which can be utilized for band structure engineering of graphene is given by superimposing an electrostatically defined two-dimensional superlattice on the charge carriers in graphene. This is realized by the combination of a uniform back gate and a few-layer graphene patterned bottom gate [7] (see Fig. 1.1 (a)) and represents a method complementary to alternative approaches like moiré superlattices [8–10] and patterned dielectric superlattices [11]. This double-gate technique provides the possibility to fabricate superlattices with arbitrary geometry and highly tunable modulation potential, and has already been used successfully to create one-dimensional graphene superlattices allowing the observation of Weiss oscillations [12]. A two-dimensional graphene superlattice implemented by this double-gate technique gives rise to well-pronounced band structure modifications [13]. In such a gate-controllable artificial crystal the emergence of minibands and satellite Dirac points is observable. And in combination with a magnetic field, a fractal energy spectrum − the Hofstadter butterfly [14] − manifests (see Fig. 1.1 (b)). Furthermore, superlattice induced quantum oscillations, so-called band conductivity or Brown-Zak oscillations [15], emerge and can be examined in more detail.

The present thesis is organized as follows:
In the second chapter, the theoretical and experimental background is presented. The basic properties of graphene and, in particular, the crystal structure, the electronic band structure, and effects like the ambipolar electric field effect and the quantum Hall effect are briefly discussed. Furthermore, a short overview of basic aspects of electrical transport and magnetotransport is given. Also heterostructures of graphene and hexagonal boron nitride are introduced, which represent the basic material system used in this work. Moreover, information about superlattice physics in general and in graphene are presented, ranging from the theoretical description to the experimental manifestation in transport measurements with focus on the Hofstadter butterfly energy spectrum. In the last part, an overview of graphene antidot lattices is given with focus on the emergence of energy gaps and their parallels to graphene nanoribbons.
The third chapter provides information about the sample fabrication, starting with a van der Waals stacking process used to fabricate graphene/hexagonal boron nitride heterostructures. Moreover, details on the fabrication of antidot lattices and gate-tunable superlattices in graphene by means of electron beam lithography and reactive ion etching are presented. Also information about the measurement setup is given.
In the fourth chapter, the experimental results are presented. First, transport measurements on graphene antidot lattices are discussed, mainly in view of the emergence of magnetically tunable energy gaps. In the second part, gate-tunable superlattice effects in graphene induced by the aforementioned double-gate technique are investigated, including the emergence of minibands, satellite Dirac points, and the Hofstadter butterfly energy spectrum. Also band conductivity oscillations are examined and discussed in more detail. In addition, the interplay between an artificial gate-defined superlattice and a moiré superlattice is investigated.
The last chapter summarizes all the results and gives a short outlook on possible future directions concerning gate-defined superlattices in graphene.

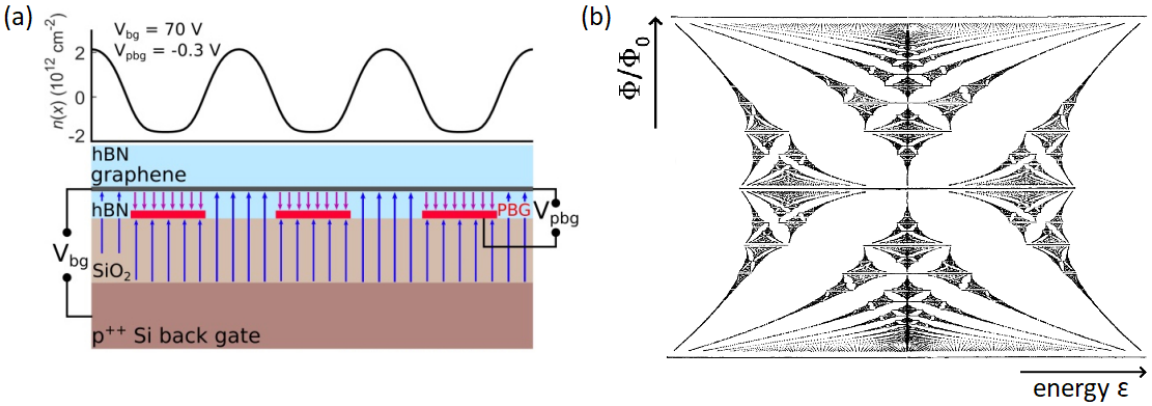

Figure 1.1: (a) Sample design used to induce gate-tunable superlattices in graphene realized by the combination of a uniform back gate (V_{bg}) and a patterned bottom gate (V_{pbg}). Upper graph shows the induced periodic charge carrier density modulation for a certain set of gate voltages. [13] **(b)** The Hofstadter butterfly energy spectrum emerging in a two-dimensional superlattice in combination with a magnetic field. Energy values ϵ are plotted as a function of magnetic flux per superlattice unit cell in units of the magnetic flux quantum Φ/Φ_0. Adapted from [14].

CHAPTER 2

THEORETICAL AND EXPERIMENTAL BACKGROUND

2.1 Basics of Graphene and Electrical Transport

In this section, an overview of basic properties of graphene including the crystal structure and the electronic band structure is given. Furthermore, fundamental aspects of electrical transport and magnetotransport are presented. In the last part, graphene/hexagonal boron nitride heterostructures − the basic material system used in this work − are introduced.

2.1.1 Crystal Structure and Electronic Band Structure of Graphene

Crystal Structure

Graphene, a two-dimensional (2D) material with extraordinary properties [16–20], consists of a single layer of carbon atoms arranged in a honeycomb crystal lattice [21, 22], as schematically depicted in Fig. 2.1 (a). A single carbon atom contains six electrons which occupy the $1s$, $2s$ and $2p$ orbitals. Carbon atoms in graphene are bound by three in-plane sp^2 hybrid orbitals emerging from mixing of $2s$, $2p_x$ and $2p_y$ orbitals. Three of four valence electrons in a carbon atom reside in the three in-plane hybrid orbitals that are orientated at 120° angle to each other and build up strong covalent bonds (σ bonds) to three neighbouring carbon atoms giving rise to the honeycomb crystal structure. The last valence electron occupies the out-of-plane $2p_z$ orbital. Fig. 2.1 (c) schematically shows the orientation of the sp^2 hybrid orbitals and the $2p_z$ orbital of a single carbon atom in graphene. The entirety of $2p_z$ orbitals creates π bands (valence and conduction band) which determine the extraordinary electronic properties of graphene: Graphene is a zero-gap semiconductor/zero-overlap semimetal with charge carriers mimicking relativistic particles and forming a two-dimensional gas of massless chiral Dirac fermions [2].
The honeycomb crystal lattice of graphene is not a Bravais lattice but can be described by two triangular Bravais sublattices labelled by A and B, equivalent to a single triangular crystal lattice with a basis of two atoms A and B. Consequently, the unit cell of graphene (defined by lattice vectors $\vec{a}_1$ and $\vec{a}_2$ and area $A_{uc} = |\vec{a}_1 \times \vec{a}_2|$) contains two identical carbon atoms sitting on different sublattices. Fig. 2.1 shows the crystal structure of graphene in real space and the corresponding first Brillouin zone in reciprocal space. The lattice constant of graphene is $a_0 \sim 2.46$ Å. The lattice vectors in real space ($\vec{a}_1$ and $\vec{a}_2$) and the reciprocal lattice vectors ($\vec{b}_1$ and $\vec{b}_2$), expressed by the nearest-neighbour distance $a_{gr} = a_0/\sqrt{3} \sim 1.42$ Å, are given by [21]:

$$\vec{a}_1 = \frac{a_{gr}}{2}(3, \sqrt{3}) \qquad \vec{a}_2 = \frac{a_{gr}}{2}(3, -\sqrt{3}) \tag{2.1}$$

$$\vec{b}_1 = \frac{2\pi}{3a_{gr}}(1, \sqrt{3}) \qquad \vec{b}_2 = \frac{2\pi}{3a_{gr}}(1, -\sqrt{3}) \tag{2.2}$$

The inequivalent K and K' points at the corners of the first Brillouin zone are usually referred to as K and K' valleys or Dirac points and will be important in the description of the electronic band structure and electronic properties of graphene.

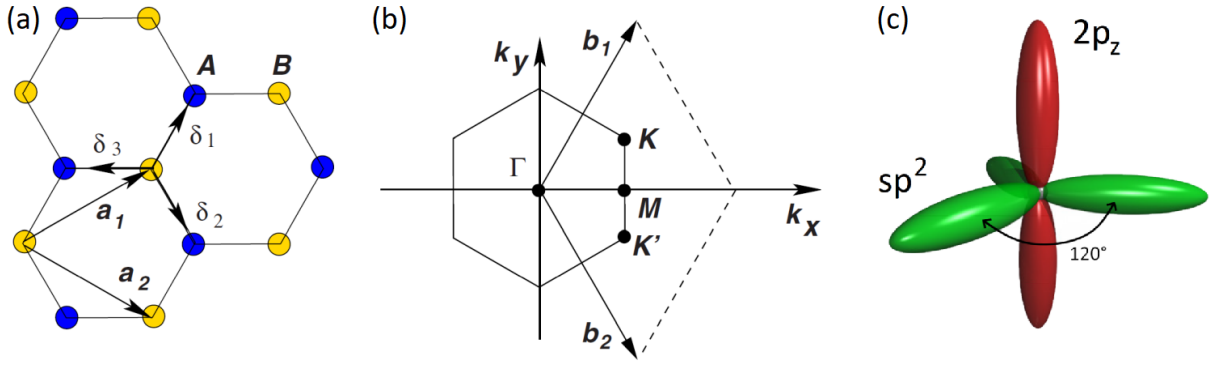

Figure 2.1: (a) The crystal structure of graphene in real space with two sublattices A and B and lattice vectors $\vec{a}_1$ and $\vec{a}_2$. The $\vec{\delta}$ vectors define the position of the nearest neighbours. [21] **(b)** Reciprocal space with reciprocal lattice vectors $\vec{b}_1$ and $\vec{b}_2$ and K and K' points at the corners of the first Brillouin zone. [21] **(c)** Orientation of the three sp^2 hybrid orbitals (green) and the $2p_z$ orbital (red) of a single carbon atom in graphene. The angle of 120° between the sp^2 orbitals determines the honeycomb crystal structure of graphene. Adapted from [23].

Electronic Band Structure

The electronic band structure of graphene can be derived from a tight-binding model [1, 24]. By solving the corresponding Schrödinger equation $H\Psi_{\vec{k}}(\vec{r}) = E(\vec{k})\Psi_{\vec{k}}(\vec{r})$ with Bloch wave functions $\Psi_{\vec{k}}(\vec{r})$, based on a linear combination of atomic orbitals ($2p_z$ orbitals), one obtains the single-particle energy spectrum [21, 22]. The resulting energy spectrum, i.e. the allowed energy values $E(\vec{k})$ as a function of wave vector $\vec{k} = (k_x, k_y)$, of a π-electron in graphene restricted to nearest-neighbour hopping (i.e. hopping between sublattices A and B) is given by [21]:

$$E(\vec{k}) = \pm t_0 \sqrt{3 + f(\vec{k})} \tag{2.3}$$

with the function

$$f(\vec{k}) = 2\cos(\sqrt{3}k_y a_{gr}) + 4\cos\left(\frac{\sqrt{3}k_y a_{gr}}{2}\right)\cos\left(\frac{3k_x a_{gr}}{2}\right) \tag{2.4}$$

and with nearest-neighbour distance a_{gr} and nearest-neighbour hopping energy $t_0 \sim 3$ eV. The $(-)$ sign corresponds to the completely filled valence band (π band) and the $(+)$ sign corresponds

to the empty conduction band (π^* band). Fig. 2.2 displays the electronic band structure of graphene. The Fermi energy E_F of intrinsic (i.e. undoped) graphene lies at zero energy (referred to as charge neutrality point: CNP), i.e. at the K and K' points, at which valence and conduction band touch each other. The energy spectrum in the vicinity of the Dirac points (referred to as Dirac cones due to the conical shape) can be described in first-order approximation by a linear energy dispersion relation obtained by expanding the band structure close to K and $K^{'}$ [21, 22]:

$$E(\vec{k}) = \pm\hbar v_F \left|\vec{k}\right| \tag{2.5}$$

with relative wave vector $\vec{k}$ measured from the K and K' points, constant Fermi velocity $v_F = 3t_0 a_{gr}/2 \sim 10^6$ m/s in graphene, and reduced Planck constant $\hbar = \frac{h}{2\pi} \sim 1.055 \times 10^{-34}$ Js. In general, also including doped graphene with certain charge carrier density n, charge carriers at the Fermi level possess the Fermi energy $E_F = \pm\hbar v_F k_F$ with Fermi wave vector $k_F = \frac{2\pi}{\lambda_F} = \sqrt{\frac{4\pi n}{g_s g_v}} = \sqrt{\pi n}$ (including spin degeneracy $g_s = 2$ and valley degeneracy $g_v = 2$), and Fermi wave length λ_F.
The linear energy dispersion relation determines the fundamental and exceptional electronic properties of graphene − charge carriers behave similar to massless relativistic particles travelling at constant Fermi velocity $v_F = \frac{1}{\hbar}\frac{dE}{dk} \sim c/300 \sim 10^6$ m/s (with c the speed of light in vacuum) in stark contrast to 2D electron gas (2DEG) systems with parabolic dispersion relation and massive charge carriers.

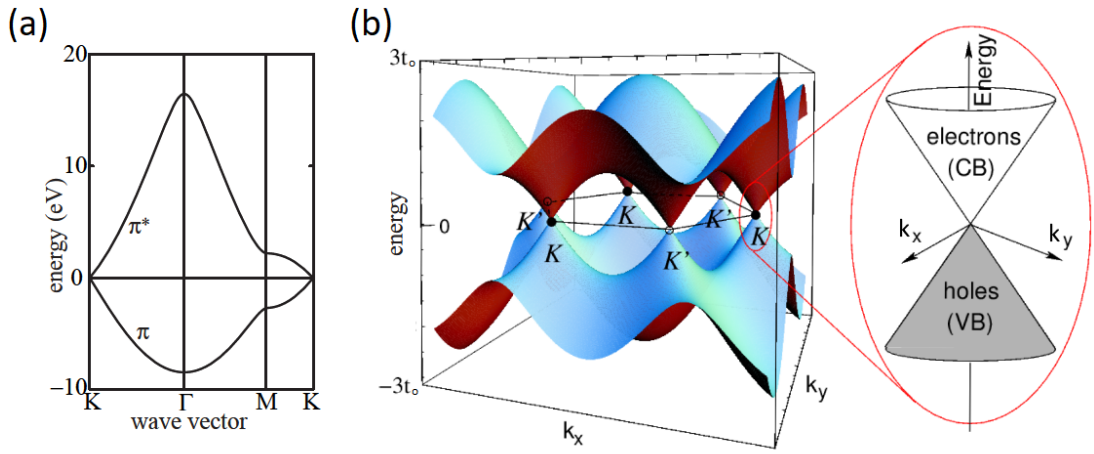

Figure 2.2: **(a)** Electronic band structure of graphene along high symmetry points of the first Brillouin zone. [25] **(b)** The overall energy spectrum of graphene. Valence and conduction band touch each other at the Dirac points (K and K'). In the vicinity of the Dirac points the energy dispersion relation is linear (forming the Dirac cones) in accordance with the quasi-relativistic nature of charge carriers. Adapted from [26].

Spin and Valley Isospin

Due to the existence of two inequivalent Dirac points, i.e. K and K', charge carriers in graphene exhibit an additional degree of freedom (besides the spin degree of freedom) which is expressed

in an additional valley degeneracy of $g_v = 2$ ("valley isospin") [22, 27]. In combination with the spin degeneracy $g_s = 2$, graphene exhibits an overall four-fold degeneracy $g_s g_v = 4$. In general, these degeneracies can be lifted by interaction effects and symmetry breaking effects [27–33].

Density of States

The density of states $D(E)$ per unit cell (with area A_{uc}) is shown in Fig. 2.3. In the vicinity of the Dirac points, the density of states can be approximated by the following expression with a linear dependency on energy E [21]:

$$D(E) = \frac{2A_{uc}|E|}{\pi\hbar^2 v_F^2} \tag{2.6}$$

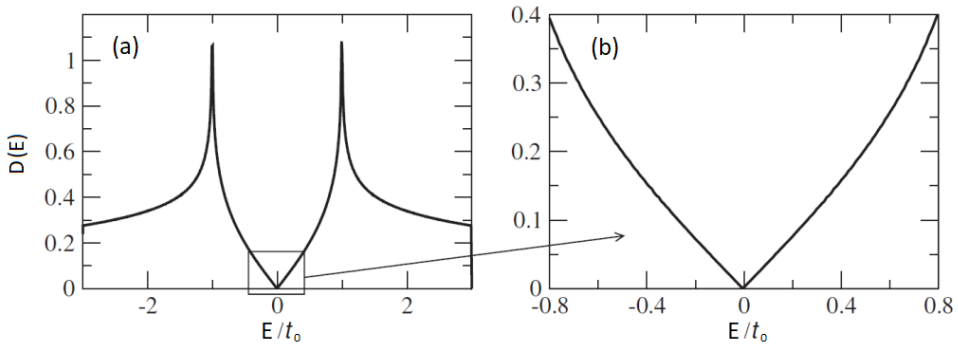

Figure 2.3: (a) Density of states D per unit cell in graphene as a function of energy E in units of the nearest-neighbour hopping parameter t_0. **(b)** Density of states in the vicinity of the Dirac points. [21]

Effective Mass

The effective (cyclotron) mass m^* of charge carriers in graphene is linearly dependent on the crystal momentum and extrapolates to vanishing mass at the Dirac points confirmed by cyclotron mass experiment. This emphasizes the relativistic nature of graphene's Dirac fermions [2, 34, 35]:

$$m^* = \frac{\hbar k_F}{v_F} = \frac{\hbar\sqrt{\pi n}}{v_F} \tag{2.7}$$

Sublattice Pseudospin and Berry Phase

In general, the linear energy spectrum in the vicinity of the Dirac points K and K' can be obtained from the Dirac equation with Hamiltonian $H_{K(K')}$ and 2D spinor wave functions $\Psi_{\pm,K(K')}$ [21, 22]:

$$H_{K(K')} = \hbar v_F \vec{\sigma}^{(*)} \vec{k} \tag{2.8}$$

$$\Psi_{\pm,K}(\vec{k}) = \frac{1}{\sqrt{2}} \begin{pmatrix} \exp(-i\Theta_{\vec{k}}/2) \\ \pm\exp(i\Theta_{\vec{k}}/2) \end{pmatrix} \tag{2.9}$$

$$\Psi_{\pm,K'}(\vec{k}) = \frac{1}{\sqrt{2}} \begin{pmatrix} \exp(i\Theta_{\vec{k}}/2) \\ \pm\exp(-i\Theta_{\vec{k}}/2) \end{pmatrix} \tag{2.10}$$

with Pauli matrices $\vec{\sigma} = (\sigma_x, \sigma_y)$, $\vec{\sigma}^* = (\sigma_x, -\sigma_y)$, the angle in momentum space $\Theta_{\vec{k}} = \arctan(\frac{k_x}{k_y})$, and $(\pm)$ corresponding to the energy eigenvalues $E = \pm\hbar v_F \left|\vec{k}\right|$. The 2D spinors correspond to a pseudospin instead of the usual spin. Consequently, charge carriers in graphene exhibit a pseudospin which originates from the existence of the two sublattices A and B – two possible positions of charge carriers ("sublattice pseudospin") [21, 22, 27]. In the K-valley, the pseudospin is antiparallel (parallel) to the wave vector in the valence band (conduction band). As a consequence, the valence band (conduction band) induces negative (positive) chirality, i.e. the projection of pseudospin on the direction of motion. The relations are reversed in the K'-valley. The conservation of pseudospin is the origin of exceptional effects in graphene like Klein tunnelling which describes full transmission of charge carriers through a potential barrier upon normal incidence, if intervalley scattering and sublattice symmetry breaking effects can be neglected [21, 36]. Klein tunnelling is schematically depicted in Fig. 2.4. Another aspect of the 2D spinor wave functions is that under rotation of $\Theta_{\vec{k}}$ by 2π the wave functions change sign which indicates a phase of π – the so-called Berry phase. Consequently, charge carriers in graphene travelling on a closed trajectory acquire an extra phase of π which has significant impact on e.g. quantum interference effects and Landau quantization in graphene [21, 37].

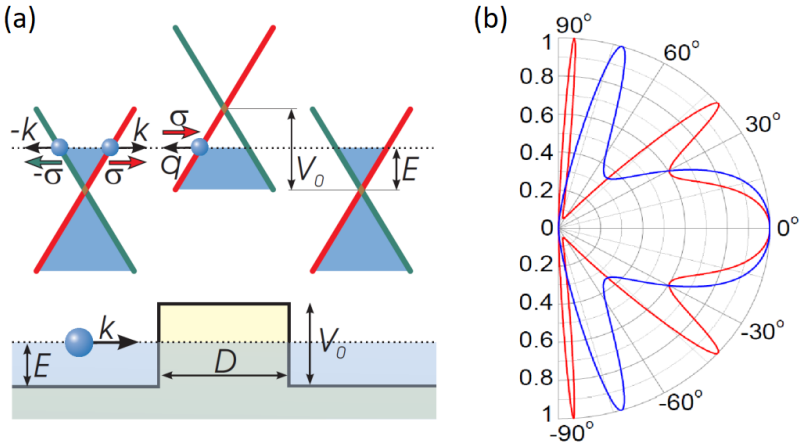

Figure 2.4: Illustration of Klein tunneling in graphene. **(a)** Schematic picture of an electron with energy E, momentum $\vec{k}$, and pseudospin σ moving across a potential barrier with height $V_0 > E$ realized by a n-p-n junction (n = negative: electron doped region, p = positive: hole doped region). The red and green branches of the depicted Dirac cone correspond to energy bands originating from the two different sublattices in graphene. Transport across the potential barrier takes place by a hole state with momentum $\vec{q}$. The pseudospin is conserved. Backscattering would require pseudospin-flip processes. [36] **(b)** Transmission probability of an electron with energy $E = 80$ meV through a potential barrier for two different barrier heights ($V_0 = 200/285$ meV, corresponding to the red/blue curve) as a function of incidence angle. At normal incidence (0°) full transmission – Klein tunneling – takes place. [36]

2.1.2 Electrical Transport and Ambipolar Electric Field Effect

Basics of Electrical Transport Measurements

In this section, basic aspects of electrical transport measurements are presented, following mainly Refs. [25, 38–43]. In general, electrical transport measurements are a versatile tool to probe intrinsic physical properties of a material. In particular, transport measurements provide the possibility to study graphene's Dirac fermions and to explore the electronic properties of artificially modified graphene structures in view of new physical effects and applications. In order to extract information about intrinsic properties of a material by means of electrical transport measurements, one can use a Hall bar design of the investigated material system with length L between voltage probes and width W of the conduction channel (see Fig. 2.5). A current I is applied between source and drain contact and the longitudinal and transverse voltages (V_{xx} and V_{xy}) are measured. The corresponding longitudinal and transverse resistances (R_{xx} and R_{xy}) are given by the macroscopic version of Ohm's law:

$$R_{xx/xy} = \frac{V_{xx/xy}}{I} \tag{2.11}$$

The resistances are evaluated as a function of external parameters like temperature, gate voltages (to tune e.g. charge carrier density), and magnetic field, from which insight into internal properties and processes can be gained. By including the geometrical factor (W/L) of the Hall bar, the material-specific resistivities and conductivities can be obtained from the sample-specific resistances R_{xx} and R_{xy}. In the case of a 2D system, the longitudinal and transverse resistivities are given by:

$$\rho_{xx} = R_{xx}\frac{W}{L} \qquad\qquad \rho_{xy} = R_{xy} \tag{2.12}$$

In general, resistivities ρ_{xx} and ρ_{xy} are components of the resistivity tensor

$$\boldsymbol{\rho} = \begin{pmatrix} \rho_{xx} & \rho_{xy} \\ \rho_{yx} & \rho_{yy} \end{pmatrix} \tag{2.13}$$

and conductivities are calculated by tensor inversion $\boldsymbol{\sigma} = \boldsymbol{\rho}^{-1}$. In the case of an isotropic system, the relations $\rho_{xx} = \rho_{yy}$ and $\rho_{xy} = -\rho_{yx}$ hold true and the conductivities are given by:

$$\sigma_{xx} = \frac{\rho_{xx}}{\rho_{xx}^2 + \rho_{xy}^2} \qquad\qquad \sigma_{xy} = -\frac{\rho_{xy}}{\rho_{xx}^2 + \rho_{xy}^2} \tag{2.14}$$

The corresponding sample-specific conductances are:

$$G_{xx} = \sigma_{xx}\frac{W}{L} \qquad\qquad G_{xy} = \sigma_{xy} \tag{2.15}$$

The conductivity tensor $\boldsymbol{\sigma}$ determines the current density $\vec{j}$ in a material under application of an electric field $\vec{E}$ which is expressed in the microscopic version of Ohm's law:

$$\vec{j} = \boldsymbol{\sigma}\vec{E} \tag{2.16}$$

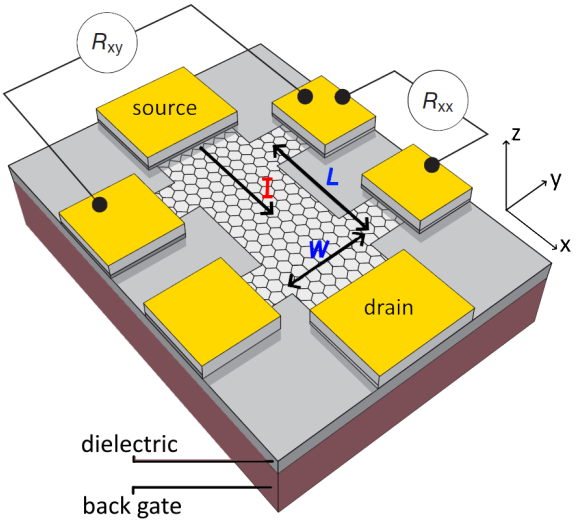

Figure 2.5: Graphene sample in Hall bar geometry with length L between voltage probes and width W of the conduction channel used for electrical transport measurements. A current I is applied between source and drain contact and longitudinal and transverse resistance (R_{xx} and R_{xy}) are determined. A gate electrode, separated from the graphene layer by a dielectric, is used as a back gate. Adapted from [44].

Drude Model Parameters

Classical charge carrier transport in electric and magnetic fields can be described by the Drude model [25, 38, 40] which is a simplified but sufficient approach to determine and quantify fundamental electrical transport parameters. In an applied electric field and at zero magnetic field, charged particles with charge $q = \pm e$ (with the elementary charge $e \sim 1.602 \times 10^{-19}$ C) and effective mass m^* experience an electric force $\vec{F}_{el} = q\vec{E}$. In order to extract transport parameters, one can solve the corresponding Newton's equation of motion:

$$m^*\left(\frac{d\vec{v}}{dt} + \frac{\vec{v}}{\tau}\right) = \vec{F}_{el} \tag{2.17}$$

Scattering is taken into account by the Drude mean time τ between scattering events. In the stationary case with electric field $\vec{E} = (E_x, 0)$, constant current density $\vec{j} = (j_x, 0) = qn\vec{v}$ with charge carrier density n and average drift velocity $\vec{v}$, and $d\vec{v}/dt = 0$ one obtains:

$$\rho_{xx} = \frac{E_x}{j_x} = \frac{m^*}{e^2 n\tau} \qquad \rho_{xy} = 0 \tag{2.18}$$

Parameters which quantify a material's ability to carry current are the charge carrier mobility μ, the mean free path l_{mfp}, and the average scattering time τ [44]. The mobility μ connects the drift velocity of charge carriers to the electric field:

$$v = \mu E = \frac{\sigma_{xx}}{en}E = \frac{e\tau}{m^*}E \tag{2.19}$$

The mean free path l_{mfp} is the average distance a charge carrier is able to travel before being scattered. It is connected to the Drude mean time τ between scattering events over $l_{mfp} = v_F\tau$. In the case of graphene, l_{mfp} is given by:

$$l_{mfp} = \frac{\hbar}{e}\mu\sqrt{\pi n} \tag{2.20}$$

Scattering Processes

The overall scattering time τ in a system includes scattering times from all contributing scattering mechanisms (τ_1, τ_2, τ_3, ...) expressed by Matthiessen's rule [40]:

$$\frac{1}{\tau} = \frac{1}{\tau_1} + \frac{1}{\tau_2} + \frac{1}{\tau_3} + ... = \sum_i \frac{1}{\tau_i} \tag{2.21}$$

Scattering processes can be roughly divided into two categories: intrinsic and extrinsic scattering mechanisms [44]. Intrinsic scattering includes phonon scattering and scattering at lattice disorder and defects. Extrinsic scattering mechanisms are e.g. Coulomb scattering caused by charged impurities. Also scattering at phonons of an underlying substrate can play a role.
In absence of all other scattering mechanisms, phonon scattering sets an intrinsic mobility limit to graphene at finite temperature [45]. Due to the fact that phonon scattering at longitudinal acoustic phonons (the dominant intrinsic phonon-induced scattering mechanism in graphene) is relatively weak, the room-temperature mobility limit lies at about 20 m^2/Vs, approached in suspended graphene devices [46–48] and in graphene/hexagonal boron nitride heterostructures [49, 50] (see chapter 2.1.4). Substrates can limit the mobility due to scattering of charge carriers at remote interfacial phonons [51–53]. However, it is also possible to modify acoustic phonon bands in graphene by a suitable substrate which enhances room-temperature mobility to values even surpassing the intrinsic mobility limit [54].
Short-range scattering due to lattice disorder includes e.g. defects, vacancies, foreign atom substitutions, chemical bonds, grain boundaries, mechanical distortions, dislocations, adsorbates, and sample edges. This kind of defects can give rise to localized states at or near the CNP and resonantly scatter charge carriers [55], causing a roughly linear dependency of the conductivity σ_{xx} on the charge carrier density n in graphene [37, 55].
Long-range Coulomb scattering in graphene can be caused by charged impurities in the vicinity of graphene (e.g. in the substrate). Charged impurities may give rise to random fluctuations of local charge carrier density and localized puddles of electrons and holes occur at the CNP [44, 56–58]. A linear dependency of the conductivity σ_{xx} on the charge carrier density n can be derived from a Boltzmann model of charged impurity scattering [59–61]. Charged impurities can also cause doping of graphene, i.e. the Fermi level is shifted away from the CNP into the valence (hole doping) or conduction band (electron doping) [62].

Diffusive and Ballistic Transport

Electrical transport can be classified in two main categories: diffusive and ballistic transport of charge carriers [39, 44, 63, 64]. The transport regime is determined by the relation between the mean free path l_{mfp} and the dimensions (in general the dominant length scales) of the sample, e.g. the length L and width W of the conduction channel. For $l_{mfp} > L$ the system is in the ballistic transport regime and charge carriers in a typical mesoscopic device are only scattered at sample edges. In this case, the conductivity σ_{xx} of graphene is proportional to $\sqrt{n}$ [65]. For $l_{mfp} < L$ the system is in the diffusive transport regime and charge carriers are exposed to scattering processes along the conduction channel. Graphene in the diffusive transport regime exhibits a linear dependency of conductivity σ_{xx} on the charge carrier density n. Furthermore, one can define a quasi-ballistic regime with $W < l_{mfp} < L$ in which boundary scattering and internal impurity scattering are of equal importance [39].
In addition, one can distinguish between a classical and a quantum regime specified by the Fermi wavelength λ_F and the phase coherence length l_ϕ (the distance a charge carrier travels phase-coherently) [39, 44, 63, 64]. For diffusive transport (with $\lambda_F \ll L$) the system is in the classical regime if $l_\phi < l_{mfp}$ is fulfilled. In the quantum regime, with $l_\phi > l_{mfp}$, additional quantum interference effects [39] like weak (anti-)localization [66] and universal conductance fluctuations [67] appear which originate from the wave like nature of charge carriers. In the case of ballistic transport (with $l_\phi > L$), the classical regime holds for $\lambda_F \ll L$ and charge carriers can be described as solid point particles. The transition into the quantum regime takes place, once the Fermi wave length λ_F becomes comparable to and exceeds the dominant geometrical length scale in the system (one requirement for the observation of quantized conductance steps in quantum point contacts [64, 65, 68, 69]).
In ultra-clean graphene also a third transport regime, induced by electron-electron interactions, can be observed: a hydrodynamic transport regime in which the entirety of charge carriers moves like a viscous fluid. In this super-ballistic transport regime, the interacting charge carriers are able to circumnavigate around edges and corners in a collective movement which enhances the overall conductance even above the limit of free electrons [70, 71].

Ambipolar Electric Field Effect and Quantum Capacitance

In electrical transport measurements on graphene it is possible to tune the charge carrier density over a wide range and change the type of charge carriers between electrons and holes by using a gate electrode parallel to the graphene layer (see e.g. the sample design with a back gate in Fig. 2.5). This effect is called ambipolar electric field effect which describes the fact that the Fermi energy E_F can be efficiently shifted through the electronic band structure of graphene [16, 37, 72]. The response of the system in electrical transport measurements, given by the conductivity σ_{xx}, reflects the density of states at the Fermi energy. This is expressed in the Einstein relation $\sigma_{xx} = \mathrm{D}e^2 D(E_F)$ (with diffusion constant $\mathrm{D} = \frac{1}{2} v_F^2 \tau$) which connects the density of states at the Fermi level $D(E_F)$ to the conductivity σ_{xx} [39, 73]. Fig. 2.6 (a) shows the experimental manifestation of the electric field effect in graphene. The resistivity is plotted as a function of gate voltage V_g. The Fermi energy of intrinsic (undoped) graphene lies at the CNP (minimal density of states) and the resistivity reaches its maximum. At negative gate voltages (relative to the CNP) the Fermi energy is shifted into the valence band and charge carrier transport is governed by holes. At positive gate voltages (relative to the CNP) the Fermi energy is shifted into the conduction band and into the electron regime.

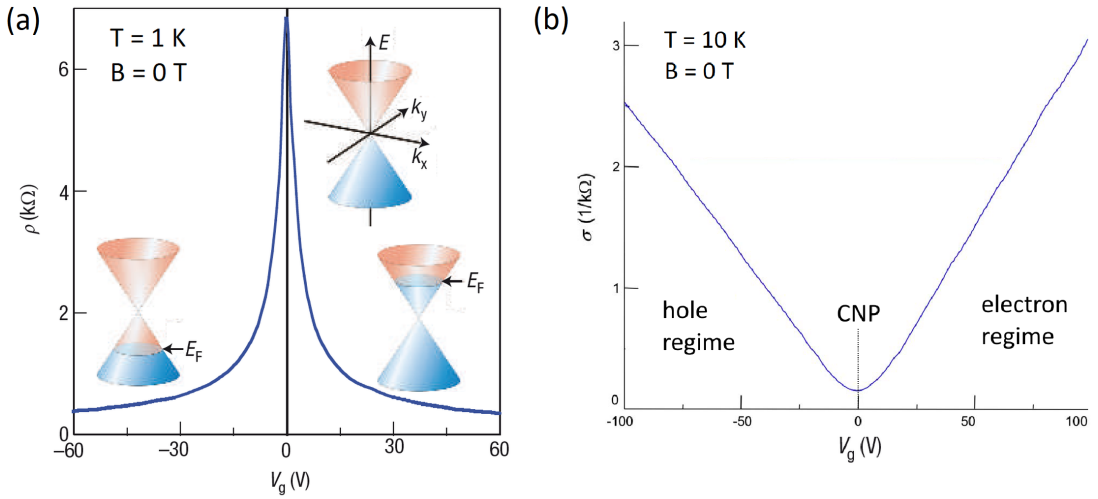

Figure 2.6: **(a)** Experimental manifestation of the ambipolar electric field effect. By applying a gate voltage V_g, the Fermi energy E_F can be shifted through the band structure. The position of the Fermi energy relative to the Dirac point changes the charge carrier type and tunes the charge carrier density and, in consequence, the resistivity. The point of maximum resistivity, at which the Fermi energy lies at the Dirac point, is called the Dirac peak or charge neutrality point (CNP). Adapted from [16]. **(b)** Conductivity σ_{xx} as a function of gate voltage V_g with hole/electron regime and the CNP. The slope of the σ_{xx} curve in the hole/electron regime determines the hole/electron mobility. Adapted from [2].

By applying the electric field effect, it is possible to extract the charge carrier density n and field effect mobility μ_{FE} [37, 72]. A simplified approximation is a plate capacitor model: the system graphene and gate electrode can be described as a plate capacitor. A dielectric with a certain thickness d and dielectric constant ε_r separates graphene and the gate electrode (see e.g. Fig. 2.5). The gate coupling $c_g = C_g/A$ (gate capacitance C_g per area A) in this model is determined as:

$$c_g = \frac{C_g}{A} = \frac{\varepsilon_r \varepsilon_0}{d} \tag{2.22}$$

with the dielectric constant of free space $\varepsilon_0 \sim 8.854 \cdot 10^{-12} \frac{F}{m}$.
The gate voltage dependent charge carrier density n in graphene is calculated by:

$$n = \frac{c_g}{e} \cdot |V_g - V_{CNP}| \tag{2.23}$$

with gate coupling c_g, elementary charge e, applied gate voltage V_g, and gate voltage value V_{CNP} at the position of the CNP. The charge carrier type is given by $\mathrm{sgn}(V_g - V_{CNP})$ (with the signum function sgn): electron transport takes place if $\mathrm{sgn}(V_g - V_{CNP}) = +1$, hole transport if $\mathrm{sgn}(V_g - V_{CNP}) = -1$. Usually, $n \to \mathrm{sgn}(V_g - V_{CNP})n = \pm n$ is used in order to express the charge carrier density in the case of electrons $(+)$ or holes $(-)$.
In the case of graphene one has to include a quantum correction to the capacitance which takes into account the square root dependency of the density of states on the charge carrier density.

This is done by an additional quantum capacitance which decreases the overall capacitance of the system. The charge carrier density, including the quantum correction, is given by [74]:

$$n = n_C + \mathrm{sgn}(n_C) n_Q \left(1 - \sqrt{1 + 2\frac{|n_C|}{n_Q}} \right) + \mathrm{sgn}(n_0)\sqrt{2|n_0|n_Q} \tag{2.24}$$

with the classical contribution from the plate capacitor model n_C, the contribution from quantum capacitance $n_Q = \frac{\pi}{2}(\frac{\hbar v_F c_g}{e^2})^2$, and a contribution n_0 due to doping. The third term in eq. 2.24 is typically weak for a reasonable n_0 [74] and can be neglected. And for sufficiently thick dielectric materials the quantum capacitance contribution can be neglected and the classical plate capacitor model is a valid approximation. Fig. 2.7 displays a comparison between the charge carrier density n as a function of dielectric thickness d in the classical and the quantum corrected model.

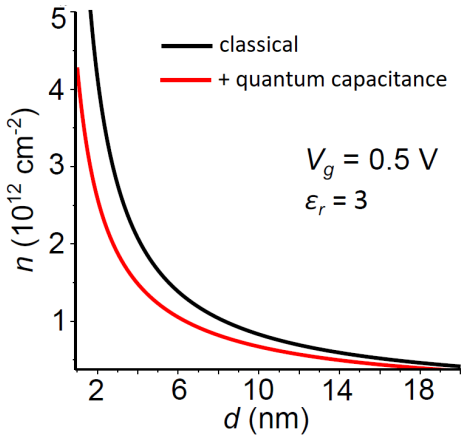

Figure 2.7: Calculated charge carrier density n in a graphene device at a gate voltage of $V_g = 0.5$ V. The gate electrode is separated from the graphene layer by a dielectric with dielectric constant $\varepsilon_r = 3$ and thickness d. For small d a quantum correction is necessary to correctly determine the charge carrier density. In the case of sufficiently thick dielectric materials, the classical plate capacitor model is a suitable approximation. Adapted from [12].

The field-effect mobility μ_{FE} of electrons and holes can be determined in a conductivity vs. gate voltage measurement, as depicted in Fig. 2.6 (b), by extracting the slope $\frac{d\sigma_{xx}}{dV_g}$ in the linear regime around the CNP. The conductivity σ_{xx} in graphene can be expressed by:

$$\sigma_{xx} = ne\mu + \sigma_0 \tag{2.25}$$

The universal value of finite residual conductivity σ_0 in ideal graphene (despite vanishing charge carrier density) is theoretically given by $\sigma_0 = \frac{4e^2}{\pi h}$ [75, 76] but usually obscured in real graphene samples [77, 78]. The field-effect mobility μ_{FE} can be determined by:

$$\mu_{FE} = \left| \frac{d\sigma_{xx}}{dV_g} \right| \cdot \frac{1}{c_g} \tag{2.26}$$

The hole/electron mobility is given in the linear hole (with $\mathrm{sgn}(\frac{d\sigma_{xx}}{dV_g}) = -1$) / electron (with $\mathrm{sgn}(\frac{d\sigma_{xx}}{dV_g}) = +1$) transport regime.

2.1.3 Magnetotransport and Quantum Hall Effect

Classical Magnetotransport

In low uniform magnetic fields applied perpendicular to the plane of a 2DEG system, charge carrier transport and the emerging ordinary Hall effect can be described within the Drude model [25, 38–43]. The corresponding Newton's equation of motion of charge carriers is given by:

$$m^*\left(\frac{d\vec{v}}{dt}+\frac{\vec{v}}{\tau}\right)=\vec{F_L} \tag{2.27}$$

In general, charged particles with charge $q=\pm e$ and effective mass m^* in an electric field $\vec{E}$ in combination with a magnetic field $\vec{B}$ experience the Lorentz force $\vec{F_L}=q(\vec{E}+\vec{v}\times\vec{B})$. The trajectories of the charge carriers are given by a circular motion around a guiding centre with cyclotron frequency $\omega_c=eB/m^*$ and cyclotron radius $R_c=\frac{v_F}{\omega_c}=\frac{\hbar k_F}{eB}$ in combination with a drift motion of the guiding centre with drift velocity $\vec{v}_d=\frac{\vec{E}\times\vec{B}}{B^2}$. By including scattering (via τ), also a drift motion along the electric field takes place. From the Drude model in the stationary case with constant current density $\vec{j}=(j_x,0,0)=qn\vec{v}$, electric field $\vec{E}=(E_x,E_y,0)$ with electric field component E_y compensating the Lorentz force ($\rightarrow$ ordinary Hall effect), and magnetic field applied perpendicular to the sample plane $\vec{B}=B(0,0,1)$, one obtains a constant longitudinal resistivity ρ_{xx} independent of magnetic field B and equal to the resistivity value at zero magnetic field (ρ_0). The resulting transverse resistivity ρ_{xy} (Hall resistivity) is proportional to the magnetic field B. Overall, the following relations are given:

$$\rho_{xx}=\frac{1}{en\mu}=\rho_0 \qquad\qquad \rho_{xy}=\frac{E_y}{j_x}=\frac{B}{qn} \tag{2.28}$$

Fig. 2.8 shows a typical magnetotransport measurement on a 2DEG system with classical transport in the low magnetic field region. It is possible to extract the charge carrier density n and the charge carrier mobility, i.e. Hall mobility μ_{Hall}, from magnetotransport measurements in the low magnetic field regime:

$$n=\frac{1}{e|\frac{d\rho_{xy}}{dB}|} \qquad\qquad \mu_{Hall}=\frac{1}{en\rho_0} \tag{2.29}$$

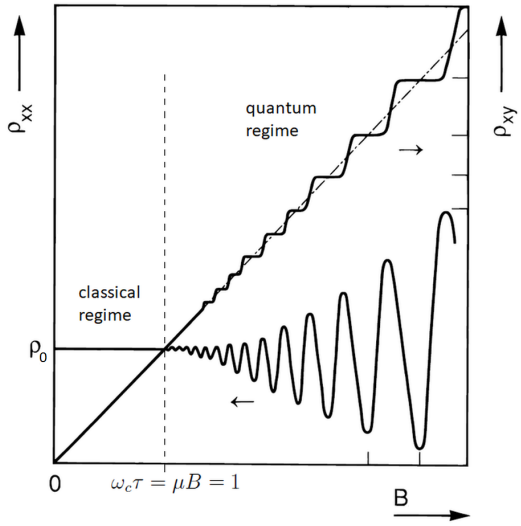

Figure 2.8: Magnetotransport in a 2DEG system. Longitudinal and transverse resistivity (ρ_{xx} and ρ_{xy}) are plotted as a function of magnetic field. In the low magnetic field regime transport can be described by the Drude model (classical regime). The onset of the high magnetic field regime is expressed by the condition $\omega_c\tau = \mu B = 1$ (dashed vertical line). In the high magnetic field regime quantum effects come into play and Shubnikov-de-Haas oscillations in ρ_{xx} and quantum Hall plateaus in ρ_{xy} are observable − manifestations of Landau quantization. Adapted from [39].

Landau Quantization in Graphene

By applying high uniform magnetic fields perpendicular to the plane of a 2DEG system, the wave-like nature of charge carriers comes into play and the system exhibits Landau quantization and enters the Quantum Hall Effect (QHE) regime [79, 80]. Further and more detailed information about Landau quantization and the QHE can be found e.g. in Refs. [31, 42, 73, 81, 82]. The onset of the high magnetic field regime is expressed by the condition $\omega_c\tau = \mu B = 1$ [39, 83], as illustrated in Fig. 2.8. If this condition holds, electrons are able to fulfil complete cyclotron orbits and interfere with themselves before being scattered. The cyclotron orbits of charge carriers become quantized, i.e. charge carriers occupy orbits with discrete energy values and the density of states condenses into discrete energy levels (Landau levels), as illustrated in Fig. 2.9 (a). In the ideal case, without disorder and scattering, discrete energy levels emerge. In real samples, including scattering and potential fluctuations, Landau levels are broadened to a finite width Γ due to collision broadening and exhibit extended and localized states, as depicted in Fig. 2.9 (b). An estimation of the characteristic Landau level broadening Γ is given within a self-consistent Born approximation $\Gamma = 2\sqrt{\frac{1}{2\pi}\hbar\omega_c\frac{\hbar}{\tau}}$ which connects Γ to the scattering time τ [25].
The Landau level energy spectrum is obtained quantum-mechanically by solving the single-particle Schrödinger equation in which the magnetic field is included by the Peierls substitution $\vec{p} \rightarrow \vec{p} + e\vec{A}(\vec{r})$. The corresponding Hamilton operator in the case of graphene is given by [84]:

$$H = v_F\vec{\sigma}(-i\hbar\nabla + e\vec{A}) \tag{2.30}$$

with vector potential $\vec{A}(\vec{r})$ which generates the magnetic field $\vec{B} = \nabla \times \vec{A}(\vec{r})$ [82, 85].

The result is a unique Landau level spectrum and, in consequence, a half-integer QHE – in contrast to the Landau level spectrum and integer QHE in 2DEG systems with parabolic dispersion relation. Overall, the Landau level energy spectrum in graphene is given by [35, 82]:

$$E_N(B) = \mathrm{sgn}(N) v_F \sqrt{2e\hbar B|N|} \tag{2.31}$$

with integer number $N = 0, \pm 1, \pm 2, ...$ (Landau level index) and magnetic field B. The Landau level spectrum in graphene as a function of magnetic field B is depicted in Fig. 2.10.

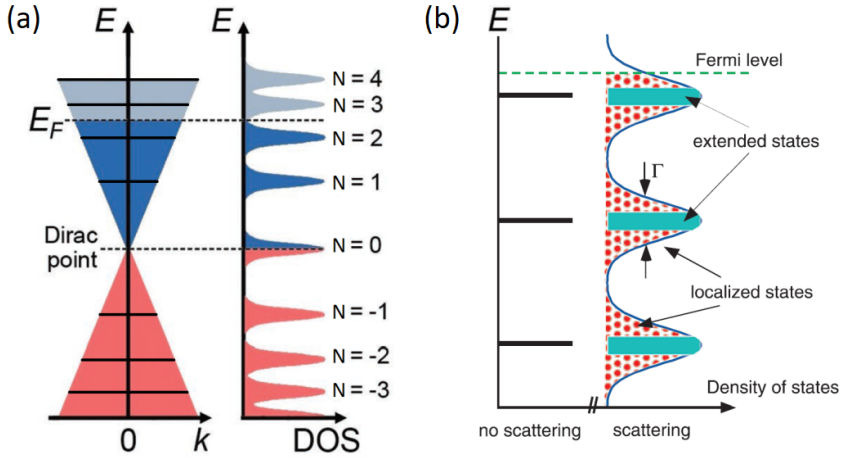

Figure 2.9: **(a)** Landau quantization in graphene. The system exhibits discrete energy levels. The corresponding density of states includes collision broadening due to scattering. Adapted from [86]. **(b)** Density of states in the case of Landau quantization. Depicted are discrete Landau levels in the ideal case and collision-broadened Landau levels with extended and localized states. Adapted from [87].

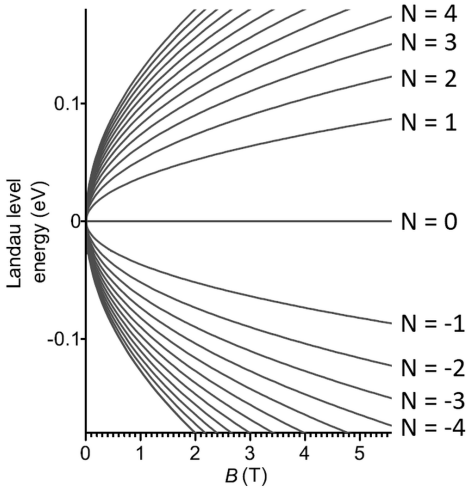

Figure 2.10: Landau level energy spectrum in graphene. Energy for several Landau levels N is plotted as a function of magnetic field B. Adapted from [88].

The number of available states per unit area in the highly degenerate Landau levels, n_L, is connected to the number of magnetic flux quanta $\Phi_0 = h/e$ per unit area in the sample [73]: $n_L = g_s g_v B/\Phi_0$ with spin and valley degeneracy (g_s and g_v). In graphene one has to take into account the half-filled Landau level at zero energy with number of available states per unit area $n_{L_0} = \frac{1}{2} n_L$. Therefore, in the case of complete filling of the Nth Landau level, one can calculate the charge carrier density n for electron-like (+, $N \geq 0$) and hole-like (−, $N \leq 0$) Landau levels [89]:

$$n = \pm(|N| + \frac{1}{2}) n_L = \pm \frac{4(|N| + \frac{1}{2})B}{\Phi_0} = \frac{\nu B e}{h} \tag{2.32}$$

The parameter $\nu = \pm g_s g_v (|N| + \frac{1}{2}) = \pm 4(|N| + \frac{1}{2})$ corresponds to the Landau level filling factor in graphene.
Compared to Landau quantization in 2DEGs with parabolic dispersion relation, the Landau level spectrum in graphene shows remarkable differences originating from the linear energy dispersion relation in the vicinity of the Dirac points [85]. The most peculiar feature of Landau quantized Dirac fermions is the magnetic field independent zero-energy Landau level ($N = 0$) which is equally shared by electrons and holes. In addition, Landau levels with index $|N| > 0$ show a square root dependency on magnetic field B and Landau level index N − in contrast to the linear dependency in the case of 2DEG systems with parabolic energy dispersion relation. As a consequence, Landau level spacing ΔE (i.e. the energy gap between adjacent Landau levels) in graphene is increased, which makes it possible to observe effects of Landau quantization and in particular the Quantum Hall Effect (QHE) in magnetotransport measurements even at room temperature T_{rt} since the Landau level spacing exceeds the thermal energy $E_{th} = k_B T$ (with temperature T and the Boltzmann constant $k_B \sim 1.381 \times 10^{-23}$ J/K) at sufficiently high magnetic fields: $\Delta E \gg E_{th}(T_{rt}) \sim 25$ meV [83].

Quantum Hall Effect in Graphene

In magnetotransport experiments resistances are determined as a function of charge carrier density at fixed magnetic field or as a function of magnetic field at constant charge carrier density in order to probe the Landau level spectrum. The behaviour of longitudinal and transverse resistance reflects the density of states at the Fermi level. Landau quantization manifests as the Shubnikov-de-Haas effect in longitudinal resistivity and as the Quantum Hall effect in transverse resistivity. Fig. 2.8 shows a typical magnetotransport measurement on a 2DEG with parabolic dispersion relation showing the integer QHE. In longitudinal resistivity (ρ_{xx}) $1/B$-periodic oscillations (Shubnikov-de-Haas oscillations) are visible. The transverse resistivity (ρ_{xy}) exhibits quantized Hall plateau values at positions of the minima in longitudinal resistivity.
The $1/B$-periodic Shubnikov-de-Haas oscillations originate from a scattering contribution (scattering conductivity) which depends on the density of states $D(E_F)$ at the Fermi energy: $\sigma_{xx} \propto D^2(E_F)$ [43, 90]. The oscillations reflect the density of states given by Landau quantization. The QHE can be explained in the framework of an edge channel picture, see e.g. Refs. [39, 41, 42, 91, 92]. Fig. 2.11 (a) shows the Landau level spectrum as a function of position for a finite sample with width W. In a finite sample, the energy levels increase in energy at the sample edges due to the confinement potential. If the Fermi level inside the sample is situated between Landau levels, there is an intersection of E_F and Landau levels at the sample edges, which gives rise to one-dimensional (1D) edge channels contributing to transport. The current at opposite sample edges flows in opposite directions and, under the prerequisite of a sufficient spatial separation

of the opposing transport channels, backscattering is suppressed. Inside the sample localized states are present which do not contribute to transport, as illustrated in Fig. 2.11 (b). In conclusion, the bulk is insulating and the current flows dissipationless along the sample edges and, in consequence, ρ_{xx} (and also σ_{xx}) approach zero value. The number of completely filled Landau levels (corresponding to the number of edge channels) which contribute to transport determines the plateau values in ρ_{xy} (and σ_{xy}) since every 1D edge channel adds one conductance quantum $g_s g_v e^2/h$ to the overall conductance (the half-filled Landau level at zero energy contributes with $\frac{1}{2} g_s g_v e^2/h$). The plateau values are given by the von Klitzing constant $R_K = h/e^2 \sim 25813\ \Omega$ and the Landau level filling factor ν. The corresponding sequence of quantized Hall plateaus is given by [2]:

$$\sigma_{xy} = \frac{\nu}{R_K} = \pm 4\left(|N| + \frac{1}{2}\right)\frac{e^2}{h} \tag{2.33}$$

If the Fermi energy is shifted across a collision-broadened Landau level, extended states inside and across the sample are occupied and scattering between edge channels takes place, which increases longitudinal resistivity/conductivity and transverse resistivity/conductivity approaches the next quantum Hall plateau.

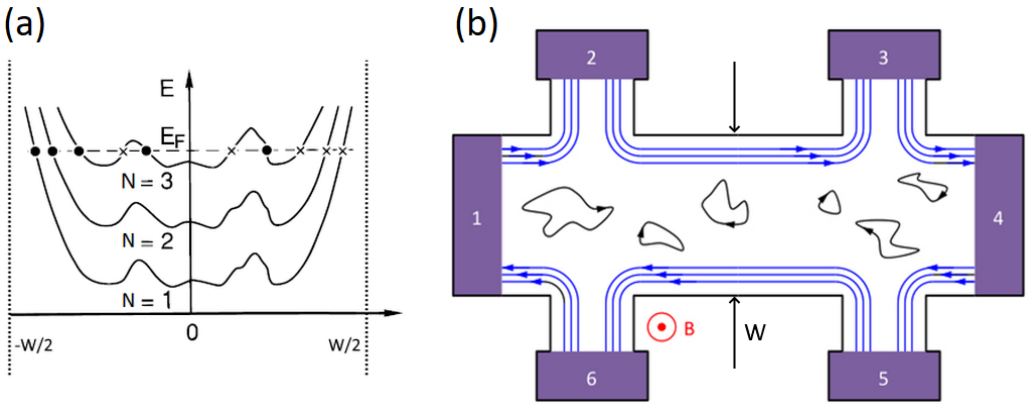

Figure 2.11: **(a)** Landau levels are broadened by a fluctuating potential landscape inside the sample and increase in energy at the sample edges due to the confinement potential. This gives rise to 1D edge channels and localized or extended states, depending on the position of E_F. Adapted from [39]. **(b)** Schematic sample in Hall bar geometry with 1D transport channels along the Hall bar edges and localized states inside the sample which do not contribute to transport. Adapted from [93].

Fig. 2.12 (a) shows a typical result of a magnetotransport measurement on graphene at a temperature of $T = 4$ K. The longitudinal resistivity ρ_{xx} and transverse conductivity σ_{xy} are plotted as a function of charge carrier density n at a constant magnetic field of $B = 14$ T. The system exhibits Landau quantization and the half-integer QHE emerges. The period of oscillations Δn in ρ_{xx} is given by $\Delta n = \frac{4Be}{h}$. Additionally conducting measurements as a function of magnetic field and plotting the received data in a so-called Landau fan diagram, as shown in Fig. 2.12 (b), allows the identification of Landau levels and energy gaps in the spectrum.
Overall, magnetotransport measurements are a versatile tool to probe the Landau level spectrum and to map out and characterize energy gaps in the magnetic band structure, i.e. the electronic band structure in combination with a magnetic field.

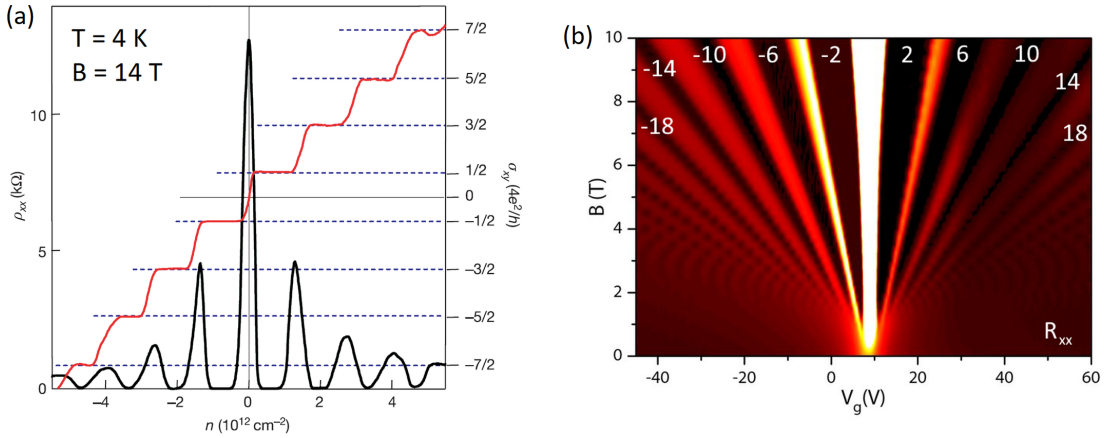

Figure 2.12: **(a)** Quantum Hall effect in graphene at $T = 4$ K and $B = 14$ T. Longitudinal resistivity ρ_{xx} and Hall conductivity σ_{xy} are plotted as a function of charge carrier density n. The half-integer quantum Hall plateaus and the zero-energy Landau level are observable. Adapted from [2]. **(b)** Landau fan diagram of graphene. The longitudinal resistance R_{xx} is plotted as a function of gate voltage V_g and magnetic field B. Energy gaps in the Landau level spectrum, corresponding to minima in R_{xx} (dark regions in the Landau fan diagram) and quantum Hall plateaus in R_{xy}, are labelled with their Landau level filling factor ν. Adapted from [94].

Magnetic Band Structure of Bloch Electrons

The Landau level spectrum is in fact only a small part of the magnetic band structure of 2D Bloch electrons in a crystal (in general in a 2D periodic potential). If the magnetic length $l_B = \sqrt{\frac{\hbar}{eB}}$ becomes comparable to the crystal lattice constant a, i.e. if the magnetic flux Φ per lattice unit cell is of the order of one magnetic flux quantum Φ_0, the energy spectrum is given by a fractal, self-similar structure − the Hofstadter butterfly energy spectrum [14] (see chapter 2.2.3 for more detailed information). Fig. 2.13 shows the Hofstadter butterfly in graphene. Usually, the Hofstadter spectrum in natural crystals is experimentally out of reach with today's standard technology since magnetic fields of several thousands of Tesla would be necessary in order to probe the Hofstadter spectrum. But the butterfly can be experimentally observed in artificial crystals with larger lattice constants realized by 2D superlattices (see chapter 4.2).

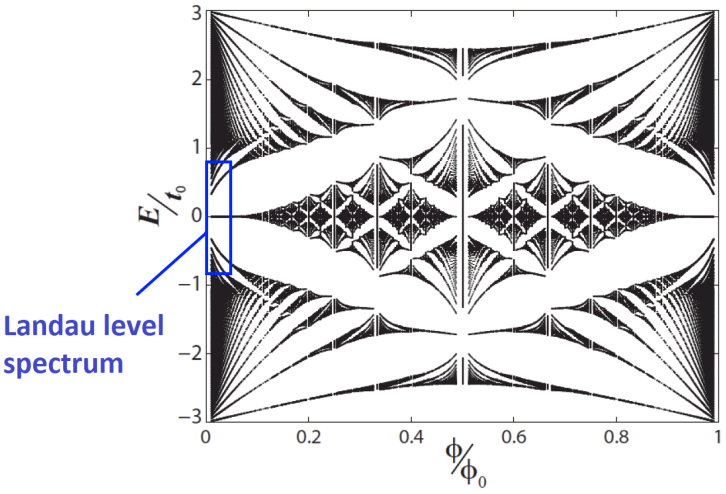

Figure 2.13: Hofstadter butterfly energy spectrum in graphene. The allowed energy values (in units of the zero-field hopping energy t_0) are plotted as a function of magnetic flux Φ per lattice unit cell (in units of the magnetic flux quantum Φ_0). Adapted from [95].

2.1.4 Graphene/hBN Heterostructures

Preparation of Graphene

In order to obtain high quality graphene for basic research, one can use a mechanical exfoliation method with adhesive tape and a graphite crystal [37, 44]. Graphite consists of many graphene layers. Interlayer bonding between adjacent layers is given by relatively weak van der Waals forces, see Fig. 2.14. As a consequence, these layers can be easily separated from each other by a piece of adhesive tape which is used to peel off graphite layers from an initial graphite crystal. Consecutive separation and removal of layers further reduces the thickness of the graphite flakes until few-layer and monolayer graphene flakes remain which can be transferred onto a substrate like a standard Si/SiO_2 chip. Graphene flakes produced this way typically have lateral dimensions of the order of a few tens of micrometres and can be used for further processing.
Due to the fact that graphene has only surface and no bulk and that the electronic properties of graphene are mainly determined by the out-of-plane $2p_z$ orbitals, its properties are strongly influenced by the environment of the graphene layer. In particular, the electronic properties can be altered by e.g. adsorbed atoms/molecules or materials which are used as a substrate or cover layer. Electrical transport experiments on graphene on a Si/SiO_2 substrate usually show diffusive transport with long-range Coulomb scattering and short-range scattering due to lattice disorder as the dominant scattering sources [96, 97]. By using a different substrate like hexagonal boron nitride, scattering can be reduced, which allows the observation of ballistic transport in graphene [49].

Hexagonal Boron Nitride

In general, hexagonal boron nitride (hBN) can be used as a substrate, protection layer, and dielectric material for graphene based electronic devices [49, 98]. It is an atomically flat and electrically insulating material (band gap ~ 6 eV) with practical dielectric properties (dielectric constant $\varepsilon_r \sim 3$, breakdown voltage ~ 0.7 V/nm) and a lattice constant comparable to graphene (with a lattice constant mismatch of about $\sim 1.8\%$ [58]).
Fig. 2.14 displays the crystal structure of hBN which is similar to graphite with boron atoms and nitrogen atoms at positions of the two sublattices A and B. Like graphite, a hBN crystal consists of monolayers stacked on top of each other with weak interlayer van der Waals bonding forces, which allows the mechanical exfoliation of thin hBN flakes from hBN crystals.

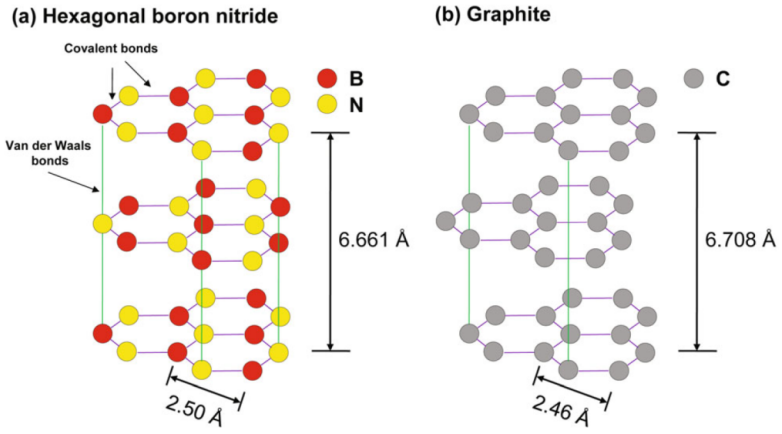

Figure 2.14: **(a)** Crystal structure of hBN. Few-layer hBN consisting of monolayers with honeycomb crystal lattice structure. Interlayer bonding is given by weak van der Waals forces. **(b)** Crystal structure of graphite for comparison. Adapted from [99].

Fig. 2.15 shows a schematic comparison between SiO_2 and hBN as a substrate for graphene. Graphene on atomically flat hBN exhibits less height variation than on SiO_2 [49, 100]. Additionally, in contrast to SiO_2, hBN has no dangling bonds/adatoms and no trapped charges which significantly worsen the electronic properties of graphene due to an induced inhomogeneous potential landscape across the graphene layer, resulting in an inhomogeneous charge carrier density distribution [49]. Fig. 2.16 demonstrates how a proper choice of the underlying substrate reduces charge carrier density inhomogeneities in graphene. Graphene on SiO_2 is exposed to rough potential fluctuations. As a consequence, intrinsic graphene on SiO_2 exhibits localized areas of electrons and holes, so-called electron-hole puddles, which influence the electronic transport [56, 57]. By using hBN as a substrate, such spatial fluctuations of charge carrier density are reduced [58, 100]. Even further improvement is possible by using an additional graphite layer as a gate material underneath the hBN which screens the electric field of trapped charges in the SiO_2 [98]. A comparison of the topography and charge carrier density distribution between graphene on SiO_2 and graphene on hBN is given in Fig. 2.17.
In order to fully protect the graphene layer from the environment (especially in view of chemicals and polymers used in further processing steps to fabricate e.g. electronic devices) a second hBN flake on top of graphene can be used as a protection layer − resulting in a hBN/graphene/hBN stack.

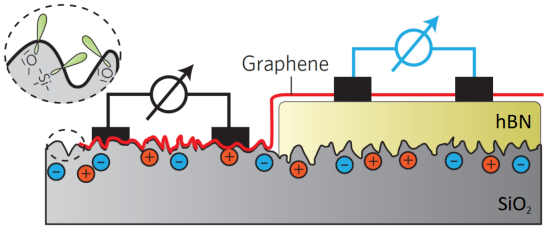

Figure 2.15: Schematic picture of graphene on SiO_2 and on hBN. Unlike SiO_2, hBN is atomically flat and has no dangling bonds and no trapped charges. It therefore enhances the electrical properties of graphene if used as a substrate. Adapted from [101].

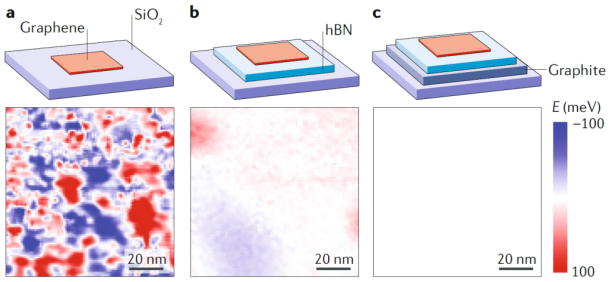

Figure 2.16: Potential landscape across a graphene layer **(a)** on SiO_2 **(b)** on hBN **(c)** on hBN with an additional graphite bottom layer. Charge carrier density inhomogeneities in the graphene layer, caused by a substrate induced inhomogeneous potential landscape, are reduced by the use of a suitable substrate. [98]

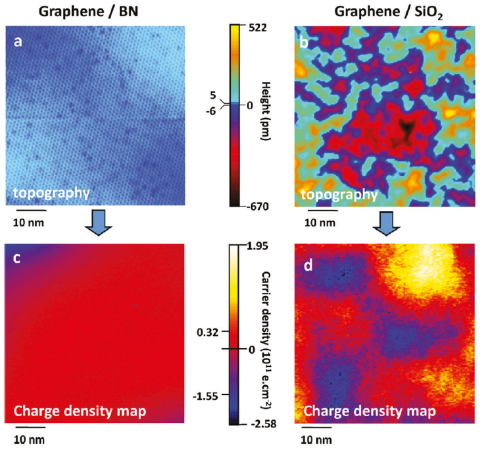

Figure 2.17: Topography of graphene **(a)** on hBN and **(b)** on SiO_2 examined by scanning tunneling microscopy. By using hBN as a substrate, the height variation of the graphene layer is reduced. **(c) and (d)** Charge density maps show a significant reduction of charge carrier density fluctuations in the case of graphene on hBN (c) compared to SiO_2 (d). [100]

hBN/Graphene/hBN Stacks

Graphene fully encapsulated between hBN – a hBN/graphene/hBN stack – serves as the basic material system for various graphene-based devices. Fig. 2.18 gives an example of the assembly of a typical hBN/graphene/hBN stack by using a van der Waals stacking method [50, 102]. In order to quantitatively evaluate the electronic quality of a material and compare effects of certain substrates, one can evaluate the charge carrier mobility. Mobilities in graphene on SiO_2 are typically of the order of 1 m^2/Vs [103]. The theoretical limit of room-temperature mobility in graphene on SiO_2 due to remote phonon scattering lies at about 4 m^2/Vs [52]. In the case of hBN/graphene/hBN stacks, room temperature mobilities in excess of 14 m^2/Vs can be reached which lies close to the theoretical intrinsic mobility limit of $\sim$ 20 m^2/Vs [50]. At cryogenic temperatures and reduced phonon scattering mobilities over 100 m^2/Vs are achievable [50, 104–106]. In this regime transport in typical mesoscopic devices is fully ballistic and mainly limited by scattering at graphene edges.

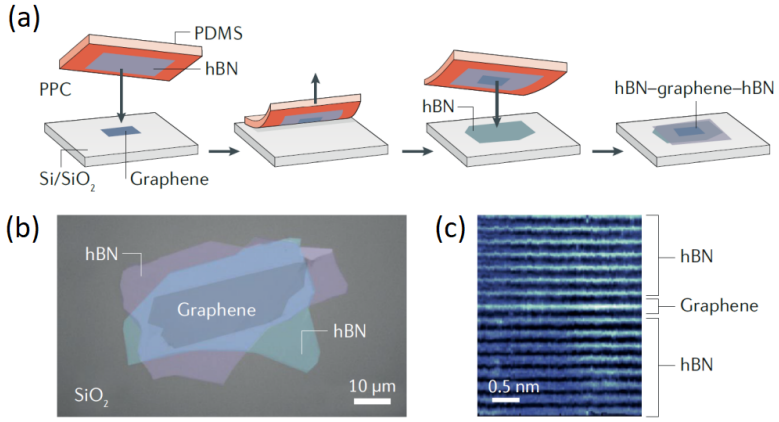

Figure 2.18: **(a)** One example of a van der Waals stacking technique used to assemble a hBN/graphene/hBN stack by using a polymer stamp. **(b)** Optical microscope image of a finished heterostructure on SiO_2. **(c)** High-resolution transmission electron microscope image of a heterostructure showing atomically sharp and impurity-free interfaces. Adapted from [50].

The fabrication of graphene/hBN heterostructures is now a common method to produce high-quality graphene devices with enhanced electrical transport properties [98, 102, 104]. The techniques developed in this field can be also used and extended to fabricate devices consisting of any material available from the variety of 2D materials, see e.g. [107, 108], in order to exploit not only individual properties of single 2D materials but also to generate new features realized by combining materials [107, 109]. Only to mention a few, there are moiré superlattices in graphene/hBN heterostructures [8–10], spin-orbit proximity effect in graphene with transition metal dichalcogenides [110–113], magnetic proximity effect in graphene with magnetic 2D materials [114, 115], and insulating, superconducting, and ferromagnetic states in twisted bilayer graphene [116–118]. Usually, the fabrication of such devices takes place by exfoliation and stacking methods. But there is a variety of techniques under development in order to produce 2D materials and heterostructures also in view of industrial applications [119–132]. The field of 2D materials opens up new playgrounds in which not only electronics but also photonics and optoelectronics [133–135], spintronics [136–138], valleytronics [139, 140], straintronics [141, 142], and twistronics [143–147] give rise to new physical effects and potential applications.

2.2 Superlattice Effects: Electrons in a Periodic Potential

The following section gives an overview of the impact of superlattices on the electronic band structure of graphene. After a short introduction to the basics of superlattice physics, the theoretical and experimental background of one-dimensional (1D) and two-dimensional (2D) superlattices in graphene is presented. Furthermore, properties of 1D and 2D superlattices in magnetic fields are discussed with focus on the Hofstadter butterfly energy spectrum and magnetotransport.

2.2.1 Modification of Electronic Band Structure

Modifying the electronic band structure of a material like graphene and producing tailor-made electronic properties lies at the heart of condensed matter physics and nanoscience. One possibility to achieve this goal is given by superimposing a periodic potential on the electrons in the system. The physics in such a superlattice − which can be seen as an artificial crystal − is in general equivalent to the physics in a natural crystal: electrons in a periodic potential occupy energy bands and follow Bloch's theorem. The following overview mainly follows the descriptions in Refs. [25, 38, 40, 148, 149].
The electronic band structure of a 2DEG system with superimposed periodic modulation potential can be obtained by solving the corresponding single-particle Schrödinger equation $H\Psi = E\Psi$ with Hamiltonian H corresponding to quasi-free electrons in a periodic modulation potential $V(\vec{r})$:

$$H = H_0 + V(\vec{r}) \tag{2.34}$$

H_0 is the Hamiltonian of the unperturbed system. For electrons with parabolic dispersion relation $H_0 = \frac{\hbar^2 k^2}{2m^*}$. In graphene $H_0 = \hbar v_F \vec{\sigma}^{(*)} \vec{k}$ at the K (K') point and $V(\vec{r}) \rightarrow I_2\, V(\vec{r})$ with the 2×2 identity matrix I_2 [150–152]. The superlattice, i.e. the periodic potential, is defined by $V(\vec{r})$ with $V(\vec{r} + \vec{R}) = V(\vec{r})$ under translation with a lattice vector $\vec{R}$ of the superlattice.
The wave functions $\Psi_{n,\vec{k}}(\vec{r})$ (Bloch waves) which solve the corresponding Schrödinger equation are given by plane waves $e^{i\vec{k}\vec{r}}$ modulated by periodic functions $u_{n,\vec{k}}(\vec{r})$ with the same periodicity as the superlattice ($u_{n,\vec{k}}(\vec{r} + \vec{R}) = u_{n,\vec{k}}(\vec{r})$):

$$\Psi_{n,\vec{k}}(\vec{r}) = e^{i\vec{k}\vec{r}} u_{n,\vec{k}}(\vec{r}) \tag{2.35}$$

The energy spectrum is given by the eigenvalues of the Schrödinger equation. The energy values for all $\vec{k}$ for a given n (integer band index $n = 1, 2, 3, ...$) form energy bands $E_n(\vec{k})$ (in the case of a superlattice also referred to as minibands) which are separated by energy gaps E_{gap} (minigaps). Since $E_n(\vec{k} + \vec{G}) = E_n(\vec{k})$ with reciprocal lattice vector $\vec{G}$ of the superlattice, one can use a reduced zone scheme and only consider energy bands in the first Brillouin zone of the superlattice (mini-Brillouin-zone). The emergence of energy gaps can be understood in terms of Bragg reflection. As an example, a 1D periodic potential in x-direction $V(x) = V_0 \cos(Gx)$ with modulation amplitude V_0, reciprocal lattice vector $G = \frac{2\pi}{a}$, and lattice constant a is considered: At the Brillouin zone boundaries, i.e. at $k_x = \pm i\frac{\pi}{a}$ with integer parameter $i = 1, 2, ...$, the condition for Bragg reflection is fulfilled and electrons with corresponding wave vectors $k_x = \pm i\frac{\pi}{a}$ are backscattered. Due to interference, standing waves are formed which are given by a linear

superposition of incoming and backscattered waves. This eventually results in two possible solutions with different energies giving rise to an energy gap. Fig. 2.19 gives a schematic overview of the energy spectrum of electrons with parabolic dispersion relation in a periodic potential.

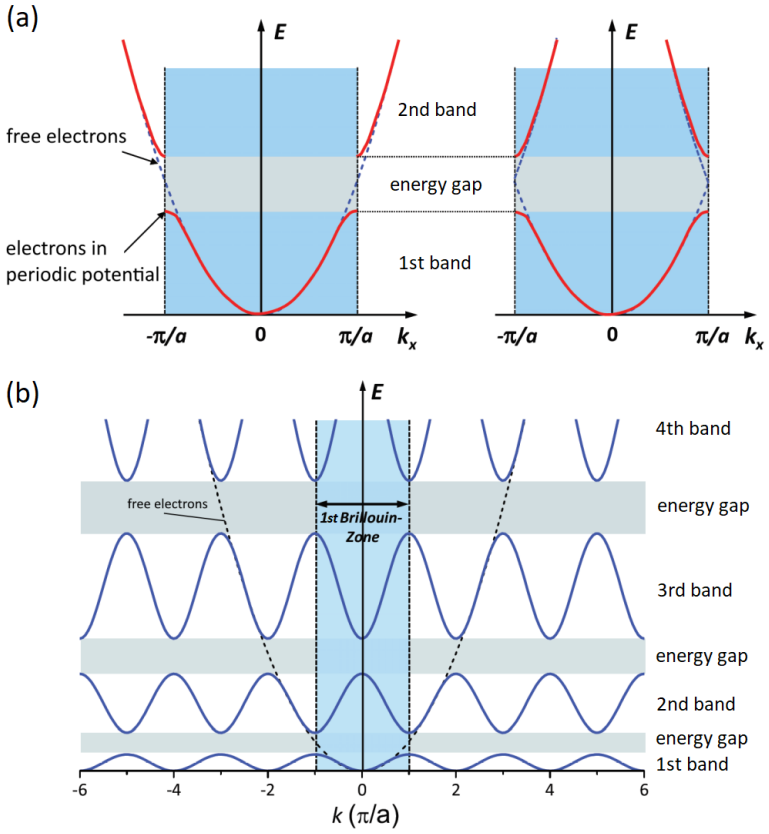

Figure 2.19: **(a)** A superlattice in x-direction with lattice constant a induces energy gaps at the mini-Brillouin-zone boundaries at $k_x = \pm i\frac{\pi}{a}$ with integer parameter $i = 1, 2, ...$ (extended zone scheme) and backfolding of energy bands into the first mini-Brillouin-zone (reduced zone scheme) with $-\frac{\pi}{a} \leq k_x \leq +\frac{\pi}{a}$. **(b)** Periodic zone scheme showing energy bands and energy gaps for electrons in a periodic potential. The dashed lines display the parabolic dispersion relation for free electrons with parabolic dispersion relation. Adapted from [40].

1D Superlattices in Graphene

Fig. 2.20 shows the impact of a 1D superlattice on the electronic band structure of graphene. The superlattice with period a and potential barrier height V_0 is orientated along the x-direction. The corresponding energy dispersion was calculated in the framework of an effective-Hamiltonian formalism [153]. Perpendicular to the direction of the 1D periodic potential modulation (i.e. in y-direction) the original Dirac cone is distorted − in accordance with a renormalization of the Fermi velocity. The velocity of charge carriers (and therefore the mobility) in that direction is reduced. In direction of the superlattice potential (i.e. in x-direction) no renormalization of the Fermi velocity takes place. Such an anisotropic renormalization of the Fermi velocity in a 1D graphene superlattice, which is tunable by the modulation amplitude, enables in principle the control of the flow of electrons preferably in one direction [153].

Due to the chiral nature of Dirac fermions in graphene, the emergence of energy gaps at the mini-Brillouin-zone boundary depends on the wave vector $\vec{k}$. In a simple picture: Upon normal incidence on the potential barriers, backscattering is suppressed due to Klein tunnelling which prevents the emergence of an energy gap. At points of vanishing energy gaps adjacent minibands touch each other and satellite Dirac points start to appear. The anisotropic distortion of the Dirac cone and the manifestation of satellite Dirac points was experimentally verified in electrical transport measurements on 1D graphene superlattices realized by a patterned dielectric technique [152].

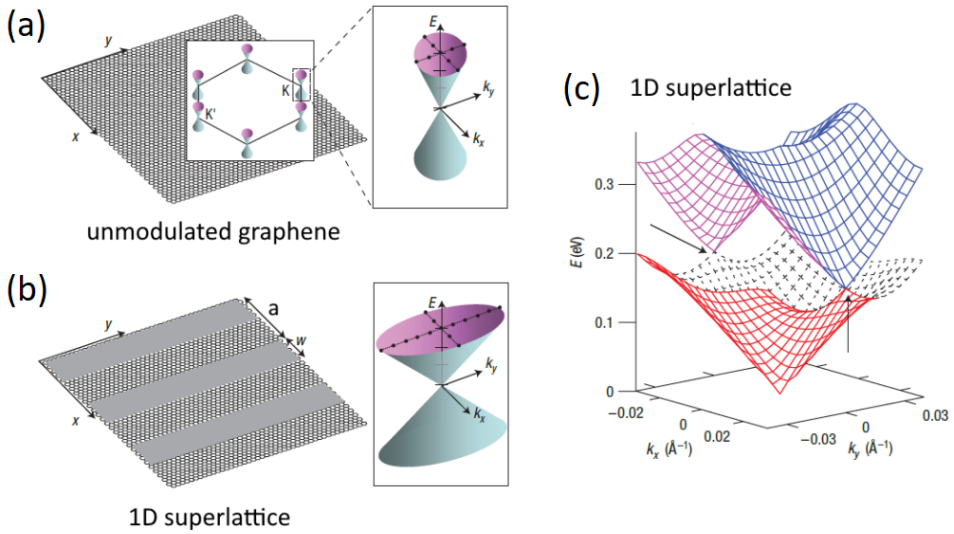

Figure 2.20: **(a)** Dirac cones in unmodulated graphene. **(b)** In a 1D superlattice (with lattice constant a) the Fermi velocity is renormalized in direction perpendicular to the modulation potential. **(c)** Modified band structure in the conduction band of graphene. Depending on the wave vector $\vec{k}$, either satellite Dirac points (black arrows) or energy gaps emerge at the mini-Brillouin-zone boundary. Adapted from [153].

In symmetric 1D graphene superlattices the emergence of additional zero-energy Dirac points and their tunability by the modulation amplitude V_0 was theoretically shown, as depicted in Fig. 2.21 [154, 155]. At zero modulation the original Dirac cone is present. By increasing the modulation strength, additional Dirac points at zero energy start to manifest. These newly generated zero-energy Dirac points also have impact on the Landau level spectrum of 1D modulated graphene, which is illustrated in Fig. 2.22. Depending on the number of additional zero-energy Dirac points a modification of the Landau level energy spectrum takes place: Landau levels at charge neutral filling become $4(2i+1)$-fold degenerate with corresponding Hall conductivity with step size $\sigma_{xy} = 4(2i+1)\frac{e^2}{h}$ [154]. The integer parameter $i = 0, 1, 2, ...$ is tunable by the potential strength and the periodicity of the superlattice [154]. Furthermore, in a 1D superlattice Landau levels are transformed into Landau bands which exhibit a finite and magnetic field dependent band width ΔE. This aspect is covered in greater detail in chapter 2.2.2.

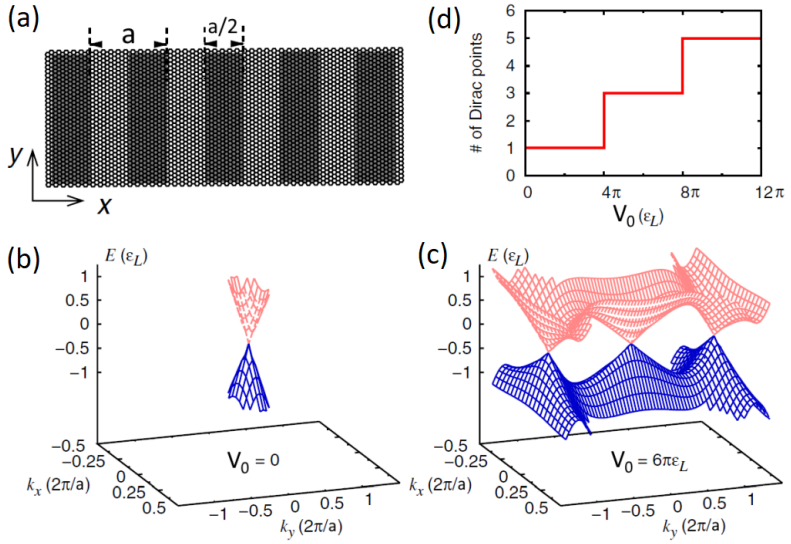

Figure 2.21: **(a)** Symmetric 1D graphene superlattice in x-direction with lattice constant a and modulation amplitude V_0. **(b)** The unperturbed Dirac cone of graphene at zero modulation potential. **(c)** Upon increasing the modulation amplitude, additional zero-energy Dirac cones start to manifest in k_y-direction. **(d)** The number of zero-energy Dirac cones depends on the potential modulation strength. Energy E and modulation amplitude V_0 are given in units of $\epsilon_L = \hbar v_F/a$. Adapted from [154].

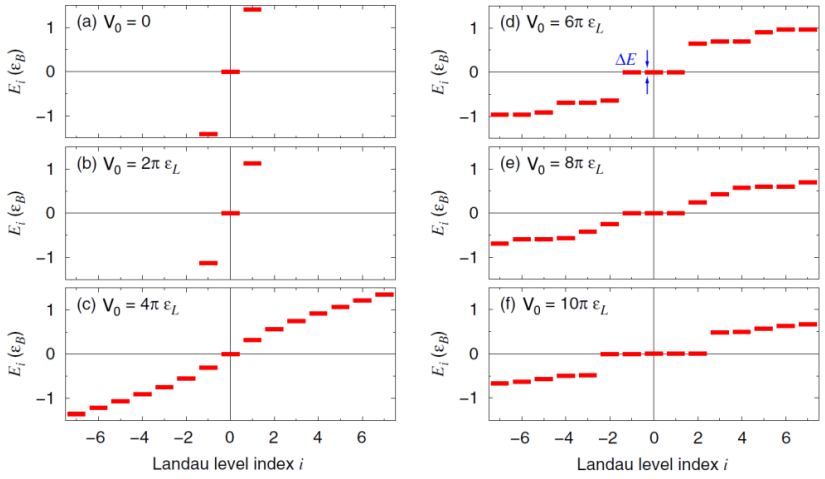

Figure 2.22: Modified Landau level spectrum of symmetric 1D graphene superlattices. Depending on the modulation amplitude V_0, which controls the number of zero-energy Dirac cones, additional Landau levels occur resulting in a modified quantum Hall effect. In addition, a 1D superlattice causes a magnetic field dependent broadening ΔE of Landau levels into Landau bands. Energy E_i is given in units of $\epsilon_B = \hbar v_F/l_B$. Modulation amplitude V_0 is given in units of $\epsilon_L = \hbar v_F/a$. Adapted from [154].

2D Superlattices in Graphene

The impact of a 2D superlattice on the electronic band structure of graphene in the case of rectangular [153] and triangular/hexagonal [151] 2D superlattices is displayed in Fig. 2.23. The results concerning the renormalization of the Fermi velocity, the emergence of energy gaps at the mini-Brillouin-zone boundary, and the manifestation of satellite Dirac points are in principle analogous to the case of a 1D superlattice: In 2D modulated graphene the Fermi velocity is renormalized in every direction and, depending on the wave vector k, additional Dirac points start to appear at the mini-Brillouin-zone boundary.

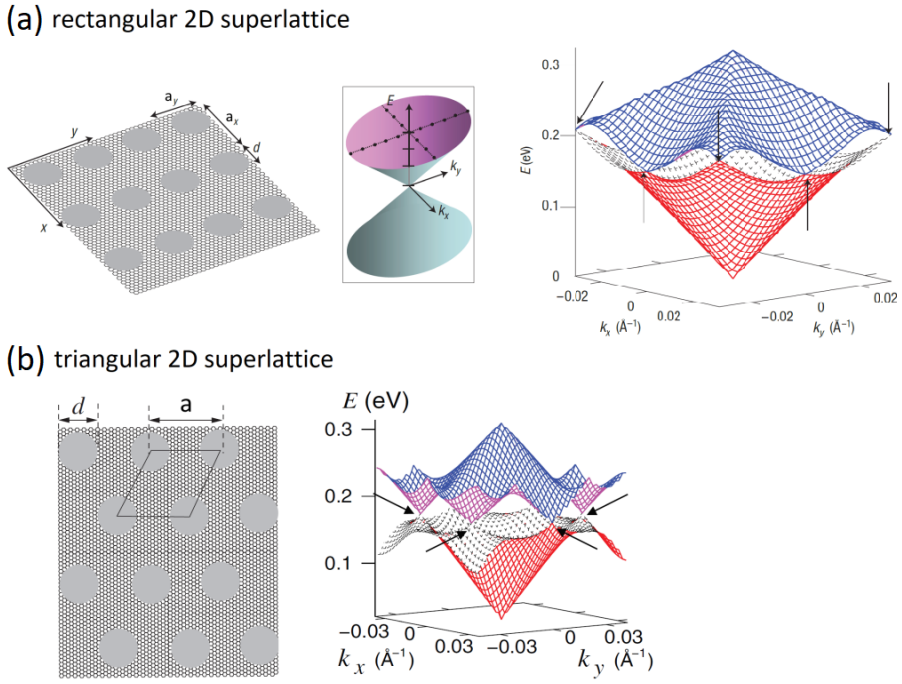

Figure 2.23: **(a)** A rectangular 2D superlattice in graphene causes an anisotropic renormalization of the Fermi velocity in every direction. Satellite Dirac points (black arrows) manifest at the corresponding mini-Brilloin-zone boundary − here shown for the conduction band of graphene. Adapted from [153]. **(b)** The situation in a triangular/hexagonal 2D superlattice in graphene: Additional and well-isolated Dirac points start to emerge (black arrows) − here, again, only the conduction band of graphene is shown. Adapted from [151].

In graphene, 2D superlattice effects were experimentally demonstrated in graphene/hBN heterostructures originating from the interplay between the two 2D materials [8–10, 156, 157]. Due to the similar crystal structure and the small lattice constant mismatch of the two materials, a moiré pattern with hexagonal symmetry and maximum lattice constant of about $a \sim 14$ nm emerges, which acts as a 2D periodic potential on the charge carriers in graphene.

The moiré wavelength, i.e. the superlattice constant a, is determined by the relative orientation between the graphene and the hBN layer (see Fig. 2.24 (a) and (b)). The superlattice constant a of such a moiré superstructure in a graphene/hBN device is given by [156]:

$$a = \frac{(1+\delta)a_0}{\sqrt{2(1+\delta)(1-\cos\phi)+\delta^2}} \tag{2.36}$$

with the lattice constant a_0 of graphene, the lattice constant mismatch δ between graphene and hBN, and the relative rotation angle ϕ between the two layers.
In moiré superlattices it is possible to experimentally observe and study the aforementioned modifications of the electronic band structure in great detail. Fig. 2.24 (c) displays electrical transport experiments on moiré superlattices in which the manifestation of satellite Dirac points was observed. By shifting the Fermi level E_F across the newly generated Dirac points in the valence and conduction band, additional maxima in the longitudinal resistance occur which are accompanied by a sign change of the Hall resistance in low magnetic fields indicating a transition of E_F over a band edge and an effective change between electron and hole like type of charge carriers. The shifting of the Fermi energy towards the position of the satellite Dirac points in the valence/conduction band is equivalent to filling up the first minibands with holes/electrons. Due to the four-fold degeneracy in graphene, the first minibands are filled at a charge carrier density corresponding to four electrons per superlattice unit cell area A_{sl}. Consequently, the gate voltage difference ΔV_g between main and the satellite Dirac points obtained in electrical transport measurements corresponds to a change in charge carrier density $\Delta n = \frac{4e}{A_{sl}}$ (and therefore depends on the superlattice unit cell area A_{sl} and superlattice constant a). In a hexagonal moiré superlattice with $A_{sl} = \frac{\sqrt{3}}{2}a^2$ the superlattice constant a can be extracted from electrical transport measurements by [9]:

$$a = \sqrt{\frac{4e}{\frac{\sqrt{3}}{2}\Delta n}} \tag{2.37}$$

Besides moiré superstructures, superlattices in graphene can be also electrostatically generated by periodically arranged/patterned gates [7, 12, 158, 159] or patterned dielectrics [11, 152, 160] which enable to induce a gate-tunable periodic charge carrier density modulation. In this work, electrostatically defined 2D superlattices are investigated realized by the combination of uniform and patterned gates [7]. This provides a less invasive method for band structure engineering than e.g. nanostructuring. In addition, graphene antidot superlattices, a special kind of nanostructured graphene, are investigated which in principle allow to induce magnetically tunable energy gaps in the initially gapless graphene (see chapter 2.3).

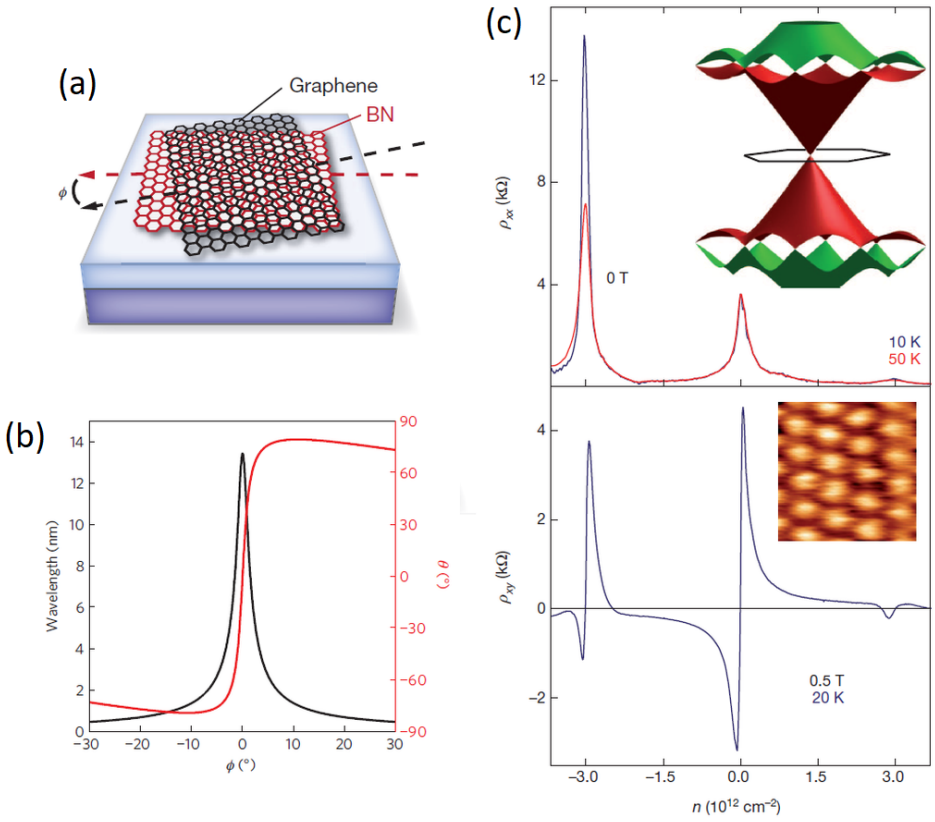

Figure 2.24: **(a)** Schematic picture of a moiré superlattice in a graphene/hBN heterostructure. The relative orientation between the two layers determines the superlattice constant. Adapted from [9]. **(b)** The wavelength, i.e. the superlattice constant a, of a moiré superlattice is plotted as a function of the relative rotation angle ϕ between the graphene and hBN layer (black curve). Also the relative orientation Θ between the moiré superstructure and the graphene lattice as a function of ϕ (red curve) is shown. [156] **(c)** Electrical transport measurements on a moiré superlattice with $a \sim 12$ nm. Besides the main Dirac point at the CNP, satellite Dirac points start to manifest originating from the modified band structure in the valence and conduction band of graphene (see upper inset). In low magnetic fields the satellite Dirac points are accompanied by a sign change of the Hall resistance pointing towards a transition of the Fermi energy across a newly generated band edge and an effective change between hole and electron type of charge carriers similar to the behaviour at the main Dirac point − the "cloned" Dirac points reflect the band structure at the main Dirac point. Lower inset shows a conductive atomic force microscope image of a moiré pattern with $a \sim 11$ nm. [10]

2.2.2 Magnetotransport in a 1D Superlattice: Landau Bands and Weiss Oscillations

The magnetic band structure of a 2DEG system subjected to a weak 1D periodic potential $V(x) = V_0 \cos(Gx)$ in x-direction with modulation amplitude V_0 and $G = \frac{2\pi}{a}$ can be calculated in first-order perturbation theory. One obtains the modified energy spectrum E_N [43]:

$$E_N = E_{N,0} + \langle Nx_0|V(x)|Nx_0\rangle \tag{2.38}$$

Here, $E_{N,0}$ is the Landau level energy in the unperturbed case, N is the Landau level index, $x_0 = -l_B^2 k_y$ is the centre coordinate of the Landau orbits, l_B is the magnetic length, and $|Nx_0\rangle$ corresponds to the Landau level wave function. The 1D superlattice lifts the degeneracy of Landau levels with respect to x_0 (and therefore k_y) and the discrete Landau levels are broadened into Landau bands with finite band width ΔE_N [161–163]. This results in the following expression for electrons with parabolic dispersion relation and $E_{N,0} = (N + \frac{1}{2})\hbar\omega_c$ [43]:

$$\langle Nx_0|V(x)|Nx_0\rangle = \Delta E_N \cos(Gx_0) = V_0 e^{-\frac{1}{2}X} L_N(X) \cos(Gx_0) \tag{2.39}$$

$L_N(X)$ is a Laguerre polynomial of N-th order and $X = \frac{1}{2}G^2 l_B^2$. Following from this, the band width of the N-th Landau band in a 1D superlattice with lattice constant a depends on the magnetic field B applied perpendicular to the sample. The band width vanishes whenever the Laguerre polynomials are zero, i.e. in the N-th Landau band there are N zero points. At these flat band conditions the discrete Landau level is restored. In graphene, with $E_{N,0} = \mathrm{sgn}(N) v_F \sqrt{2e\hbar B|N|}$, the following expression for the band width ΔE_N can be derived [84, 164]:

$$\Delta E_N = \frac{V_0}{2} e^{-\frac{1}{2}X} \{L_N(X) + L_{N-1}(X)\} \tag{2.40}$$

In semi-classical approximation the flat band condition is expressed by the cyclotron radius R_c of charge carriers and an integer parameter λ. The band width vanishes whenever the cyclotron radius is commensurable with the period a of the superlattice [12, 43, 164]:

$$2R_c = \left(\lambda - \frac{1}{4}\right) a \tag{2.41}$$

The magnetic band structure of a 1D superlattice in the case of electrons with parabolic dispersion relation and superlattice broadened Landau levels is shown in Fig. 2.25 (a). The dependency of the band width and density of states on the cyclotron radius is illustrated in Fig. 2.25 (b). Depending on the size of cyclotron orbits, the electrons "feel" an effective modulation potential which can be estimated by averaging the periodic potential over the whole cyclotron orbit. If the flat band condition is fulfilled, the effective modulation potential vanishes and the unperturbed Landau level is restored. In this case, the density of states shows its maximum value. If $2R_c = (\lambda + \frac{1}{4})a$, the band width reaches its maximum value and the density of states exhibits a minimum. The corresponding magnetic band structure of a 1D graphene superlattice is shown in Fig. 2.26.

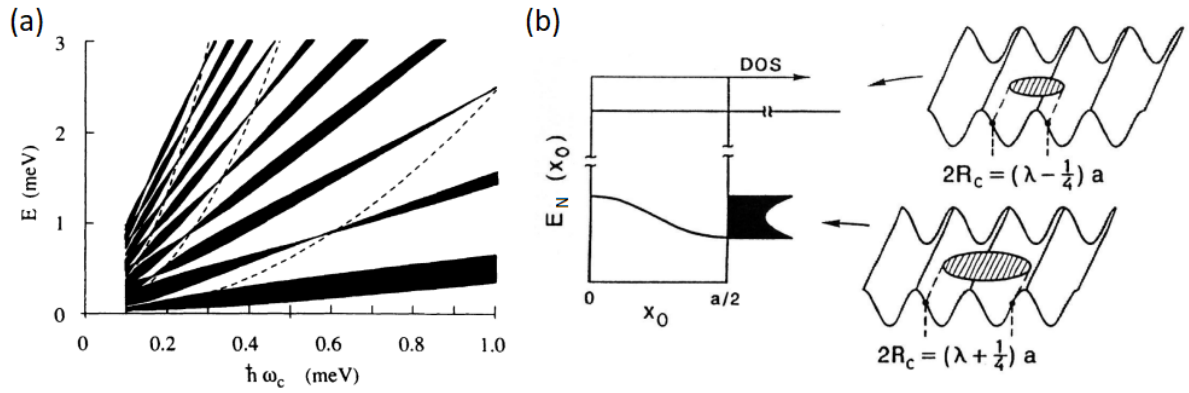

Figure 2.25: **(a)** Magnetic band structure of a 1D superlattice in the case of electrons with parabolic dispersion relation. Landau levels are broadened into Landau bands due to the 1D periodic potential modulation. The band width oscillates as a function of magnetic field. The dashed lines mark the flat band positions at which the band width vanishes and the original Landau levels are restored. **(b)** Energy of Landau levels/bands as a function of the guiding centre coordinate x_0 and corresponding density of states for two different cyclotron orbits: Upper case exhibits discrete Landau levels and maximum density of states at the flat band position. Lower case shows cyclotron orbits corresponding to maximum band width and minimum density of states. Adapted from [43].

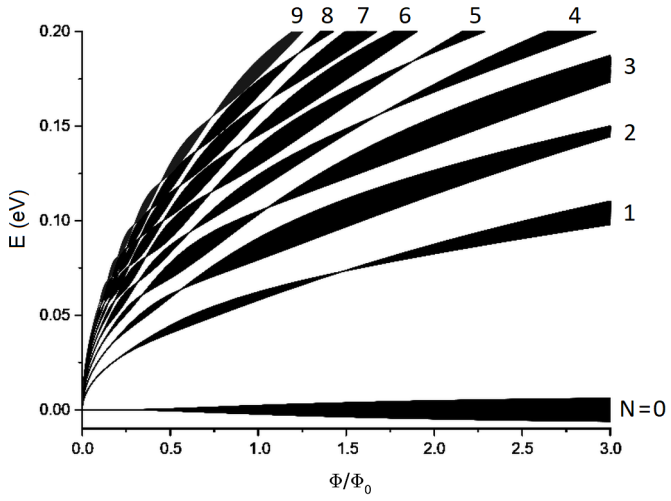

Figure 2.26: Effect of a 1D superlattice with $V_0 = 20$ meV and $a = 40$ nm on the Landau level spectrum of graphene, calculated with equations (2.38) and (2.40). The discrete Landau levels are broadened into Landau bands with magnetic field dependent band width. The band width vanishes at the flat band positions and the discrete Landau levels are restored. Landau levels/bands with $N \geq 0$ up to $N = 9$ are shown.

In magnetotransport experiments the superlattice induced and magnetic field dependent band width of Landau levels manifests as temperature robust commensurability or Weiss oscillations (see Fig. 2.27 (a)) which were first observed in high-mobility GaAs-based 2DEG systems [43, 161]. In longitudinal resistance ρ_{xx} (in direction of the 1D periodic potential modulation), $1/B$-periodic

oscillations with minima at the flat band positions occur. In ρ_{yy} (in the direction perpendicular to the potential modulation), less pronounced oscillations with maxima at the flat band positions emerge. The experimental observation of Weiss oscillations in graphene (see Fig. 2.27 (b)) was achieved by a double gating technique [12] which is also used in this work to fabricate and investigate 2D graphene superlattices. Furthermore, commensurability oscillations in ρ_{xx} and also ρ_{yy} were experimentally observed in 1D graphene superlattices realized by a patterned dielectric technique [152].

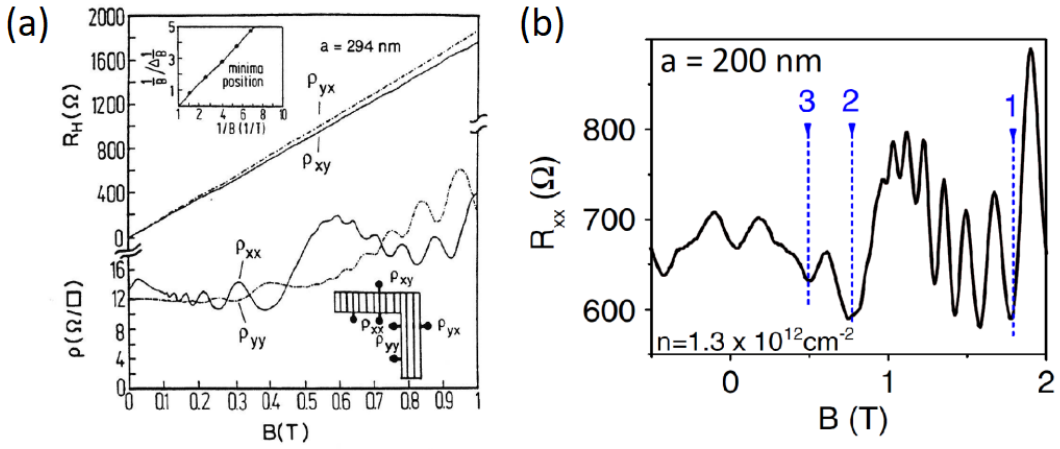

Figure 2.27: **(a)** Weiss oscillations in a 2DEG with 1D periodic potential modulation with lattice constant $a = 294$ nm. In ρ_{xx}, $1/B$-periodic oscillations occur with minima at the flat band positions. In ρ_{yy}, oscillations manifest with maxima at the flat band positions. The oscillations in ρ_{xx} can be explained by a band width dependent band conductivity contribution which is not present in ρ_{yy}. The oscillations in ρ_{yy} are caused by a density of states dependent scattering conductivity contribution. At higher magnetic fields, Shubnikov-de-Haas oscillations start to appear which are modulated by Weiss oscillations. [43, 161] **(b)** Weiss oscillations in a 1D graphene superlattice with lattice constant $a = 200$ nm. The dashed lines show the first three flat band positions with $\lambda = 1, 2, 3$ and corresponding minima in longitudinal resistance. Adapted from [12].

Weiss oscillations can in principle be explained by two additional conductivity contributions to the overall Drude conductivity induced by the 1D periodic potential: a band conductivity and a scattering conductivity contribution [43].

Band Conductivity

The band conductivity contribution originates from the superlattice induced lifting of the Landau level degeneracy with respect to k_y. The emerging dispersion of Landau bands is connected to a group velocity v_g which vanishes at the flat band positions [43]:

$$v_g = \langle Nx_0|v_y|Nx_0\rangle = \frac{1}{\hbar}\frac{dE_N}{dk_y} \tag{2.42}$$

In the framework of the Kubo formalism the group velocity matrix element $\langle Nx_0|v_y|Nx_0\rangle$ can be connected to a conductivity correction $\Delta\sigma_{yy}$, i.e. the band conductivity contribution, which is

added to the overall Drude conductivity [43]. In particular, the band conductivity correction is proportional to the square of the group velocity and therefore depends on the band width. Generally, energy bands with large band width, i.e. highly dispersive bands, exhibit a large band conductivity contribution. In graphene superlattices the band conductivity contribution is given by [84]:

$$\Delta\sigma_{yy} = A\Psi \tag{2.43}$$

with

$$A = 8\pi^2 \frac{e^2}{h} \frac{V_0^2 \tau \beta}{\hbar} \tag{2.44}$$

and with $\beta = \frac{1}{k_B T}$ and function

$$\Psi = \frac{1}{4} X e^{-X} \sum_{N=0}^{\infty} \frac{\exp(\beta(E_{N,0} - E_F))}{[\exp(\beta(E_{N,0} - E_F)) + 1]^2} [L_N(X) + L_{N-1}(X)]^2 \tag{2.45}$$

From the tensor relationship between $\boldsymbol{\sigma}$ and $\boldsymbol{\rho}$ ($\boldsymbol{\sigma} = \boldsymbol{\rho}^{-1}$ and therefore $\sigma_{yy} \propto \rho_{xx}$), the additional band conductivity $\Delta\sigma_{yy}$ is connected to an additional resistivity contribution $\Delta\rho_{xx}$ which manifests as the observed magnetoresistance oscillations in ρ_{xx}. In principle, an increase in conductivity in y-direction causes an increase of resistivity in x-direction.
In conclusion, Weiss oscillations in ρ_{xx} (in direction of the 1D periodic potential modulation) are given by an oscillating band conductivity contribution in y-direction due to the formation of Landau bands [43]. Due to the higher Fermi velocity of Dirac electrons, Weiss oscillations in graphene are more pronounced compared to a system of electrons with parabolic dispersion relation [84]. Furthermore, Weiss oscillations in direction of a 1D periodic potential modulation (in x-direction) can be also explained by a guiding-centre drift of cyclotron orbits in y-direction emphasizing their quasi-classical nature [39] which also manifests in their high temperature robustness [84].

Scattering Conductivity

An additional conductivity contribution which has to be taken into account is the scattering conductivity σ_{sc} which stems from the density of states dependent scattering rate of electrons at the Fermi level and has therefore a purely quantum-mechanical origin [41, 43]:

$$\sigma_{sc} \propto D^2(E_F) \tag{2.46}$$

The oscillating band width, which is connected to an oscillating density of states (see Fig. 2.25 (b)), gives rise to an oscillating scattering conductivity contribution appearing as magnetoresistance oscillations in ρ_{yy} which are opposite in phase with the Weiss oscillations in ρ_{xx}. This is due to the fact that at the flat band positions the band width (and therefore the band conductivity contribution) vanishes but the density of states (and therefore the scattering conductivity contribution) reaches its maximum. The scattering conductivity contribution also occurs in ρ_{xx} but is usually obscured by the more pronounced band conductivity oscillations [43].

2.2.3 Magnetotransport in a 2D Superlattice: Hofstadter Butterfly

A 2D electron system subjected to a 2D periodic potential and a uniform magnetic field applied perpendicular to the plane of the 2DEG exhibits a fractal, self-similar energy spectrum − the Hofstadter butterfly energy spectrum − with its peculiar appearance resembling a butterfly [14]. Fig. 2.28 shows the originally calculated and visualized Hofstadter butterfly for electrons in a square lattice with lattice constant a and unit cell area $A_{sl} = a^2$. The allowed energy values ϵ of Bloch electrons are given as a function of magnetic field B expressed by $\alpha = \Phi/\Phi_0$, i.e. the magnetic flux $\Phi = BA_{sl}$ per lattice unit cell in units of the magnetic flux quantum $\Phi_0 = h/e \sim 4.136 \times 10^{-15}$ Vs. Due to the interplay between two characteristic length scales, i.e. whenever the magnetic length l_B becomes comparable and is commensurable to the lattice constant a of the crytal lattice, a single initial energy band splits up into a certain number of minibands and minigaps depending on the magnetic flux per lattice unit cell. In order to reach a regime in which the Hofstadter butterfly energy spectrum manifests, the magnetic flux piercing one lattice unit cell has to be of the order of one magnetic flux quantum.

General Derivation

In general, the motion of electrons in a magnetic field $\vec{B}$ and a periodic potential $V(\vec{r})$ can be described by a single-particle Schrödinger equation [165]:

$$H\Psi(\vec{r}) = (H' + V(\vec{r}))\Psi(\vec{r}) = E\Psi(\vec{r}) \tag{2.47}$$

$H^{'}$ is the Hamiltonian of a quasi-free electron in a magnetic field. The magnetic field $\vec{B} = \mathrm{rot}\,\vec{A}$ is taken into account by the Peierls substitution $\vec{p} \rightarrow \vec{p} + e\vec{A}(\vec{r})$ with vector potential $\vec{A}(\vec{r})$. In the case of a perpendicular magnetic field in z-direction, one can use the Landau gauge $\vec{A}(\vec{r}) = B(0, x, 0)$. The 2D periodic potential modulation, i.e. the superlattice, is determined by $V(\vec{r})$ and can be defined by vectors $\vec{R}_{i,j}$ [165]:

$$\vec{R}_{i,j} = i\vec{a} + j\vec{b} \tag{2.48}$$

with lattice vectors $\vec{a}$ and $\vec{b}$ and integer numbers i, j. In absence of an external magnetic field the eigenfunctions $\Psi(\vec{r})$ follow Bloch's theorem and the calculation can be restricted to one primitive unit cell of the superlattice. In combination with an external magnetic field, translations given by $\vec{R}_{i,j}$ do not leave $\vec{A}(\vec{r})$ invariant and eigenfunctions are not given by Bloch wave functions. The electronic wave function also acquires an additional phase factor (Aharonov Bohm phase) if moving in a vector potential which has to be taken into account. In this case, a magnetic superlattice can be defined on which a generalized version of the Bloch theorem holds [165]. At rational magnetic fields, expressed by $\alpha = \Phi/\Phi_0 = p/q$ with integer numbers p and q, one can define a magnetic superlattice with a magnetic unit cell which is q times larger than the superlattice unit cell and which is pierced by p magnetic flux quanta. The magnetic superlattice can be defined e.g. by [165]:

$$\vec{S}_{i,j} = i\vec{a} + jq\vec{b} \tag{2.49}$$

Electrons moving in such a magnetic superlattice acquire a phase shift in multiples of 2π for translations given by $\vec{S}_{i,j}$ − restoring the initial state.

The eigenfunctions in this case can be expressed by [165]:

$$\Psi(\vec{r}) = \exp(i\vec{\theta}\vec{r})u^{\vec{\theta}}(\vec{r}) \tag{2.50}$$

where $u^{\vec{\theta}}(\vec{r})$ obeys [165]:

$$u^{\vec{\theta}}(\vec{r}+\vec{S}) = \exp\left(-i\frac{e}{\hbar}BS_x y\right)u^{\vec{\theta}}(\vec{r}) \tag{2.51}$$

with the magnetic crystal momentum $\vec{\theta}$ which is restricted to the first magnetic-Brillouin-zone, i.e. the first Brillouin zone of the magnetic superlattice defined by $\vec{S}_{i,j}$. Consequently, further calculations can be restricted to one primitive unit cell of the magnetic superlattice. In principle, since the magnetic superlattice has a q times larger unit cell, the initial mini-Brillouin-zone of the lateral superlattice is further split up into q magnetic-Brillouin-zones corresponding to a splitting of an initial energy band into q magnetic minibands which are clustered into groups giving rise to the Hofstadter butterfly energy spectrum.
For irrational values of α, the initial energy band splits up into infinitely many minibands and the spectrum forms a Cantor set, i.e. an uncountable yet measure-zero set of real numbers in an interval [14].

Tight-Binding and Nearly-Free-Electron Limit

In particular, the problem of electrons in a 2D periodic potential in combination with a magnetic field can be approached in the framework of two complementary limits, both resulting in the same energy spectrum [165–169] − the tight-binding limit and the nearly-free-electron limit. The tight-binding limit, i.e. the limit of strong 2D potential modulation, was used in the original approach to solve the problem of Bloch electrons in a magnetic field [14, 166]. The leading parameter in this case is $\alpha = \Phi/\Phi_0$. At rational fractions $\alpha = \Phi/\Phi_0 = \frac{p}{q}$ the initial Bloch band splits up into q minibands which are p-fold degenerate.
In the high magnetic field regime the tight-binding approach breaks down and mixing of energy bands has to be taken into account. A description based on well-separated Landau levels becomes more appropriate, i.e. the limit of nearly-free electrons exposed to a weak 2D periodic potential in the high magnetic field regime [166, 170–172]. In this case, the leading parameter is $\alpha = \Phi_0/\Phi = \frac{q}{p}$ and initial Landau levels split up into p minibands which are q-fold degenerate. If the potential modulation is strong compared to the cyclotron energy, Landau levels start to overlap and again mixing of energy bands has to be taken into account. In the following descriptions well-separated energy bands are assumed.

Tight-Binding Limit

This section outlines the derivation of the Hofstadter butterfly energy spectrum in the tight-binding limit following the original approach by D. Hofstadter [14]. In the case of a 2D square lattice with lattice constant a, a single tight-binding Bloch band can be expressed by the Bloch energy function [14]:

$$W(\vec{k}) = 2E_0(\cos(k_x a) + \cos(k_y a)) \tag{2.52}$$

The magnetic field is added by using the Peierls substitution which transforms the Bloch energy function into an effective single-band tight-binding Hamiltonian [14, 169]. By introducing the effective Hamiltonian into a time-independent Schrödinger equation with a 2D wave function, one obtains the following eigenvalue equation [14]:

$$\begin{aligned} &E_0[\Psi(x+a,y)+\Psi(x-a,y)+\exp(-ieBax/\hbar)\Psi(x,y+a)+ \\ &+\exp(ieBax/\hbar)\Psi(x,y-a)] = E\Psi(x,y) \end{aligned} \tag{2.53}$$

The wave function Ψ at (x, y) is linked to its four nearest neighbours in the lattice. By using the substitutions $E/E_0 = \epsilon$ and $x = ma$, $y = na$ with integer numbers m and n and assuming plane-wave behaviour in y-direction (since the coefficients only involve x), the wave function can be written as $\Psi(ma, na) = \exp(i\nu n)g(m)$ and the eigenvalue equation above can be transformed into a 1D difference equation − known as Harper's equation [14, 173]:

$$g(m+1)+g(m-1)+2\cos(2\pi m\alpha-\nu)g(m) = \epsilon g(m) \tag{2.54}$$

with parameter $\alpha = \Phi/\Phi_0 = a^2B/2\pi(\hbar/e)$. This 1D difference equation can be rewritten as [14]:

$$\begin{pmatrix} g(m+1) \\ g(m) \end{pmatrix} = \begin{pmatrix} \epsilon - 2\cos(2\pi m\alpha-\nu) & -1 \\ 1 & 0 \end{pmatrix} \begin{pmatrix} g(m) \\ g(m-1) \end{pmatrix} \tag{2.55}$$

The 2×2-matrices ($:= A(m)$) are periodic in m with period q, which means that there exists an integer p such that [14]:

$$2\pi\alpha(m+q)-\nu = 2\pi\alpha m-\nu+2\pi p \tag{2.56}$$

This translates directly into the requirement on α to be a rational number [14]:

$$\alpha = p/q \tag{2.57}$$

The product of q successive matrices A is called Q. One can derive the following condition on the trace of Q [14]:

$$|Tr(Q(\epsilon))| \leq 4 \tag{2.58}$$

The trace of Q is a polynomial of degree q. Consequently, eq. 2.58 is satisfied in roughly q distinct regions on the ϵ-axis, which is equivalent to a splitting of the initial Bloch band into q distinct energy bands at $\alpha = p/q$. The condition on $|Tr(Q(\epsilon))|$ can be used to calculate the Hofstadter butterfly energy spectrum for all $\alpha = p/q$. A Python code for calculating and plotting the Hofstadter butterfly, using eq. 2.58, is given in appendix C.

The Hofstadter butterfly energy spectrum shows the following characteristic properties [14]:
i) spectrum(α) is identical to spectrum($\alpha + N$) with integer N
ii) spectrum(α) is identical to spectrum(-α)
iii) if ϵ belongs to spectrum(α) then also $-\epsilon$ belongs to spectrum(α)
iv) if ϵ belongs to spectrum(α) for any α then $-4 \leq \epsilon \leq 4$
Following from this, it is sufficient to consider values of α in the interval $[0, 1]$ and values of ϵ in the range between -4 and 4 in order to obtain the typical Hofstadter butterfly plot with two axis of reflection at $\epsilon = 0$ and $\alpha = 1/2$.

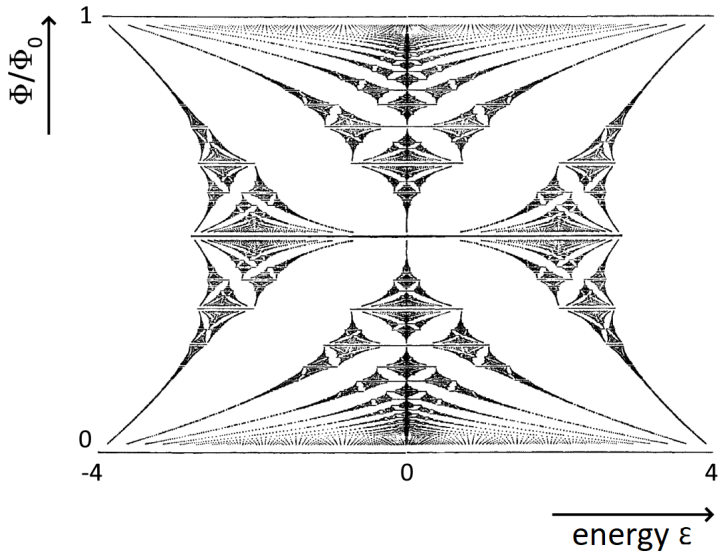

Figure 2.28: The original Hofstadter butterfly energy spectrum for Bloch electrons in a square 2D lattice exposed to a uniform magnetic field applied perpendicular to the plane of the 2D electron system. The allowed energy values are plotted as a function of energy ϵ and magnetic flux per lattice unit cell area Φ in units of the magnetic flux quantum Φ_0. The horizontal axis corresponds to the energy ϵ (ranging from -4 to 4) given over the full band width of a single initial energy band at zero magnetic field. The vertical axis is $\alpha = \Phi/\Phi_0$ (in the range of $0 \leq \Phi/\Phi_0 \leq 1$). Depending on the magnetic flux per lattice unit cell, the initial energy band splits up into a certain number of minibands and minigaps. At rational fractions $\Phi/\Phi_0 = \frac{p}{q}$, the initial Bloch band at zero magnetic field splits up into q minibands which are p-fold degenerate. At $\Phi/\Phi_0 = 1$, the initial Bloch band is restored. Adapted from [14].

Nearly-Free-Electron Limit

In the high magnetic field regime with Landau quantization present a weak 1D periodic potential modulation in x-direction lifts the degeneracy of Landau levels with respect to k_y and Landau levels obtain a magnetic field dependent band width − Landau bands emerge. In a weak 2D superlattice, i.e. by adding a periodic potential modulation in y-direction, also the degeneracy in k_x-direction is lifted and Landau bands further split up into a certain number of minibands and minigaps depending on the magnetic flux per lattice unit cell − the Landau bands exhibit an internal structure given by the Hofstadter butterfly energy spectrum.

In the following, a square 2D superlattice with lattice constant a and modulation amplitude V_0 is considered: $V(\vec{r}) = V_0(\cos(Gx) + \cos(Gy))$. The modulation potential is assumed to be weak ($V_0 \ll \hbar v_F / l_B$) such that Landau level mixing can be neglected.
In general, the corresponding energy spectrum can be derived in low-order perturbation theory by taking into account the Fourier expansion of the superlattice potential [172, 174]. The result for the considered square superlattice potential above is given by:

$$E_N = E_{N,0} + \epsilon_\alpha \mathcal{L}_N\left(\frac{1}{2} l_B^2 G^2\right) \tag{2.59}$$

$E_{N,0}$ is the unperturbed Landau level energy of the Nth Landau level, ϵ_α corresponds to the Hofstadter butterfly energy spectrum, and $\mathcal{L}_N(x) = e^{-\frac{1}{2}x} L_N(x)$ in the case of electrons with parabolic dispersion relation whereas $\mathcal{L}_N(x) = e^{-\frac{1}{2}x}\{L_N(x) + L_{N-1}(x)\}$ in the case of graphene with Laguerre polynomials $L_N(x)$. By plotting $\epsilon_\alpha = \epsilon(\vec{k}, j)$ with subband index $j = 1...p$ against $\alpha = \Phi_0/\Phi = q/p \in [0, 1]$ for all $\vec{k}$ in the first magnetic-Brillouin-zone one obtains the Hofstadter butterfly energy spectrum (see Fig. 2.29 (a)). In general, the shape of the Hofstadter butterfly depends on the details of the superlattice (lattice geometry and potential amplitudes) [172, 174]. All Landau levels exhibit the same internal structure determined by ϵ_α. The magnetic band structure of non-relativistic electrons in a 2DEG exposed to a 2D superlattice is depicted in Fig. 2.29 (b) showing the internal structure of Landau bands. At the flat band positions the band width vanishes and the original Landau levels are restored. In graphene the situation is in principle analogous: the superlattice broadened Landau levels exhibit an internal structure given by the Hofstadter butterfly, as shown in Fig. 2.30. The spectrum exhibits extended minibands at rational fractions of the magnetic flux quantum Φ_0 per superlattice unit cell which give rise to an enhanced band conductivity contribution analogous to the case of a 1D superlattice.

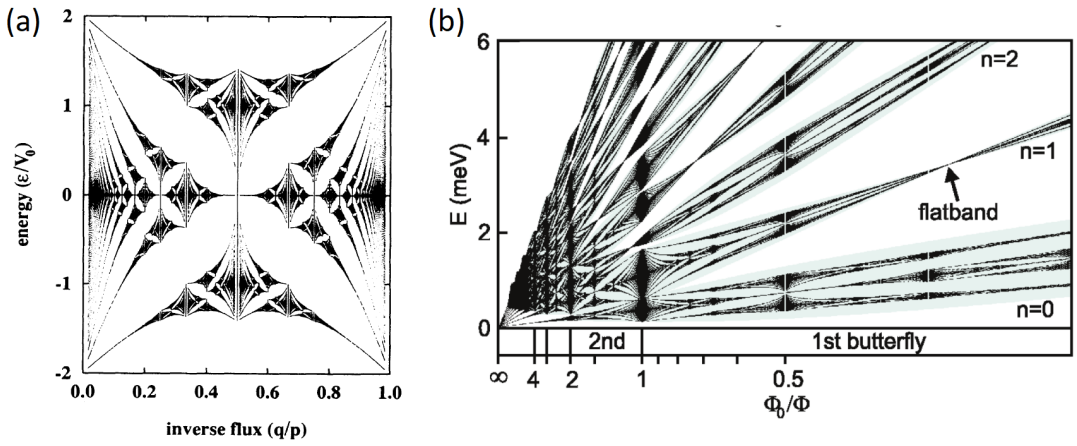

Figure 2.29: (a) Hofstadter butterfly in the nearly-free-electron limit for a 2D electron system with parabolic dispersion relation. The allowed energy values are plotted as a function of inverse magnetic flux. The modulation potential amplitude V_0 determines the energy band width. [172] **(b)** Effect of a 2D superlattice (with $a = 100$ nm and $V_0 = 2.4$ meV) on the Landau level spectrum of a 2DEG system with parabolic dispersion relation. Landau levels are broadened into Landau bands and exhibit an internal structure which is determined by the Hofstadter butterfly energy spectrum. At the flat band positions the initial discrete Landau levels are restored. [175]

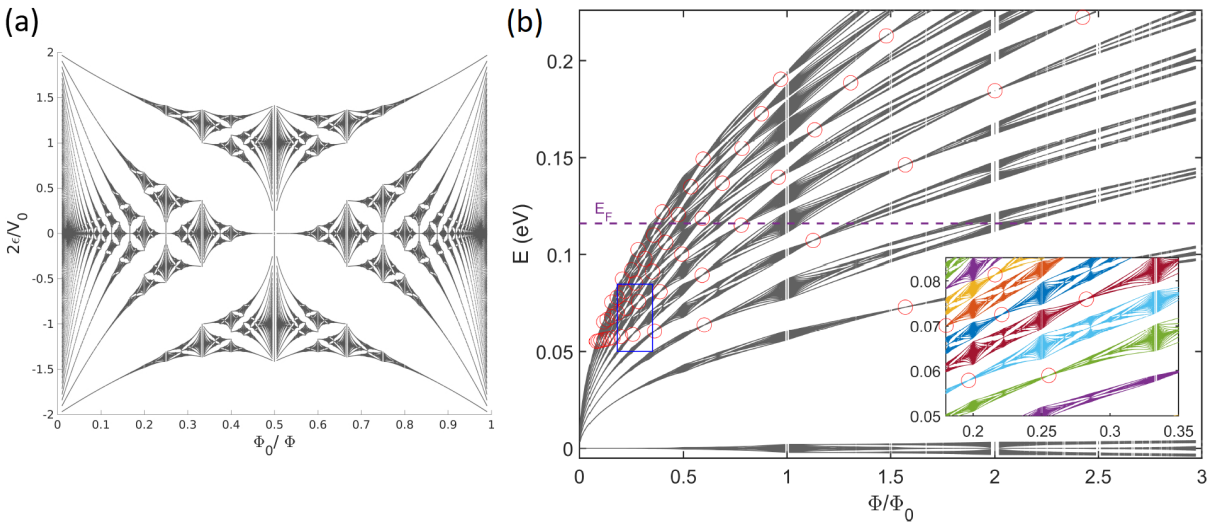

Figure 2.30: **(a)** Hofstadter butterfly in graphene in the nearly-free-electron limit. The allowed energy values are plotted as a function of inverse magnetic flux. The modulation potential amplitude V_0 determines the energy band width. [174] **(b)** Graphene in the high magnetic field limit exposed to a 2D periodic potential modulation (with $a = 40$ nm and $V_0 = 12$ meV): Landau bands exhibit an internal structure given by the Hofstadter butterfly energy spectrum. Here, only Landau bands with $N \geq 0$ (up to $N = 11$) are shown. Landau levels with $N < 0$ can be obtained by reflection at $E = 0$. At unit fractions of the magnetic flux quantum Φ_0 per superlattice unit cell the spectrum exhibits extended minibands across the full Landau band width giving rise to an enhanced band conductivity contribution analogous to the case of 1D modulation. Inset shows a detail of the overall spectrum (blue box) with the modulated Hofstadter butterflies determining the internal structure of the Landau bands. The red circles mark the flat band positions at which the usual Landau levels are restored. Data from [174] and graph generated by [176].

Wannier Diagram

If the parameter space is changed by transforming the energy scale of the Hofstadter butterfly plot into a band filling factor, the energy gaps in the Hofstadter spectrum follow straight lines of constant chemical potential and can be characterized by a Diophantine equation [9, 167, 177]. The resulting graph is called a Wannier diagram [167] – revealing the "skeleton of the butterfly" [178, 179] – which allows a straightforward identification of energy gaps in the energy spectrum. In the tight-binding limit the Bloch band filling factor is given by $\frac{n}{n_0}$ which is in principle the number of electrons per lattice unit cell (with charge carrier density n, $n_0 = \frac{1}{A_0}$ and the lattice unit cell area A_0). The energy gaps in the tight-binding limit can be characterized by the following Diophantine equation with integer parameters s and t [9, 167]:

$$\frac{n}{n_0} = t\left(\frac{\Phi}{\Phi_0}\right) + s \tag{2.60}$$

Here, the parameter s corresponds to the number of completely filled Bloch bands. Fig. 2.31 shows the transformation of the Hofstadter butterfly into a Wannier diagram with parameters $\frac{n}{n_0}$ and $\frac{\Phi}{\Phi_0}$ highlighting some energy gaps in the spectrum.

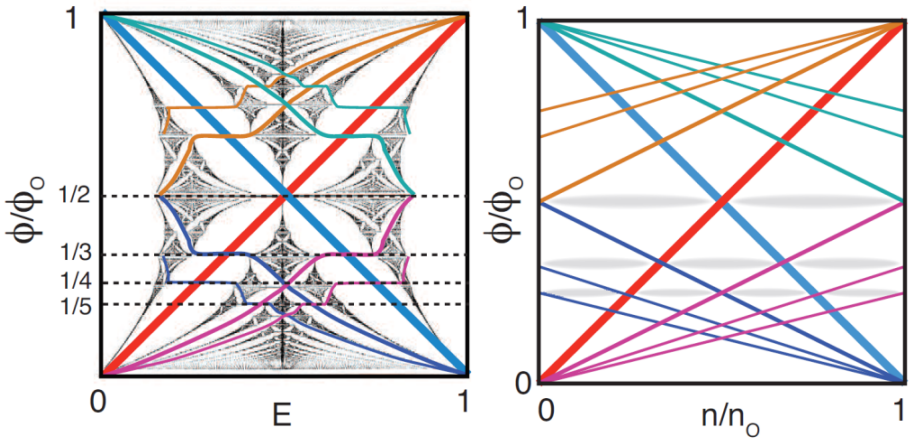

Figure 2.31: Transformation of the Hofstadter butterfly energy spectrum into a Wannier diagram with band filling factor $\frac{n}{n_0}$. Energy gaps in a Wannier diagram follow straight lines of constant chemical potential (coloured lines) and can be characterized by a Diophantine equation: $\frac{n}{n_0} = t(\frac{\Phi}{\Phi_0}) + s$ with integer parameters s and t. [9]

In the nearly-free-electron limit an equivalent Diophantine equation can be derived with the Landau level filling factor ν and the inverse magnetic flux $\frac{\Phi_0}{\Phi}$ as leading parameters. The corresponding Diophantine equation can be obtained from the equation in the tight-binding case by using the relation $n = \frac{\nu B}{\Phi_0}$ [9, 171]:

$$\nu = s\left(\frac{\Phi_0}{\Phi}\right) + t \tag{2.61}$$

In this case, energy gaps with $s = 0$ correspond to the usual Landau level energy spectrum and energy gaps with $s \neq 0$ correspond to Hofstadter minigaps.

The integer parameter t is a topological invariant and is connected to the quantized Hall conductivity, as shown by Thouless *et al.* [180–182]. If the Fermi energy lies inside an energy gap, the Hall conductivity σ_{xy} exhibits a quantized plateau value which is determined by the parameter t [180, 183]:

$$\sigma_{xy} = t\frac{e^2}{h} \tag{2.62}$$

Fig. 2.32 shows the Hofstadter butterfly with Hall conductivity contribution of the largest energy gaps in units of the conductance quantum $\frac{e^2}{h}$ (corresponding to the parameter t) in the tight-binding and nearly-free-electron limit.

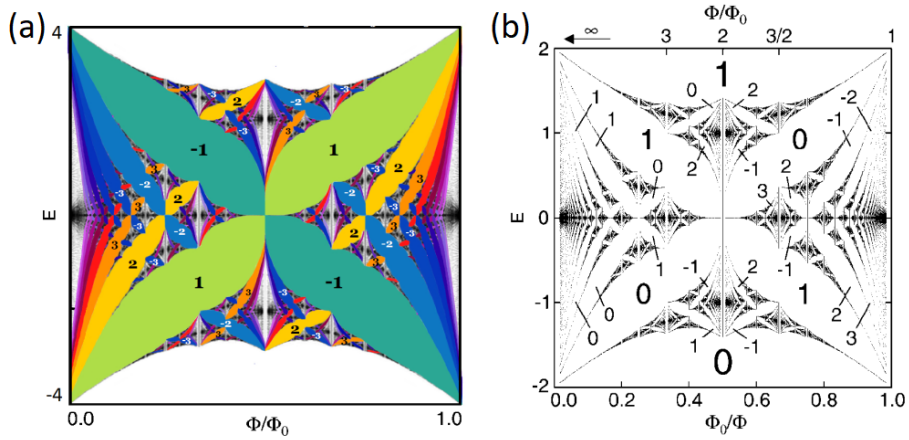

Figure 2.32: The contribution of energy gaps to the Hall resistance in units of the conductance quantum $\frac{e^2}{h}$ (corresponding to the parameter t). **(a)** The Hofstadter butterfly in the tight-binding limit. Different colours represent different values of t. Adapted from [184]. **(b)** The Hofstadter butterfly in the nearly-free-electron limit. The numbers inside the gaps correspond to the parameter t. [177]

Experimental Manifestation

In magnetotransport measurements the minigaps in the Hofstadter butterfly energy spectrum manifest in form of additional minima in longitudinal resistance accompanied by their corresponding Hall conductivity contribution. Depending on the resolved energy gaps, this can give rise to a non-trivial sequence of quantum Hall plateaus, as theoretically shown by Thouless *et al.* [180, 183]. The possibility to experimentally resolve energy gaps in the spectrum depends on the size of energy gaps E_{gap} (determined by the geometry of the superlattice and the modulation potential strength) compared to collision broadening Γ and thermal energy $E_{th} = k_B T$ [185]. Only if the effect of scattering and thermal smearing is sufficiently small, i.e. in samples with high mobility ($\Gamma \ll E_{gap}$) and at low temperatures ($E_{gap} \gg E_{th}$), one can expect to observe a direct and clear manifestation of signatures of the Hofstadter butterfly energy spectrum in magnetotransport experiments. Furthermore, magnetic fields of the order of one magnetic flux quantum Φ_0 per lattice unit cell are required. Fig. 2.33 shows the magnetic field value B_0 corresponding to one magnetic flux quantum Φ_0 per unit cell area as a function of lattice period for square and hexagonal lattices.

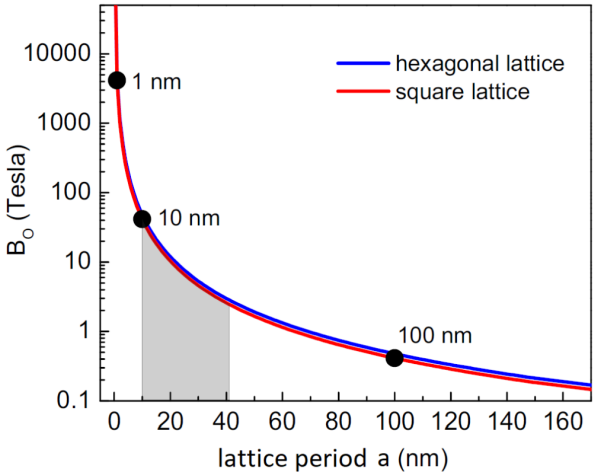

Figure 2.33: Magnetic field B_0 corresponding to one magnetic flux quantum Φ_0 per unit cell area as a function of lattice period a for square and hexagonal lattices. The grey region corresponds to ideal lattice periods in order to study the Hofstadter butterfly energy spectrum with magnetic field values B_0 accessible by laboratory magnets. Adapted from [9].

In natural crystals with lattice constants $a < 1$ nm magnetic fields of several thousands of Tesla are necessary to observe signatures of the fractal energy spectrum, which is impossible to realize in experiment. In order to circumvent this obstacle, superlattice structures can be utilized to increase the unit cell area and consequently shift the necessary magnetic fields to values which are accessible by laboratory magnets. In experiments using high-mobility GaAs-based 2DEG systems with superimposed 2D periodic potentials and superlattice periods of about $a \sim 100$ nm, a first glimpse and signatures of the Hofstadter butterfly energy spectrum could be observed [175, 177, 186, 187]. And eventually moiré superlattices in graphene/hBN heterostructures with superlattice periods $a \sim 10$ nm made it possible to study the Hofstadter butterfly energy spectrum in great detail [8–10]. Fig. 2.34 shows magnetotransport measurements on a moiré superlattice in graphene. Besides the main Landau fan also secondary Landau fans develop emerging from satellite Dirac points at $\frac{n}{n_0} = \pm 4$. All features in the magnetotransport data can be identified by using the corresponding Wannier diagram and by including the four-fold degeneracy of graphene (consequently four electrons/holes per superlattice unit cell are needed to fill up one miniband). Fig. 2.35 shows additional magnetotransport data of a sample with bilayer-graphene on hBN, also exhibiting satellite Dirac points at $\frac{n}{n_0} = \pm 4$ from which secondary Landau fans emerge and interfere with the original Landau fan which originates from $\frac{n}{n_0} = 0$. A linecut at $B = 25$ T shows a clear manifestation of a non-monotonic sequence of quantum Hall plateaus in transverse conductivity with corresponding minima in longitudinal conductivity caused by superlattice induced energy gaps. Again, the resolved energy gaps can be identified by the corresponding Diophantine equation and are labelled with their characteristic integer parameters (s, t).

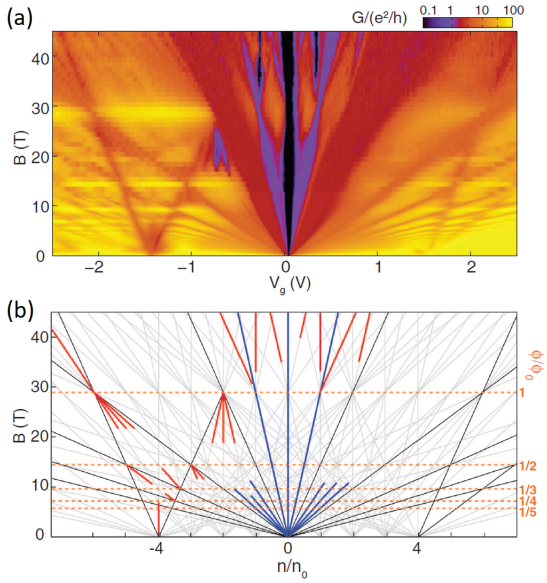

Figure 2.34: **(a)** Magnetotransport measurement on a graphene/hBN moiré superlattice. The longitudinal conductance is shown as a function of gate voltage V_g and magnetic field B. The data exhibit secondary Landau fans emerging from satellite Dirac points at $\frac{n}{n_0} = \pm 4$ (see (b)). **(b)** Corresponding Wannier diagram (grey lines) with band filling factor $\frac{n}{n_0}$ and magnetic flux $\frac{\Phi}{\Phi_0}$, in which the observed features in the magnetotransport data can be identified (coloured lines). [8]

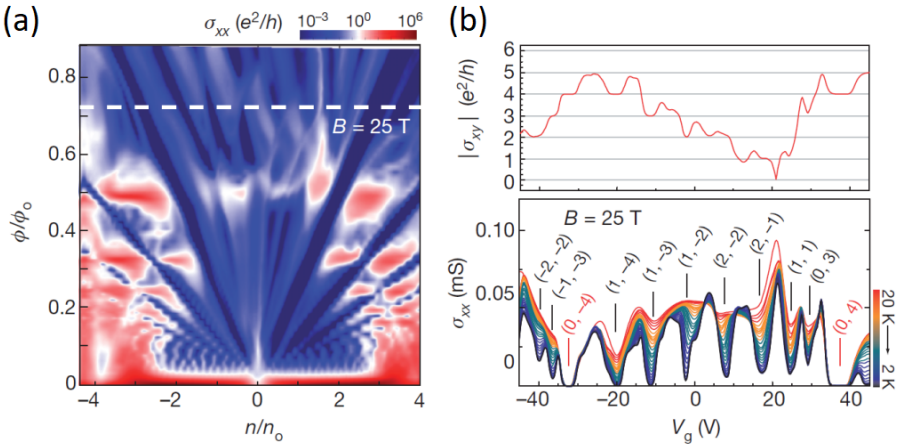

Figure 2.35: **(a)** Magnetotransport measurement on a moiré superlattice in bilayer graphene. Besides the main Landau fan additional Landau fans emerge from the satellite Dirac points at $\frac{n}{n_0} = \pm 4$ giving rise to the Hofstadter butterfly energy spectrum. **(b)** Linecut at $B = 25$ T showing transverse and longitudinal conductivity. Superlattice induced energy gaps manifest in transverse conductivity σ_{xy} as a non-trivial, non-monotonic sequence of quantum Hall plateaus which are accompanied by minima in longitudinal conductivity σ_{xx}. The energy gaps in the spectrum can be identified by the corresponding Diophantine equation with integer parameters (s, t). [9]

Band Conductivity Oscillations in a 2D Superlattice

In 2D superlattices the band conductivity contribution due to extended Landau bands becomes suppressed if collision broadening is small enough to resolve the Hofstadter spectrum [172, 186, 188]. In magnetotransport charge carrier density independent features appear, which correspond to the band width of minibands in the fractal energy spectrum and reflect the periodicity of the superimposed periodic potential [15].
Analogous to the mechanism discussed in the case of 1D superlattices (see chapter 2.2.2), the band width of minibands is connected to an additional band conductivity contribution, which is enhanced for the most extended minibands in the magnetic band structure at certain rational fractions of $\frac{\Phi}{\Phi_0} = \frac{p}{q}$. Overall, this manifests as temperature robust magnetoresistance oscillations, i.e. band conductivity oscillations in a 2D superlattice, reflecting the hierarchy of the width of magnetic minibands in the energy spectrum [15].
Band conductivity oscillations are usually obscured by the details of the Hofstadter butterfly in transport measurements conducted at cryogenic temperatures and are most pronounced and best visible at elevated temperatures, at which apparent superlattice induced features and the fine-structure of the Hofstadter butterfly vanish due to thermal smearing. In addition, at high temperature the Fermi step becomes smeared over several minibands which all contribute to the band conductivity correction [15], further increasing the visibility of band conductivity related features. Band conductivity oscillations in a 2D superlattice, experimentally observed in graphene/hBN-based moiré superlattices (see Fig. 2.36), were labelled Brown-Zak oscillations [15] due to their description in terms of magnetic Bloch states by Brown [189] and Zak [190]. The magnetic band structure of a graphene/hBN-based moiré superlattice, consisting of minibands with band widths varying in dependence of the magnetic flux per moiré unit cell, is shown in Fig. 2.37. The most extended minibands emerge at unit fractions of $\frac{\Phi}{\Phi_0}$ and give rise to pronounced $1/B$-periodic band conductivity oscillations, from which the period of the superlattice can be determined since $\frac{\Phi}{\Phi_0} = \frac{BA_{sl}}{\Phi_0}$ with $A_{sl} = \frac{\sqrt{3}}{2}a^2$.

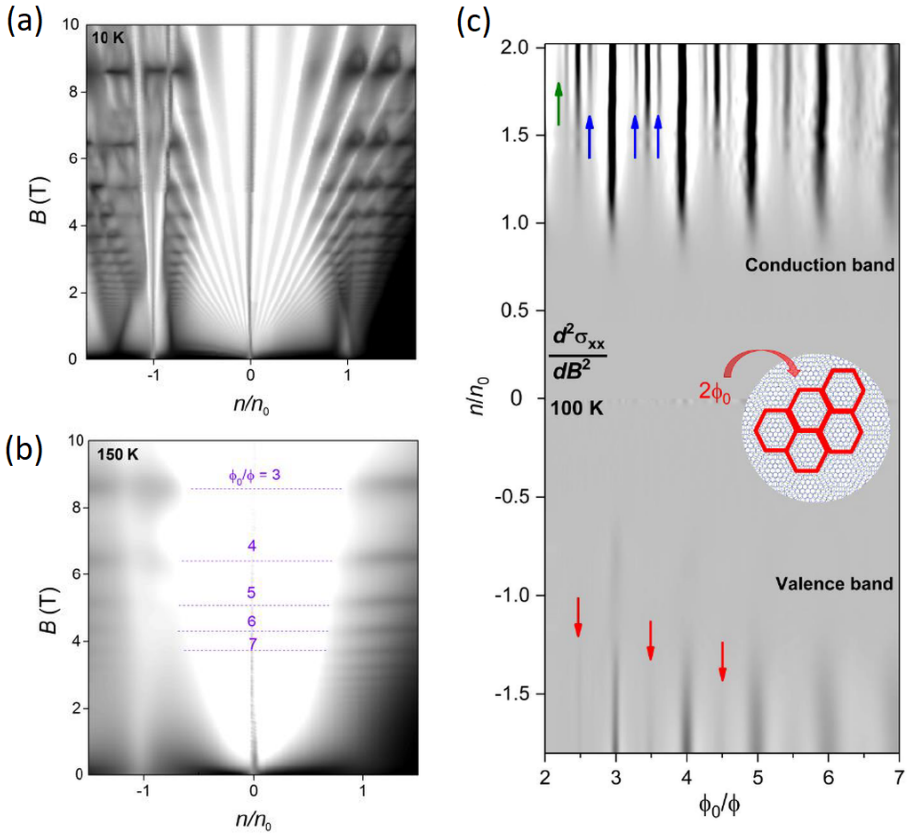

Figure 2.36: **(a)** Hofstadter butterfly in a graphene/hBN moiré superlattice at a temperature of $T = 10$ K. The longitudinal conductivity σ_{xx} is plotted as a function of band filling factor $\frac{n}{n_0}$ and magnetic field B. Logarithmic grey scale: white 0.015 mS, black 15 mS. [15] **(b)** At an elevated temperature of $T = 150$ K, Landau quantization vanishes and band conductivity oscillations (Brown-Zak oscillations) remain with most pronounced features at unit fractions of $\frac{\Phi}{\Phi_0}$. Logarithmic grey scale: white 0.1 mS, black 10 mS. [15] **(c)** The second derivative of the longitudinal conductivity σ_{xx} as a function of $\frac{n}{n_0}$ and $\frac{\Phi_0}{\Phi}$ at a temperature of $T = 100$ K. White corresponds to 0 mS/T^2 and black to -0.05 mS/T^2. The most pronounced features in magnetotransport at rational fractions of the magnetic flux quantum per superlattice unit cell originate from extended minibands in the Hofstadter butterfly energy spectrum, giving rise to an enhanced band conductivity contribution. Besides the fundamental features at $\frac{\Phi}{\Phi_0} = p/q$ with $p = 1$ also high-order states with $p > 1$ manifest corresponding to the next order of extended minibands in the magnetic band structure (shown by arrows). Inset illustrates the state at $\frac{\Phi}{\Phi_0} = 2/5$ which corresponds to an extended unit cell of five original moiré unit cells pierced by two magnetic flux quanta. [191]

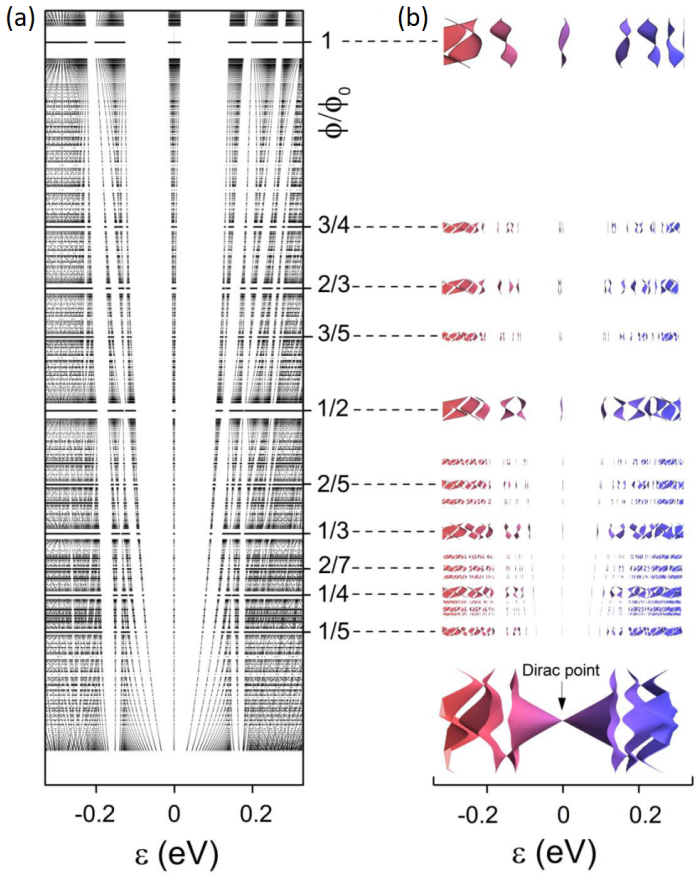

Figure 2.37: **(a)** Magnetic band structure of a graphene/hBN moiré superlattice showing the occurrence of minibands with varying band width. The most extended minibands, in particular at unit fractions of $\frac{\Phi}{\Phi_0}$, give rise to an enhanced band conductivity contribution which manifests as band conductivity (Brown-Zak) oscillations in magnetotransport measurements. **(b)** Dispersion relation of several magnetic minibands at certain rational fractions of the magnetic flux quantum per moiré unit cell. The dispersion relation at the bottom depicts the situation at zero magnetic field. [191]

2.3 Graphene Antidot Superlattices

The following section gives an overview of graphene antidot superlattices − a special kind of nanostructured graphene − in which magnetically tunable energy gaps emerge. First, the theoretical framework of ideal graphene antidot lattices (GALs) in view of induced energy gaps is summarized. Afterwards, realistic GALs and their connections to graphene nanoribbons are discussed. Furthermore, the tunability of energy gaps by an applied magnetic field and commensurability effects are presented.

2.3.1 Band Gap Engineering

The exceptional electronic properties and high mobility make graphene to an outstanding material for potential applications, but there is one major drawback: the absence of an intrinsic band gap, which limits its use e.g. as a field-effect transistor since the current can not be completely switched off. There are several methods and approaches with the goal to open a band gap, i.e. a fundamental energy gap between valence and conduction band, in graphene and to transform it into a gapped semiconductor.
In bilayer graphene, the emergence of an energy gap in a perpendicular electric field was demonstrated [192]. In monolayer graphene, an energy gap can be induced e.g. by interactions with a substrate [193, 194] like SiC [195] or hBN (in graphene/hBN moiré superlattices) [196]. Also in electrostatically modulated graphene, the emergence of an energy gap originating from a local sublattice symmetry breaking was theoretically shown [197]. Another possibility is given by nanostructuring graphene [198] into quantum dots [199], graphene nanoribbons (GNRs) [200–203], graphene nanomeshes [204, 205] or graphene antidot lattices (GALs) [4, 206–208] − a special kind of 2D superlattice in which fundamental energy gaps emerge due to quantum confinement and resultant band structure modifications.
In general, antidot lattices induce a strong hard-wall modulation potential (with modulation potential strength V_0 and $E_F \ll V_0$) in a material like graphene with vanishing electron probability density at the superlattice sites (see Fig. 2.38 (a) for a schematic illustration) [43]. In particular, a GAL is a perforated graphene layer with a periodic array of holes in which the details of the antidot lattice (like the lattice unit cell, the lattice constant, and the diameter of the holes) determine the size of the energy gap. Moreover, the induced energy gaps are tunable by an applied magnetic field [5, 6]. GALs are therefore of particular interest for electronic band structure engineering of graphene. Fig. 2.38 (b) shows a schematic sample design of an antidot lattice with lattice period a, hole diameter d, and minimal neck width $w = a - d$ etched into a hBN/graphene/hBN stack. By defining the antidot lattice geometry, it is possible to tune the energy gap in GALs and tailor the electronic properties of this semiconducting nanostructured graphene.

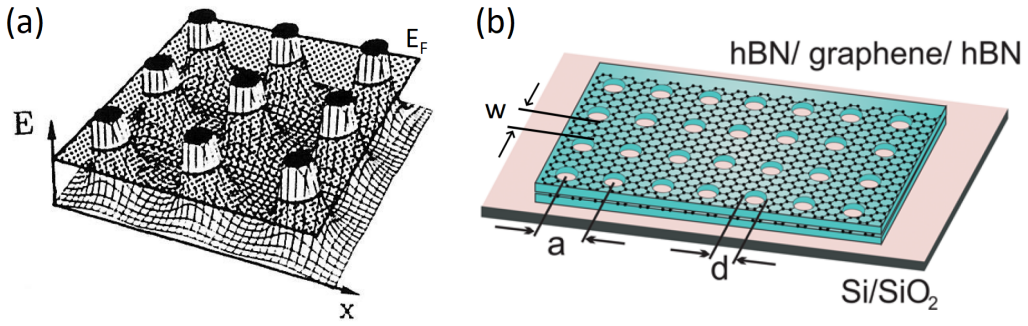

Figure 2.38: (a) Strong lateral modulation potential in an antidot lattice device. The dotted plane corresponds to the Fermi energy E_F. Adapted from [43]. **(b)** Schematic picture of a graphene antidot lattice with square geometry, lattice period a, antidot diameter d, and neck width w in a hBN/graphene/hBN stack on a Si/SiO_2 substrate. Adapted from [3].

Ideal GALs

Fig. 2.39 presents electronic band structures of several ideal (i.e. without disorder) GALs obtained from tight-binding and density functional theory calculations demonstrating the emergence of an energy gap with magnitude depending on the size of the antidot lattice unit cell and the radius of the holes. It was theoretically shown in tight-binding calculations that the scaling of the energy gap E_{gap} in GALs with hexagonal unit cells and circular holes depends on the total number of carbon atoms N_{total} and the number of removed carbon atoms $N_{removed}$ in the unit cell of the antidot lattice, as displayed in Fig. 2.40 (a) [4, 209]:

$$E_{gap} \propto \frac{\sqrt{N_{removed}}}{N_{total}} \tag{2.63}$$

In calculations considering hexagonal unit cells and holes a strong dependency of the energy gap on the edge configuration of the holes (armchair or zigzag) and the exact lattice geometry was derived [207, 210], as depicted in Fig. 2.40 (b). An approximated scaling rule was determined by using the Dirac equation and not taking into account edge states and by considering cylindrical unit cells and holes, as depicted in Fig. 2.40 (c) [207]:

$$E_{gap} = 4\sqrt{\pi}\hbar v_F \frac{\sqrt{A_{removed}}}{A_{total}} = 4\hbar v_F \frac{R}{R_e^2} = 4\hbar v_F \frac{d/2}{(a/2)^2} \tag{2.64}$$

with the total area of the unit cell A_{total}, the area of the hole in the unit cell $A_{removed}$, the radius R of holes, and the radius R_e of the cylindrical unit cell, as illustrated in Fig. 2.40 (c).

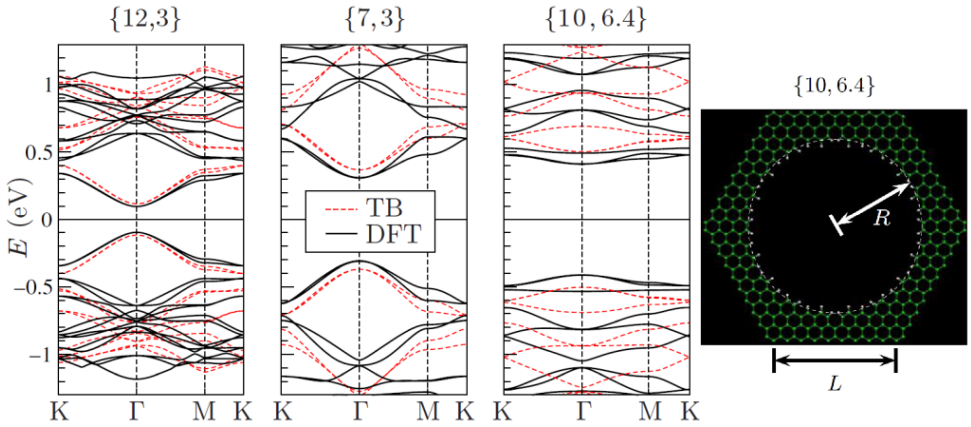

Figure 2.39: Electronic band structure of three different GALs with hexagonal unit cells and circular holes (labelled with $\{L, R\}$) calculated in the framework of a tight-binding (TB) and density functional theory (DFT) model. All GALs show the emergence of an energy gap at the Γ-point of the antidot graphene (corresponding to the K and K' points of pristine graphene) with magnitude depending on the size L of the antidot lattice unit cell and the hole radius R. L and R are given in units of the graphene lattice constant $a_0 = 0.246$ nm. [206]

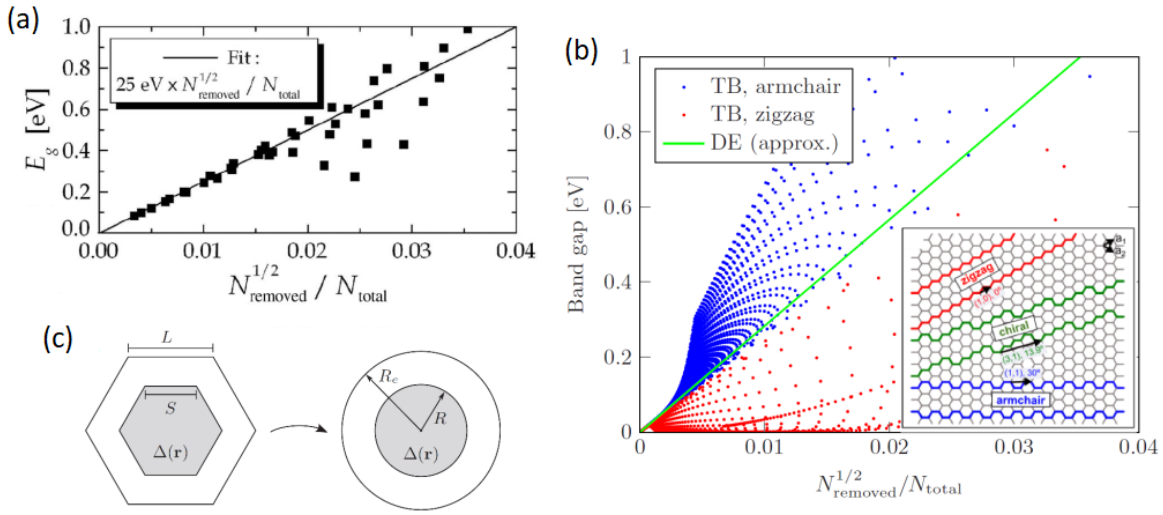

Figure 2.40: **(a)** Calculated scaling law of energy gaps in GALs with hexagonal unit cell and circular holes. The energy gap depends on the total number of atoms N_{total} and the number of removed atoms $N_{removed}$ in the unit cell of the antidot lattice. [4] **(b)** Energy gaps from tight-binding (TB) calculations for GALs with hexagonal holes with armchair and zigzag type edges. The size of energy gaps strongly depends on the type of edge structure of the holes. Calculations using the Dirac equation (DE) and not taking into account edge states give an approximated scaling law (green line). Adapted from [207]. Inset shows different crystallographic directions in graphene corresponding to different types of edges [211]. **(c)** By using an equivalent circular geometry of the hexagonal unit cell and hole, one obtains an approximation of the scaling of the energy gap: $E_{gap} \propto \frac{R}{R_e^2}$. [207]

In a tight-binding approach in combination with an effective Hamiltonian of antidot graphene the following dispersion relation of hexagonal graphene antidot lattices with periodicity a and hole diameter d was derived [212]:

$$E(k) = \pm\sqrt{\hbar^2 v_F^{*2} k^2 + m_i^2} \tag{2.65}$$

Here, the + (−) sign corresponds to the conduction (valence) band of the GAL, v_F^* is the effective Fermi velocity in the system, and the constant m_i corresponds to the intervalley scattering strength which is caused by intervalley scattering at atomically sharp defects at the edges of the holes and couples the K and K' valleys in a GAL. The parameters v_F^* and m_i depend on the geometry of the GAL and are determined by [212]:

$$v_F^* = (1 - 0.67)\gamma v_F \qquad\qquad m_i = 0.056\gamma t \frac{13nm}{a} \tag{2.66}$$

with $\gamma = d/a$, the Fermi velocity v_F of intrinsic graphene, and $t_0 \sim 3$ eV corresponding to the hopping parameter. Following from the effective dispersion relation, the energy gap between the valence and conduction band in a GAL is given by [212]:

$$E_{gap} = 2m_i = 0.112\gamma t \frac{13nm}{a} \tag{2.67}$$

Fig. 2.41 displays several calculated band structures for different values of γ of an antidot system showing the emergence of an energy gap. In addition, it was shown that the energy gap derived in the effective Hamiltonian approach is robust against small-scale random perturbations on the edge of the holes which are unavoidable in top-down fabrication methods like etching of the antidot pattern into graphene [212].

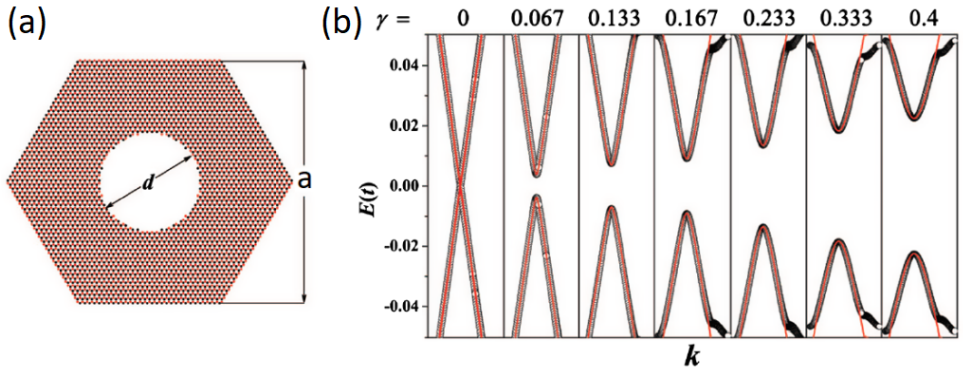

Figure 2.41: (a) Antidot graphene considered in a tight-binding model with periodicity a and hole diameter d. Red and black dots represent the carbon atoms on sublattice A and B. **(b)** Calculated band structures of hexagonal GALs with different $\gamma = d/a$ and fixed periodicity $a = 13$ nm derived from a tight-binding model (black) and an effective Hamiltonian (red). The energy gap is controlled by the parameter γ. [212]

Realistic GALs Including Disorder

In general, disorder and poorly defined holes and edges can have significant impact on the properties of energy gaps and transport properties of GALs [213–217]. It was theoretically shown that by including edge disorder, the scaling rule of energy gaps in GALs changes into an overall $\frac{1}{w}$ dependency similar to the case of GNRs, as illustrated in Fig. 2.42 (a) [213]. Consequently, GALs can be seen as a network of GNRs with width w corresponding to the minimum neck width between adjacent antidots and a comparison between both types of nanostructured graphene concerning the emergence and scaling of energy gaps seems to be justified. Furthermore, it was shown that in the case of disordered edges the length of sequential zigzag sections has significant impact on the band structure of GALs due to localized states at the zigzag type edge structures which correspond to flat bands and do not contribute to transport [218].
Overall, the following scaling rule of energy gaps E_{gap} in GALs (and GNRs) can be derived determined by a scaling parameter α and the (neck) width w [200, 213, 219]:

$$E_{gap} = \frac{\alpha}{w} \tag{2.68}$$

For example GNRs fabricated by oxygen plasma etching of graphene on Si/SiO_2 showed a scaling rule of $E_{gap} = \frac{\alpha}{w-w^*}$ with $\alpha = 0.2$ eV nm and an additional width correction w^* taking into account inactive edge regions due to localized states and inaccurate width determination [200]. Measurements on chemically derived GNRs on Si/SiO_2 revealed a scaling of E_{gap} with $\alpha = 0.8$ eV nm [220]. In graphene nanomeshes (i.e. a graphene layer with a dense, quasi-periodic array of holes) a comparable scaling law with an overall $1/w$ dependency and a scaling parameter of $\alpha = 0.95$ eV nm was determined (see Fig. 2.42 (b)) [219]. A hexagonal GAL fabricated by etching holes into a hBN/graphene/hBN stack showed the emergence of an energy gap corresponding to $\alpha = 2$ eV nm [6] – comparable to the expected energy level spacing ΔE obtained from quantum confinement [221]: $E_{gap} = \Delta E = \hbar v_F \Delta k$ with $\Delta k = \pi/w$.
Overall, theoretically and experimentally derived scaling parameters in a range of about $\alpha = 0.2$ - 2 eV nm are reported in literature. One reason for this wide distribution is that the theoretically derived energy gaps of GALs and GNRs crucially depend on the (neck) width and details of the edge structure [207, 218, 222–224]. Discrepancies in experimental studies could be explained by varying sample quality, different and varying edge structures and varying type and amount of disorder due to different material systems (e.g. graphene on Si/SiO_2 [200] or hBN/graphene/hBN stacks [6]) and fabrication methods (e.g. electron beam lithography [200] or chemically derived GNRs [220]).

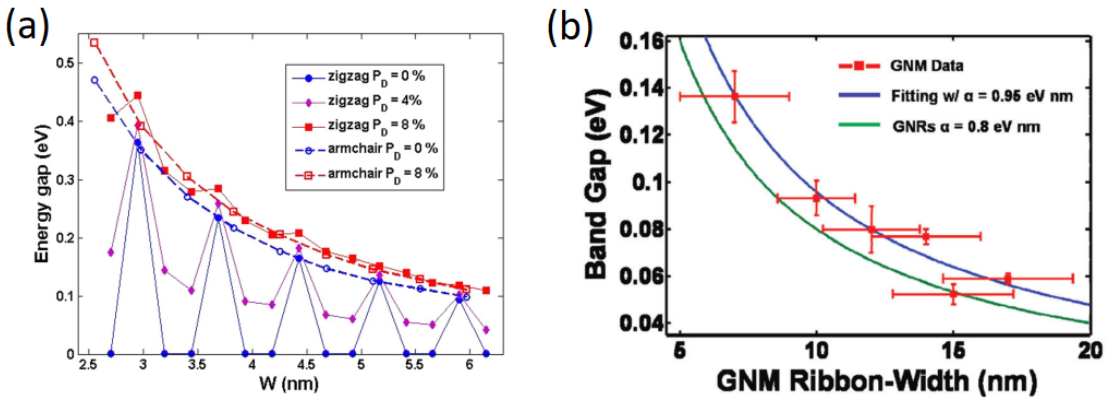

Figure 2.42: **(a)** Calculated energy gaps E_{gap} as a function of neck width w determined for GALs with holes with armchair and zigzag edge structures. P_D determines the probability of removing a carbon atom at the edges and is a measure for edge disorder. By including edge disorder, the differences between different types of edges start to vanish and an overall $1/w$ scaling law of energy gaps can be derived. [213] **(b)** Experimentally determined energy gaps in graphene nanomeshes (GNM) as a function of neck width w. A $1/w$ dependency of the derived energy gaps was observed with a scaling parameter $\alpha = 0.95$ eV nm (blue curve) comparable to the case of GNRs (green curve). [219]

Transport Gap

Transport measurements on different kinds of graphene nanoconstrictions, fabricated by top-down methods, also revealed the emergence of a so-called transport gap originating from a fundamental energy gap in combination with disorder and potential fluctuations [198, 225–231]. The situation in disordered graphene nanoconstrictions, compared to large-area graphene, is schematically depicted in Fig. 2.43 (a). In large-area graphene a disorder potential gives rise to electron-hole puddles at low charge carrier densities. Transport across these charge puddles is mainly transparent due to Klein tunnelling. In graphene nanoconstrictions, e.g. in GNRs or GALs, a confinement gap is induced and the charge puddles become separated by tunnel barriers. A transport gap regime manifests, as depicted in Fig. 2.43 (b). If the Fermi energy lies inside the transport gap, conduction is suppressed and transport mainly takes place by real tunnelling across the isolated charge puddles and is mainly governed by variable range hopping between localized states [232, 233] and/or (statistical) Coulomb blockade [228, 234–236]. Also strong localization at rough, disordered edges influences charge carrier transport in narrow constrictions [215, 216, 237, 238], as shown in Fig. 2.44 which displays calculations of the local density of states along a GNR. Charge carries, localized at the edges, do not contribute to transport and a region of reduced charge carrier density inside the constriction emerges which suppresses current flow through the device. Like in the case of GNRs [239] and graphene nanoconstrictions [240], it can be expected that edge disorder tends to induce wave function localization also in GALs, eventually contributing to a transport gap. Overall, the impact of isolated charge puddles and localization of charge carriers manifests as a transport gap extending over a finite energy range which is determined by the magnitude of the confinement gap and the extent of the disorder potential (see Fig. 2.43 (b)). The emergence of a disorder induced transport gap usually obscures the impact of a fundamental energy gap in transport measurements, which complicates the

determination of pure energy gaps and probably also explains – to some extent – the varying experimental results in literature. As an alternative to top-down fabrication methods, which usually induce an inevitable amount of (edge) disorder and a transport gap, there is also the possibility to obtain graphene nanostructures by bottom-up processes, e.g. chemical synthesis of GNRs with well-defined edges [211] and direct growth of graphene nanostructures [132, 241–243].

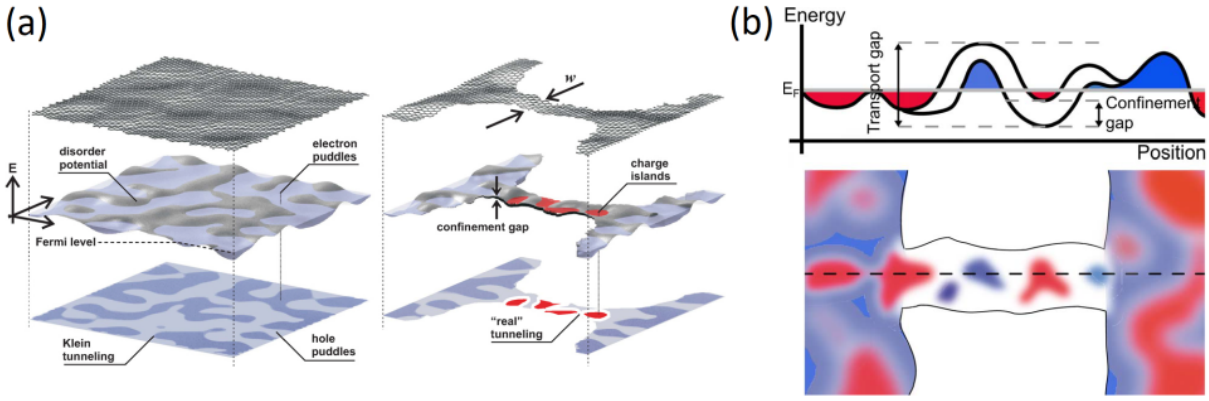

Figure 2.43: **(a)** In extended graphene areas a disorder potential gives rise to electron-hole puddles at low charge carrier densities which are mainly transparent due to Klein tunnelling. In nanoconstrictions the charge puddles become isolated due to emergence of a confinement gap and real tunnelling takes place. Conduction is suppressed and a transport gap occurs. [228] **(b)** Formation of isolated electron (red) and hole (blue) puddles along a graphene nanoconstriction. The black curve in the upper graph shows the energy of the bottom of the conduction band and the top of the valence band as a function of position along the dashed line in the bottom picture. Inside the constriction a transport gap manifests consisting of a disorder potential in combination with a confinement gap. [226]

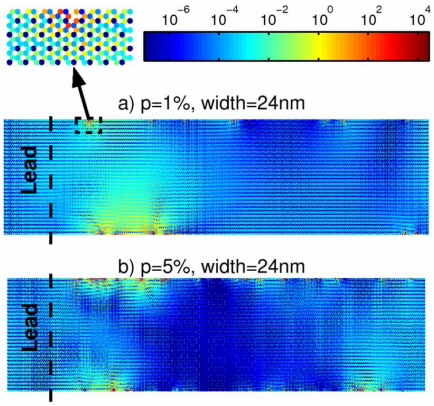

Figure 2.44: Calculated local density of states along a GNR with width $w = 24$ nm and varying amount of edge disorder (given by the defect concentrations $p = 1\%$ and $p = 5\%$). If the defect concentration at the edges of a graphene nanoconstriction is high enough (b), charge carriers become strongly localized at the edges and the density of states inside the constriction is reduced (dark blue regions) – transmission through the device is suppressed. Adapted from [237].

Estimated Size of Energy Gaps in GALs

Fig. 2.45 shows the magnitude of energy gaps E_{gap} as a function of neck width w for typical devices with $w = 10 - 40$ nm – realisable by standard top-down fabrication methods. The energy gaps are given for GALs with $a = 50$ nm estimated by $E_{gap} = 4\hbar v_F \frac{d/2}{(a/2)^2}$ and $E_{gap} = 0.112\gamma t \frac{13nm}{a}$. Also energy gap values determined by $E_{gap} = \frac{\alpha}{w}$ with $\alpha = 0.2$ eV nm and 2 eV nm are shown. Overall, this rough estimation shows the typical order of magnitude and possible range of energy gaps in GALs.

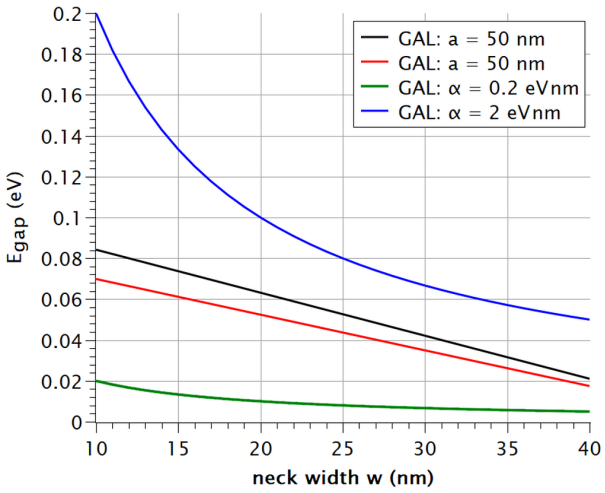

Figure 2.45: Rough estimation of the possible size and range of energy gaps E_{gap} in GALs as a function of neck width w, calculated via the following formulas: E_{gap} in a GAL with $a = 50$ nm derived by $E_{gap} = 4\hbar v_F \frac{d/2}{(a/2)^2}$ (black curve) and $E_{gap} = 0.112\gamma t \frac{13nm}{a}$ (red curve). E_{gap} in a GAL derived by $E_{gap} = \frac{\alpha}{w}$ with $\alpha = 0.2$ eV nm (green curve) and $\alpha = 2$ eV nm (blue curve).

Magnetic Field Tunable Energy Gaps

Besides the emergence of an energy gap in GALs, also the tunability and quenching of the induced energy gap by an applied magnetic field was presented in theory [5, 244] and in experiment [6] – similar to observations in GNRs [236]. Fig. 2.46 (a) shows details of the magnetic band structure, i.e. the Hofstadter butterfly, of graphene with a hexagonal antidot lattice. The characteristic features in the energy spectrum are the zeroth Landau levels which are separated by the induced energy gap. By increasing an applied magnetic field perpendicular to the GAL, the energy gap decreases and closes completely if the magnetic length $l_B = \sqrt{\frac{\hbar}{eB}}$ is sufficiently smaller than the minimum neck width w of the GAL. In a simple picture: The size of cyclotron orbits decreases upon increasing the magnetic field and at sufficiently small cyclotron orbits the electrons do not probe the antidot lattice anymore [5]. In consequence, effects of the antidot lattice vanish and the energy gap closes since the lowest Landau levels shift towards zero energy. At higher magnetic fields Landau quantization of intrinsic graphene is restored and the usual QHE begins to set in.

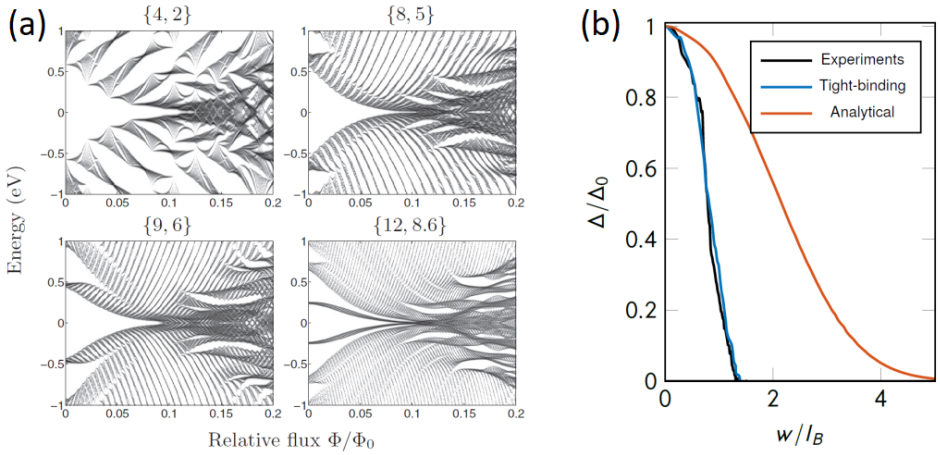

Figure 2.46: **(a)** Calculated energy spectra in a magnetic field of several GALs with different sizes of unit cells and holes but with similar neck widths. Plotted are the allowed energy values as a function of magnetic flux Φ per graphene unit cell in units of the magnetic flux quantum Φ_0. In all cases the energy gap at zero magnetic field closes upon increasing the magnetic field. [5] **(b)** Experimentally observed quenching of the energy gap in a hexagonal GAL. The half energy gap value Δ normalized to the zero magnetic field value Δ_0 is shown as a function of w/l_B with neck width w and magnetic length l_B. If l_B becomes sufficiently smaller than the neck width w, the energy gap closes completely. The experimentally observed behaviour is quantitatively in good agreement with corresponding tight-binding calculations. An additional analytical calculation qualitatively reproduces the overall tendency. [6]

2.3.2 Commensurability Effects

If an antidot system enters the classical ballistic transport regime, i.e. if the Fermi wavelength λ_F becomes smaller than the dominant geometrical length scale (corresponding to the neck width w in antidot lattices), new phenomena start to appear in magnetotransport originating from the interplay between cyclotron orbits and the geometry of the periodic hole lattice. Resonances in longitudinal resistance R_{xx} occur whenever the cyclotron diameter $2R_c = \frac{2\hbar k_F}{eB}$ is commensurable to the lattice constant a [43, 245–247]. In general, electrons in the classical ballistic regime are described as solid point particles which bounce off the periodic hard wall potential defined by the holes in the material. In such an electron pinball system fundamental characteristic trajectories appear, as shown in Fig. 2.47 (a) in the case of a square antidot lattice. The low field resonances can be explained within an electron pinball model based on the Drude model [43, 248]. Electrons with cyclotron diameters commensurable to the lattice geometry can be pinned around a certain number n of antidots. These localized electrons do not contribute to transport any more and the longitudinal resistance increases. Fig. 2.47 shows some possible pinned electron orbits around n antidots in a square antidot lattice (with $n = 1, 2, 4, 9, 21$). The cyclotron orbit around one antidot gives rise to the fundamental antidot peak in magnetoresistance given by the relation $2R_c = \frac{2\hbar k_F}{eB} = a$. Depending on the lattice geometry and the ratio between hole diameter d and lattice constant a only certain resonances can appear: in general, the full cyclotron orbit has to fit in the antidot lattice. Furthermore, it was shown that classical chaotic motion, manifesting as an extreme sensitivity of the electron trajectories on the initial conditions, plays an important role in the occurrence of the observed magnetoresistance features due to temporarily trapped electrons

whirling around antidots [246, 249]. In some antidot samples also B-periodic Aharanov-Bohm-like oscillations were observed originating from a modified electron spectrum which is dominated by a few quantized periodic cyclotron orbits [250–252].
At sufficiently high magnetic fields the cyclotron orbits fit in between adjacent holes (corresponding to the condition $2R_c \sim w = a - d$) and drift almost unperturbed through the antidot lattice. In this case, commensurability effects vanish and the system enters the usual quantum Hall regime. Fig. 2.48 (a) shows magnetotransport measurements on a square antidot lattice etched into a high-mobility GaAs-based 2DEG [253]. In the low magnetic field regime antidot peaks manifest in longitudinal resistance. In the high magnetic field regime the system exhibits Shubnikov-de-Haas oscillations and the quantum Hall effect. The antidot features in magnetotransport are well reproduced in an electron pinball model and correspond to cyclotron orbits pinned around $n = 1, 2, 4$ antidots, as depicted in Fig. 2.48 (b). Fig. 2.49 (a) shows magnetotransport measurements on a graphene antidot lattice with square geometry realized by etching a periodic array of holes into a hBN/graphene/hBN stack [3]. Even after etching a dense array of holes into a graphene/hBN heterostructure high mobilities were preserved allowing the observation of ballistic transport phenomena and in particular commensurability effects [3, 254]: Antidot peaks corresponding to cyclotron orbits around $n = 1, 2, 4$ antidots emerge. Due to their semi-classical origin, the observed low field features remain unchanged even at elevated temperatures at which quantum effects usually disappear, as shown in Fig. 2.49 (b). Furthermore, the ambipolar field effect in graphene allows to study the transition into the quantum regime, i.e. a regime in which the Fermi wavelength exceeds the neck width w, which causes a suppression of commensurability effects, also depicted in Fig. 2.49 (b).

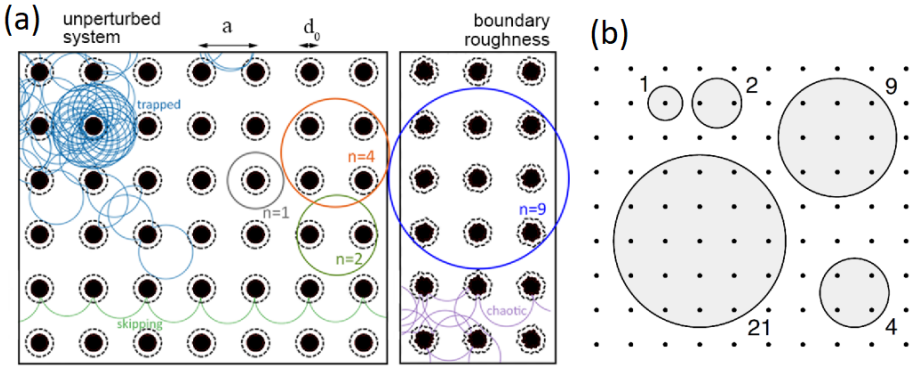

Figure 2.47: **(a)** Characteristic electron trajectories in a square antidot lattice in the low magnetic field regime. At certain magnetic fields cyclotron orbits can be pinned around antidots (here shown for $n = 1, 2, 4, 9$) and do not contribute to transport any more, which manifests as maxima in magnetoresistance. [255] **(b)** Schematic picture of cyclotron orbits pinned around antidots in a square antidot lattice giving rise to the resonances in magnetotransport. [256]

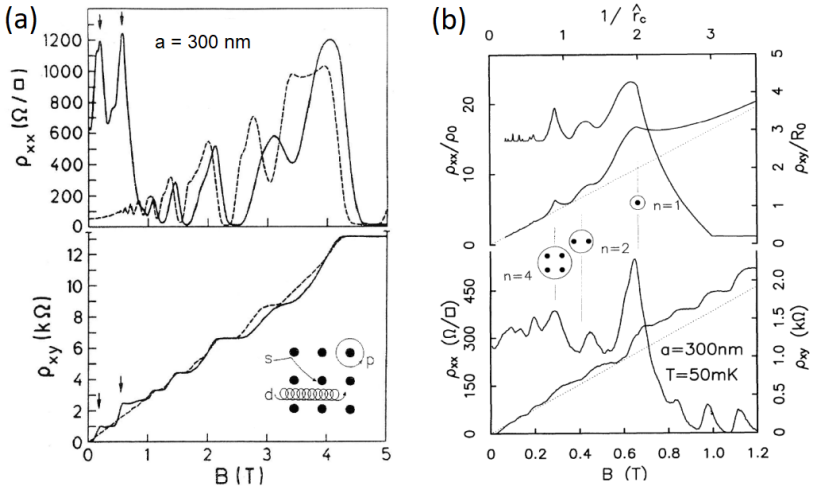

Figure 2.48: **(a)** Commensurability effects in a square antidot lattice etched into a high-mobility GaAs-based 2DEG. In the low magnetic field regime well-pronounced resonances occur, in contrast to the reference measurement without antidots (dashed curve). Inset shows possible electron trajectories: Skipping orbits (s) contribute to the transport. Pinned orbits (p) around antidots do not contribute to transport − the resistance increases. At high magnetic fields drifting orbits (d) are able to move unperturbed between adjacent antidots and the system enters the quantum Hall regime. Adapted from [253]. **(b)** Comparison between experiment (bottom curves) and theory (top curves). The antidot features can be well reproduced within an electron pinball model. The peaks correspond to pinned orbits around $n = 1, 2, 4$ antidots. [253]

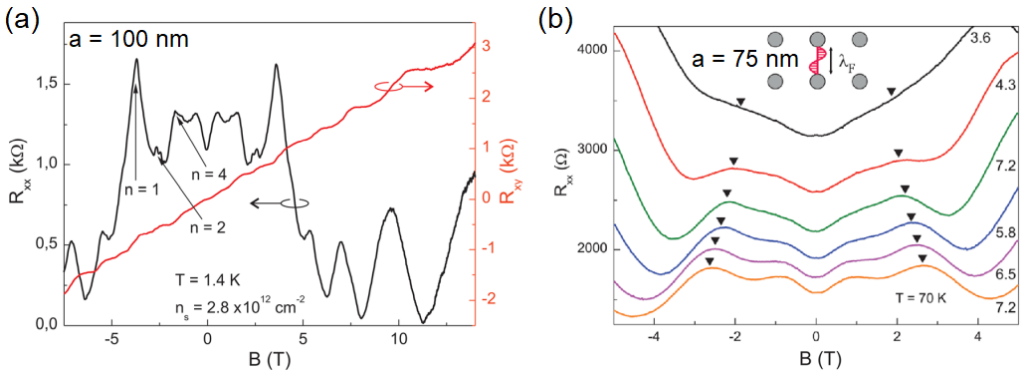

Figure 2.49: **(a)** Commensurability effects in a square graphene antidot lattice. R_{xx} is plotted as a function of magnetic field B. Antidot peaks are observable which correspond to cyclotron orbits around $n = 1, 2, 4$ antidots. **(b)** R_{xx} plotted as a function of B for several charge carrier densities (3.6 to 7.2 $\times$ 10^{15} cm^{-2}) at $T = 70$ K. At elevated temperatures quantum effects and Landau quantization vanishes but antidot peaks can be still observed due to their semi-classical origin. The ambipolar field effect in graphene allows to study the transition into the quantum regime. In the quantum regime the antidot features start to vanish. In the classical regime, i.e. if the Fermi wavelength λ_F is smaller than the neck width w (see inset), antidot resonances occur. The (expected) position of the fundamental antidot peak is marked with a black triangle. Adapted from [3].

CHAPTER 3

SAMPLE PREPARATION AND MEASUREMENT SETUP

In this chapter, an overview of the main fabrication steps and of the measurement setup is given. First, the used van der Waals stacking process for the assembly of graphene/hBN heterostructures and the basic sample geometry are described. Then, the fabrication of graphene antidot lattices and gate-defined graphene superlattices is addressed. The last section provides information about the measurement setup.

A complete process documentation of all fabrication steps is given in appendix A.

3.1 Fabrication of Graphene/hBN Heterostructures

Van der Waals Stacking Process

The basic material system used in this work are hBN/graphene/hBN stacks fabricated by a dry (i.e. graphene does not get in contact with liquid chemicals) van der Waals stacking process. The stacking setup is installed in an optical microscope and consists of a polymer stamp − a dome-shaped PDMS (polydimethylsiloxane) drop placed on a microscope slide and covered by a PC (polycarbonate) layer − and a heatable sample stage with maximum temperature T up to about 185 °C. Fig. 3.1 schematically depicts the stacking setup. Chips with target material (graphene and hBN flakes mechanically exfoliated onto Si/SiO_2 chips with 90 nm SiO_2) reside on the sample stage during the stacking procedure. The target flakes are picked up by using the polymer stamp. The x, y, and z-position of the polymer stamp, sitting above the target flakes, is controlled by control knobs of the microscope. The stacking process was optimized in the framework of a bachelor thesis [257] in which an existing stacking procedure [105] was modified. Fig. 3.2 illustrates the individual steps in fabricating a typical hBN/graphene/hBN stack. By carrying out the stacking process at elevated temperatures, impurities (e.g. air, water, hydrocarbons) trapped between the layers become mobile and can be pressed out and are mostly removed during stacking. This provides a simultaneous cleaning effect enhancing the quality of the finished devices [105]. After the stacking procedure, the final stack is transferred onto a Si/SiO_2 chip with 285 nm SiO_2 and can be further processed.

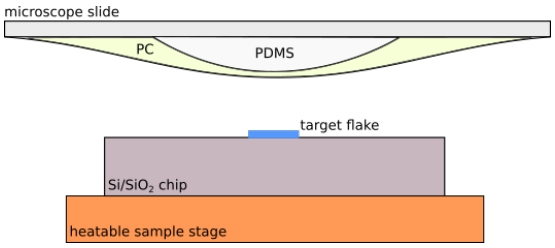

Figure 3.1: Schematic stacking setup. A movable polymer stamp (consisting of a dome-shaped PDMS drop on a microscope slide covered by a PC layer) is used to pick up a target flake on a Si/SiO_2 chip. The target chip resides on a heatable sample stage during the stacking procedure.

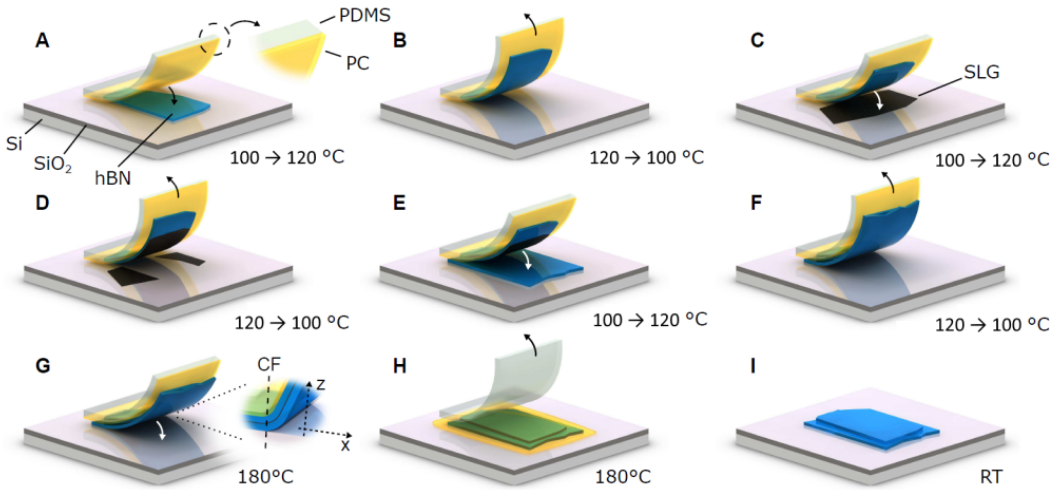

Figure 3.2: Van der Waals stacking process for fabrication of hBN/graphene/hBN stacks. **A**: A PDMS/PC stamp is used to pick up an initial hBN flake which was exfoliated onto a Si/SiO_2 chip. At a temperature of $T \sim 100\,°C$ the polymer stamp is brought into contact with the substrate chip near the target hBN flake. By increasing the temperature to $T \sim 120\,°C$, the contact front (CF) of the polymer stamp expands and moves across the target flake. The movement speed of the CF can be controlled by the heating procedure. **B**: If the polymer stamp completely covers the target flake, the temperature is decreased to $T \sim 100\,°C$ during which the CF withdraws. The hBN flake sticks to the PC and is picked up. **C-F**: The same procedure is carried out in order to pick up a graphene flake which sticks to the initial hBN flake by van der Waals forces. Subsequently, a second hBN flake is picked up in the same way. The final hBN/graphene/hBN stack sticks to the polymer stamp. **G-H**: In the last step the hBN/graphene/hBN stack is brought into contact with a target substrate at a temperature of $T \sim 180\,°C$. The PC layer melts and the hBN/graphene/hBN stack (and the PC layer) is transferred onto the target substrate (usually a Si/SiO_2 chip with 285 nm SiO_2). **I**: The PC layer is removed with chloroform or oxygen plasma. The final stack on the chip is ready for further processing. Adapted from [105].

Basic Sample Geometry and 1D Edge Contacts

Further processing of hBN/graphene/hBN stacks is done via standard electron beam lithography (EBL) and reactive ion etching (RIE) in order to define the sample geometry and mesa (Hall bar geometry, see Fig. 3.3) and to provide metal contacts to the encapsulated graphene layer. The p^{++} doped Si layer of the chip is utilized as a back gate. Fig. 3.4 gives a schematic overview of further fabrication steps. RIE of graphene/hBN heterostructures can be carried out with CHF_3/O_2 as reactive gas etching both hBN and graphene with well-defined and controllable etch rates [50, 258, 259]. Furthermore, a selective etching step with SF_6 can be applied preferably etching hBN and stopping at graphene [260, 261]. Depending on the material system and desired sample geometry, a suitable choice of etching steps has to be made. After etching of an initial hBN/graphene/hBN stack into e.g. Hall bar geometry, graphene edges are exposed on the side walls of the mesa. A subsequent EBL step defines the wiring of the device and, eventually, metal leads and contact pads are fabricated by evaporation of Cr (5 nm) / Au (80 nm) providing 1D edge contacts to the graphene layer [50], as schematically depicted in Fig. 3.4. Final devices are glued into a chip carrier by two-component epoxy adhesive and contact pads on the sample are connected to electrodes on the chip carrier by ultrasonic wire bonding of aluminium wires.

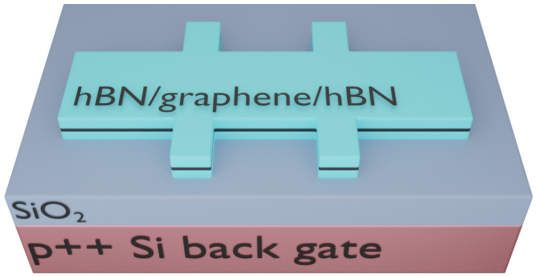

Figure 3.3: Schematic picture of the basic sample geometry: A hBN/graphene/hBN stack patterned into Hall bar geometry by EBL and RIE on a Si/SiO_2 chip with 285 nm SiO_2. The p^{++} doped Si layer is used as a back gate.

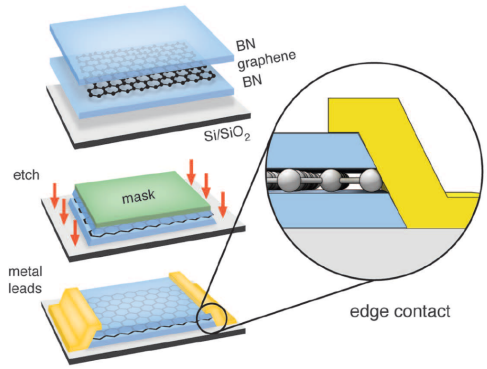

Figure 3.4: Fabrication of 1D edge contacts to graphene encapsulated between two hBN flakes. A hBN/graphene/hBN stack is etched by RIE exposing the edges of graphene. Subsequently, the graphene layer is contacted by metal leads consisting of Cr (5 nm) / Au (80 nm). [50]

3.2 Fabrication of Graphene Antidot Lattices

GALs were fabricated by employing EBL and RIE with CHF_3/O_2 and etching a periodic array of holes into an initial hBN/graphene/hBN Hall bar. Manifestation and experimental observability of electronic band structure modifications in GALs like the emergence of energy gaps crucially depend on minimum feature sizes in the system (e.g. the neck width). Therefore, in order to obtain nanostructures with feature sizes as small as possible, i.e. at the limit of the available technology, the EBL process was optimized. A thin (~ 80 nm) high-resolution positive e-beam resist (CSAR 62 [262, 263]) with enhanced plasma etch stability was used which withstands the applied RIE step and enables the fabrication of the desired structure sizes. The EBL step itself was carried out at highest available acceleration voltage (30 kV) with small working distance (~ 3.5 mm) and small aperture (10 μm). Furthermore, development of the e-beam exposed resist was done in cold developer ($T \sim 10\,^{\circ}\mathrm{C}$), which improves pattern resolution [263–265]. After transferring the nanostructure into hBN/graphene by means of RIE, the resist was rinsed off and remaining residues were removed in a gentle oxygen plasma cleaning step (see Fig. 3.6). Fig. 3.7 shows scanning electron microscopy (SEM) images of typical finished devices with square and hexagonal antidot lattices. Overall, antidot lattices with hole diameters of down to ~ 10 nm and lattice periods of down to ~ 35 nm were realized, as shown in Fig. 3.8.

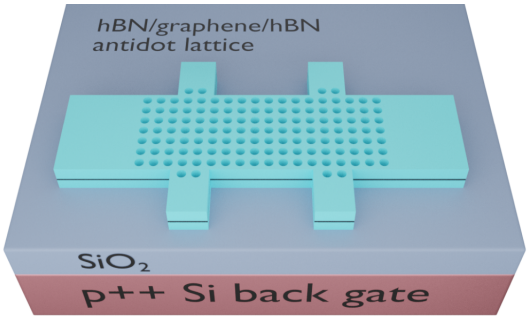

Figure 3.5: Schematic sample geometry of a GAL realized by etching a periodic array of nanoholes into a hBN/graphene/hBN Hall bar.

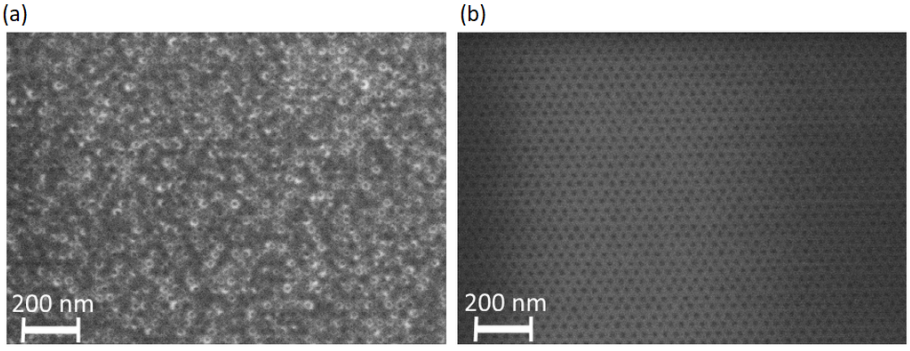

Figure 3.6: **(a)** SEM image of resist residues on hBN after fabricating a periodic array of holes by EBL and RIE. **(b)** The same hBN flake after oxygen plasma cleaning during which resist residues are removed. The patterned array of holes becomes visible.

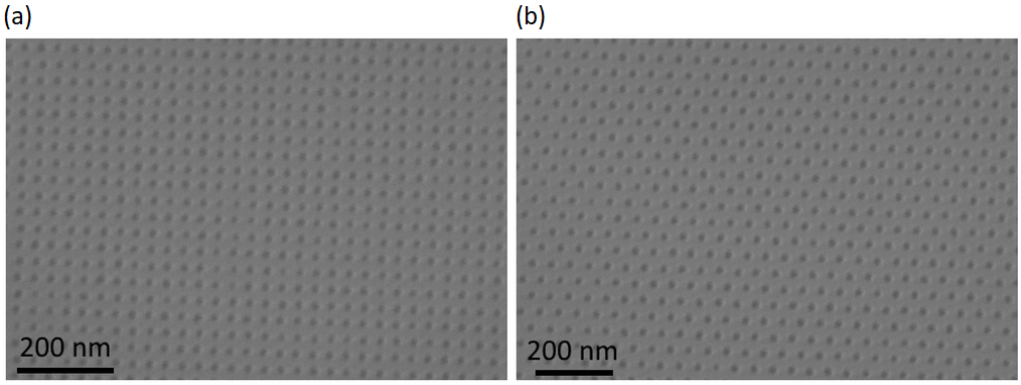

Figure 3.7: **(a)** SEM image of a square antidot lattice in hBN/graphene/hBN with lattice constant $a = 40$ nm **(b)** SEM image of a hexagonal antidot lattice in hBN/graphene/hBN with lattice constant $a = 50$ nm.

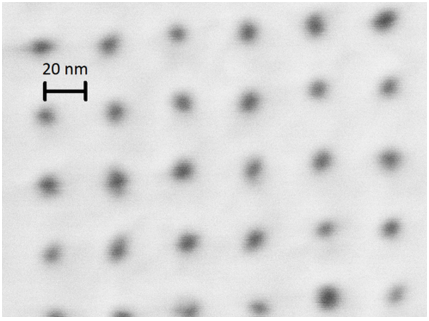

Figure 3.8: SEM image of a square antidot lattice in hBN with minimum feature sizes: hole diameter $d \sim 10$ nm and lattice constant $a \sim 35$ nm.

One aspect of RIE of hBN/graphene/hBN stacks which has to be taken into account is the actual etching profile in hBN. Depending on the etching profile, the apparent hole diameter in the upper hBN layer is not necessarily equivalent to the hole diameter in the encapsulated graphene layer. In order to estimate the etching profile, a single hBN flake with known thickness was patterned into a hole lattice and the hole diameter was determined by SEM. The hBN was completely etched through, consequently also etching the SiO_2 underneath. After removing the hBN by using adhesive tape or by ultrasonication in isopropyl alcohol, the hole diameter in SiO_2 was determined by SEM. With the knowledge of the patterned hole diameters in hBN and SiO_2 and the thickness of the hBN layer it is possible to draw conclusions regarding the etching profile and angle by geometrical considerations. As a result, a conical etching profile with an angle $\alpha \sim 60°$ was estimated, schematically depicted in Fig. 3.9 and in agreement with values from literature ($\alpha \sim 66°$ with a similar etching process [6]).

In conclusion, the actual hole diameter in graphene d_{AD} depends on the initial hole diameter in the top hBN layer D_{AD} and the thickness of the top hBN layer $d_{hBN,top}$. The actual hole diameter in graphene can be estimated by:

$$d_{AD} = D_{AD} - \frac{2d_{hBN,top}}{\tan(\alpha)}$$

The conical etching profile sets a limit to the maximum thickness of the top hBN layer for a fixed antidot lattice geometry with specific hole diameter. As a consequence, top hBN layers with thicknesses $d_{hBN,top} \leq 10$ nm were used for the preparation of short-period antidot lattices in order to guarantee pattern transfer into the encapsulated graphene layer. Fig. 3.10 shows SEM images of a finished hexagonal GAL with lattice period $a = 40$ nm fabricated by etching a dense array of holes into a hBN/graphene/hBN Hall bar.

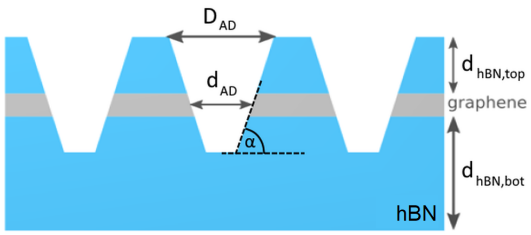

Figure 3.9: Schematic side view of holes etched into a hBN/graphene/hBN stack. The conical etching profile in hBN determines the actual hole diameter d_{AD} in graphene and, consequently, d_{AD} depends on the initial hole diameter D_{AD} in the top hBN layer and the thickness $d_{hBN,top}$ of the top hBN layer. The etching angle was estimated to be about $\alpha \sim 60°$.

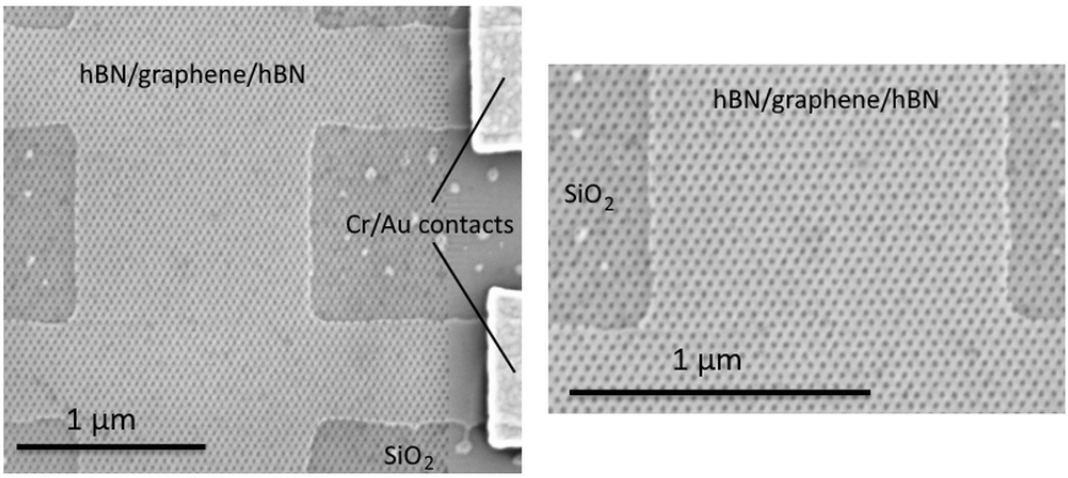

Figure 3.10: SEM images of a finished hexagonal GAL with lattice constant $a = 40$ nm realized by etching a nanohole array into a hBN/graphene/hBN Hall bar.

3.3 Fabrication of Gate-Defined Two-Dimensional Superlattices

In order to induce gate-tunable superlattice effects in graphene, a double-gate sample design was utilized [7] which has already been used successfully to realize 1D superlattices in graphene demonstrating the manifestation of Landau bands and enabling the observation of Weiss oscillations in magnetotransport experiments [12, 158]. Furthermore, it was shown that this technique is also suitable to induce a rich variety of gate-tunable effects in 2D superlattice structures ranging from tunable mobility over Weiss oscillations to the observation of antidot resonances in a strong potential modulation regime [159].
In this work, the fabrication of gate-tunable 2D superlattices was further optimized and superlattice periods were minimized in order to induce and experimentally observe well-pronounced electronic band structure modifications in graphene including the generation of minibands and satellite Dirac points and the manifestation of the Hofstadter butterfly energy spectrum. High-mobility graphene superlattices with lattice periods of about $a \sim 40$ nm were fabricated and investigated. The magnetic field value B_0 in the fabricated devices, necessary to obtain one magnetic flux quantum per superlattice unit cell, lies at about $B_0 \sim 3$ T (see Fig. 2.33) which is easily accessible by standard laboratory magnets. Therefore, in contrast to moiré superstructures for which magnetic fields of about $B_0 \sim 25$ T have to be applied in order to reach one magnetic flux quantum per unit cell, the realized artificial superlattice devices with lattice periods of a few tens of nanometres also allow to probe a regime exceeding one magnetic flux quantum per unit cell and make it possible to gain further insight into physics of graphene superlattices.
The schematic picture in Fig. 3.11 illustrates the double-gate sample design. By the combined action of a global back gate (p^{++} doped Si) and a patterned bottom gate (PBG) made from few-layer graphene, a periodic charge carrier density modulation can be induced in an encapsulated graphene layer transferred on top of the PBG. In principle, few-layer graphene patterned gates can be easily fabricated by standard EBL and RIE with oxygen plasma and can be implemented in van der Waals stacking procedures (including the pick-up and transfer of patterned few-layer graphene gates, see appendix B) allowing flexible use of superlattices with arbitrary geometry.

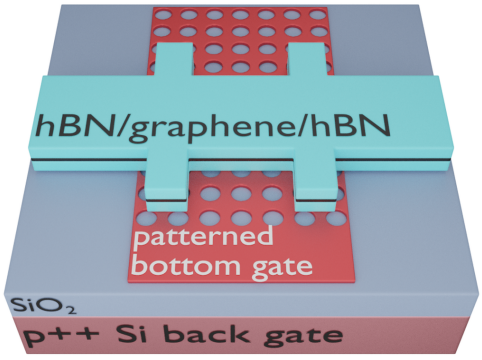

Figure 3.11: Schematic double-gate sample design used to induce a gate-tunable periodic potential modulation in graphene. By the combined action of a global back gate and a few-layer graphene patterned bottom gate (PBG), a periodic charge carrier density modulation can be induced in the encapsulated graphene layer transferred on top of the pattered bottom gate.

The PBGs used in this work were made from few-layer graphene flakes with thicknesses between 2 to 5 layers which were mechanically exfoliated onto a Si/SiO_2 chip with 285 nm SiO_2 and subsequently patterned into short-period antidot lattices by EBL and RIE with oxygen plasma. A thin layer ($\sim$ 60 nm) of PMMA 950k 2% was used as e-beam resist leaving fewer and more easily removable residues on the samples after patterning compared to CSAR 62. The EBL step was carried out at highest available acceleration voltage (30 kV) with small working distance ($\sim$ 3.5 mm) and small aperture (10 μm). The e-beam-exposed PMMA resist was gently developed in a cold ($T \sim 10\,^{\circ}\mathrm{C}$) mixture of isopropyl alcohol : H_2O (7:3) for increased pattern resolution [263, 266–268].
After RIE several cleaning steps were applied: cleaning in strong resist stripper (Remover PG from Microchem) at 60 °C and subsequent annealing in vacuum (pressure: $\sim$ 10 mbar) at 400 °C in order to remove PMMA and other residues. An oxygen plasma cleaning step can not be applied since the few-layer graphene would be etched. Afterwards, the PBGs were examined by means of an atomic force microscope (AFM) and sufficiently clean and suitable PBGs were chosen for further processing. Fig. 3.12 depicts AFM images of few-layer graphene PBGs with square and hexagonal superlattice geometry and a lattice constant of $a = 40$ nm. In the next step the van der Waals stacking technique was used to encapsulate graphene between two hBN flakes. The finished graphene/hBN heterostructure was transferred on top of the PBG. The bottom hBN layer was chosen to be only a few nm in thickness ($\sim$ 5 nm) in order to achieve a well-defined and pronounced modulation potential. Usually, the yield of suitable and sufficiently thin hBN flakes by standard mechanical exfoliation is quite low. An alternative method to obtain thin hBN dielectrics by precise etching of thicker hBN flakes is suggested in appendix B. After the stacking process the final hBN/graphene/hBN stack was shaped into Hall bar geometry by EBL and selective RIE with SF_6 and O_2. In the last step 1D edge contacts were fabricated by EBL and evaporation of Cr (5 nm) / Au (80 nm).
Fig. 3.13 (a) schematically depicts the final sample geometry and the working principle of the double-gate design. The global back gate is mainly screened by the PBG and controls the charge carrier density in graphene areas above the holes of the PBG, i.e. the back gate mainly induces the periodic potential modulation tunable by the applied back gate voltage V_{bg} and dependent on the geometry of the PBG and the thickness of the bottom hBN layer. The PBG voltage V_{pbg} mainly controls the average charge carrier density in the entire graphene layer. The top graph in Fig. 3.13 (a) displays the calculated charge carrier density modulation profile at a certain gate configuration for a device with dielectric thicknesses of $d_{SiO_2} = 285$ nm (SiO_2) and $d_{hBN,bot} = 5$ nm (bottom hBN). Fig. 3.13 (b) and (c) show an optical microscope image of a finished device and an AFM image of the corresponding PBG with square superlattice and a lattice constant of $a = 40$ nm.

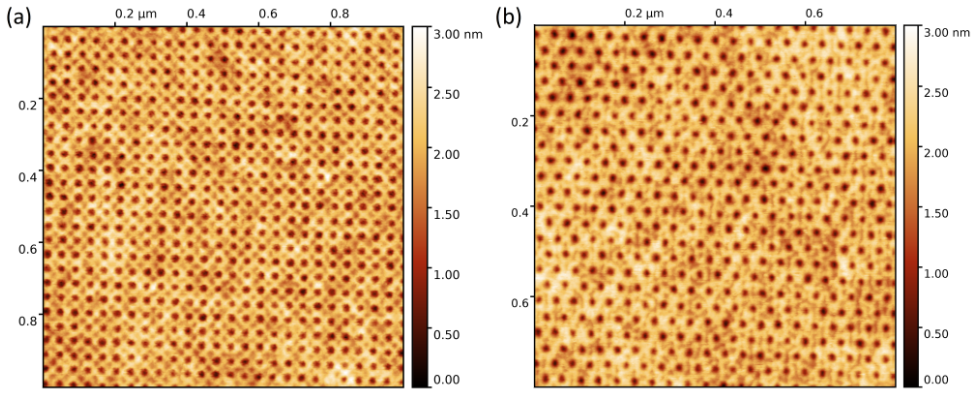

Figure 3.12: AFM topography images of patterned few-layer graphene. **(a)** Square antidot lattice with $a = 40$ nm. **(b)** Hexagonal antidot lattice with $a = 40$ nm.

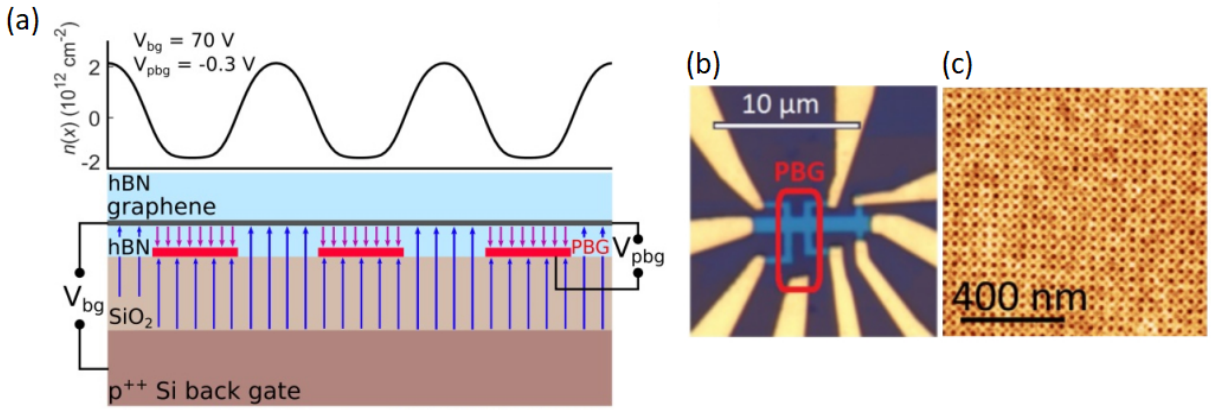

Figure 3.13: **(a)** Sample design with encapsulated graphene, global back gate, and few-layer graphene patterned bottom gate (PBG). Blue and red arrows represent electric field lines corresponding to the applied gate voltages V_{bg} and V_{pbg}. The global back gate is mainly screened by the PBG except at positions of the patterned holes. Consequently, this induces a periodic charge carrier density modulation in the graphene layer. The induced modulation reflects the patterned lattice geometry. The PBG mainly controls the average charge carrier density in the overall graphene layer. The top graph shows the calculated charge carrier density modulation profile at a certain gate configuration for a device with square superlattice and a lattice constant of $a = 40$ nm with dielectric thicknesses of $d_{SiO_2} = 285$ nm (SiO_2) and $d_{hBN,bot} = 5$ nm (bottom hBN) [269]. **(b)** Optical microscope image of a finished device (sample $SL1$, see chapter 4.2) with encapsulated graphene in Hall bar geometry and the PBG (red outline). **(c)** AFM image of the PBG in (b) with square antidot lattice and $a = 40$ nm. [13]

3.4 Measurement Setup

Electrical transport measurements were conducted in a ^{4}He cryostat with a base temperature of $T = 1.4$ K. Fig. 3.14 shows a cross-section and the main components of a typical ^{4}He cryostat. The sample is mounted onto a probe and inserted into the VTI (variable temperature insert). By opening a needle valve which connects the helium bath to the VTI and pumping on the VTI, the sample can be cooled down to base temperature. In addition, heating elements in the VTI enable to perform measurements up to $T \sim 180$ K. Furthermore, a superconducting coil inside the helium bath allows to apply uniform magnetic fields up to $B = 10 - 14$ T (depending on the cryostat used). Control and sensing wires connect the sample, magnetic coil, heater, and temperature sensors inside the VTI to the corresponding measurement equipment and a PC for controlling the experimental setup and data acquisition. Fig. 3.15 schematically depicts the AC measurement setup with standard lock-in technique. A master lock-in amplifier, operating at an oscillator frequency of 13 Hz, in combination with a series resistance provides a maximum source-drain current of $I = 1 - 10$ nA applied to the investigated graphene devices in Hall bar geometry. Additional lock-in amplifiers are used to simultaneously measure longitudinal (V_{xx}) and transverse (V_{xy}) voltages. For gate-bias spectroscopy a DC measurement setup is used, as schematically shown in Fig. 3.16. In this case, a DC voltage source provides a source-drain bias voltage V_{bias}. The current through the device is amplified and converted into a voltage signal which is measured by a voltmeter. In both setups, the available gates are connected to SMUs (source measure units) in order to apply well-defined gate voltages (back gate voltage V_{bg} and PBG voltage V_{pbg}). The measurement devices are connected to a PC over GPIB (general purpose interface bus) cables. Device control and data acquisition is done via the Lab::Measurement [270] environment.

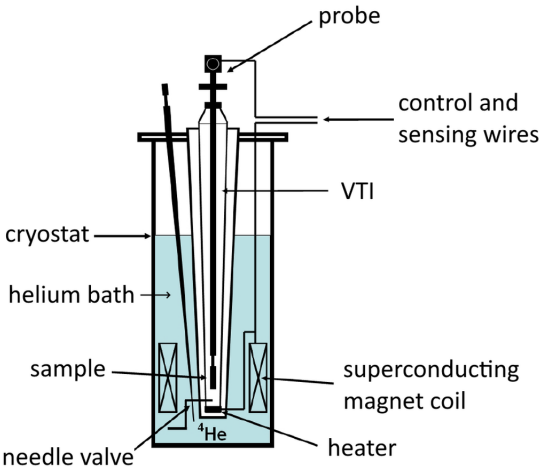

Figure 3.14: Main components of a ^{4}He cryostat with a base temperature of $T = 1.4$ K. The sample is mounted onto a probe and inserted into the VTI. A needle valve connecting the VTI to a helium bath and heating elements inside the VTI allow temperature controlled measurements. A superconducting magnet coil allows to apply uniform magnetic fields up to $B = 10 - 14$ T. Control and sensing wires connect the sample and controllable cryostat components to the measurement equipment and a PC. Adapted from [271].

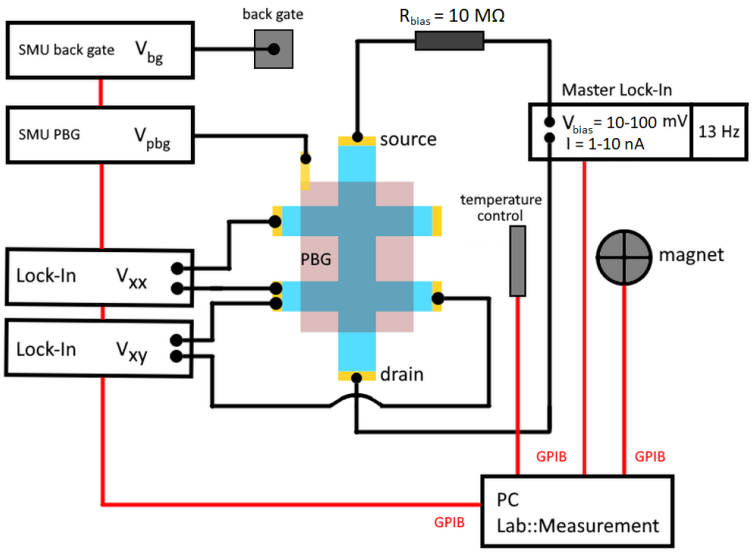

Figure 3.15: AC measurement setup with standard lock-in technique. A master lock-in amplifier in combination with a series resistance ($R_{bias} = 10$ MΩ) is used to apply a maximum source-drain current of $I = 1 - 10$ nA to a graphene device in Hall bar geometry. Longitudinal (V_{xx}) and transverse (V_{xy}) voltages are measured by additional lock-in amplifiers. Gate voltages are applied by SMUs (back gate voltage V_{bg} and PBG voltage V_{pbg}). Device control and data acquisition is done via GPIB cables (red) and a PC with Lab::Measurement [270] environment.

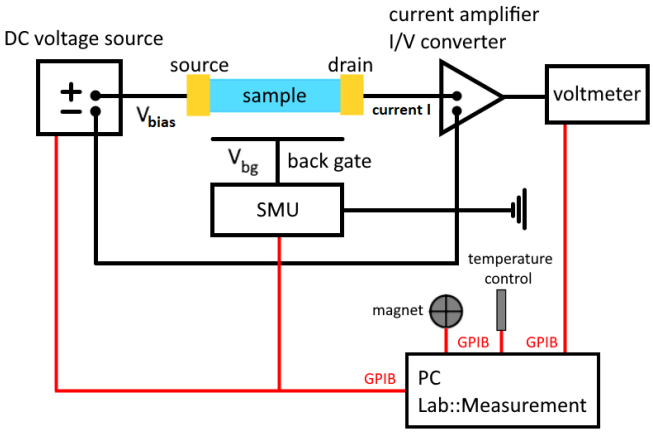

Figure 3.16: DC measurement setup for gate-bias spectroscopy. A DC voltage source provides a source-drain bias voltage V_{bias}. The current through the device is amplified and converted into a voltage signal which is measured by a voltmeter. A back gate voltage V_{bg} is applied by a SMU. Device control and data acquisition is done via GPIB cables (red) and a PC with Lab::Measurement [270] environment.

CHAPTER 4

EXPERIMENTAL RESULTS

4.1 Transport Measurements on Graphene Antidot Lattices

The following section discusses transport measurements on two graphene antidot lattice (GAL) devices (AD1 and AD2). Besides the general characterization and the observation of commensurability features, the emergence and tunability of energy gaps are investigated. The following table provides some basic information about the two examined GAL samples:

sample	$d_{hBN,top}$	$d_{hBN,bot}$	antidot lattice geometry	lattice constant a	neck width w
AD1	10 nm	55 nm	square	50 nm	40 nm
AD2	5 nm	25 nm	hexagonal	40 nm	25 nm

4.1.1 Characterization and Commensurability Effects

The following measurements were conducted on **sample AD1** – a GAL in Hall bar geometry with square antidot lattice (lattice constant $a = 50$ nm, estimated hole diameter $d_{AD} \sim 10$ nm, and neck width $w \sim 40$ nm). The geometrical factor of the sample is $W/L \sim 0.54$ with $L \sim 2.5$ μm and the classical gate coupling between graphene and the back gate is given by $c_g \sim 0.97 \times 10^{-4}$ F/m^2. The quantum capacitance is not taken into account due to the relatively thick SiO_2 dielectric (285 nm). An unpatterned reference region of the Hall bar allowed to work out the actual impact of the antidot region on the electronic properties of monolayer graphene by comparison to the nanostructured part of the sample.

Fig. 4.1 (a) shows the longitudinal resistance R_{xx} of the antidot region and of the unpatterned region as a function of back gate voltage V_{bg} at $T = 1.4$ K. Overall, the gate response of the antidot region exhibits strongly increased resistance compared to the pristine area. At the CNP the resistance of the GAL reaches about 200 kΩ and the on/off conductance ratio G_{on}/G_{off} of the device in the accessible gate voltage range is in the order of magnitude of ~ 100. The field-effect mobility of the unpatterned region is about $\mu_{pristine} \sim 120\,000$ cm^2/Vs, reflecting the overall high quality of the encapsulated graphene layer. The apparent field-effect mobility in the patterned region is about $\mu_{patterned} \sim 2000$ cm^2/Vs, strongly decreased due to additional scattering at the antidot edges. Although the protective hBN layer on top was relatively thin

($d_{hBN,top} \sim 10$ nm) and a dense array of nanoholes was etched into graphene by means of EBL and RIE (during which the sample was exposed to e-beam resist, chemicals and reactive gases), no severe doping effect of the patterned graphene region can be observed as evident from the absence of a noticeable shift of the Dirac peak position. In magnetotransport measurements on the GAL, shown in Fig. 4.1 (b), the quantum Hall effect starts to appear at relatively low magnetic fields of a few Tesla, indicating a high intrinsic charge carrier mobility in the remaining graphene areas. Overall, encapsulation between hBN preserved the intrinsic high quality of graphene even during the invasive lithography steps which were employed to fabricate short-period antidot lattices with neck widths of only a few tens of nanometres.

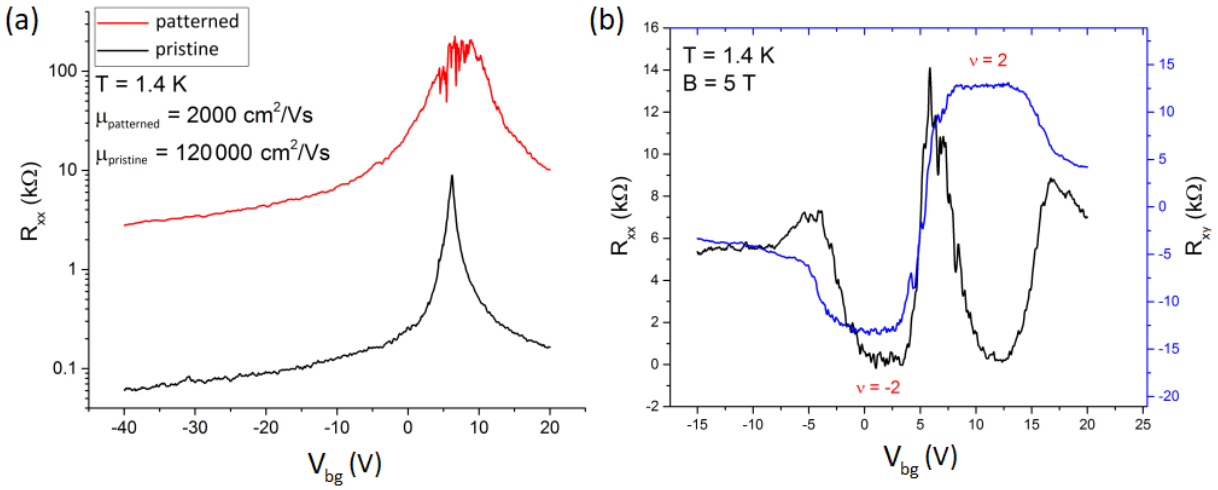

Figure 4.1: (a) Gate response of a square GAL with $a = 50$ nm in comparison with the gate response of pristine graphene in an unpatterned reference region. The longitudinal resistance R_{xx} is plotted as a function of back gate voltage V_{bg}. The extracted field-effect mobility in the unpatterned region lies at about 120 000 cm^2/Vs. The apparent field-effect mobility in the patterned antidot region is reduced to about 2000 cm^2/Vs and the overall resistance is strongly increased. **(b)** R_{xx} and R_{xy} as a function of back gate voltage V_{bg} in the antidot region at a magnetic field of $B = 5$ T. Quantum Hall states with $\nu = \pm 2$ are observable.

The preserved high intrinsic charge carrier mobility in the GAL allows the observation of ballistic effects and commensurability features in magnetotransport. Fig. 4.2 (a) displays the longitudinal resistance R_{xx} as a function of magnetic field B at a back gate voltage of $V_{bg} = -5$ V which corresponds to a charge carrier density of $n = -7.1 \times 10^{11}$ 1/cm^2. At this value of charge carrier density the Fermi wavelength $\lambda_F \sim 42$ nm is comparable to the neck width $w \sim 40$ nm – the system is in the quantum transport regime. Consequently, no antidot resonances can be observed at the expected magnetic field positions.

By increasing the charge carrier density to $n = -3.2 \times 10^{12}$ 1/cm^2 which corresponds to a Fermi wavelength of $\lambda_F \sim 20$ nm − now well below the neck width w − the system enters the classical transport regime and antidot peaks start to emerge at magnetic field values corresponding to pinned cyclotron orbits around 1 and 2 antidots, as depicted in Fig. 4.2 (b). At lower magnetic field values no additional (or at least no clearly distinguishable) antidot resonances can be identified. At high magnetic fields, if the cyclotron diameter is reduced below the neck width, the system enters the quantum Hall regime.
The resistance peak at zero magnetic field is caused by weak localization of charge carriers [66], from which a phase coherence length of about $l_\phi \sim 200$ nm can be extracted (see Fig. 4.3). This value lies well above the lattice spacing and shows that the patterned holes do not induce severe phase breaking scattering processes. Otherwise, the intervalley scattering length $l_i \sim 50$ nm, also extracted from the weak localization feature, is comparable to the lattice spacing and points towards enhanced intervalley scattering at the rough edges of the patterned nanoholes.

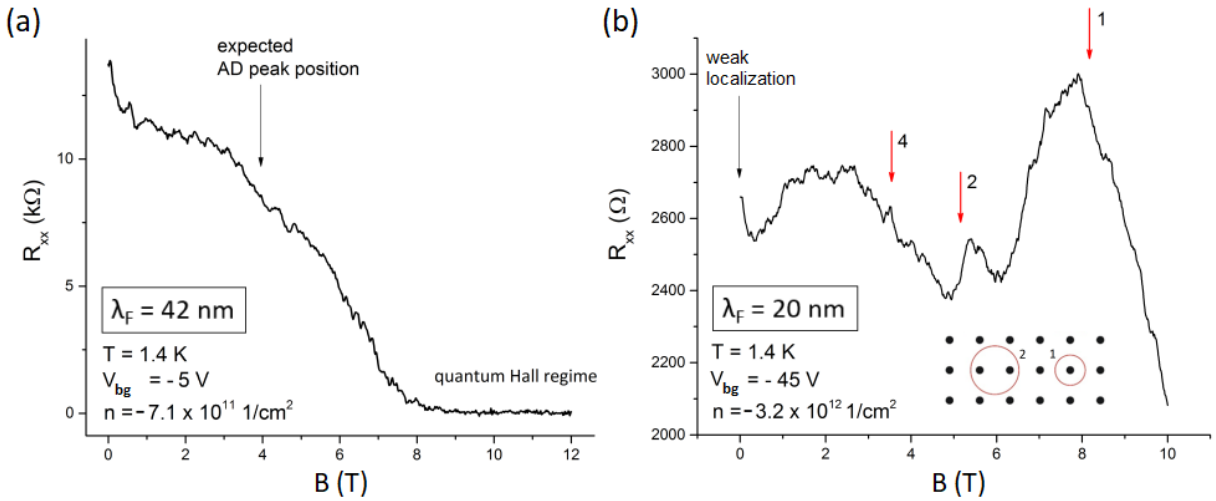

Figure 4.2: **(a)** Magnetotransport data at $V_{bg} = -5$ V. R_{xx} is plotted as a function of magnetic field B. The Fermi wavelength $\lambda_F \sim 42$ nm is comparable to the neck width w of the GAL − the system is in the quantum regime and no antidot resonances are observable. The arrow indicates the expected position of the fundamental antidot peak (corresponding to pinned orbits around one antidot). At high magnetic fields the system enters the quantum Hall regime. **(b)** At higher back gate voltages, i.e. higher charge carrier density, the Fermi wavelength is reduced below the neck width w and antidot features start to develop. Antidot resonances, corresponding to pinned orbits around 1 and 2 antidots (see inset), are clearly visible. No clearly resolved antidot resonance around 4 antidots can be identified. The enhanced resistance at zero magnetic field is caused by weak localization.

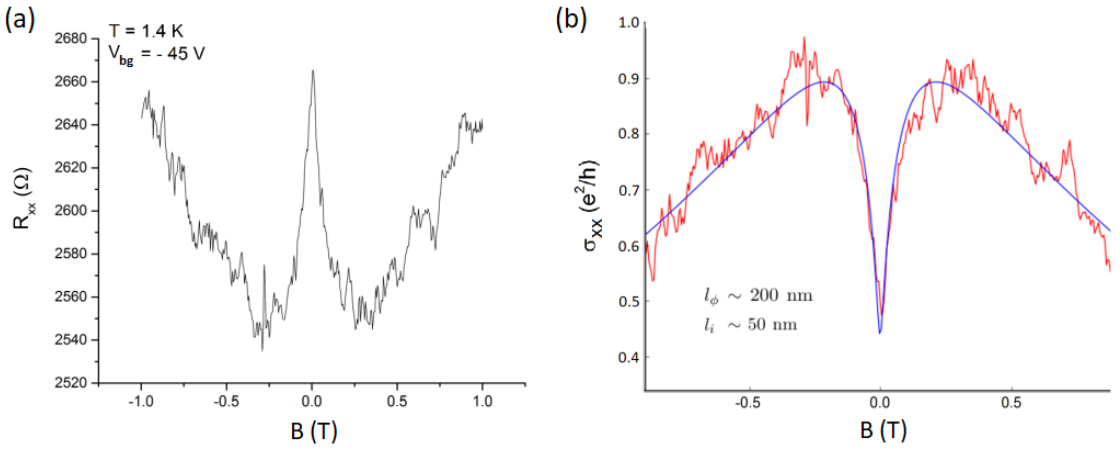

Figure 4.3: **(a)** R_{xx} around zero magnetic field displaying weak localization of charge carriers. **(b)** By fitting the data (red) to theory (blue curve, [66]), the phase coherence length l_ϕ and intervalley scattering length l_i can be extracted. The conductivity scale is shifted and the fitting was done via a fitting tool provided by Jan Bundesmann (University of Regensburg/chair Prof. Dr. K. Richter).

The fine oscillations superimposed on the magnetoresistance, see e.g. Fig. 4.2 (b), are reproducible (as illustrated in Fig. 4.4 (a)) and could indicate universal conductance fluctuations [67]. Another possible origin of these oscillations are contributions from quantized cyclotron orbits around antidots [251]. A fast Fourier transform (FFT) of the oscillations, averaged over several charge carrier densities, reveal a frequency of $f \sim 0.8$ 1/T (see Fig. 4.4 (b)). This corresponds to the addition of approximately one magnetic flux quantum Φ_0 per area $A \sim (57)^2$ nm^2, which is comparable to the antidot lattice unit cell area $A_{AD} = a^2 = (50)^2$ nm^2.

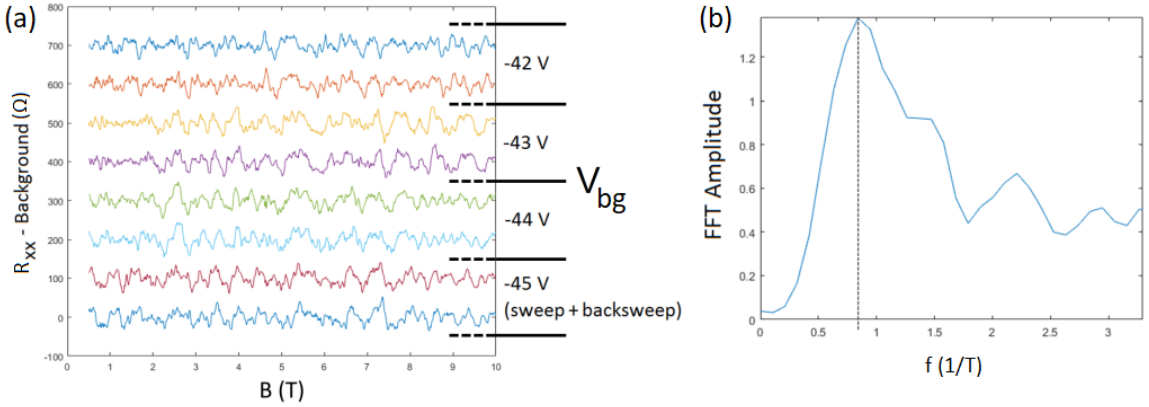

Figure 4.4: **(a)** R_{xx} as a function of magnetic field B at several back gate voltages V_{bg} after background subtraction. For every V_{bg}, sweep and backsweep is shown, illustrating the reproducibility of the observed oscillations. The curves are shifted for clarity. **(b)** Averaged FFT of the data shown in (a). The FFT peak at a frequency of about $f \sim 0.8$ 1/T corresponds to one magnetic flux quantum per area $A \sim (57)^2$ nm^2, which is comparable to the lattice unit cell area $a^2 = (50)^2$ nm^2. Data processing was done via a Matlab code provided by Johannes Ziegler (University of Regensburg/chair Prof. Dr. D. Weiss).

4.1.2 Magnetically Tunable Energy Gap

In the following section, the emergence of energy gaps in GALs and their tunability by a magnetic field are investigated. The first measurements were conducted on **sample AD1**. Energy gaps E_{gap} can be determined from temperature dependent measurements by applying Arrhenius law of temperature-activated transport [6, 25]:

$$G_{min} \propto e^{\left(\frac{-E_{gap}}{2k_B T}\right)} \tag{4.1}$$

In the case of fundamental energy gaps in graphene, G_{min} corresponds to the minimum conductance (i.e. maximum resistance) at the CNP. Pristine graphene, lacking an intrinsic energy gap, exhibits only a weak temperature dependency of resistance at the CNP. This is illustrated in Fig. 4.5 (a) which displays back gate voltage sweeps at low (8 K) and elevated (140 K) temperature measured in the unpatterned region of the Hall bar.
For comparison, Fig. 4.5 (b) shows gate sweeps at temperatures between $T = 8$ K and $T = 140$ K in the antidot region. In the nanopatterned graphene region the resistance at the CNP is strongly increased and the GAL shows insulating behaviour. The evolution of the conductance as a function of temperature reflects temperature activated transport. Overall, this points towards the existence of a fundamental energy gap in the GAL.
Fig. 4.6 (a) displays the minimum conductance G_{min} at the CNP as a function of inverse temperature $1/T$. The saturation of G_{min} at low temperatures could be attributed to limitations of the lock-in measurement setup with finite AC current bias [225]. Since the performed lock-in measurements were carried out with a finite AC current bias, one also has to take into account the voltage drop V_{xx} across the patterned area and the current I through the device, both shown in Fig. 4.7. The maximum voltage drop of about $V_{xx} \sim 2$ mV can be associated with a temperature of about $T \sim 20$ K ($V_{xx}e = k_B T$). Consequently, one can expect a reduced impact of the energy gap on the transport properties at lower temperatures. Additionally, if the voltage drop exceeds the size of the energy gap, the resistance at the CNP starts to saturate [225]. Another origin of the observed onset of saturation could be variable range hopping which may also have significant impact on the transport properties of GALs at low temperatures, generally causing a temperature dependency of the conductance which is different from simply temperature-activated behaviour [232, 233].
By employing eq. 4.1 and applying a linear fit to the high temperature region in the Arrhenius plot, an energy gap of about $E_{gap} \sim 6$ meV is estimated, as depicted in Fig. 4.6 (b). In comparison with theoretically expected values for the corresponding neck width (see Fig. 2.45), the experimental value seems to be underestimated since it lies at the lower limit. Similar experiments on comparable short-period GALs showed energy gaps at the upper limit of the expected range [6]. One reason for the apparent discrepancy could be the fact that the used temperature range was not sufficient to probe the overall size of the energy gap. In Ref. [6], temperatures above $T = 200$ K were necessary in order to correctly determine the actual size of the energy gap in a short-period GAL (with neck width $\sim 12 - 15$ nm). Unfortunately, the available maximum temperature in the used experimental setup was limited to about $T \sim 180$ K and temperatures well below this limit were applied.

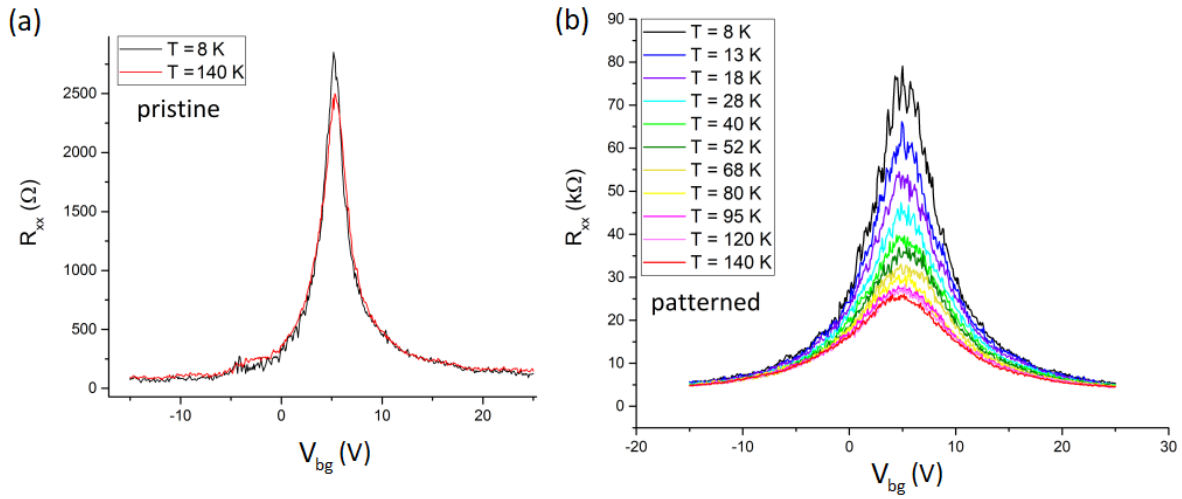

Figure 4.5: **(a)** Pristine graphene: R_{xx} as a function of back gate voltage V_{bg} at $T = 8$ K and $T = 140$ K. Pristine graphene exhibits nearly no temperature-dependent behaviour of resistance in the considered temperature range. **(b)** Patterned antidot region: R_{xx} displays temperature activated transport at the CNP, indicating the emergence of an energy gap.

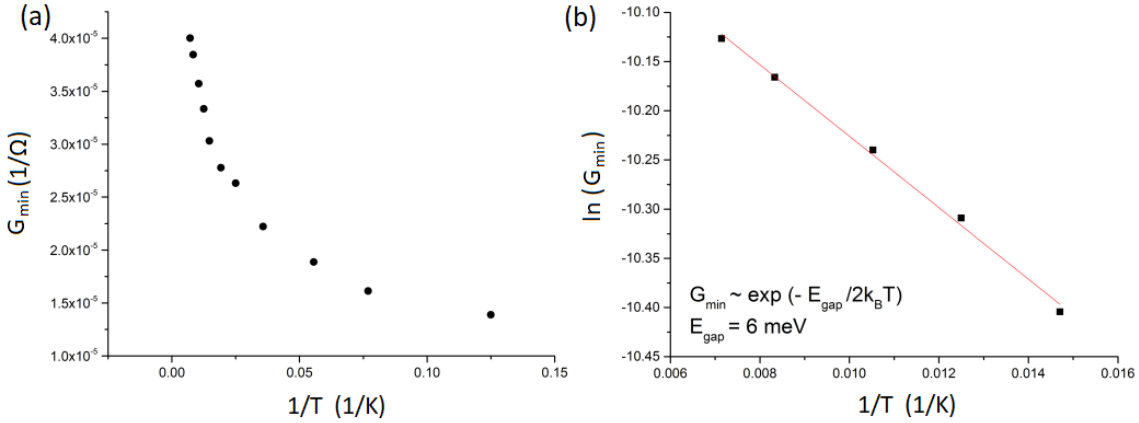

Figure 4.6: **(a)** Minimum conductance G_{min} at the CNP as a function of inverse temperature $1/T$. **(b)** Arrhenius Plot: Determination of the size of the energy gap by Arrhenius law of temperature-activated transport. The fit used for extraction of the energy gap was applied in the linear high temperature region. The estimated size of the energy gap is about $E_{gap} \sim 6$ meV.

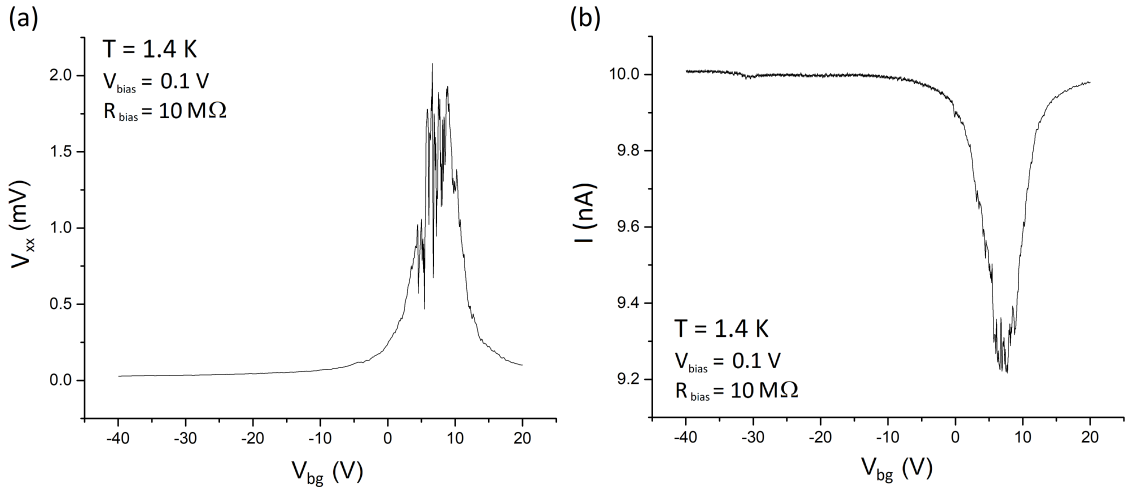

Figure 4.7: (a) Voltage drop V_{xx} across the antidot region as a function of back gate voltage V_{bg}. The applied source-bias voltage is $V_{bias} = 0.1$ V. **(b)** The current I through the device as a function of back gate voltage V_{bg}. By using a series resistor of $R_{bias} = 10$ MΩ, the maximum current I through the device is limited to $I = 10$ nA.

Besides Arrhenius law of temperature-activated transport, an alternative method was used in order to estimate the size of energy gaps in the investigated GALs by considering the gate voltage range ΔV_{bg} of the transport gap region at low temperature. In general, this gate voltage range can be associated with a certain energy range ΔE and is, in the ideal case, identical to the extent of the fundamental energy gap E_{gap} in the electronic band structure. But since the transport gap in realistic devices also contains contributions from disorder [226, 230], the estimated magnitude of energy gaps can only give an upper limit and should be treated with caution. Furthermore, the following estimation neglects Fermi level pinning at midgap states, originating from e.g. defects, which ideally also has to be taken into account.
The (simplified) estimation of energy gaps E_{gap} by considering the transport gap region ΔV_{bg} is given by [6, 239, 272, 273]:

$$E_{gap} = \Delta E = 2\hbar v_F \sqrt{\pi c_g \Delta V_{bg}/2e} \tag{4.2}$$

The gate voltage range ΔV_{bg} of the transport gap region can be estimated in two ways:
Method (1) (see Fig. 4.8 (a)): The transport gap region is determined by taking the gate voltage range in which the conductivity σ_{xx} drops below one conductance quantum, which is equivalent to the Ioffe-Regel criterion for localization in 2D semiconductors [6, 274]. If the Ioffe-Regel criterion $k_F \cdot l_{mfp} \sim 1$ is fulfilled, a transition into an insulating regime occurs which manifests if $k_F \cdot l_{mfp} \ll 1$.
Method (2) (see Fig. 4.8 (b)): The transport gap region is determined by extrapolating the linear regions of conductivity σ_{xx} to zero conductivity. The thereby defined gate voltage range corresponds to the transport gap region [227].
The result in both methods shows overall larger gap values compared to the value extracted from temperature activated transport. For sample AD1, values of about $E_{gap} \sim 120$ meV (method (1)) and $E_{gap} \sim 100$ meV (method (2)) are estimated, exceeding the upper limit of the expected range

in Fig. 2.45 and pointing towards the presence of non-negligible disorder in the device. Also the emergence of conductance peaks inside the transport gap region indicates the presence of midgap states and resonant conduction paths through localized states [239] probably originating from (edge) disorder and defects.

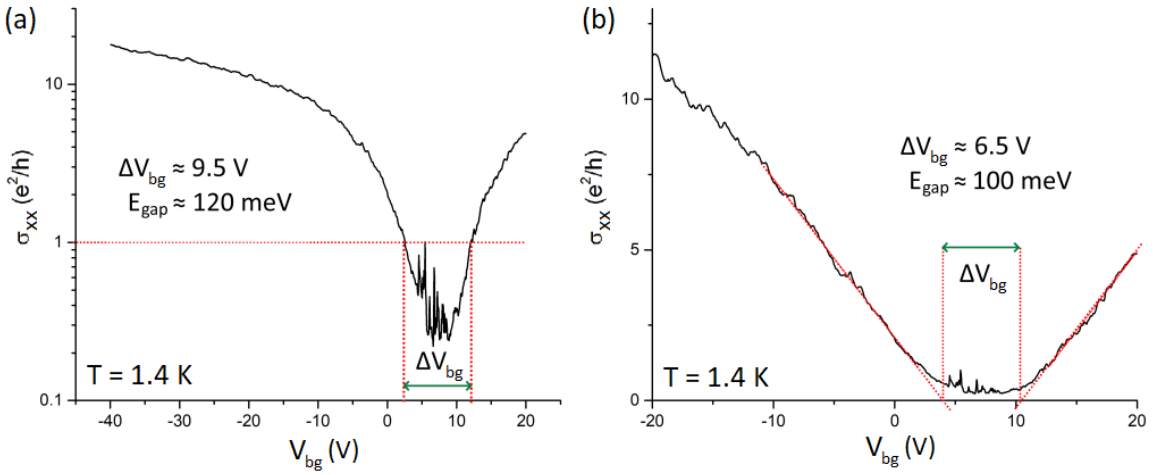

Figure 4.8: Determination of the transport gap fo a square GAL with lattice constant $a = 50$ nm and neck width $w = 40$ nm: **(a)** Conductivity σ_{xx} on a logarithmic scale as a function of back gate voltage V_{bg}. Method (1) used to determine the transport gap region: the gate voltage range of the transport gap is determined by the region in which σ_{xx} drops below the conductance quantum e^2/h. **(b)** Conductivity σ_{xx} on a linear scale as a function of back gate voltage V_{bg}. Method (2) used to determine the transport gap region: the gate voltage range of the transport gap regime is extracted by extrapolating the regions of linear increase of σ_{xx} to zero conductivity.

In the following, **sample AD2** with a hexagonal antidot lattice (lattice constant of $a = 40$ nm, an estimated hole diameter of $d_{AD} \sim 15$ nm, and a neck width of $w \sim 25$ nm) is examined in more detail. The geometrical factor of the sample is $W/L \sim 0.53$ with $L \sim 1.9$ μm and the classical gate coupling between graphene and the back gate is given by $c_g \sim 1.09 \times 10^{-4}$ F/m^2. In this sample the observation of commensurability features was not possible since the maximum applicable back gate voltage was limited to values not sufficient for probing antidot resonances due to increasing leakage currents through the gate at higher back gate voltages.
Fig. 4.9 (a) shows the voltage drop V_{xx} across the antidot region and Fig. 4.9 (b) displays the source-drain current I as a function of back gate voltage V_{bg} measured at base temperature $T = 1.4$ K. By using a series resistor of $R_{bias} = 10$ MΩ, the maximum current I through the device was limited to $I = 1$ nA. Again, at the CNP, V_{xx} strongly increases and the current through the device significantly decreases which reflects a regime of high resistance. The maximum voltage drop of about $V_{xx} \sim 1.5$ mV corresponds to a temperature of about $T \sim 15$ K. Fig. 4.9 (c) shows the longitudinal resistance R_{xx} as a function of V_{bg}. The sample exhibits insulating behaviour at the CNP, where the longitudinal resistance R_{xx} reaches a few MΩ. Fig. 4.9 (d) displays the corresponding longitudinal conductivity $\sigma_{xx} = \frac{1}{R_{xx}} \frac{L}{W}$ from which a field-effect mobility of about $\mu \sim 800$ cm^2/Vs is determined. The G_{on}/G_{off}-ratio of the GAL device in the accessible gate voltage range is in the order of magnitude of ~ 100.

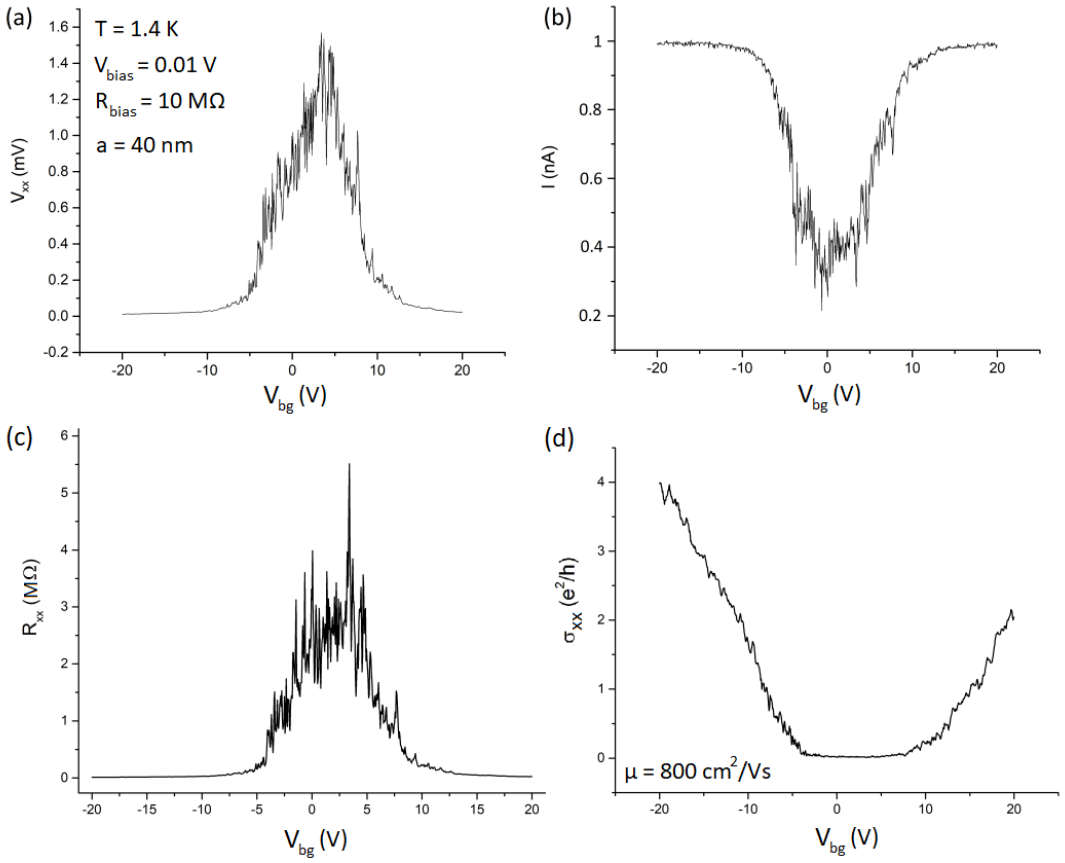

Figure 4.9: Sample AD2: Hexagonal GAL with lattice constant $a = 40$ nm and neck width $w = 25$. **(a)** Voltage drop V_{xx} across the antidot region as a function of back gate voltage V_{bg}. The applied source-bias voltage is $V_{bias} = 0.01$ V. **(b)** The current I through the device as a function of back gate voltage V_{bg}. By using a series resistor of $R_{bias} = 10$ MΩ, the maximum current I through the device is limited to $I = 1$ nA. **(c)** R_{xx} as a function of back gate voltage V_{bg}. The resistance at the CNP is strongly increased. **(d)** Conductivity σ_{xx} as a function of back gate voltage V_{bg} from which a field-effect mobility of $\mu \sim 800$ cm^2/Vs is extracted. σ_{xx} is strongly suppressed in the insulating regime around the CNP.

Fig. 4.10 displays the measured longitudinal voltage drop V_{xx} and the current I through the device as a function of back gate voltage V_{bg} at different perpendicular magnetic fields B and temperatures T. Fig. 4.11 shows the corresponding longitudinal resistances R_{xx} as a function of back gate voltage V_{bg}. By applying a perpendicular magnetic field to the sample, the resistance at the CNP decreases and the insulating regime starts to vanish, which indicates a quenching of the energy gap (see Fig. 4.11 (a)). This becomes also apparent in temperature-dependent measurements conducted at $B = 0, 2, 4$ T, as plotted in Fig. 4.11 (b)-(d). Again, a strong temperature dependency of R_{xx} and temperature-activated transport behaviour at the CNP is observed. Upon increasing the applied magnetic field, the device exhibits a negative magnetoresistance and the effect of temperature-activated transport decreases.

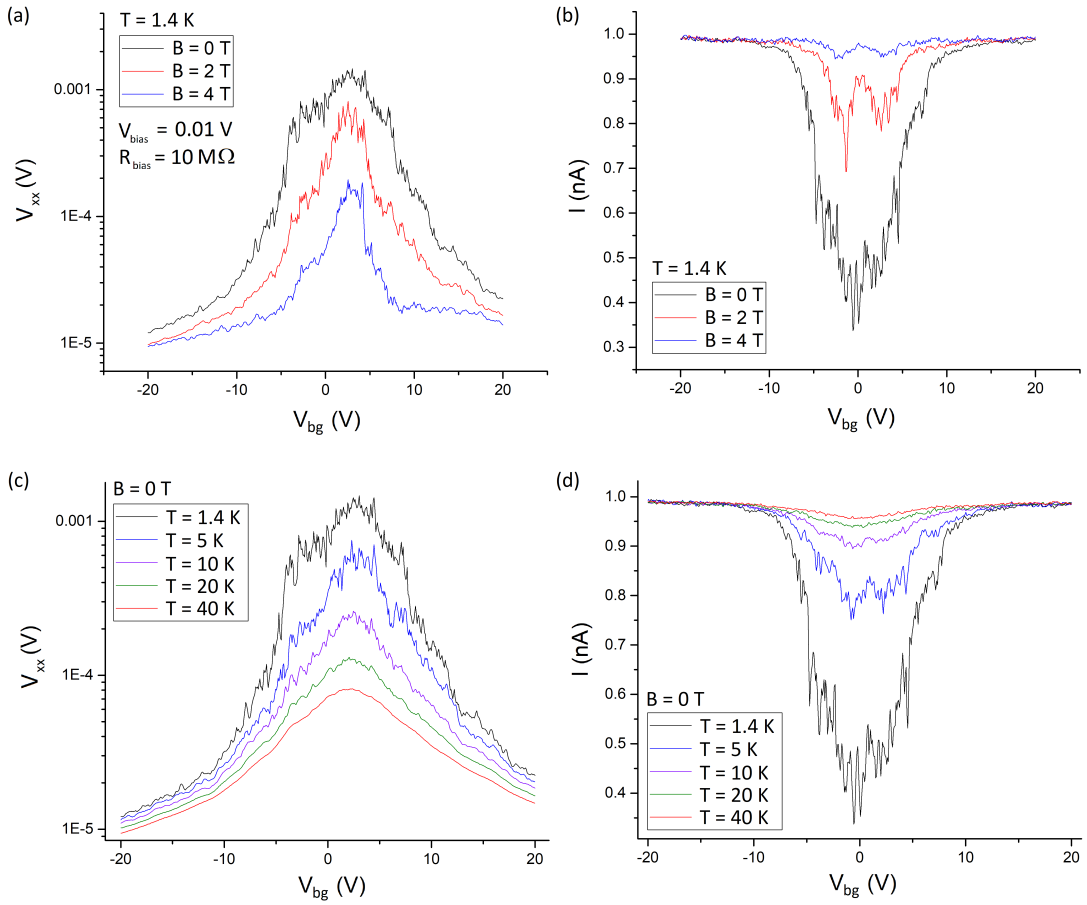

Figure 4.10: **(a)** Voltage drop V_{xx} across the antidot region as a function of back gate voltage V_{bg} at $B = 0$ T, $B = 2$ T, and $B = 4$ T. The applied source-bias voltage is $V_{bias} = 0.01$ V. **(b)** The corresponding current I through the device as a function of back gate voltage V_{bg}. By using a series resistor of $R_{bias} = 10$ MΩ, the maximum current I through the device is limited to $I = 1$ nA. **(c)** Voltage drop V_{xx} across the antidot region as a function of back gate voltage V_{bg} at different temperatures and $B = 0$ T. **(d)** The corresponding current I as a function of back gate voltage V_{bg}.

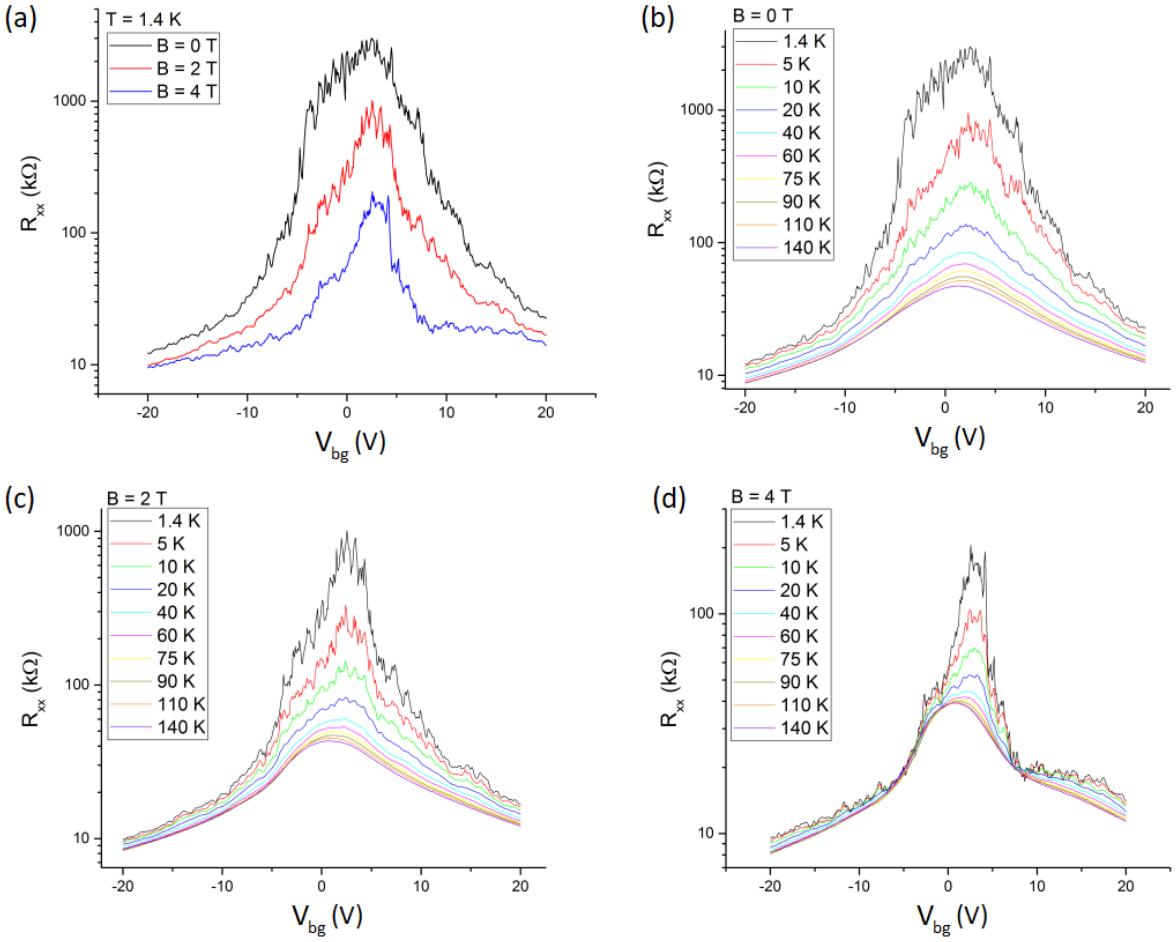

Figure 4.11: **(a)** Gate sweeps of R_{xx} at $B = 0$ T, $B = 2$ T, and $B = 4$ T. The negative magnetoresistance at the CNP indicates a diminishing of the energy gap upon applying a magnetic field. **(b)-(d)** Temperature-dependent gate sweeps at (b) $B = 0$ T, (c) $B = 2$ T, and (d) $B = 4$ T.

In the following, the corresponding conductivities, given by $\sigma_{xx} = \frac{\rho_{xx}}{\rho_{xx}^2+\rho_{xy}^2}$, are evaluated. Fig. 4.12 (a) shows the minimum conductivity σ_{min} at the CNP as a function of inverse temperature $1/T$. Energy gaps, determined in Arrhenius plots, are displayed in Fig. 4.12 (b). A zero-field value of about $E_{gap} \sim 6.8$ meV is estimated which again lies at the lower limit of the expected range (see. Fig. 2.45). Furthermore, by increasing the applied magnetic field, a decrease of the apparent magnitude of the energy gap is observed. At $B = 2$ T the energy gap is reduced to about $E_{gap} \sim 3.8$ meV. At $B = 4$ T the size of the apparent energy gap shrinks to about $E_{gap} \sim 1.5$ meV.

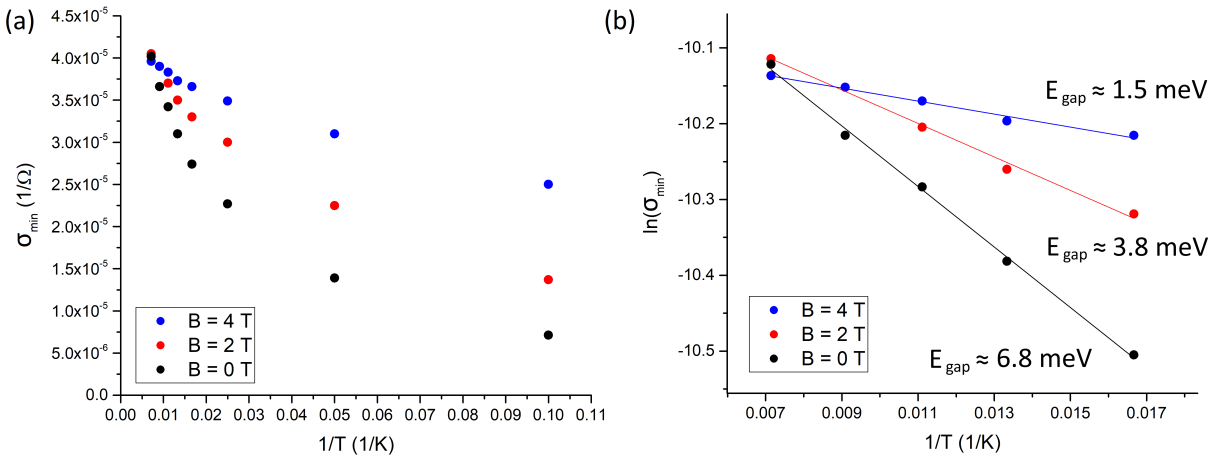

Figure 4.12: **(a)** Minimum conductivity σ_{min} as a function of inverse temperature $1/T$ extracted from the data in Fig. 4.11. **(b)** Corresponding Arrhenius plots from which the magnitude of energy gaps at different magnetic fields is estimated. By increasing the applied magnetic field, the apparent energy gap in the GAL decreases from about $E_{gap} \sim 6.8$ meV at $B = 0$ T to $E_{gap} \sim 1.5$ meV at $B = 4$ T.

The magnitude of energy gaps is also estimated by the two alternative methods (1) and (2) considering the transport gap region. The results are depicted in Fig. 4.13 (a) and Fig. 4.13 (b). Again, the resulting values are larger compared to the values extracted from Arrhenius plots and exceed the upper limit of the expected range (see Fig. 2.45). The zero-field value obtained from method (1) lies at about $E_{gap} \sim 200$ meV. The value determined from method (2) is about $E_{gap} \sim 150$ meV. The magnetic field dependency of energy gaps, derived from all three methods, is plotted in Fig. 4.14 in which the size of energy gaps is normalized to the corresponding zero-field value. In all cases, a diminishing of an initial energy gap upon increasing the applied magnetic field is observed. By extrapolating the data to zero value, done by applying linear fits, a complete closing of the energy gap in a magnetic field range roughly between $B \sim 3$ T and ~ 9 T is estimated, corresponding to a magnetic length $l_B < 15$ nm well below the neck width. At higher magnetic fields, the usual quantum Hall effect of pristine graphene manifests, as depicted in Fig. 4.15.

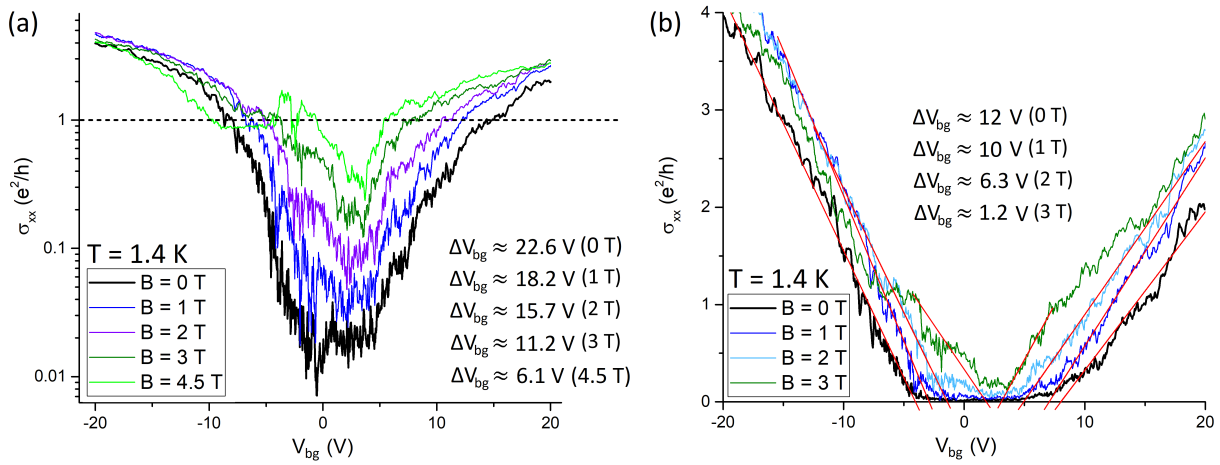

Figure 4.13: **(a)** Conductivity σ_{xx} plotted on a logarithmic scale as a function of back gate voltage V_{bg} at different magnetic fields B. Method (1): The gate voltage range of the transport gap is determined by the region in which σ_{xx} drops below one conductance quantum e^2/h. **(b)** Conductivity σ_{xx} plotted on a linear scale as a function of back gate voltage V_{bg} at different magnetic fields B. Method (2): The gate voltage range of the transport gap is extracted by extrapolating the linear regions of σ_{xx} to zero conductivity. At $B \geq 4.5$ T no transport gap region can be defined with method (2).

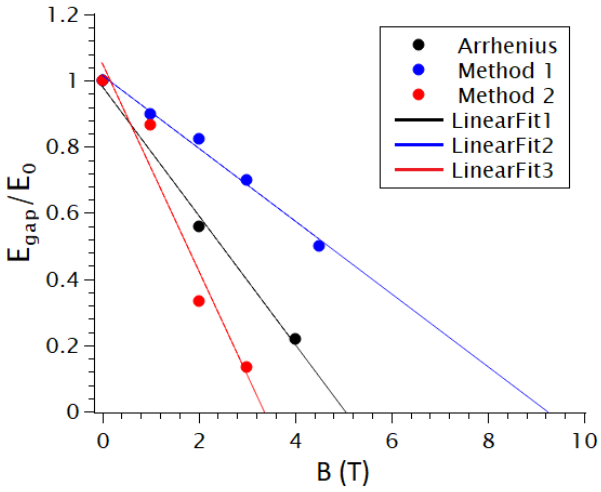

Figure 4.14: Energy gaps E_{gap} normalized to their zero-field value (E_0) as a function of magnetic field B. Energy gaps were extracted from Arrhenius plots (see Fig. 4.12) and from two alternative methods (1)+(2) by evaluating the gate voltage range of the transport gap (see Fig. 4.13). The linear fits in all three cases point towards a complete closing of a zero-field energy gap in a magnetic field range roughly between $B \sim 3$ T and $B \sim 9$ T.

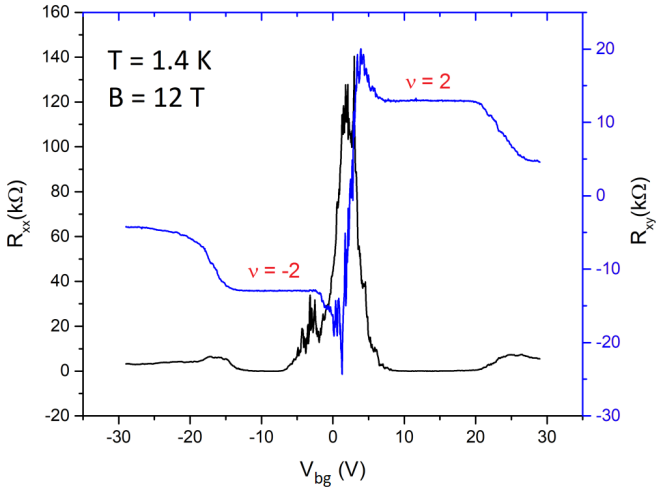

Figure 4.15: Longitudinal and Hall resistance as a function of back gate voltage at $B = 12$ T. At high magnetic fields the usual quantum Hall effect of pristine graphene manifests.

Conclusion

Overall, a quantitative and reliable determination of the actual size of energy gaps in the investigated GAL devices was not possible by the employed methods since strongly differing gap sizes were obtained, ranging between ~ 6 meV and ~ 200 meV. Consequently, the extracted values can be only seen as rough, qualitative estimations. But the experimental results indicate the emergence of magnetically tunable energy gaps in GALs since the estimated zero-field gap values, obtained in all employed methods, exhibited a diminishing in an applied magnetic field. In addition, the measurement results point towards the presence of a non-negligible amount of disorder (probably mainly edge disorder [240]) influencing the charge carrier transport through the investigated devices and obscuring the impact of a fundamental energy gap. Also the on/off conductance ratio obtained in the fabricated GAL devices (in the order of magnitude of ~ 100 at $T = 1.4$ K) is too low to allow real transistor action at room temperature since the current flow through the devices can not be completely switched off. Consequently, further improvements in device quality are necessary in order to reduce (edge) disorder. Also the neck widths of GAL devices should be further reduced (ideally below 10 nm [23]) in order to increase the magnitude of the induced energy gaps which would consequently enhance the on/off conductance ratio and enable efficient transistor action, but with the drawback of a further decrease in charge carrier mobility [275, 276].

4.1.3 Gate-Bias Spectroscopy

In principle, magnetically tunable energy gaps allow to control (and in the ideal case to completely switch off) the current flow through a GAL device. An exemplary working principle is given in the following gate-bias spectroscopy measurements on **sample AD2** conducted at $B = 0$ T and $B = 3$ T, as depicted in Fig. 4.16. Fig. 4.16 (a) schematically shows the principle of gate-bias spectroscopy. The current I is measured as a function of applied bias voltage V_{bias} at different gate voltages V_{bg}. At zero magnetic field the I/V_{bias}-curves exhibit non-linear behaviour due to suppressed current flow at the CNP in an extended V_{bias} range around $V_{bias} = 0$ V, see Fig. 4.16 (b). One can define a bias gap region $\Delta V_{bias} \sim 14$ mV in which the I/V_{bias}-characteristics deviate from linear behaviour (determined by the grey dashed lines in Fig. 4.16 (b)). The corresponding differential conductance dI/dV_{bias} in this regime is reduced, see Fig. 4.16 (c). By applying a magnetic field of $B = 3$ T, the I/V-curves change and display nearly linear behaviour − as expected for an Ohmic conductor like pristine graphene − (see Fig. 4.16 (b)) and the region of suppressed differential conductance starts to vanish (see Fig. 4.16 (c)). Fig. 4.17 shows colour map plots of the conducted gate-bias spectroscopy measurements. In Fig. 4.17 (a) and (b), the current I and the corresponding differential conductance dI/dV_{bias} are plotted as a function of V_{bias} and V_{bg} at $B = 0$ T. At zero magnetic field the current flow through the GAL around the CNP is suppressed and an island of reduced differential conductance emerges. A transport gap region ($\Delta V_{bg} \sim 12$ V $\rightarrow E_{gap} \sim 150$ meV − approximately identical to the gap value estimated from method (2)) and a bias gap region [239] ($E_{gap} = e\Delta V_{bias} \sim 14$ meV − identical to the bias gap value extracted in Fig. 4.16 (b)) can be defined, as illustrated in Fig. 4.17 (b). In the ideal case, these energy ranges (which should be identical) correspond to the fundamental energy gap in the GAL, but again, probably due to remaining disorder in the investigated device, a trivial one-to-one correspondence between the values extracted from the gap regions and a fundamental energy gap is not given − similar to the case of GNRs [239]. At $B = 3$ T, as depicted in Fig. 4.17 (c) and (d), the suppression of current at the CNP is reduced and the region of reduced differential conductance starts to vanish − the GAL exhibits nearly Ohmic behaviour.

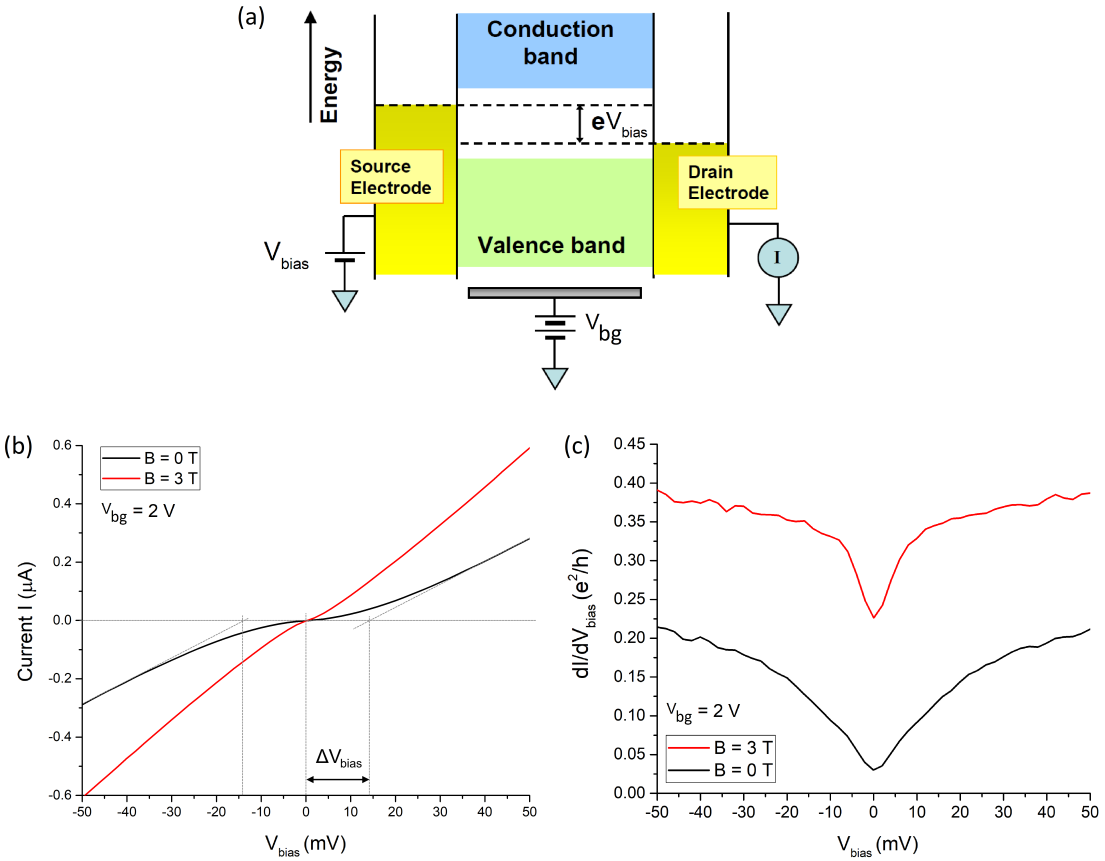

Figure 4.16: **(a)** Principle of gate-bias spectroscopy. An applied bias voltage V_{bias} between source and drain contact opens a bias window eV_{bias}. Depending on available states inside the bias window, current between source and drain is able to flow or is blocked. By an applied back gate voltage V_{bg}, energy levels of the studied device can be effectively shifted up and down in energy. Adapted from [239]. **(b)** I/V_{bias}-curves of sample AD2 at a back gate voltage of $V_{bg} = 2$ V in the vicinity of the CNP at $B = 0$ T and $B = 3$ T. At zero magnetic field the GAL exhibits non-Ohmic behaviour. The current flow in an extended V_{bias} range around $V_{bias} = 0$ V is suppressed. By extrapolating the linear regions of the I/V_{bias}-curve to zero current, a bias gap region $\Delta V_{bias} \sim 14$ mV can be defined (grey dashed lines). By applying a magnetic field, the character of the I/V_{bias}-curve changes to nearly linear behaviour as expected for an Ohmic conductor like pristine graphene. **(c)** The corresponding differential conductance dI/dV_{bias} plotted as a function of V_{bias} at $B = 0$ T and $B = 3$ T. dI/dV_{bias} increases upon applying a magnetic field.

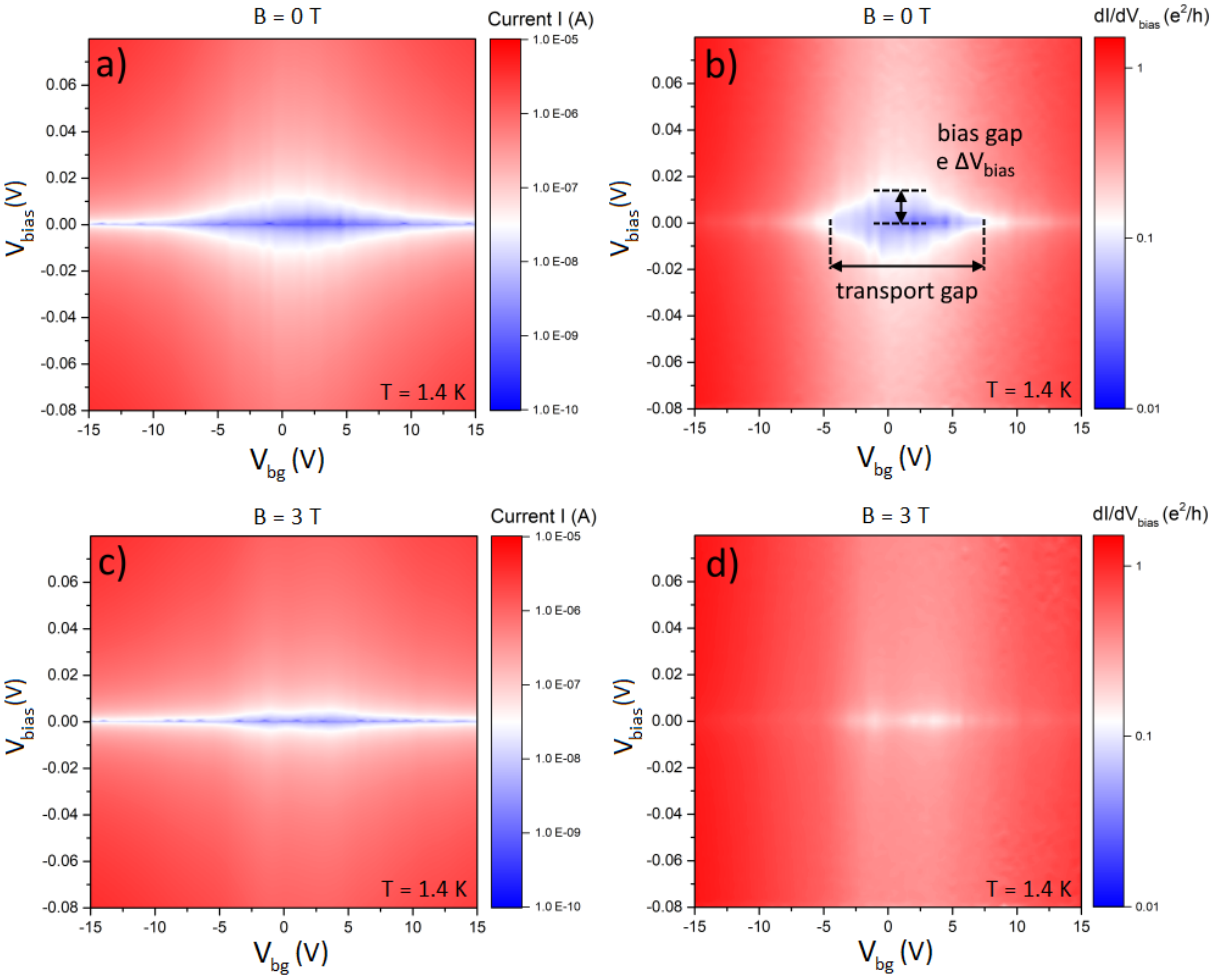

Figure 4.17: Gate-bias spectroscopy conducted on sample AD2: **(a)** Zero magnetic field: Current I as a function of bias voltage V_{bias} at different back gate voltages V_{bg}. **(b)** The corresponding differential conductance dI/dV_{bias}. At zero magnetic field the current flow through the GAL in the insulating region around the CNP is suppressed and a region of reduced differential conductance emerges. A transport gap region ($\Delta V_{bg} \sim 12$ V $\rightarrow E_{gap} \sim 150$ meV) and a bias gap region ($E_{gap} = e\Delta V_{bias} \sim 14$ meV) can be defined. **(c)** At $B = 3$ T: Current I as a function of bias voltage V_{bias} at different back gate voltages V_{bg}. **(d)** Differential conductance dI/dV_{bias} at $B = 3$ T. By applying a magnetic field, the suppression of current through the device and the gap regions vanish.

4.1.4 Non-Local Resistance

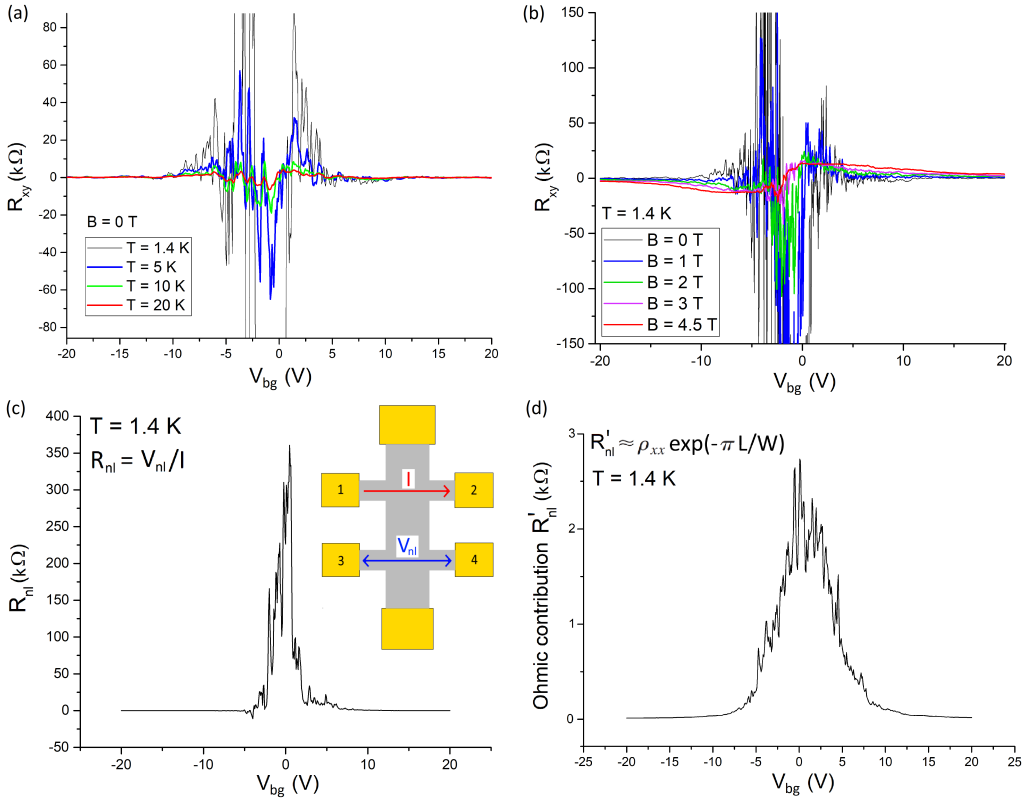

Figure 4.18: Hall resistance R_{xy} as a function of back gate voltage V_{bg} measured in sample AD2. **(a)** Zero-field R_{xy} at different temperatures. **(b)** R_{xy} at different magnetic fields. **(c)** Non-local resistance R_{nl} as a function of V_{bg}. Inset shows the measurement setup. A current I is applied between contacts 1 and 2 and the non-local voltage drop V_{nl} is measured between contacts 3 and 4. R_{nl} exceeds the expected value given by the Ohmic contribution (see (d)). **(d)** Expected Ohmic contribution R'_{nl} to the non-local resistance.

Another phenomenon, observed in the studied GALs, is a pronounced zero-field Hall resistance R_{xy} which strongly decreases upon increasing the temperature (see Fig. 4.18 (a)) or by increasing a magnetic field applied perpendicularly to the sample (see Fig. 4.18 (b)). Also additional non-local measurements show a pronounced non-local signal R_{nl} (see Fig. 4.18 (c)) which exceeds the expected Ohmic contribution $R'_{nl} \sim \rho_{xx} \exp(-\pi L/W)$ [277] (see Fig. 4.18 (d)). The origin of such large non-local signals is not completely clear. One explanation could be directed scattering of electrons into voltage probes due to the present ensemble of antidots. Another explanation, given in the special case of GALs and in gapped graphene in general, is that the energy gap induces a non-zero Berry curvature $\vec{\Omega}$ which is connected to a force $\vec{F} \propto \vec{k} \times \vec{\Omega}$ acting on the charge carriers [212, 278]. The non-zero Berry curvature $\vec{\Omega}$ effectively acts as a magnetic field in k-space, which can give rise to a non-zero Hall response R_{xy}. The emergence of such Berry-curvature-induced, non-local signals has already been observed in graphene/hBN devices with moiré-induced energy gaps [279, 280]. Also the GAL device in Ref. [6], similar to the studied device here, exhibited a pronounced non-zero Hall resistance which could not be explained solely by simple geometric effects and directed current flow and was attributed to a gap-induced non-zero Berry curvature.

4.2 Gate-Tunable Two-Dimensional Superlattices in Graphene

The following section presents experimental and theoretical results concerning gate-tunable two-dimensional superlattices in graphene. First, results at zero magnetic field in view of modifications of the electronic band structure of graphene are discussed. Corresponding magnetotransport results exhibit signatures of the Hofstadter butterfly energy spectrum and pronounced band conductivity oscillations. Furthermore, the interplay between an artificial gate-defined superlattice and a moiré superlattice is examined. Some of the results presented here are published in Ref. [13]. The following table provides some basic information about the two investigated superlattice devices (SL1 and SL2):

sample	$d_{hBN,top}$	$d_{hBN,bot}$	superlattice geometry	superlattice constant a_{sl}
SL1	25 nm	5 nm	square	40 nm
SL2	35 nm	7 nm	hexagonal	40 nm

4.2.1 Gate-Tunable Modification of Electronic Band Structure

The realization of superlattice effects and electronic band structure modifications in graphene by means of the double-gate technique presented in chapter 3.3 is demonstrated in **sample SL1** (see Fig. 3.13) which consists of a hBN/graphene/hBN Hall bar on top of a few-layer graphene PBG with square lattice symmetry and lattice constant $a_{sl} = 40$ nm in combination with a global, uniform p^{++} doped Si back gate. The geometrical factor of the sample is $W/L \sim 0.88$ with $L \sim 1.4$ μm and the classical gate coupling between graphene and the PBG is given by $c_g \sim 5.3 \times 10^{-4}$ F/m^2. The relatively thin hBN dielectric with $d_{hBN,bot} \sim 5$ nm allows to induce a well-pronounced modulation potential in the graphene layer. But due to the thin dielectric, the quantum capacitance (see eq. 2.24) has to be included in the calculation of charge carrier densities.

Fig. 4.19 (a) displays the gate map of the device showing the longitudinal resistance R_{xx} as a function of PBG voltage V_{pbg} and back gate voltage V_{bg} measured at a temperature of $T = 1.5$ K and $B = 0$ T. Fig. 4.19 (b) shows line cuts of R_{xx} at $V_{bg} = 5, 70, -70$ V and a line cut of the Hall resistance R_{xy} at $V_{bg} = 70$ V and $B = 200$ mT as a function of normalized charge carrier density n/n_0 with $n_0 = 1/A_{sl}$. A_{sl} is the lattice unit cell area $A_{sl} = a_{sl}^2$ of the electrostatically defined superlattice. In PBG voltage sweeps around $V_{bg} = 0$ V only a single Dirac peak is visible as expected for pristine, unmodulated graphene (see. e.g. the line cut at $V_{bg} = 5$ V). The apparent field-effect mobility of the fully encapsulated graphene, extracted at low back gate voltage, is about $\mu \sim 40\,000$ cm^2/Vs. By increasing the back gate voltage, i.e. increasing the potential modulation strength, the gate response of the device exhibits a clear manifestation of satellite Dirac peaks besides the main Dirac peak. When the polarity of the back gate voltage is reversed, all extra features in the gate map are mirrored at the main Dirac peak. The position of the main Dirac point lies at $n/n_0 = 0$. The most pronounced satellite peaks appear at positions corresponding to filling up the superlattice unit cell area with four additional electrons/holes, i.e. at $n/n_0 = \pm 4, \pm 8$, reflecting the four-fold degeneracy of graphene. Increasing the charge carrier density up to these values is equivalent to filling up newly generated mini-Bloch-bands in the electronic band structure which are created by the superimposed periodic potential. At high back gate voltage also faint lines at higher charge carrier densities start to appear, indicating further and more complicated band structure modifications. The most pronounced satellite peaks in R_{xx}

are accompanied by sign changes of the Hall resistance R_{xy} at low magnetic fields (see the upper panel in Fig. 4.19 (b)). This indicates a shift of the Fermi energy across band edges and an effective change of the type of charge carriers, which further confirms the presence of well-defined superlattice-induced minibands.

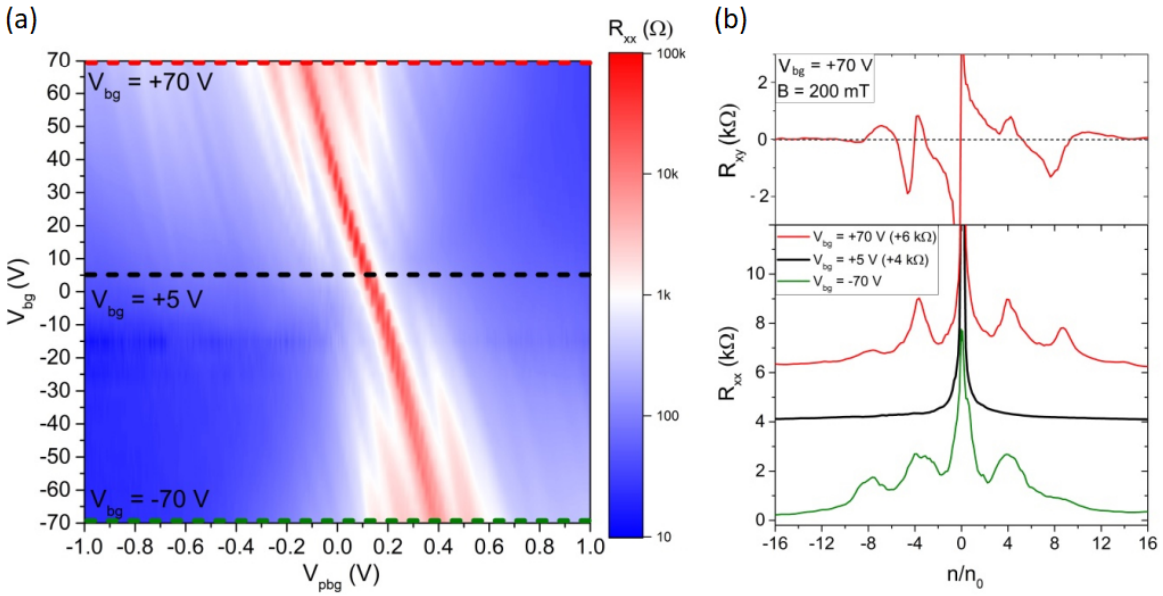

Figure 4.19: (a) Gate map of device SL1 measured at a temperature of $T = 1.5$ K and $B = 0$ T. Longitudinal resistance R_{xx} is plotted as a function of PBG voltage V_{pbg} and back gate voltage V_{bg}. Around zero back gate voltage, i.e. at low modulation potential strength, a single Dirac peak can be observed. By increasing the back gate voltage (and therefore increasing the periodic potential strength), additional peaks besides the main Dirac peak start to manifest. **(b)** Lower panel: Line cuts of R_{xx} at $V_{bg} = 5, 70, -70$ V as a function of normalized charge carrier density n/n_0 with $n_0 = 1/a_{sl}^2$. The position of the main Dirac point is at $n/n_0 = 0$. The most pronounced satellite peaks in R_{xx}, visible at high back gate voltage, appear at positions $n/n_0 = \pm 4, \pm 8$. Upper panel: Hall resistance R_{xy} at $V_{bg} = 70$ V and $B = 200$ mT. A sign change of R_{xy} at positions of the satellite peaks in R_{xx} can be observed. [13]

Electrostatic Simulations

Finite-element-based electrostatic simulations of the device show the effect of the two different gates on the periodic modulation potential and charge carrier density [13]. All presented electrostatic simulations are provided by Ming-Hao Liu and Szu-Chao Chen [269].
The polarity map in Fig. 4.20 (a) shows the different modulation regimes in the gate map ranging from unipolar to bipolar potential modulation calculated by examining the type of charge carriers at positions 1 ($\mathrm{sgn}(n_1)$) and 2 ($\mathrm{sgn}(n_2)$) in the potential landscape induced by the superlattice (see inset of Fig. 4.20 (a)). Fig. 4.20 (b) displays the corresponding potential strength, i.e. the potential difference $V_1 - V_2$ between positions 1 and 2. The white dashed lines in Fig. 4.20 (b) are equipotential lines with corresponding potential strength ranging from zero modulation to several hundred meV. Fig. 4.20 (c) shows the calculated average charge carrier density in the system as a function of V_{pbg} and V_{bg}.

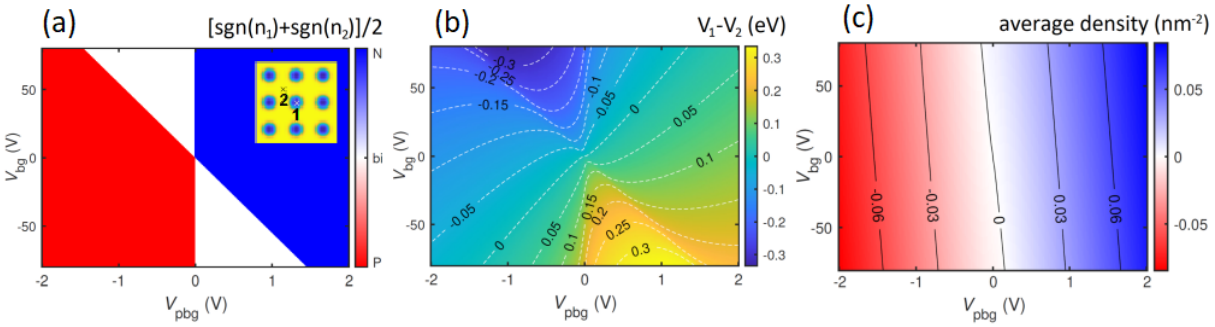

Figure 4.20: Results of electrostatic simulations for device SL1. The position of the main Dirac peak at $V_{bg} = 0$ V is shifted to $V_{pbg} = 0$ V. **(a)** Polarity map of the device illustrating different modulation regimes ranging from unipolar (red represents only p-type charge carriers (holes) and blue only n-type charge carriers (electrons) in the system) to a bipolar (white region) potential modulation. Inset shows the considered geometry with positions 1 and 2. **(b)** Periodic potential strength as a function of V_{pbg} and V_{bg}. The modulation strength, i.e. potential difference between positions 1 and 2, ranges from zero to several hundred meV. **(c)** Calculated average density in the system as a function of V_{pbg} and V_{bg}. The black lines correspond to positions of constant average charge carrier density. [13, 269]

Transport Simulations and Miniband Structure

Quantum transport simulations (in the framework of a scaled tight-binding model and the Landauer-Büttiker formalism) and calculated miniband structures at $B = 0$ T, both using the realistic square superlattice potential obtained from the electrostatic simulations and taking into account the geometry of the investigated device, accurately reproduce and explain the observed features in the experimental data [13]. The presented transport simulations and the calculated miniband structures are provided by Ming-Hao Liu and Szu-Chao Chen [269].
Fig. 4.21 presents the results of the transport calculations and the corresponding miniband structures. Fig. 4.21 (a) displays the simulated longitudinal resistance R_{xx} as a function of V_{pbg} at fixed $V_{bg} = 58$ V. Fig. 4.21 (b) shows the full gate map of the considered six-terminal Hall bar (see left inset of Fig. 4.21(b)). The transport simulations accurately reproduce the observed features in the transport measurements in Fig. 4.19. At large positive back gate voltage two satellite Dirac peaks to the right and one to the left of the main Dirac peak can be seen, which is consistent with the experimental results. Also the sign change of the Hall resistance R_{xy} at the positions of the satellite peaks at low magnetic fields is reproduced in the transport simulations (see Fig. 4.21 (g)). Like in experiment, the gate response depicted in Fig. 4.21 (b) shows a pronounced main Dirac peak throughout all back gate voltages, accompanied by additional lines parallel to the main Dirac line emerging with increasing V_{bg}, i.e. upon increasing the modulation potential strength.

The occurrence of satellite peaks can be connected to features in the electronic band structure. Fig. 4.21 (c)-(f) presents miniband structures corresponding to the positions depicted in Fig. 4.21 (a). If the Fermi level lies at the Dirac point of the unperturbed graphene band structure, the main Dirac peak manifests. The first satellite peak (c for the hole and e for the electron side) originates from secondary and tertiary Dirac points at the X and M points of the mini-Brillouin-zone (see right inset of Fig. 4.21 (b)). The second satellite peak (f) emerges due to an additional Dirac cone at the Γ-point of the mini-Brillouin-zone (see right inset of Fig. 4.21 (b)). At higher charge carrier densities also higher-order minibands start to manifest, partially overlapping and intersecting the Fermi level, which makes it more difficult to resolve additional peaks. Fig. 4.22 shows calculated potential profiles at exemplary positions in the gate map in Fig. 4.21 (b) and provides further details of the induced modulation potential.

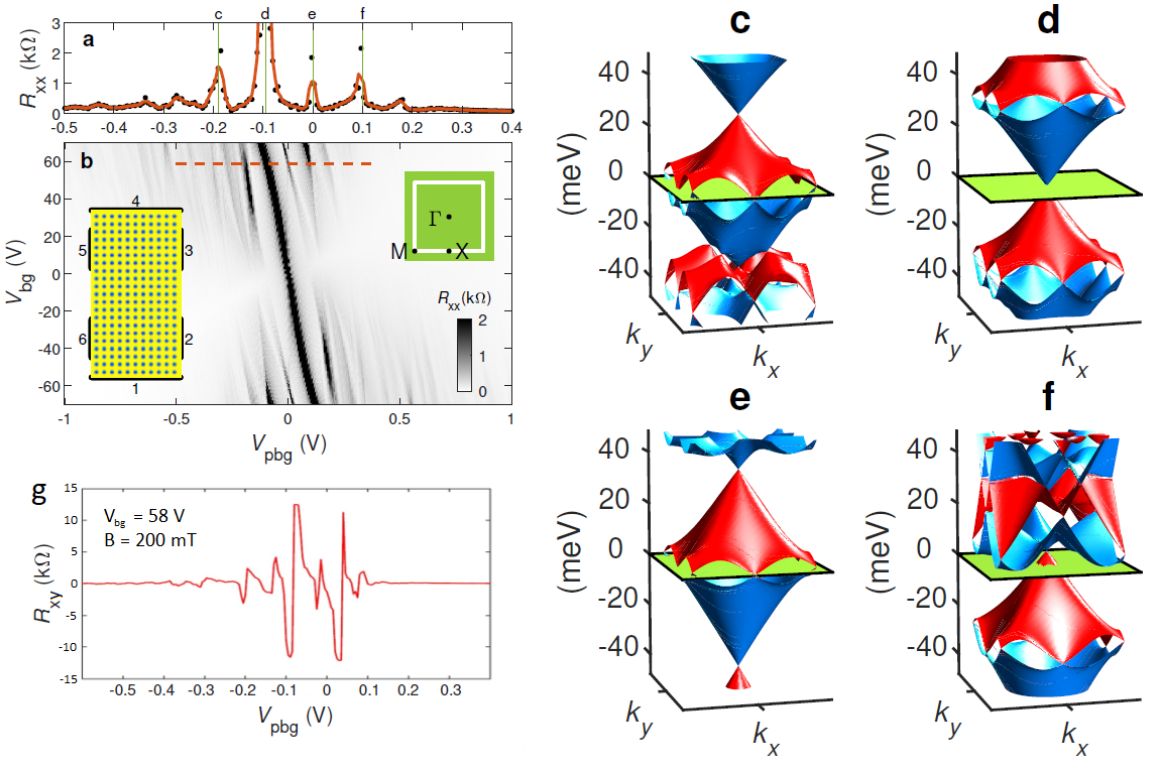

Figure 4.21: **(a)** Calculated R_{xx} as a function of V_{pbg} at fixed $V_{bg} = 58$ V. The emergence of satellite peaks at high back gate voltages can be reproduced. **(b)** Simulated gate map. The calculated transport data shows strong correspondence to the experimental results in Fig. 4.19 (a). Left inset: Considered device geometry. Right inset: mini-Brillouin-zone of the square superlattice with high symmetry points. **(c)-(f)** Calculated miniband structures corresponding to the highlighted positions in (a). The minibands are highlighted in red and blue. The Fermi energy is fixed at zero energy (green plane). The satellite Dirac points in the spectrum correspond to satellite peaks in R_{xx}. **(g)** Calculated R_{xy} as a function of V_{pbg} at fixed $V_{bg} = 58$ V and at $B = 200$ mT showing sign changes at positions of the satellite peaks in R_{xx} in (a). [13, 269]

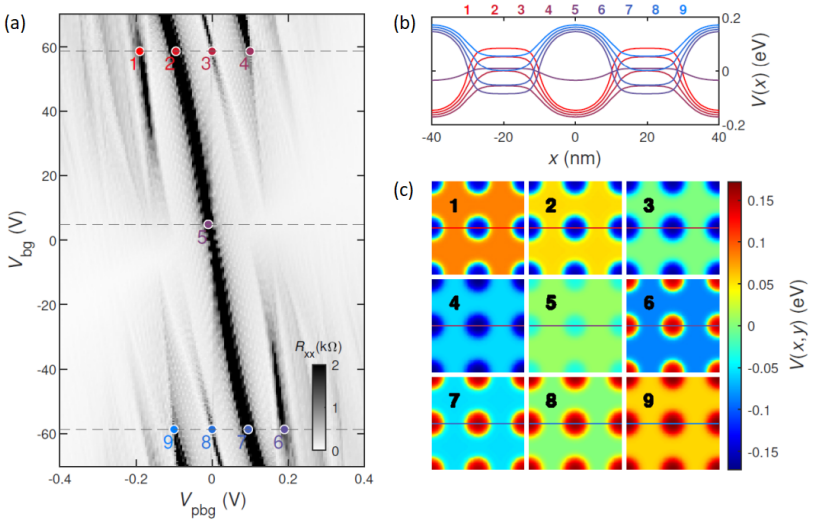

Figure 4.22: **(a)** Central part of the simulated gate map in Fig. 4.21 (b). Potential profiles are calculated at points 1 to 9. **(b)** Potential profiles extracted from the calculated lateral potential landscapes in **(c)** in which the potential strength $V(x, y)$ is given as a function of position (x, y). [13, 269]

Energy Gap at the Main Dirac Point

Compared to pristine graphene, the resistance at the main Dirac peak of the modulated graphene is strongly enhanced, which could point towards the existence of a fundamental energy gap − similar to GALs. To further investigate this possibility, temperature dependent measurements of R_{xx} were conducted. The result is shown in Fig. 4.23 in which the temperature evolution of R_{xx} between $T = 40$ K and $T = 140$ K is plotted as a function of PBG voltage V_{pbg} at two different back gate voltages $V_{bg} = 10$ V and $V_{bg} = 80$ V. Due to small variations of the position of the main Dirac point between different temperatures, all curves are shifted so that the position of the main Dirac point is located at $V_{pbg} = 0$ V. Fig. 4.24 shows the corresponding Arrhenius plots in which the minimum conductance G_{min} at the main CNP is plotted as a function of inverse temperature $1/T$. The data indicates temperature-activated transport from which an energy gap of $E_{gap} \sim 9$ meV at $V_{bg} = 80$ V and an energy gap of $E_{gap} \sim 17$ meV at $V_{bg} = 10$ V are estimated. Also by considering the transport gap region, analogous to the case of GALs (see chapter 4.1.2), one can extract an energy gap of $E_{gap} \sim 17$ meV (method (1), see Fig. 4.24 (a)) and $E_{gap} \sim 15$ meV (method (2), see Fig. 4.24 (b)) at $V_{bg} = 10$ V. These values are in good agreement with the estimation from the temperature-activated transport behaviour. For the data at high back gate voltages, as exemplary shown for $V_{bg} = 70$ V in Fig. 4.24, no consistent transport gap region can be defined by methods (1) and (2). Overall, the experimental results point towards an energy gap at the main Dirac point (in contrast to the calculated miniband structures shown in Fig. 4.21) which seems to be tunable by the applied back gate voltage in a counterintuitive manner since it decreases by increasing the potential strength. In fact, the emergence of an energy gap in periodically gated graphene is in principle possible and was theoretically determined in tight-binding calculations, predicting a non-trivial dependence of the energy gap on the gate potential [197]. It was shown that, after reaching a maximum magnitude, the calculated energy gap quenches by further increasing the potential strength, which would

be qualitatively consistent with the non-trivial behaviour extracted from the Arrhenius plots and the apparent decrease of the energy gap upon increasing the potential strength. But the gap in the case of periodic gating, caused by a local sublattice asymmetry at the edges of the gated regions, is expected to be highly fragile and crucially dependent on the potential profile, potential strength, and edge geometry of the gated region. Furthermore, the emergence of an energy gap in realistic devices with smooth potential steps is expected to be difficult to achieve and the size of energy gaps is expected to be vanishingly small – in contrast to the measured values here. Overall, the transport measurements indicate the emergence of an energy gap at the main CNP with non-trivial dependence on the strength of the periodic potential. But further and more detailed investigations are necessary to confirm these findings – also in view of the calculations in Ref. [197].

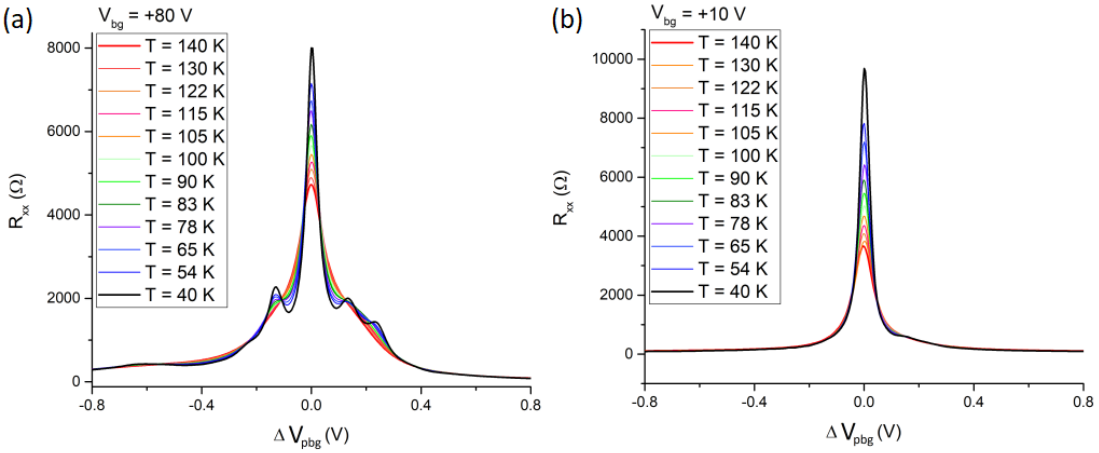

Figure 4.23: Temperature dependent measurements of R_{xx} at **(a)** $V_{bg} = 80$ V and **(b)** $V_{bg} = 10$ V. The position of the main Dirac peak in all curves is shifted to $V_{pbg} = 0$ V. The strong temperature dependency of R_{xx} at the main CNP indicates temperature activated transport.

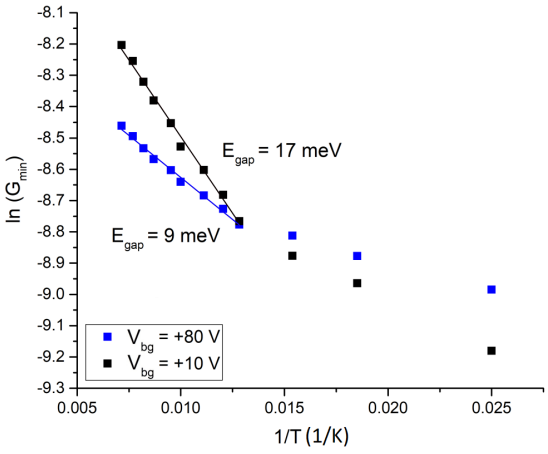

Figure 4.24: Arrhenius plots of the data in Fig. 4.23. The minimum conductance G_{min} at the main CNP is plotted as a function of inverse temperature $1/T$. Energy gaps of $E_{gap} = 9$ meV (at $V_{bg} = 80$ V) and $E_{gap} = 17$ meV (at $V_{bg} = 10$ V) are estimated.

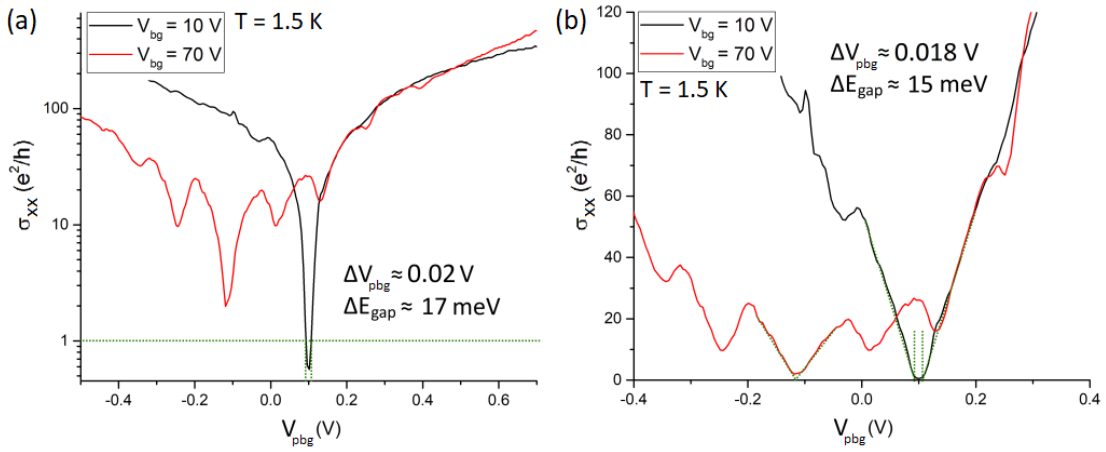

Figure 4.25: Estimation of energy gaps by evaluating the transport gap region (green dotted lines). At high back gate voltage (here shown for $V_{bg} = 70$ V) no transport gap region can be defined. **(a)** Method (1): An energy gap of about $E_{gap} = 17$ meV is extracted at $V_{bg} = 10$ V. **(b)** Method (2): An energy gap of about $E_{gap} = 15$ meV is extracted at $V_{bg} = 10$ V.

4.2.2 Resolving the Hofstadter Butterfly

The following section will focus on the magnetotransport data and in particular the manifestation of features of the Hofstadter butterfly energy spectrum. Fig. 4.26 provides information about the impact of the periodic potential on the Landau level spectrum of graphene. Landau fan diagrams at $V_{bg} = 0$ V and $V_{bg} = 29$ V are shown in which the longitudinal resistance R_{xx} is plotted as a function of PBG voltage V_{pbg} and magnetic field B. At low back gate voltages, i.e. at low potential modulation, the magnetotransport data mainly display the Landau level spectrum of pristine, unmodulated graphene. By increasing the strength of the periodic potential, at $V_{bg} = 29$ V, the Landau fan diagram exhibits faint features in the low magnetic field regime emerging besides the main Dirac point. Furthermore, a significant modulation of the Landau level spectrum, mainly in the bipolar region (roughly in which the PBG and back gate voltage have opposite sign), is visible. In the unipolar region (roughly in which the PBG and back gate voltage have the same sign) and at high magnetic fields the Landau level spectrum of pristine graphene is present.
Fig. 4.27 displays magnetotransport data at $V_{bg} = 70$ V which will be discussed in more detail. The longitudinal resistance R_{xx} is plotted as a function of normalized charge carrier density n/n_0 and magnetic field B. The magnetic field value B_0 at which one magnetic flux quantum Φ_0 pierces one superlattice unit cell is determined to be about $B_0 \sim 2.7$ T (see chapter 4.2.3). Besides the main Landau fan also additional weaker Landau fans emerge from the positions of the most pronounced satellite peaks at zero magnetic field, i.e. at $n/n_0 = \pm 4, \pm 8$. In the bipolar region a variety of features manifests and a highly distorted Landau fan can be observed. In the unipolar region the main Landau fan of pristine graphene is still recognizable but exhibits additional minima in longitudinal resistance which can be traced back to the satellite Dirac points at zero field, indicating a splitting of initial Landau levels by superlattice induced minigaps.

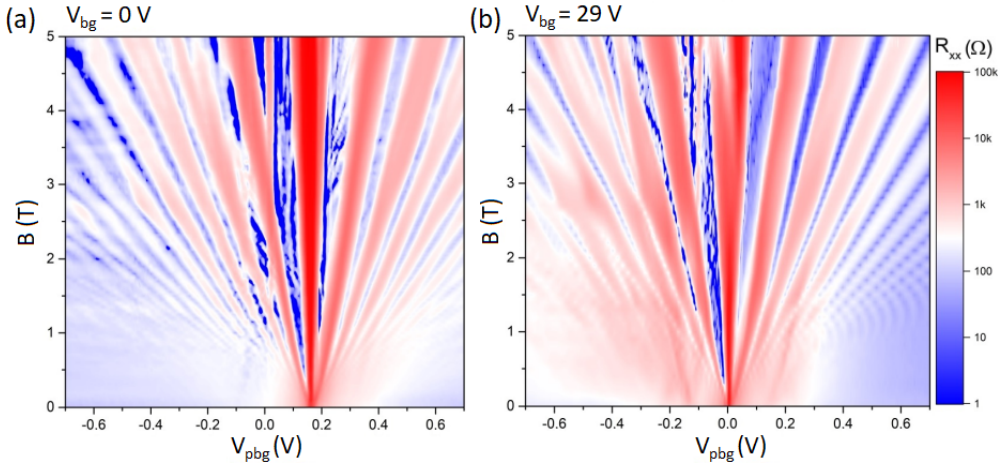

Figure 4.26: R_{xx} plotted as a function of PBG voltage V_{pbg} and magnetic field B at $V_{bg} = 0$ V and $V_{bg} = 29$ V. **(a)** Landau fan diagram at $V_{bg} = 0$ V. The main Landau fan, corresponding to the usual QHE of pristine graphene, emerges from the main Dirac point at zero magnetic field. **(b)** Landau fan diagram at $V_{bg} = 29$ V. Weak features besides the main Dirac peak start to appear. In the bipolar region (roughly in which PBG and back gate voltage have opposite sign) the Landau fan exhibits pronounced modifications. In the unipolar regime (roughly in which PBG and back gate voltage have the same sign) the usual Landau fan of pristine graphene is visible. The colour scale bar is the same for (a) and (b). [13]

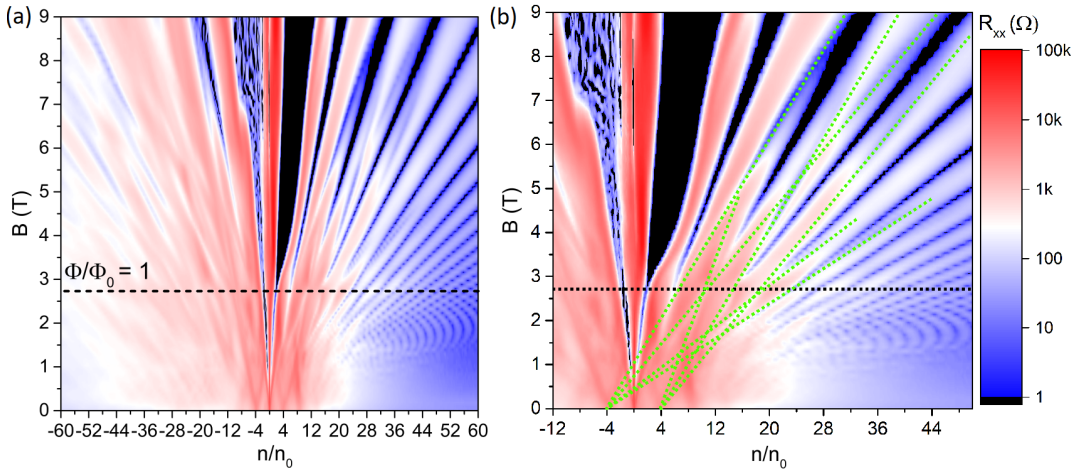

Figure 4.27: **(a)** Landau fan diagram at $V_{bg} = 70$ V. R_{xx} is plotted as a function of normalized charge carrier density n/n_0 and magnetic field B. At about $B_0 \sim 2.7$ T one magnetic flux quantum Φ_0 pierces one superlattice unit cell (i.e. $\Phi/\Phi_0 = 1$). In the low magnetic field regime additional Landau fans emerge from the satellite peaks in R_{xx} at zero magnetic field (i.e. at $n/n_0 = \pm 4, \pm 8$). In the high magnetic field regime quantum Hall states of pristine graphene can be identified. In addition, superlattice-induced minigaps manifest as additional minima in R_{xx}. In the bipolar regime a variety of features occurs. In the unipolar regime a splitting of Landau levels due to superlattice-induced energy gaps can be observed. **(b)** Detail of the plot in (a). The green dotted lines highlight minigaps which give rise to a splitting of Landau levels and can be traced back to the satellite Dirac points at $n/n_0 = \pm 4$. The colour scale bar is the same for (a) and (b). [13]

Description in the Tight-Binding Limit

Following the tight-binding description, the superlattice induces mini-Bloch-bands which split up in a magnetic field due to Landau quantization − the Landau levels determine the internal modulation of the minibands. In the Wannier diagram in the tight-binding limit of the data in Fig. 4.27, see Fig. 4.28 (a), magnetotransport results in the vicinity of the main Dirac point are displayed. R_{xx} is plotted as a function of normalized charge carrier density n/n_0 in a magnetic field range corresponding to $\Phi/\Phi_0 = 0$ to 1. Signatures of additional Landau fans, emerging from the satellite Dirac peaks at $B = 0$ T, are visible. The extent of the first minibands in the spectrum is highlighted. In order to increase the visibility of the newly generated features and to reveal more details, the second derivative of R_{xx} with respect to n/n_0 is plotted, as displayed in Fig. 4.28 (b). Now it is possible to identify the emerging features by the Diophantine equation $n/n_0 = (\Phi/\Phi_0)t + s$, as illustrated in Fig. 4.28 (c). Theoretically expected positions of energy gaps with $s = 0, \pm 4, \pm 8$ and $t = \pm 2, \pm 6$, highlighted by red dashed lines, are in good agreement with the observed features in the magnetotransport data. This is also in accordance with the picture of newly generated minibands in the band structure which exhibit Landau quantization in a magnetic field, although the corresponding energy gaps are not fully developed and resolved in experiment.

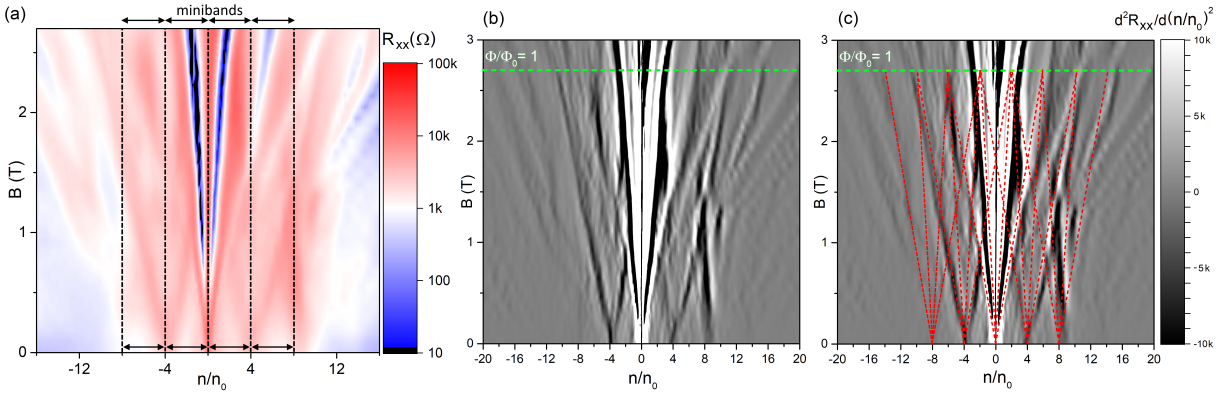

Figure 4.28: (a) Wannier diagram in the tight-binding limit corresponding to the data in Fig. 4.27. R_{xx} is plotted as a function of normalized charge carrier density n/n_0 in a magnetic field range corresponding to Φ/Φ_0 between 0 and 1. Black dashed lines mark the extent of the first minibands in the band structure. The minibands split up in a magnetic field. Landau fans emerge from the main Dirac peak at $n/n_0 = 0$ and from the satellite peaks at $n/n_0 = \pm 4, \pm 8$. **(b)** Second derivative of R_{xx} with respect to n/n_0. The green dashed line corresponds to $\Phi/\Phi_0 = 1$. Faint features, emerging from the satellite peaks, become better visible and can be identified. **(c)** Same plot as in (b). The red dashed lines correspond to expected positions of energy gaps following the Diophantine equation in the tight-binding limit with $s = 0, \pm 4, \pm 8$ and $t = \pm 2, \pm 6$.

Description in the Nearly-Free-Electron Limit

The value of $\Phi/\Phi_0 = 1$ can be seen as a transition point into a regime in which a description in the framework of the nearly-free-electron and high magnetic field limit becomes more appropriate. First, the unipolar regime is discussed in more detail.

Unipolar regime:

At high magnetic fields the system is fully Landau-quantized and exhibits the QHE of pristine graphene with modifications due to the 2D superlattice which acts as a weak perturbation on the quasi-free charge carriers. Fig. 4.29 (a) shows a Wannier diagram of the second and third Landau level − now plotted as a function of inverse magnetic flux per unit cell on the ordinate − and Fig. 4.29 (b) illustrates the expected internal structure of the two Landau levels given by the Hofstadter butterfly. In the Wannier diagram the longitudinal resistance R_{xx} is displayed as a function of inverse magnetic flux Φ_0/Φ and Landau level filling factor ν between $\nu = 6$ and $\nu = 14$. The minima in R_{xx} correspond to energy gaps in the magnetic band structure. The vertical minima at $\nu = 6$, $\nu = 10$ and $\nu = 14$ can be identified as energy gaps between adjacent Landau levels, which is consistent with features in pristine graphene showing the usual QHE. Furthermore, the Wannier plot reveals the internal structure of Landau levels. Diagonal minima in R_{xx} inside the Landau levels are visible which can be identified as signatures of the largest energy gaps in the Hofstadter butterfly.

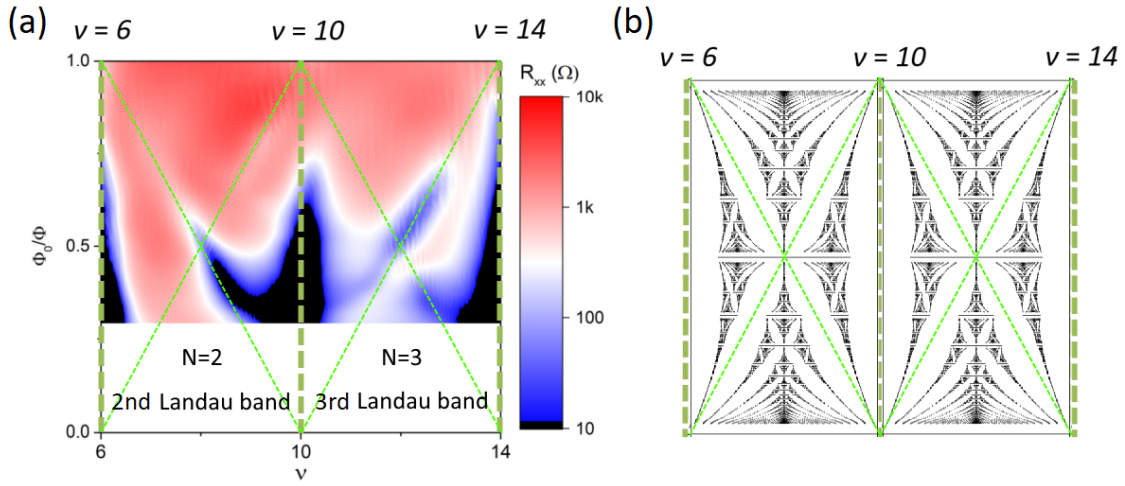

Figure 4.29: (a) Wannier diagram in the nearly-free-electron and high magnetic field limit. Longitudinal resistance R_{xx} is plotted as a function of inverse magnetic flux Φ_0/Φ and Landau level filling factor ν between $\nu = 6$ and $\nu = 14$. An internal structure of Landau levels, originating from superlattice-induced energy gaps, is visible. Vertical minima in R_{xx} correspond to Landau gaps between Landau levels (vertical green dashed lines). Additional diagonal minima correspond to superlattice-induced minigaps (diagonal green dashed lines). **(b)** The internal structure of Landau levels is given by the Hofstadter butterfly energy spectrum. The observed diagonal features in (a) correspond to the largest minigaps, i.e. the wings of the butterfly (highlighted by diagonal green dashed lines). Here, the Hofstadter butterfly was generated with the Python code in appendix C.

Fig. 4.30 (a) displays an extended Wannier diagram of the high magnetic field region in which energy gaps can be identified. Energy gaps in the spectrum correspond to minima in R_{xx} and plateaus in R_{xy} − following the Diophantine equation $\nu = (\Phi_0/\Phi)s + t$. Features in the Wannier plot belonging to quantum Hall states of pristine graphene ($s = 0$, $t = 2, 6, 10, ...$) appear as vertical minima in R_{xx} while superlattice-induced energy gaps of the Hofstadter spectrum ($s \neq 0$) form diagonal lines. The largest energy gaps with $s \pm 4$ are clearly resolved. This is also highlighted by dotted lines in Fig. 4.30 (a), in the second and third Landau level. The dotted lines follow the positions of Landau gaps (vertical) and the most pronounced Hofstadter minigaps (diagonal) which are labelled with their integer parameters (s, t). In Fig. 4.30 (b), the Landau level band width in units of V_0 is plotted (i.e. $|\Delta E_N|$, calculated using eq. 2.40). As expected, features of the Hofstadter butterfly in experiment are most pronounced and best visible in regions of largest Landau level band width.
Furthermore, in Fig. 4.30 (c)-(e), line cuts of R_{xx} and R_{xy} at three different magnetic fields (dashed horizontal lines in Fig. 4.30 (a)) are shown, emphasizing the evolution of the magnetic band structure upon changing the magnetic flux per superlattice unit cell. At high magnetic fields ($\Phi_0/\Phi = 0.29$) the usual sequence of quantum Hall plateaus of intrinsic graphene can be observed (see Fig. 4.30 (e)).
By changing the magnetic flux ratio to $\Phi_0/\Phi = 0.5$, a splitting of Landau levels into two minibands occurs. Additional minima in R_{xx} can be observed, accompanied by well-developed quantum Hall plateaus (see Fig. 4.30 (d)). At a magnetic flux ratio of $\Phi_0/\Phi = 0.73$ the quantum Hall resistance shows signatures of the two largest gaps (with $s \pm 4$) of the Hofstadter butterfly (see Fig. 4.30 (c)). This is best visible in the second Landau level between $\nu = 6$ and $\nu = 10$ where R_{xx} develops two additional minima. The corresponding quantum Hall resistance R_{xy} exhibits a non-trivial sequence, qualitatively following the expected sequence of quantum Hall values if the Fermi energy is shifted into the largest energy gaps in the Hofstadter spectrum (red dashed line in Fig. 4.30 (b) − determined by $R_{xy} = \frac{h}{te^2}$). This confirms the prediction by Thouless *et al.* [180] in a gate-defined graphene superlattice. In Fig. 4.31 (b) the corresponding Wannier plot of the Hall resistance R_{xy} is shown, highlighting the trace of the minigap with $(s, t) = (4, 6)$ which gives rise to the most pronounced feature of the non-trivial quantum Hall response − although the energy gap is not fully developed and resolved since the plateau value is not quite reached and the corresponding minimum in R_{xx} does not reach zero value. But the tendency is clearly visible. In the second Landau level, in a region of largest Landau band width, there is also a weak signature of an energy gap with $(s, t) = (-8, 14)$ visible which corresponds to the next iteration of the self-similar spectrum. This feature becomes better visible by considering the second derivative of R_{xx} with respect to ν (see Fig. 4.31 (a)).
Overall, the non-trivial quantum Hall response is qualitatively in good agreement with the expected sequence of quantum Hall plateaus by including the most pronounced energy gaps (red dashed line in Fig. 4.30 (b)). Although not all energy gaps are fully developed and resolved, the tendency to follow the theoretically expected curve is apparent.
Additionally, Fig. 4.32 provides the full calculated Wannier diagram corresponding to the Diophantine equation $\nu = (\Phi_0/\Phi)s + t$ including energy gaps with $s = 0, \pm 4, \pm 8$ and $t = \pm 2, 6, 10, 14, 18, 22$. Also the quantum Hall response determined by $R_{xy} = \frac{h}{te^2}$ at two different magnetic flux values is shown, illustrating the manifestation of a highly non-monotonic sequence of quantum Hall plateaus (which generally depends on the magnetic flux Φ_0/Φ and the considered energy gaps) and a monotonic sequence of quantum Hall plateaus at high magnetic fields ($\Phi_0/\Phi \to 0$), in accordance with the experimental results.

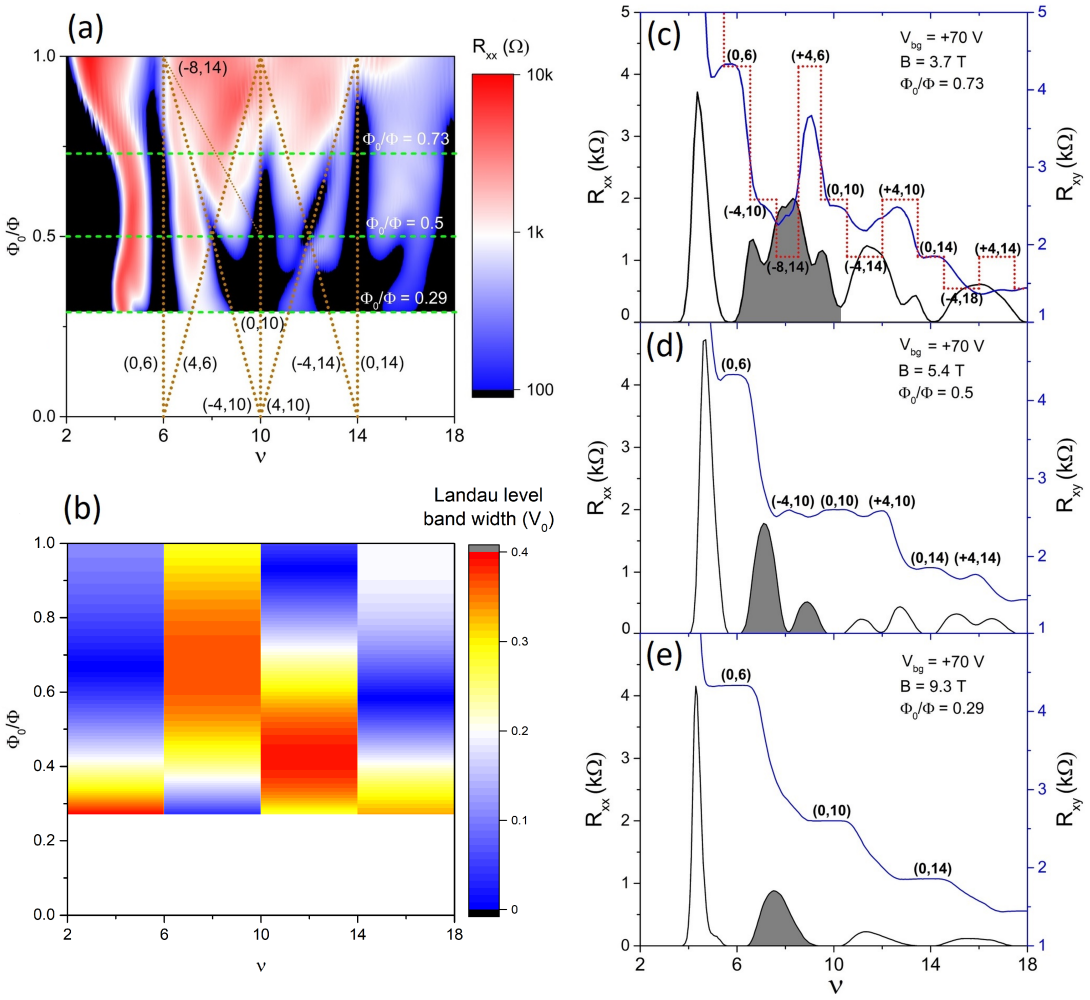

Figure 4.30: **(a)** Wannier diagram at $V_{bg} = 70$ V: Longitudinal resistance R_{xx} is plotted as a function of inverse magnetic flux Φ_0/Φ and Landau level filling factor ν between $\nu = 2$ and $\nu = 18$. Energy gaps correspond to minima in R_{xx}. Vertical minima belong to quantum Hall states of pristine graphene with $s = 0$, $t = 2, 6, 10, ...$ Hofstadter minigaps form diagonal features with $s \neq 0$. Some of the most pronounced energy gaps are highlighted by dashed lines and labelled with their integer parameters (s, t). **(b)** Landau level band width in units of V_0, corresponding to the Wannier diagram in (a). Features of the Hofstadter butterfly are most pronounced and best visible in regions of largest Landau level band width. **(c)-(e)** Line cuts of R_{xx} and corresponding R_{xy} at magnetic flux ratios given by the green dashed lines in (a). (c) At $\Phi_0/\Phi = 0.73$ signatures of the most pronounced energy gaps can be observed. The quantum Hall response shows non-monotonic character and is in good agreement with the expected sequence of quantum Hall plateaus by including the most pronounced energy gaps (red dashed line in Fig. 4.30 (b), [176]). (d) At $\Phi_0/\Phi = 0.5$ a clear splitting of Landau levels is visible. Additional minima in R_{xx} can be observed, accompanied by well-developed quantum Hall plateaus. (e) At high magnetic fields the data display the usual quantum Hall states of pristine graphene. The grey-shaded area in (c)-(e) in the data of R_{xx} illustrates the evolution of the second Landau level as a function of magnetic flux per superlattice unit cell area. [13]

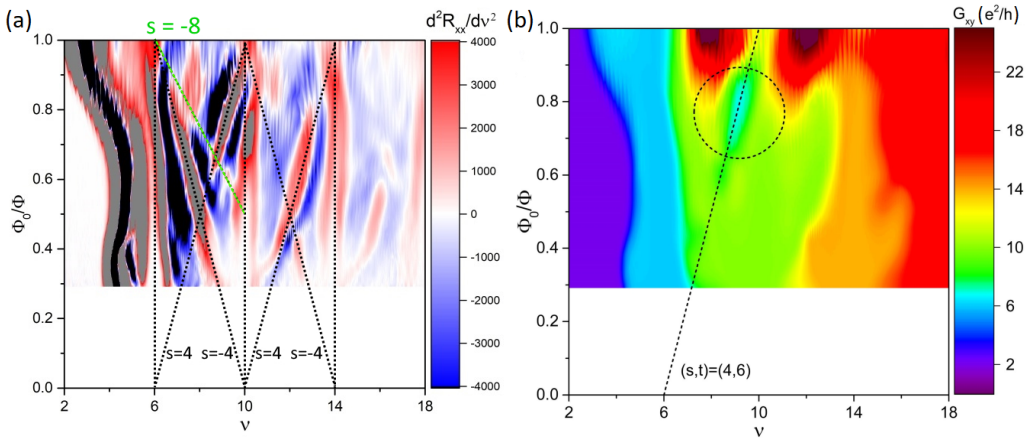

Figure 4.31: **(a)** Second derivative of R_{xx} with respect to ν. Features with $s = \pm 4$, corresponding to the largest energy gaps in the Hofstadter butterfly, are clearly visible (black dotted lines). In addition, traces of an energy gap with $s = -8$ inside the second Landau level can be identified (green dotted line). **(b)** Wannier diagram of the Hall response corresponding to the data in Fig. 4.30 (a). The transverse conductance G_{xy} is plotted as a function of inverse magnetic flux Φ_0/Φ and Landau level filling factor ν. The energy gap with $(s, t) = (4, 6)$, which gives rise to the most pronounced feature in the non-monotonic quantum Hall response, is highlighted by a circle. [13]

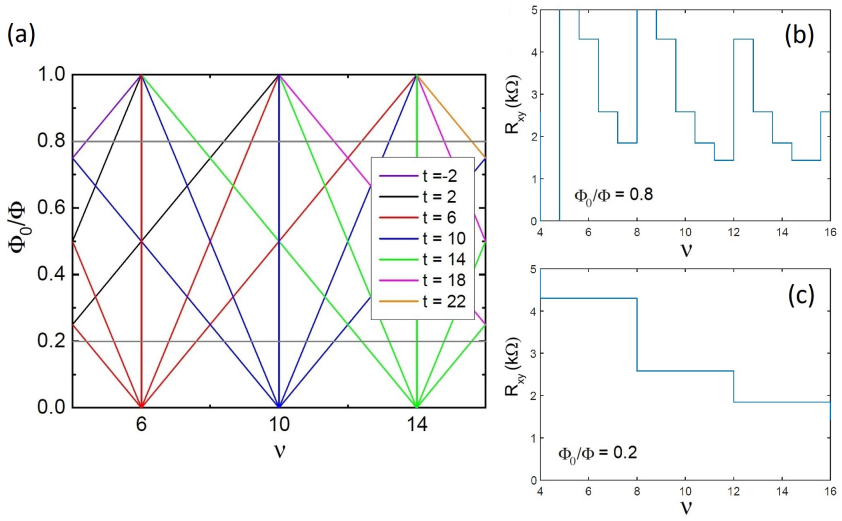

Figure 4.32: **(a)** Calculated Wannier diagram corresponding to the Diophantine equation $\nu = (\Phi_0/\Phi)s + t$ including energy gaps with $s = 0, \pm 4, \pm 8$ and $t = \pm 2, 6, 10, 14, 18, 22$. The coloured lines correspond to different quantum Hall plateau values determined by $R_{xy} = \frac{h}{te^2}$. **(b)** Expected sequence of quantum Hall values at $\Phi_0/\Phi = 0.8$ (corresponding to the upper horizontal grey line in (a)). The sequence of Hall plateaus is highly non-monotonic due to the considered energy gaps. **(c)** Expected sequence of quantum Hall values at $\Phi_0/\Phi = 0.2$ (corresponding to the lower horizontal grey line in (a)). At high magnetic fields ($\Phi_0/\Phi \to 0$) the emerging monotonic quantum Hall response resembles that of pristine graphene, in accordance with the experimental results. Graphs generated by [176]. [13]

In the following, the observed apparent lack of symmetry of the Hofstadter-related features and the splitting of Landau levels at $\Phi_0/\Phi = 0.5$ into two minibands (see e.g. Fig. 4.29 and Fig. 4.30) is briefly discussed. In the ideal Hofstadter case considered so far − with modulation potential $V(\vec{r}) = V_0(\cos(Gx) + \cos(Gy))$ − the spectrum is highly symmetric and the two minibands at $\Phi_0/\Phi = 0.5$ touch each other at the centre of the spectrum (see e.g. Fig. 2.30 (a)). No energy gap between the two minibands and therefore no splitting of Landau bands should occur − in contrast to the experimental results. The discrepancy between theory and experiment can be resolved by considering more realistic superlattice potentials. In the tight-binding limit it can be shown that by including also next-nearest-neighbour hopping into the calculations, the Hofstadter spectrum gets distorted and a gap occurs which separates the two minibands at $\Phi/\Phi_0 = 0.5$, as shown in Fig. 4.33 (a) [281]. Also in the high magnetic field and weak modulation limit, by considering more general superlattice potentials like $V(\vec{r}) = V_x \cos(G_x x) + V_y \cos(G_y y) + V_{xy}(\cos(G_x x)\cos(G_y y))$ (e.g. a rectangular superlattice with $G_{x/y} = 2\pi/a_{x/y}$ or a modulation potential with $V_{xy} \neq 0$), it was shown that the internal structure of Landau levels, given by the Hofstadter butterfly, gets distorted and becomes different in different Landau levels, as illustrated in Fig. 4.33 (b) and (c) [172]. Also in this case a gap can appear which separates the two minibands at $\Phi_0/\Phi = 0.5$. Overall, in the case of more complicated superlattice potentials (generally by the inclusion of higher harmonics of the superlattice potential which alter the details of the spectrum [172]), a symmetric representation of the energy spectrum, as in the ideal Hofstadter case, is not necessarily given any more [172], which is also apparent in the experimental results of the studied device reflecting the more realistic modulation potential.

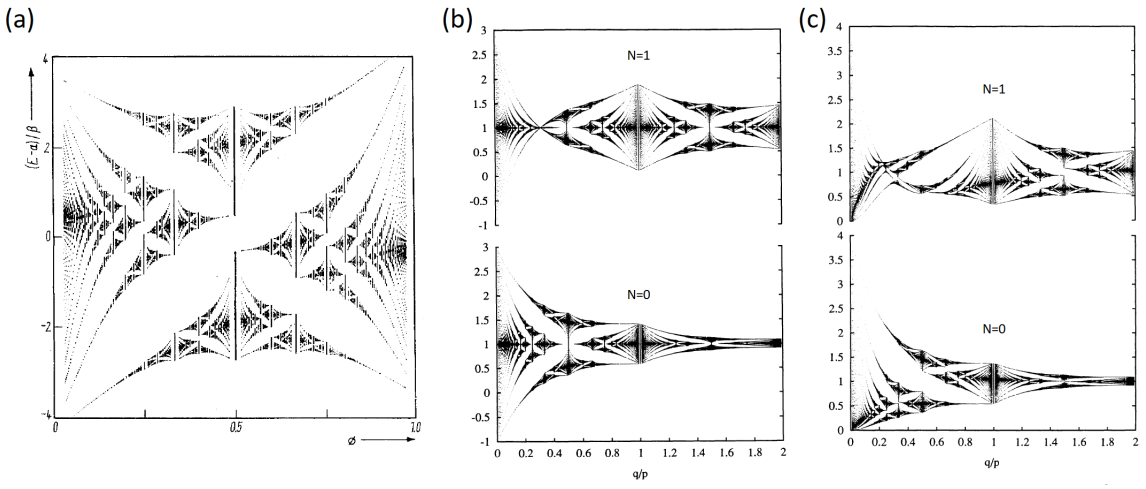

Figure 4.33: (a) Distorted Hofstadter butterfly calculated in the tight-binding limit including next-nearest-neighbour hopping. A gap separates the two minibands at $\Phi/\Phi_0 = 0.5$. [281] **(b)** Calculated energy correction in units of V_0 plotted versus $\Phi_0/\Phi = q/p$ in the weak modulation limit for a system with parabolic dispersion relation. The usual Hofstadter case with modulation potential $V(\vec{r}) = V_0(1 + \cos(Gx) + \cos(Gy))$ for Landau levels $N = 0$ and $N = 1$ is shown. Adapted from [172]. **(c)** In a more general case, here for a superlattice potential $V(\vec{r}) = V_0(1 + \cos(Gx))(1 + \cos(Gy))$, the usual Hofstadter butterfly gets distorted and the internal structure is different in different Landau levels. A gap occurs which separates the two minibands at $\Phi_0/\Phi = 0.5$. Adapted from [172].

Bipolar regime:

Fig. 4.34 presents transport measurement results in the bipolar regime at $V_{bg} = 70$ V. Fig. 4.34 (a) shows R_{xx} as a function of ν and Φ_0/Φ and Fig. 4.34 (b) displays the corresponding Hall resistance $|R_{xy}|$. In Fig. 4.34 (c), the second derivative of R_{xx} with respect to ν is plotted in order to increase the visibility of features in longitudinal resistance. Overall, the measurement results exhibit many, partially not fully-developed features which can not be easily associated with energy gaps obtained from the simple Hofstadter model. This becomes also apparent in Fig. 4.34 (d)-(f) which show line cuts at the same magnetic flux ratios as in the unipolar regime (see Fig. 4.30(c)-(e)). Again, at high magnetic fields, the system exhibits features comparable to pristine graphene, mainly reflecting usual quantum Hall states (see Fig. 4.34 (f)). At intermediate magnetic flux ratios, depicted in Fig. 4.34 (d) and (e), a complex sequence of minima in G_{xx} and quantum Hall plateaus in σ_{xy} occur. The origin of the observed complicated and irregular behaviour in the bipolar regime lies probably in the fact that the assumption of well-separated energy bands is not given any more. This can also be seen in the miniband structures in Fig. 4.21 (c)-(f). The non-trivial band structure with overlapping minibands in the bipolar regime at zero magnetic field manifests as faint lines in experiment and simulation (see e.g. Fig. 4.19 (a) and Fig. 4.21 (b)) eventually giving rise to a complicated magnetic band structure. Therefore, mixing of energy bands and Landau band coupling [169, 175, 282] has to be taken into account in order to be able to fully describe and identify the details in experiment.

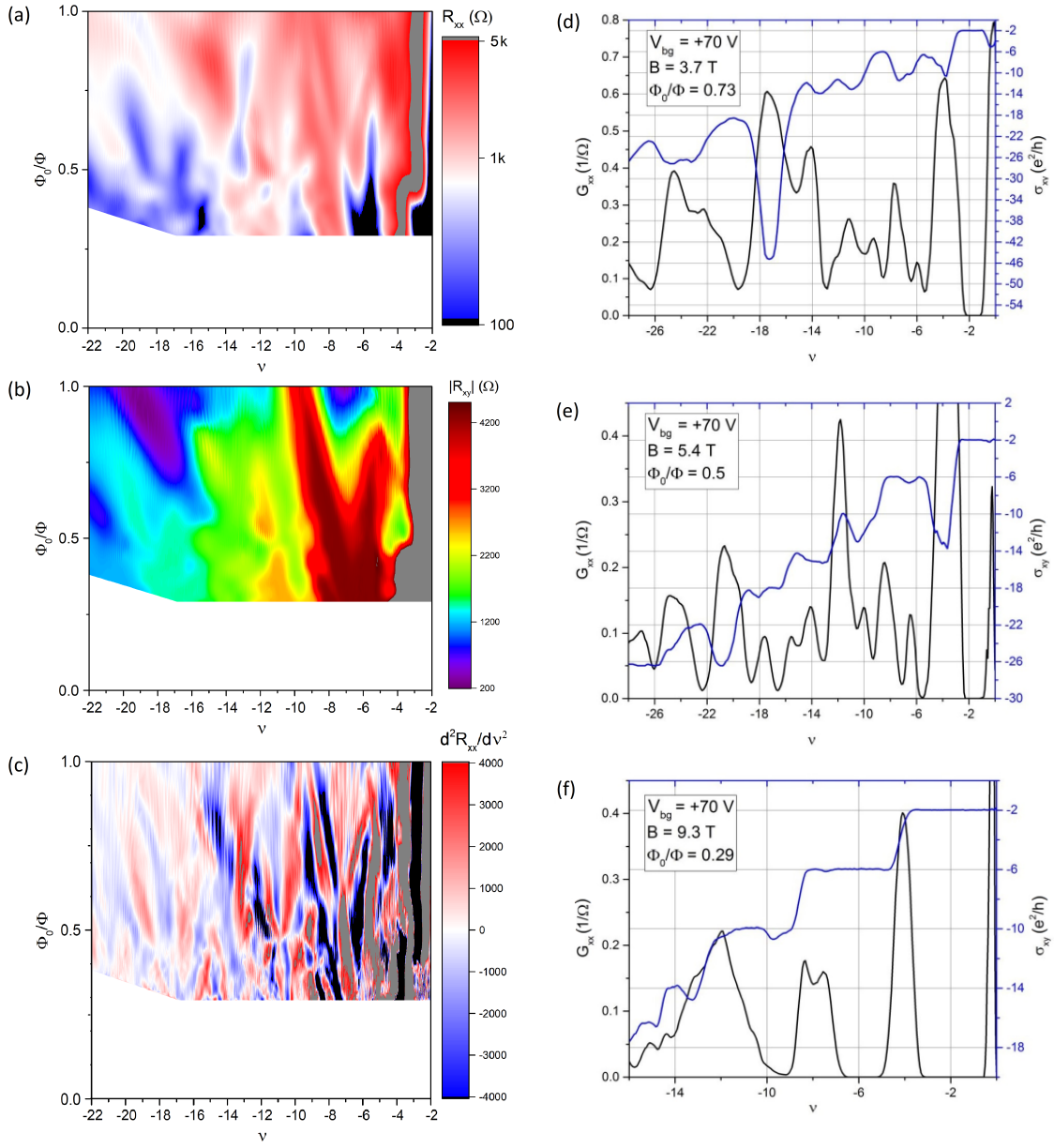

Figure 4.34: Transport measurement results in the bipolar regime **(a)** R_{xx} as a function of ν and Φ_0/Φ at $V_{bg} = 70$ V. **(b)** Corresponding Hall resistance $|R_{xy}|$. **(c)** Second derivative of R_{xx} with respect to ν. **(d-f)** Line cuts at the same magnetic flux ratios as in the unipolar regime (see Fig. 4.30 (c)-(e)). Longitudinal conductance G_{xx} and Hall conductivity σ_{xy} are plotted as a function of Landau level filling factor ν. **(d),(e)** At intermediate magnetic flux ratios a complex, non-trivial sequence of minima in G_{xx} and quantum Hall plateaus in σ_{xy} occurs. **(f)** At high magnetic fields the system mainly displays usual quantum Hall states of pristine graphene. [13]

Transport Simulations Including Magnetic Fields

Transport in magnetic fields was also simulated for device SL1, as shown in Fig. 4.35, in good agreement with the experimental results [13]. The transport simulations are provided by Ming-Hao Liu and Szu-Chao Chen [269]. Since disorder was not taken into account in the calculations, superlattice-induced energy gaps are more clearly resolved as in experiment and also signatures of higher-order energy gaps up to $s = \pm 8$ manifest. Overall, the simulated data shows a strong correspondence with the experimental results and qualitatively reproduces the variety of features in the measured magnetotransport data including the impact of minigaps in the Hofstadter butterfly.

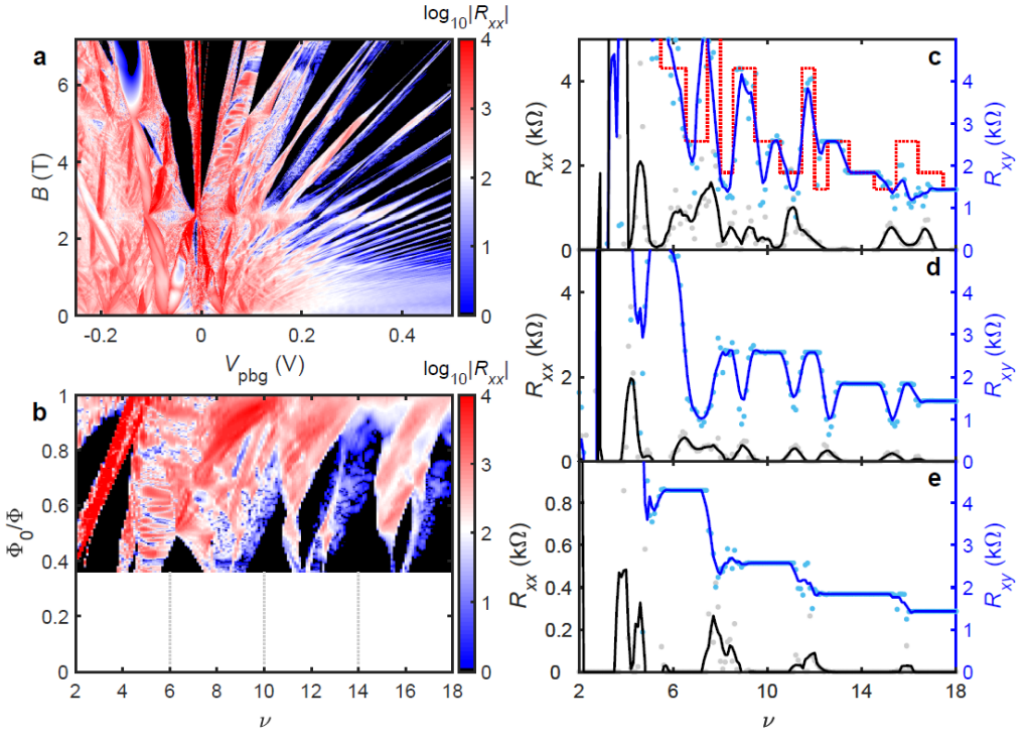

Figure 4.35: Transport simulations including a magnetic field. **(a)** Calculated Landau fan diagram at $V_{bg} = 58$ V qualitatively reproduces the data in Fig. 4.27. **(b)** The corresponding Wannier diagram plotted from the data in (a) (plot generated by [176] with data from [269]). **(c)-(e)** Line cuts of R_{xx} and R_{xy} at (c) $\Phi_0/\Phi = 0.73$, (d) $\Phi_0/\Phi = 0.5$, (e) $\Phi_0/\Phi = 0.29$. The calculated data is in good agreement with the experimental data shown in Fig. 4.30 and overall reproduces the characteristic features. The red line in (c) displays the expected sequence of quantum Hall plateaus by including energy gaps with $s = 0, \pm 4, \pm 8$ [176]. [13, 269]

4.2.3 Band Conductivity Oscillations and Weiss Oscillations

By conducting transport measurements at elevated temperatures, apparent features at zero magnetic field, originating from the 2D superlattice, start to disappear due to thermal smearing. Fig. 4.36 (a) illustrates the effect of temperature on the satellite peaks in PBG voltage sweeps which progressively start to fade away upon increasing the temperature to $T = 110$ K. Also Landau quantization and the fine structure of the Hofstadter butterfly, given by the minigaps in the spectrum, vanishes at elevated temperatures. But the 2D periodic potential has still significant impact on magnetotransport, as can be seen in Fig. 4.36 (b) which shows the longitudinal resistance R_{xx} as a function of magnetic field B and PBG voltage V_{pbg} at $V_{bg} = 80$ V and $T = 125$ K. Effects of Landau quantization have vanished. Vertical features of increased resistance occur (highlighted by vertical black dotted lines) which are independent of PBG voltage V_{pbg}, i.e. charge carrier density, which is a main characteristic of Brown-Zak oscillations reflecting the periodicity of the superimposed periodic potential.
For the present artificial superlattice with $a_{sl} = 40$ nm, a value of $B_0 \sim 2.6$ T can be calculated at which one magnetic flux quantum pierces the superlattice unit cell area a_{sl}^2. In experiment, a pronounced band conductivity feature occurs at $B \sim 2.7$ T which is in good agreement with the expected value. The value of $B \sim 2.7$ T corresponds to an actual superlattice constant of ~ 39 nm − in good agreement with the designed lattice period of $a_{sl} = 40$ nm.
Fig. 4.36 (c) displays several line cuts from the data in Fig. 4.36 (b) (grey horizontal lines) which exhibit pronounced resistance peaks at rational fractions of Φ/Φ_0, i.e. at $\Phi/\Phi_0 = 1, \frac{2}{3}, \frac{1}{2}, \frac{1}{3}$. Also a peak at $\Phi/\Phi_0 = 2$ is visible which only occurs in a narrow V_{pbg} range. Fig. 4.36 (d) shows the longitudinal conductance $G = G_{xx} = \frac{R_{xx}}{R_{xx}^2 + R_{xy}^2}$ and the Hall resistance R_{xy} plotted as a function of Φ/Φ_0 at $V_{bg} = 70$ V, $V_{pbg} = -0.7$ V, and $T = 125$ K. Conductance peaks at rational fractions of Φ/Φ_0, in particular at $\Phi/\Phi_0 = 2, 1, \frac{1}{2}, \frac{1}{3}$, can be observed which are accompanied by a dip in the Hall resistance.
Overall, the observed features in magnetotransport indicate an enhanced band conductivity contribution from extended minibands in the magnetic band structure and correspond to Brown-Zak oscillations [15] in the artificially created 2D superlattice. These band conductivity oscillations are investigated in more detail in the following magnetotransport measurements.

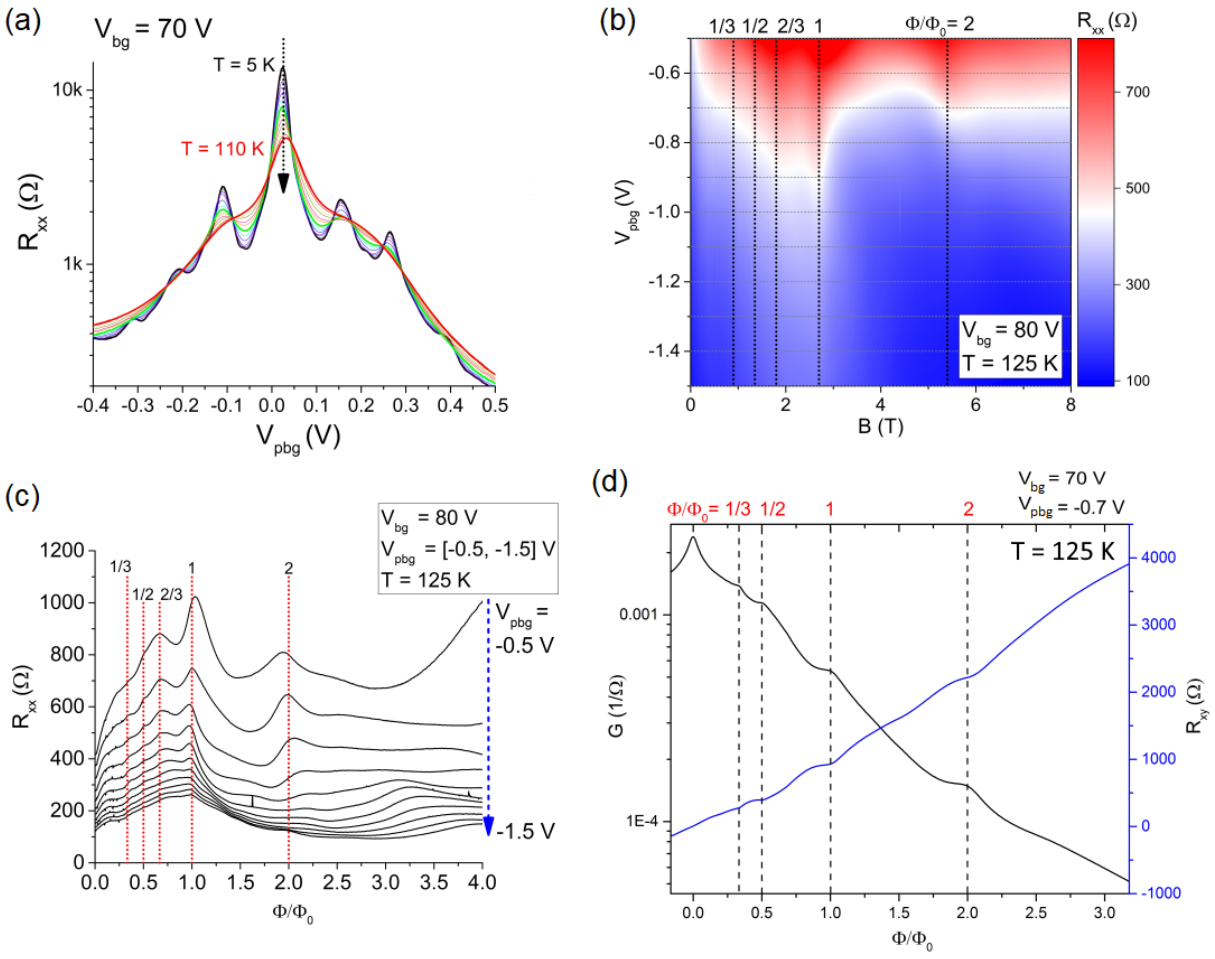

Figure 4.36: **(a)** R_{xx} as a function of V_{pbg} at $V_{bg} = 70$ V. By increasing the temperature, the satellite peaks beside the main CNP vanish due to thermal smearing. **(b)** R_{xx} as a function of magnetic field B and V_{pbg} at $V_{bg} = 80$ V and at a temperature of $T = 125$ K. Landau quantization has vanished and faint features at rational fractions of Φ/Φ_0 remain corresponding to Brown-Zak oscillations. **(c)** Line-cuts showing R_{xx} at different V_{pbg} (grey horizontal lines in (b)) as a function of Φ/Φ_0. Pronounced peaks at rational fractions of Φ/Φ_0 are visible highlighted by the vertical red dotted lines and labelled with the corresponding value of Φ/Φ_0. **(d)** Longitudinal conductance G_{xx} and Hall resistance R_{xy} as a function of Φ/Φ_0 at $V_{pbg} = -0.7$ V and $V_{bg} = 70$ V measured at $T = 125$ K. In magnetotransport superlattice-induced features are still visible. Brown-Zak oscillations can be observed with enhanced band conductivity at rational fractions of Φ/Φ_0, accompanied by a dip in the Hall resistance.

A more detailed analysis of the observed band conductivity oscillations is possible by considering the second derivative of the conductance G with respect to the magnetic field B, which effectively removes the background signal. Before taking the second derivative, the raw data was smoothed in order to remove spikes and small fluctuations due to noise. Fig. 4.38 (a) shows a grey scale plot of d^2G/dB^2 as a function of Φ/Φ_0 and V_{pbg} at $V_{bg} = 80$ V and $T = 125$ K. Due to the lattice constant of $a_{sl} = 40$ nm, also the regime of several magnetic flux quanta per superlattice unit cell can be investigated with moderate magnetic fields − in contrast to moiré superlattices which would require magnetic fields exceeding ~ 50 T. The dark vertical features in the data of Fig. 4.38 (a), which appear at rational fractions of Φ/Φ_0, correspond to an enhanced band conductivity reflecting the hierarchy of minibands in the Hofstadter butterfly.
By plotting the inverse magnetic field values at which the most pronounced features of the Brown-Zak oscillations occur (corresponding to unit fractions of Φ/Φ_0) against an integer index i, it is possible to determine the lattice constant a_{sl} of the square superlattice from the slope m of a linear fit to the data points: $a_{sl} = \sqrt{m\Phi_0}$. By evaluating the band conductivity features in Fig. 4.38 (a), a lattice constant of about ~ 39 nm is estimated (see Fig. 4.37) which is in good agreement with the designed lattice period of the artificial superlattice ($a_{sl} = 40$ nm).

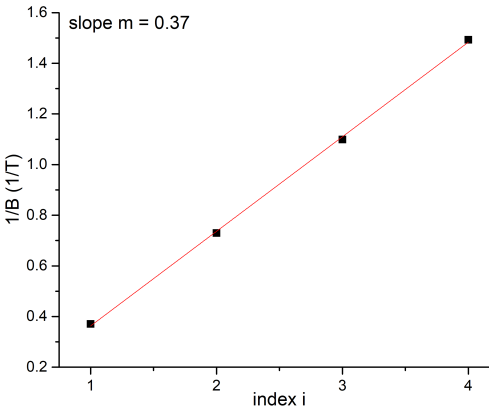

Figure 4.37: Determination of the superlattice period from Brown-Zak oscillations by evaluating the positions of the most pronounced features in Fig. 4.38 (a). Inverse magnetic field values are plotted against an integer index i. The red line is a linear fit with slope $m = 0.37$. A lattice constant of ~ 39 nm is estimated which is in good agreement with the artificially designed square superlattice ($a_{sl} = 40$ nm).

The observed features can be qualitatively explained by considering the corresponding magnetic band structure, as depicted in Fig. 4.39 (a). At unit fractions of Φ/Φ_0 the Hofstadter butterfly exhibits a single energy band which reaches the full band width of the underlying Landau band and, consequently, the band conductivity contribution reaches its maximum value giving rise to the most pronounced features in magnetotransport. At rational fractions of $\Phi/\Phi_0 = p/q$, with small parameter p, the spectrum consists of sizable minibands which still cause a measurable band conductivity contribution to the overall conductivity, corresponding to the weaker signatures of high-order states in the experimental data. At other values of Φ/Φ_0 the spectrum is heavily split into minibands and the band conductivity is suppressed. The band conductivity-related features are independent of V_{pbg}, i.e. charge carrier density, since the details of the Hofstadter butterfly are only dependent on the magnetic flux per unit cell area and not on the charge carrier density. As can be seen in Fig. 4.38 (a), band conductivity oscillations are mainly visible in the bipolar

regime and begin to fade away in the unipolar region. This is due to the fact that the periodic modulation potential is more pronounced in the bipolar regime and decreases in the unipolar region as soon as the induced modulation vanishes and a more homogenous potential landscape starts to manifest. The data also exhibit the pronounced feature at $\Phi/\Phi_0 = 2$ which is localized in a finite V_{pbg} range. But no additional features at higher values of magnetic flux are visible. Fig. 4.38 (b) displays a region of the data in Fig. 4.38 (a), also extending the measurement range of the bipolar regime towards higher charge carrier densities and adapting the grey scale contrast in order to highlight weaker features. The most pronounced features are labelled with their corresponding value of Φ/Φ_0 at which they occur. Enhanced conductivity is visible at $\Phi/\Phi_0 = 1, \frac{1}{2}, \frac{1}{3}, \frac{1}{4}, \frac{1}{5}$ and in addition also weak signatures of higher-order states at $\Phi/\Phi_0 = \frac{3}{2}, \frac{5}{4}, \frac{3}{4}, \frac{2}{3}$ are visible. The extended data also reveal more details of the feature at $\Phi/\Phi_0 = 2$ since it starts to reappear at higher charge carrier densities − it seems to be split and only occurs in certain ranges of charge carrier density. By inverting the polarity of the applied back gate voltage V_{bg}, the visible features are mirrored at the CNP (see Fig. 4.38 (c) for $V_{bg} = -80$ V).

By decreasing the back gate voltage, i.e. decreasing the modulation potential strength, more insight into the observed band conductivity oscillations is gained. Fig. 4.38 (d) shows a grey scale plot of d^2G/dB^2 as a function of Φ/Φ_0 and V_{pbg} at $V_{bg} = 10$ V. At weaker potential modulation the band width of Landau bands is reduced, which causes an overall reduction of the band conductivity contribution and, as a consequence, the majority of peaks vanishes. Only the most pronounced features, in particular the peak at $\Phi/\Phi_0 = 1$, remain. This is also illustrated in Fig. 4.39 (b) in which R_{xx} is plotted as a function of Φ/Φ_0 at $V_{bg} = 10$ V and several PBG voltages V_{pbg}. Furthermore, at weaker potential modulation, overlap of adjacent Landau bands is reduced and a more sensitive dependence of conductivity on the band width of individual Landau bands can manifest in experiment. In particular, the impact of flat bands at which the original Landau levels are restored becomes more significant as can be seen in the band conductivity feature at $\Phi/\Phi_0 = 1$ in Fig. 4.38 (d). The band conductivity contribution becomes modulated by the occurrence of flat bands in the magnetic band structure, determined by the flat band condition. In Fig. 4.38 (d) the flat band positions in semi-classical approximation are displayed as red lines with $\lambda = 1, 2, ..., 6$ and accurately reflect the positions at which the band conductivity at $\Phi/\Phi_0 = 1$ is suppressed. This becomes also apparent in the line cuts in Fig. 4.39 (b) in which the modulation of the feature at $\Phi/\Phi_0 = 1$ due to the occurrence of flat bands in the spectrum becomes apparent. In addition, the split feature at $\Phi/\Phi_0 = 2$ at higher back gate voltages can be also explained by the impact of flat bands since it lies exactly in between positions given by the flat band condition with $\lambda = 1$ and $\lambda = 2$, as depicted in Fig. 4.38 (c).

Overall, the measurements reveal an internal structure of Brown-Zak oscillations given by Weiss oscillations. In conclusion, the experimental results provide further insight into superlattice physics in graphene and corresponding band conductivity oscillations in a 2D superlattice and extend the description of Brown-Zak oscillations by including the effect of flat bands and Weiss oscillations which modulate the emerging Brown-Zak oscillations. Furthermore, the experimental results emphasize the dependence of superlattice induced effects on the details in the magnetic band structure and in particular on the emergence and band width of magnetic minibands.

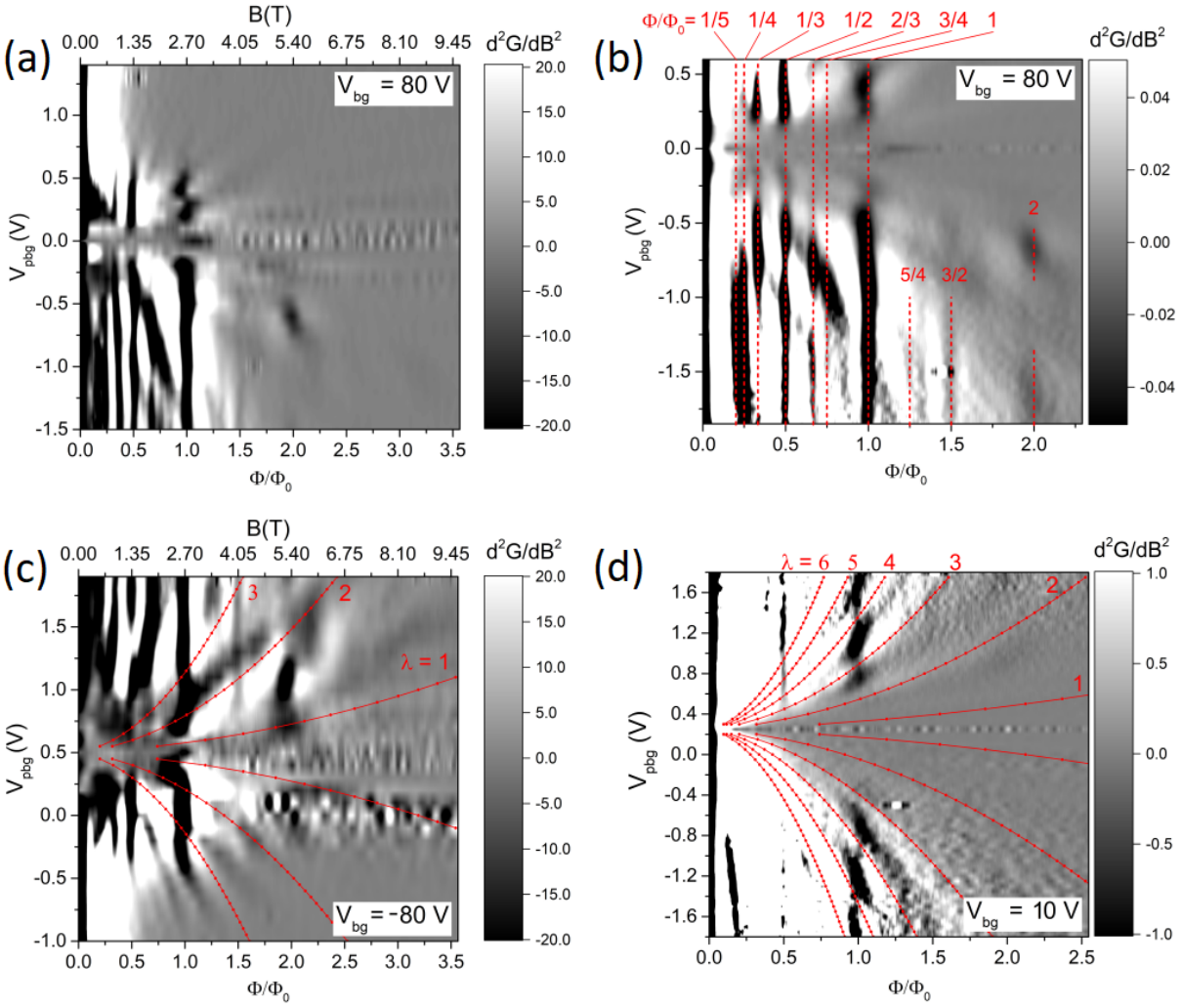

Figure 4.38: **(a)** Grey scale plot of d^2G/dB^2 as a function of Φ/Φ_0 and V_{pbg} at $V_{bg} = 80$ V and at $T = 125$ K. Dark vertical features at rational fractions of Φ/Φ_0 correspond to enhanced conductance due to an additional band conductivity contribution. **(b)** Detail of the data in (a), also extending the measurement range in the bipolar regime to higher PBG voltages V_{pbg}, i.e. higher charge carrier densities. All features are labelled with their value of Φ/Φ_0 at which they occur. **(c)** Grey scale plot of d^2G/dB^2 as a function of Φ/Φ_0 and V_{pbg} at $V_{bg} = -80$ V. Compared to the data in (a), all features are mirrored at the CNP upon changing the polarity of the back gate voltage. The red lines correspond to flat band positions in semi-classical approximation. The isolated feature at $\Phi/\Phi_0 = 2$ lies exactly between flat band positions given by $\lambda = 1$ and $\lambda = 2$. **(d)** Grey scale plot of d^2G/dB^2 as a function of Φ/Φ_0 and V_{pbg} at $V_{bg} = 10$ V. At lower back gate voltage, i.e. weaker potential modulation, the majority of features start to vanish and the internal structure of Brown-Zak oscillations becomes visible. The most pronounced feature at $\Phi/\Phi_0 = 1$ is apparently modulated by Weiss oscillations which are determined by the flat band positions with $\lambda = 1, 2, ..., 6$ (red lines).

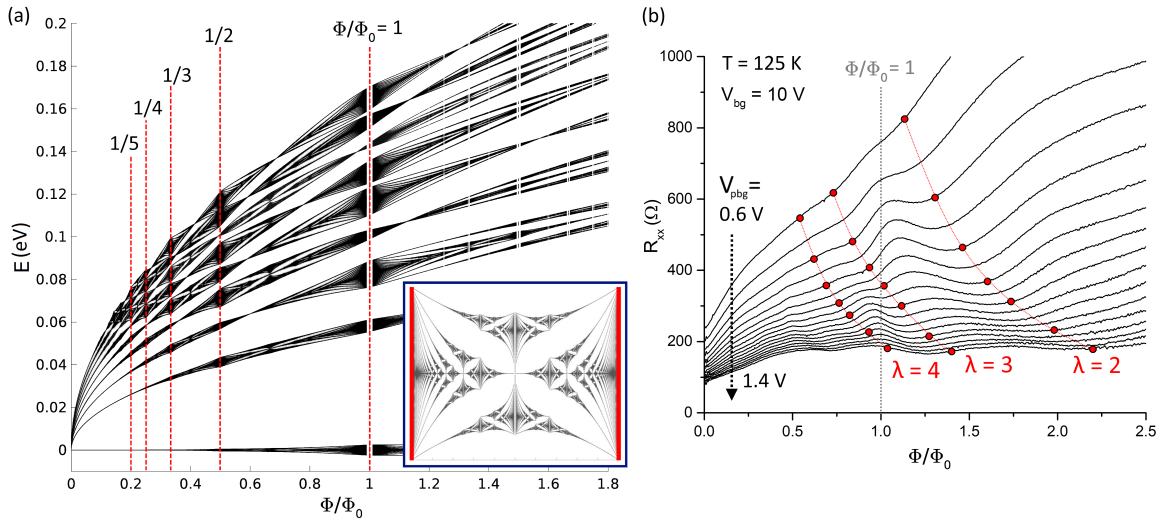

Figure 4.39: **(a)** Calculated Landau level spectrum. At unit fractions of Φ/Φ_0 (red dashed lines) the Hofstadter butterfly (see inset − red lines correspond to maximum band width) extends across the whole Landau band width, which gives rise to the largest band conductivity contribution. Adapted from [174]. **(b)** R_{xx} as a function of Φ/Φ_0 at $V_{bg} = 10$ V and several PBG voltages V_{pbg} (in 0.05 V steps), corresponding to the data in Fig. 4.38 (d). At weaker potential modulation the overall band conductivity contribution is reduced. Only the most pronounced features, in particular the peak at $\Phi/\Phi_0 = 1$ (grey dashed line), remain. The feature at $\Phi/\Phi_0 = 1$ becomes modulated by the occurrence of flat bands (red dots mark the flat band positions with $\lambda = 2, 3, 4$).

Calculated Band Conductivity Contribution

The experimental results can be semi-quantitatively reproduced by estimating the band conductivity as a function of Φ/Φ_0. These calculations were carried out and are provided by Jonathan Eroms [176]. First, the conductivity contribution $\Delta\sigma$ due to a 1D superlattice was calculated (see [84] and chapter 2.2.2) by using

$$\Delta\sigma \propto \Lambda_{1D} := Xe^{-X} \sum_{N=0}^{\infty} \frac{\exp(\beta(E_{N,0} - E_F))}{[\exp(\beta(E_{N,0} - E_F)) + 1]^2} [L_N(X) + L_{N-1}(X)]^2 \tag{4.3}$$

and including all Landau levels within $\pm 10 k_B T$ of the Fermi level. Then, the Hofstadter butterfly spectrum was obtained for every magnetic field and broadened to the full extent of the underlying Landau band. In addition, only energy gaps exceeding a minimum size were considered accounting for collision broadening of energy levels. Finally, the reduced band width due to splitting by the Hofstadter spectrum was taken into account to reduce the overall conductivity. Fig. 4.40 shows the final result which reproduces the experimental features. At rational fractions of Φ/Φ_0 an enhanced band conductivity contribution is apparent − consistent with experiment. Furthermore, the reduced band conductivity at flat band positions, given in semi-classical approximation, is visible, causing the modulation of the most pronounced feature at $\Phi/\Phi_0 = 1$ and the splitting of the feature at $\Phi/\Phi_0 = 2$.

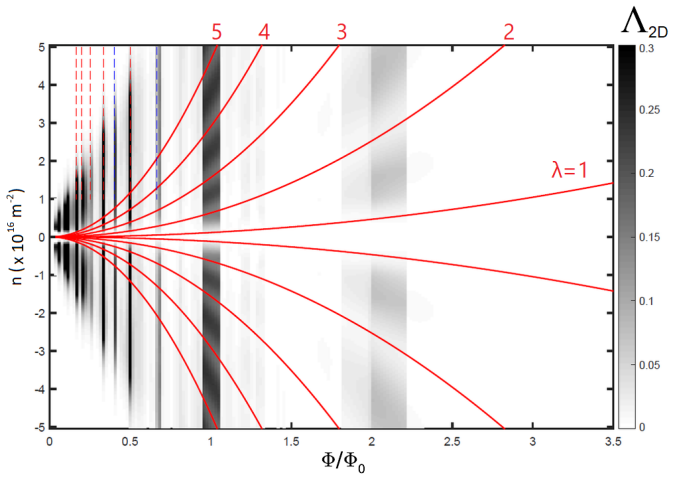

Figure 4.40: Calculated band conductivity contribution Λ_{2D} in a 2D graphene superlattice as a function of Φ/Φ_0 and charge carrier density n. The overall features in the experimental data are reproduced, including the appearance of enhanced band conductivity at rational fractions of Φ/Φ_0 and the modulation of the observed Brown-Zak oscillations by Weiss oscillations. The red lines show the semi-classical flat band condition for $\lambda = 1, 2, ..., 5$. Adapted from [176].

4.2.4 Interplay Between Artificial and Moiré Superlattice

In the following section, transport measurement results concerning **sample SL2** are discussed. The device consists of an artificial gate-defined hexagonal superlattice with $a_{sl} = 40$ nm in combination with a moiré superlattice originating from the interaction between graphene and one hBN layer. The geometrical factor of the sample is $W/L \sim 0.56$ with $L \sim 1.8$ μm and the classical gate coupling between graphene and the PBG is given by $c_g \sim 3.8 \times 10^{-4}$ F/m^2. The hBN dielectric between graphene and the PBG has a thickness of $d_{hBN,bot} \sim 7$ nm. The quantum capacitance (see eq. 2.24) is included in the calculation of charge carrier densities.
Fig. 4.41 (a) shows the gate map of the device. R_{xx} is plotted as a function of V_{pbg} and V_{bg} in which a variety of features can be identified. The gate response exhibits moiré induced satellite Dirac peaks and, by increasing the back gate voltage, satellite peaks close to the main CNP emerge originating from the electrostatically defined superlattice. The apparent field-effect mobility, extracted at $V_{bg} = 0$ V, is about $\mu \sim 40\,000$ cm^2/Vs. The period of the moiré superstructure is estimated to be about $a_m \sim 14$ nm, determined from the position of the satellite peaks relative to the main Dirac peak. Also additional gate-tunable features start to appear (highlighted by dashed ellipses) which indicate further band structure modifications caused by the interplay between the artificial and the moiré superlattice. Fig. 4.41 (b) depicts line cuts of R_{xx} as a function of n/n_0 (with $n_0 = 1/A_{sl}$ and $A_{sl} = \sqrt{3}a^2/2$ the unit cell area of the artificial superlattice) measured at $V_{bg} = 0, -100, 100$ V. The position of the main Dirac point lies at $n/n_0 = 0$. At high back gate voltages satellite peaks emerge at $n/n_0 \sim \pm 4$ originating from the artificial superlattice.

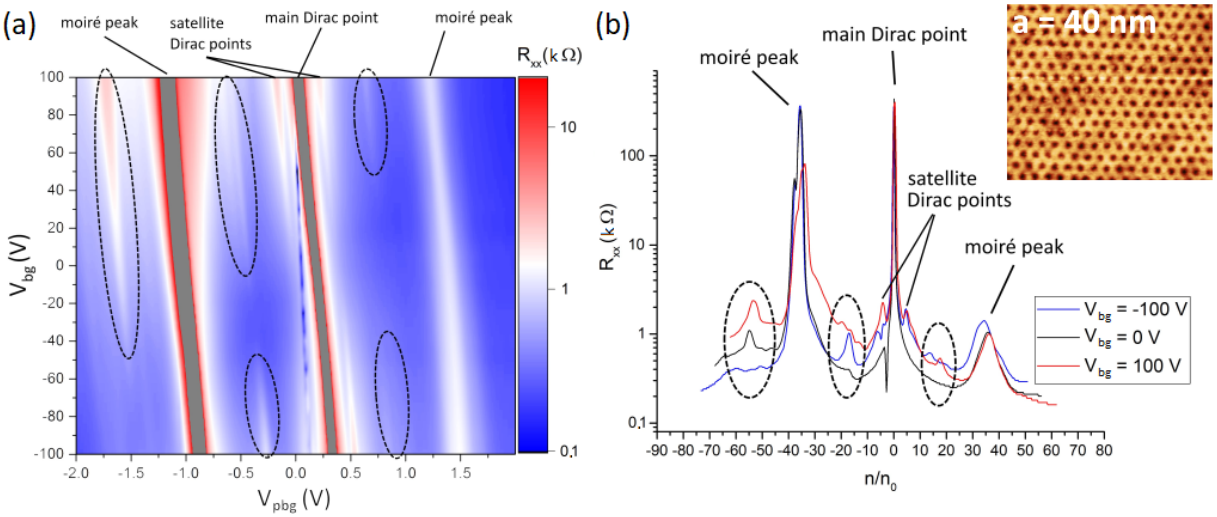

Figure 4.41: **(a)** Gate map of device SL2 measured at $T = 1.5$ K and $B = 0$ T. R_{xx} is plotted as a function of V_{pbg} and V_{bg}. Moiré induced satellite peaks are visible besides the main CNP. By increasing the back gate voltage, satellite peaks start to appear close to the main CNP stemming from the gate-defined superlattice. In addition, gate-tunable features emerge originating from the interplay between the moiré and artificial superlattice (dashed ellipses). **(b)** Line cuts at $V_{bg} = 0, -100, 100$ V showing R_{xx} as a function of n/n_0 with $n_0 = 1/A_{sl}$ and $A_{sl} = \sqrt{3}a_{sl}^2/2$ corresponding to the unit cell area of the artificial hexagonal superlattice with $a = 40$ nm. The main Dirac peak and moiré induced satellite peaks can be identified. The position of the main Dirac point lies at $n/n_0 = 0$. At high back gate voltages satellite peaks emerge at $n/n_0 \sim \pm 4$ originating from the artificial superlattice. The gate-tunable extra features, stemming from the interplay between the two superstructures, are highlighted (dashed ellipses). The inset shows an AFM image of the few-layer graphene PBG which defines the artificial hexagonal superlattice with $a = 40$ nm.

Fig. 4.42 (a) displays the line cuts of Fig. 4.41 (b) as a function of $n/n_{0,m}$ with $n_{0,m} = 1/A_{moiré}$ and $A_{moiré}$ the unit cell area of the moiré superlattice. The moiré peaks occur, as expected, at $n/n_{0,m} = \pm 4$. The gate-tunable extra peaks, stemming from the interplay between the two superstructures, occur at approximately half-filling of the moiré induced minibands, i.e. at positions corresponding to filling up the moiré unit cell with two electrons/holes. This is equivalent to filling up an area of $A = 2A_{moiré}$ with four electrons/holes, which points towards an additional third superstructure originating from the interplay between the artificial and the moiré superstructure similar to the emergence of a third superstructure in doubly aligned graphene/hBN heterostructures [283]. Also a satellite peak at $n/n_{0,m} = -6$, related to the third superstructure, is visible. Fig. 4.42 (b) and (c) depict the Hall response R_{xy} at small magnetic field $B = 200$ mT as a function of V_{pbg}. At high back gate voltages additional fluctuations of R_{xy} are visible at positions of the superlattice induced features in R_{xx}.

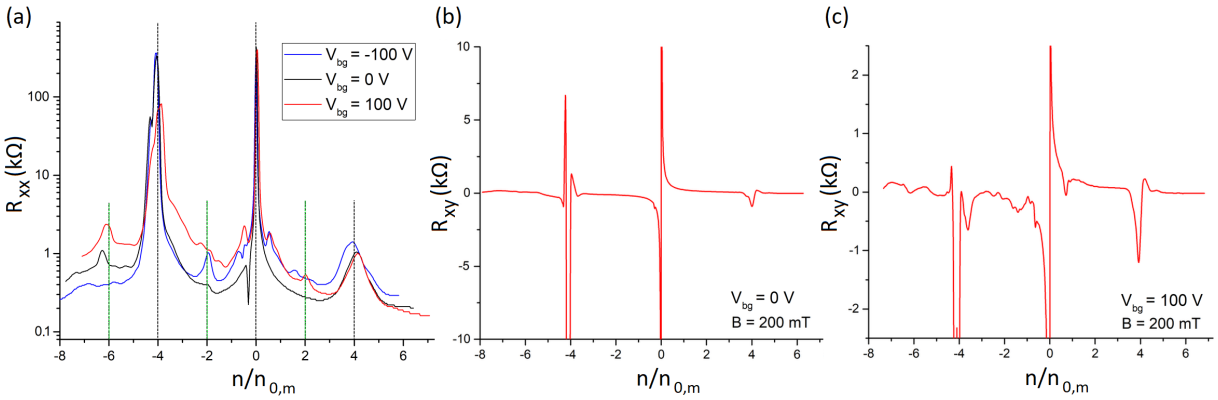

Figure 4.42: **(a)** Same line cuts as in Fig. 4.41 (b) but plotted against $n/n_{0,m}$ with $n_{0,m} = 1/A_{moiré}$ with the unit cell area of the moiré superlattice $A_{moiré}$. The position of the main Dirac point lies at $n/n_{0,m} = 0$ and the moiré peaks occur at $n/n_{0,m} = \pm 4$ (black dotted lines). The gate-tunable extra features (green dotted lines) appear at approximately half-filling of the moiré superlattice. This is equivalent to filling up an area of $A = 2A_{moiré}$ with four electrons/holes. Also a related satellite peak at $n/n_{0,m} = -6$ is visible. **(b)** R_{xy} as a function of V_{pbg} at $B = 200$ mT and $V_{bg} = 0$ V. Sign changes at the main Dirac point and at the moiré induced satellite points are visible. **(c)** R_{xy} as a function of V_{pbg} at $B = 200$ mT and $V_{bg} = 100$ V. At high back gate voltage fluctuations of R_{xy} at positions of the superlattice induced features in R_{xx} appear.

Fig. 4.43 exhibits Landau fan diagrams at $V_{bg} = 0$ V and $V_{bg} = 100$ V measured at a temperature of $T = 1.5$ K. Longitudinal resistance R_{xx} and Hall resistance R_{xy} are plotted as a function of n/n_0 (considering the unit cell area of the artificial superlattice) and magnetic field B. The magnetotransport data shows pronounced Landau fans emerging from the main Dirac point and the moiré induced satellite peaks. At $V_{bg} = 100$ V also modifications next to the main CNP manifest, stemming from the influence of the gate-defined superlattice. Furthermore, faint features occur which originate from the extra peaks of the third superstructure. But these features do not develop pronounced Landau fans. Fig. 4.44 displays details of the Landau fan diagrams in Fig. 4.43, showing the region around the main CNP in which features induced by the artificial superlattice appear. In comparison with the data at $V_{bg} = 0$ V, one can identify the impact of the gate-tunable artificial superstructure. Weak signatures of Landau fans emerge from the satellite peaks at $n/n_0 \sim \pm 4$ at high back gate voltages. Overall, the observed features in sample SL2 are not as well-developed as in sample SL1. The reason for the apparent damped effect of the electrostatically defined superlattice lies probably in the fact that the hBN dielectric between graphene and the PBG in sample SL2 ($d_{hBN,bot} \sim 7$ nm) is about 40% thicker than in sample SL1 ($d_{hBN,bot} \sim 5$ nm). Consequently, the potential modulation is not as pronounced as in sample SL1. This stresses the importance of a thin gate dielectric in order to generate a well-defined periodic potential in the graphene layer and induce well developed band structure modifications.

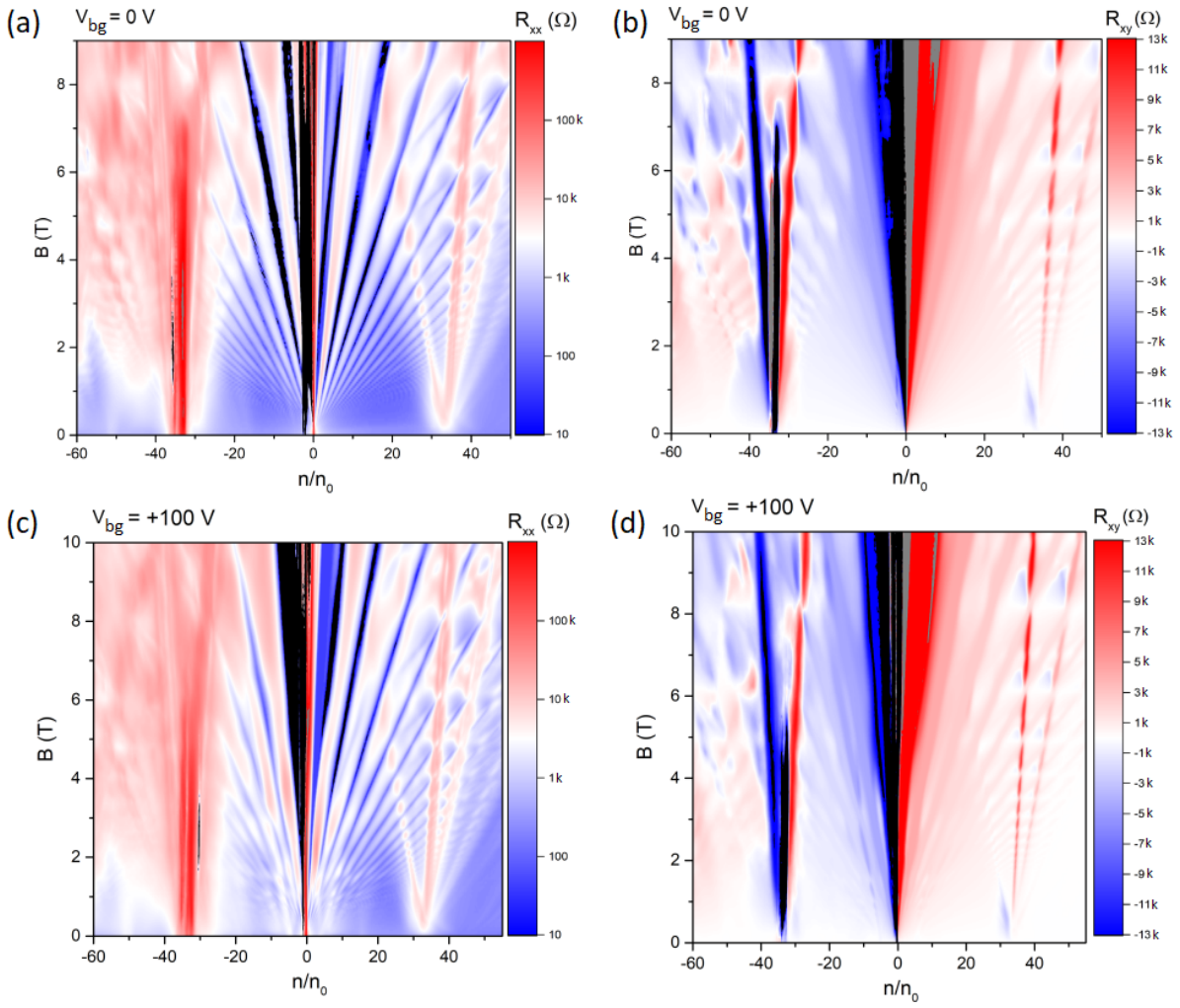

Figure 4.43: (a)+(b) Landau fan diagrams at $V_{bg} = 0$ V and at $T = 1.5$ K. (a) R_{xx} plotted as a function of n/n_0 (considering the unit cell area of the artificial superlattice) and magnetic field B. (b) Corresponding Hall resistance R_{xy} plotted as a function of n/n_0 and magnetic field B. **(c)+(d)** Landau fan diagrams at $V_{bg} = 100$ V and at $T = 1.5$ K: (c) R_{xx} and (d) R_{xy} plotted as a function of n/n_0 and magnetic field B. At high back gate voltage additional features emerge from the satellite peaks close to the main CNP induced by the gate-defined superlattice.

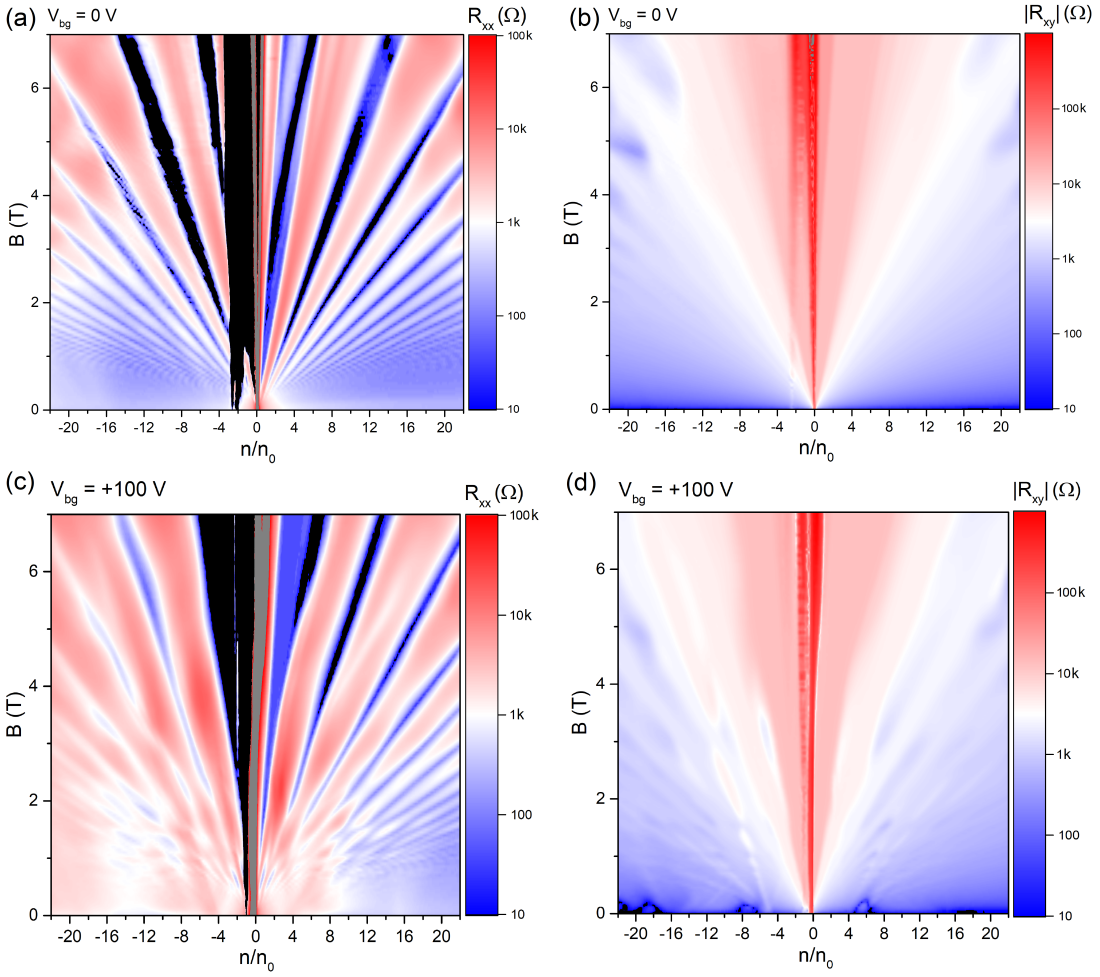

Figure 4.44: Same data as in Fig. 4.43 with focus on the region around the main CNP. By increasing the back gate voltage, i.e. increasing the modulation strength, signatures of secondary Landau fans emerge in R_{xx} and R_{xy} originating from the satellite peaks at $n/n_0 \sim \pm 4$ which are induced by the artificial superlattice.

By considering the second derivative of R_{xx} with respect to n/n_0, emerging features become better visible, as illustrated in Fig. 4.45 in which $d^2R_{xx}/d(n/n_0)^2$ is plotted as a function of n/n_0 and B. The Landau fan originating from the main CNP is modified by the artificial superlattice. In contrast, the moiré induced Landau fans exhibit no clear modifications except a decrease in visibility of the weakest features due to a decrease in charge carrier mobility at higher back gate voltages. Fig. 4.46 (a) shows the region around the main CNP in which the impact of the artificial superlattice can be seen in more detail, including the faint features corresponding to Landau fans emerging from $n/n_0 \sim \pm 4$. Fig. 4.46 (b) highlights some of the extra features stemming from the interplay between the two superlattices. In addition, traces of a Landau fan corresponding to a second-order moiré peak can be identified which is also visible at zero back gate voltage and not showing any signs of significant gate-tunable modifications. These traces can be extrapolated to a second-order moiré peak at approximately $n/n_0 \sim -70$ – out of reach for the PBG since higher gate voltages were not applied to avoid gate-leakage currents and damage to the device.

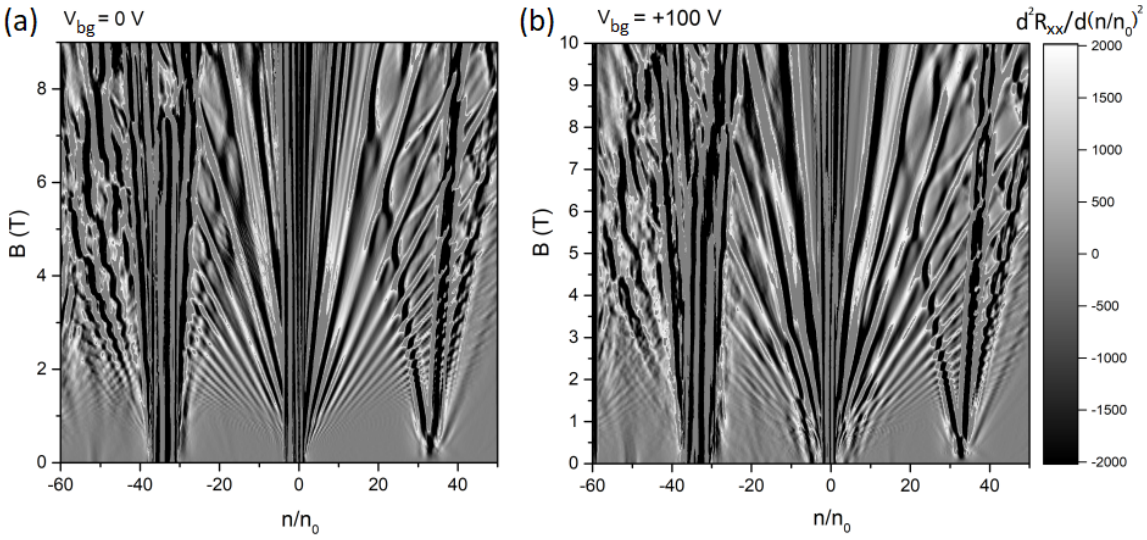

Figure 4.45: **(a)** $d^2R_{xx}/d(n/n_0)^2$ plotted as a function of n/n_0 and B at $V_{bg} = 0$ V. **(b)** $d^2R_{xx}/d(n/n_0)^2$ plotted as a function of n/n_0 and B at $V_{bg} = 100$ V. The gate-tunable features modify the Landau fan close to the main CNP. The moiré induced Landau fans exhibit no apparent sign of gate-tunable modifications. The grey scale bar is the same for (a) and (b).

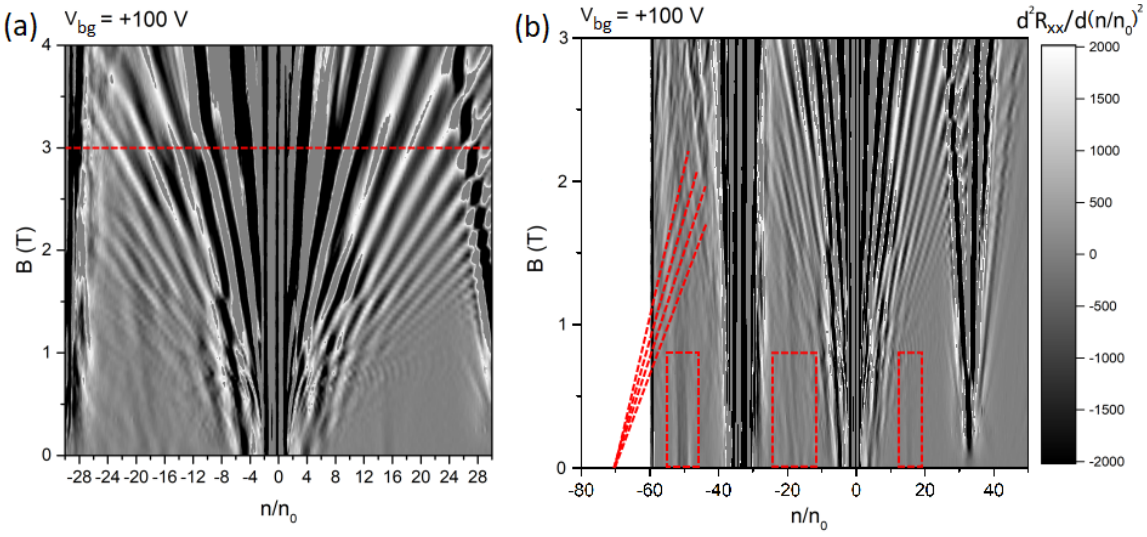

Figure 4.46: **(a)** Detail of the data in Fig. 4.45 (a). The position of one magnetic flux quantum per artificial superlattice unit cell is highlighted (red dashed line) and corresponds to about $B_0 \sim 3$ T. **(b)** Gate-tunable signatures which stem from the interplay between the artificial and the moiré superstructure are highlighted (red boxes). These faint features do not show well-developed Landau fans. Also a second-order moiré peak can be identified by extrapolating corresponding Landau fan features to $n/n_0 \sim -70$ (red dashed lines). The grey scale bar is the same for (a) and (b).

Fig. 4.47 (a) and Fig. 4.49 (a) depict Wannier diagrams of the device at $V_{bg} = 0$ V and $V_{bg} = 100$ V. R_{xx} is plotted as a function of Landau level filling factor ν and inverse magnetic flux Φ_0/Φ per unit cell area of the gate-defined superlattice. At zero back gate voltage no signatures of energy gaps induced by the artificial superlattice are visible. Only features with $s = 0$ corresponding to usual quantum Hall physics in graphene at filling factors $\nu = ..., -10, -6, -2, 2, 6, 10, ...$ and moiré induced features are observable. At high magnetic fields a splitting of the $N = 1$ Landau level is visible which can be explained by the onset of a lifting of the spin and valley degeneracy [30, 31, 49]. These spin and valley splitting related signatures follow vertical minima in R_{xx} in the Wannier diagram in Fig. 4.47 (a), i.e. correspond to energy gaps with $s = 0$, indicating usual quantum Hall physics. Fig. 4.47 (b) shows a line cut of R_{xx} and R_{xy} as a function of Landau level filling factor ν extracted from Fig. 4.47 (a) (green dashed line) at a magnetic field of $B = 5$ T. The onset of spin-splitting in the second Landau level and moiré induced features at higher Landau level filling factor can be observed. Fig. 4.48 displays a line cut at $B = 9$ T, showing the onset of spin and valley splitting in the $N = 1$ Landau level and corrections due to the moiré superlattice at higher Landau level filling factor. In contrast, the Wannier diagram in Fig. 4.49 (a), measured at $V_{bg} = 100$ V, also exhibits features originating from a Hofstadter gap with $s = 4$ which is also apparent in the line cut in Fig. 4.49 (b). This particular energy gap can be identified as the largest energy gap in the Hofstadter butterfly of a hexagonal superlattice which displays a different order of the size of minigaps compared to a square superlattice with one large gap dominating the spectrum [170] (see inset of Fig. 4.49 (b)).

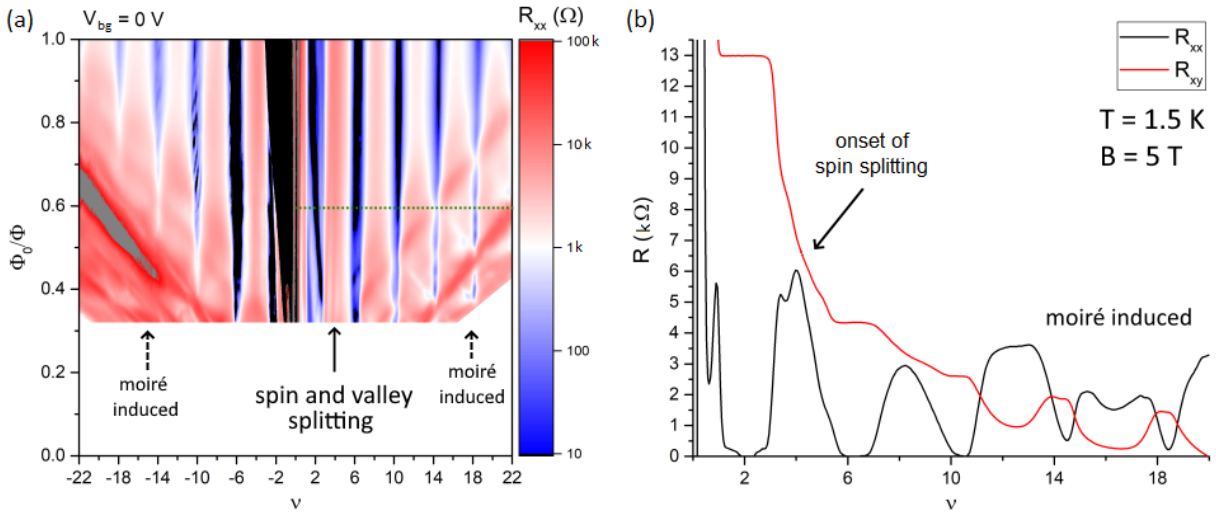

Figure 4.47: (a) Wannier diagram at $V_{bg} = 0$ V. R_{xx} is plotted as a function of Landau level filling factor ν and inverse magnetic flux Φ_0/Φ. No signatures of Hofstadter related energy gaps, induced by the artificial superlattice, can be observed. At high magnetic fields the onset of Landau level splitting due to a lifting of spin and valley degeneracy appears, visible in the first Landau level. The pronounced diagonal features correspond to the moiré superlattice. **(b)** R_{xx} and R_{xy} as a function of ν at $B = 5$ T (corresponding to the green dashed line in (a)) highlighting the onset of spin-splitting and moiré induced features. Apart from that, the device exhibits usual quantum Hall states of monolayer graphene.

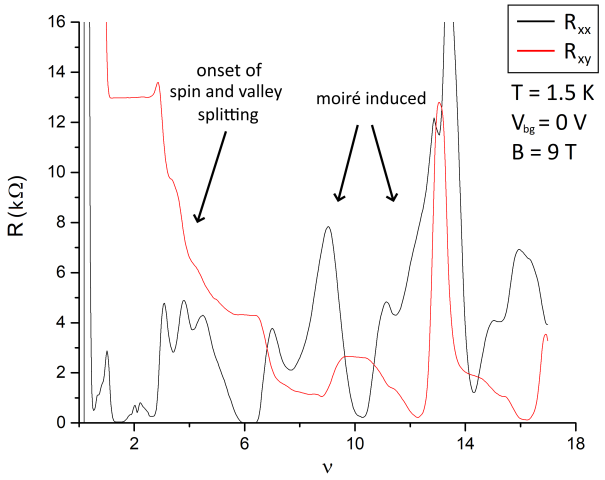

Figure 4.48: **(a)** Line cut of R_{xx} and R_{xy} as a function of ν at $V_{bg} = 0$ V and $B = 9$ T. In the first Landau level the onset of Landau level splitting due to a lifting of spin and valley degeneracy is visible. At higher Landau level filling factor corrections due to the moiré superlattice appear.

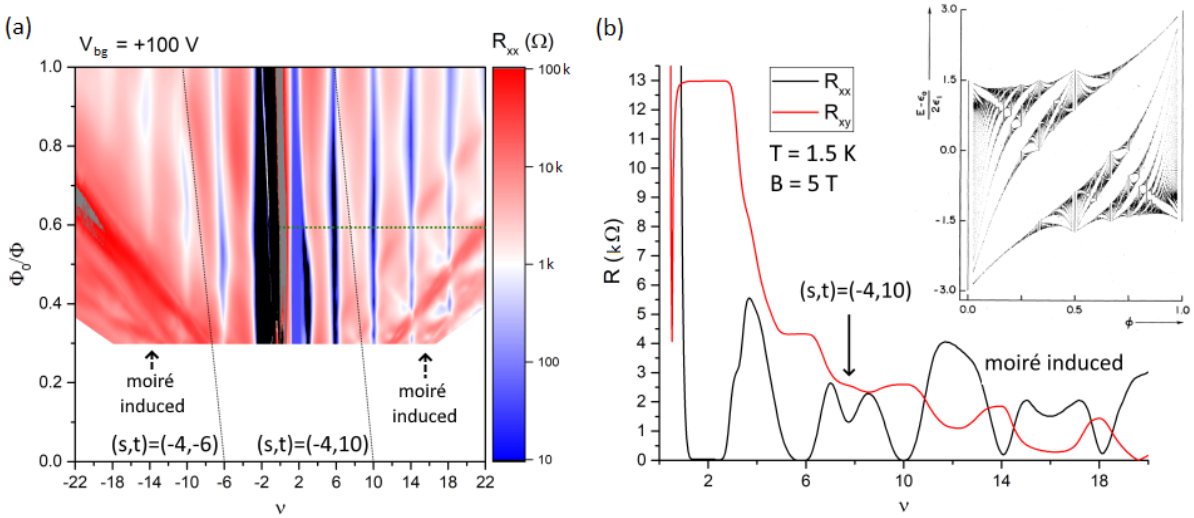

Figure 4.49: **(a)** Wannier diagram at $V_{bg} = 100$ V. R_{xx} is plotted as a function of Landau level filling factor ν and inverse magnetic flux Φ_0/Φ. Again, the pronounced diagonal features correspond to the moiré induced superlattice. In addition, Hofstadter gaps, induced by the gate-defined superlattice, can be identified and are labelled with their corresponding parameters (s, t). **(b)** R_{xx} and R_{xy} as a function of ν at $B = 5$ T (corresponding to the green dashed line in (a)). The Hofstadter gap with $(s, t) = (4, 10)$ (marked with an arrow) corresponds to the largest energy gap in the Hofstadter butterfly of a hexagonal superlattice (see inset, [170]).

In sample SL2 also characteristic band conductivity oscillations (Brown-Zak oscillations) appeared in magnetotransport originating from the two different superlattices and reflecting the two different periodicities superimposed on the charge carriers in the system. Fig. 4.50 displays a grey scale plot of d^2G/dB^2 as a function of magnetic field B and PBG voltage V_{pbg} at $V_{bg} = 100$ V measured at a temperature of $T = 125$ K. Again, before taking the second derivative, the raw data was

smoothed in order to remove spikes and small fluctuations due to noise. In the vicinity of the moiré peaks pronounced Brown-Zak oscillations occur. At lower charge carrier densities, i.e. in a region close to the main CNP, weaker features of enhanced band conductivity start to appear stemming from the artificial superlattice. Fig. 4.51 depicts R_{xx} as a function magnetic field B at two different PBG voltages V_{pbg} corresponding to the blue dashed lines in Fig. 4.50. Fig. 4.51 (a) shows data at $V_{pbg} = 1.2$ V in a region dominated by Brown-Zak oscillations of the moiré superstructure. By plotting the inverse magnetic field values at which the most pronounced resistance peaks occur (corresponding to unit fractions of Φ/Φ_0) against an integer index i, it is possible to determine the lattice period a of the hexagonal moiré superlattice from the slope m of a linear fit to the data points: $a = \sqrt{2m\Phi_0/\sqrt{3}}$. A moiré lattice constant of $a_{moiré} \sim 14$ nm is estimated which is in good agreement with the estimation from the position of the satellite Dirac peaks relative to the main Dirac peak. Fig. 4.51 (c) displays R_{xx} as a function magnetic field B at $V_{pbg} = 0.4$ V. Brown-Zak features due to the artificial hexagonal superlattice are visible with $\Phi/\Phi_0 = 1$ at about $B_0 \sim 3$ T. Again, by evaluating the peak positions, a lattice constant of about $a_{sl} \sim 40$ nm is estimated which is in good agreement with the designed lattice period of the artificial hexagonal superlattice.

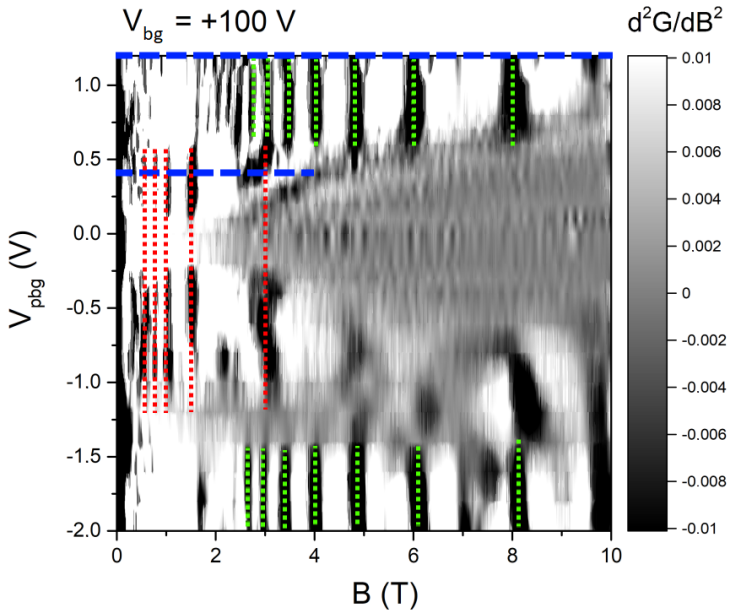

Figure 4.50: d^2G/dB^2 as a function of magnetic field B and PBG voltage V_{pbg} at $V_{bg} = 100$ V measured at a temperature of $T = 125$ K. Brown-Zak oscillations, stemming from the artificial and the moiré superlattice, can be identified. Vertical dark lines correspond to an enhanced band conductivity. In the vicinity of the moiré induced satellite peaks and at high V_{pbg}, i.e. at high charge carrier density, Brown-Zak oscillations due to the moiré superlattice dominate (highlighted by vertical green dotted lines). In the vicinity of the main CNP, i.e. at low charge carrier density, Brown-Zak oscillations, induced by the gate-defined superlattice, are visible (highlighted by vertical red dotted lines) with $\Phi/\Phi_0 = 1$ at about $B_0 \sim 3$ T. Line cuts of the longitudinal resistance R_{xx} along the horizontal blue dashed lines are displayed in Fig. 4.51.

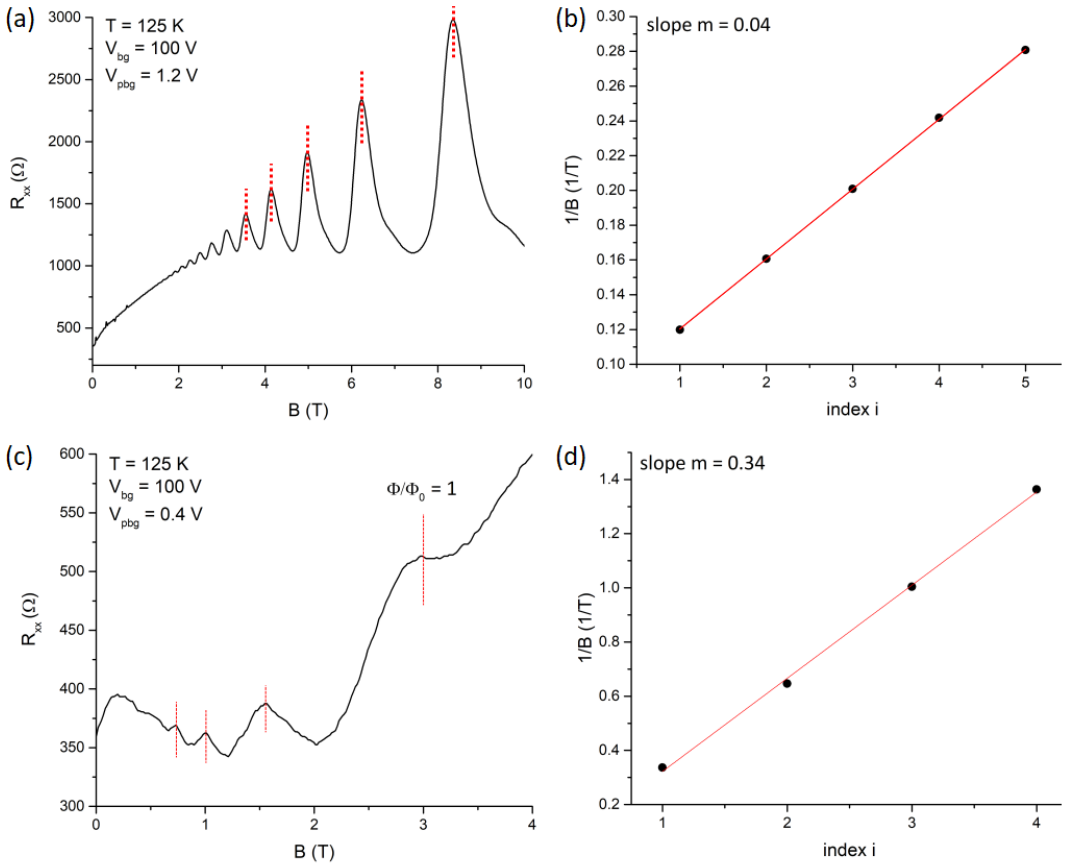

Figure 4.51: **(a)** R_{xx} plotted as a function of magnetic field B at $V_{pbg} = 1.2$ V corresponding to the upper blue dashed line in Fig. 4.50. Clear Brown-Zak oscillations, induced by the moiré superlattice, are visible. **(b)** Determination of the superlattice period by evaluating the peak positions in magnetic field in (a) (red dotted lines). Inverse magnetic field values are plotted against an integer index i. The red line is a linear fit with slope $m = 0.04$. A moiré lattice constant of $a_{moiré} \sim 14$ nm is estimated. **(c)** R_{xx} plotted as a function of magnetic field B at $V_{pbg} = 0.4$ V corresponding to the lower blue dashed line in Fig. 4.50. Brown-Zak oscillations, induced by the artificial superlattice, are visible. **(d)** Determination of the superlattice period by evaluating the peak positions in magnetic field in (c) (red dotted lines). A lattice constant of $a_{sl} \sim 40$ nm is estimated − in good agreement with the artificially designed hexagonal superlattice.

CHAPTER 5

CONCLUSION AND OUTLOOK

In this work, the impact of two-dimensional superlattices on the electronic band structure of graphene was investigated. After introducing the theoretical and experimental background and giving an overview of device fabrication and the measurement setup, the experimental results obtained from electrical transport measurements were presented and discussed.

Graphene antidot lattices with square and hexagonal lattice geometry and lattice constants of $a = 50$ nm and $a = 40$ nm were studied. The devices exhibited a pronounced insulating state at the charge neutrality point with temperature activated transport behaviour. This was attributed to the emergence of a fundamental energy gap in these antidot devices [4]. The actual size of emerging energy gaps could not be clearly determined in the carried out transport measurements, mainly due to a non-negligible amount of disorder obscuring the actual impact of energy gaps in transport. Only estimations could be given, obtained from Arrhenius plots and from the extent of the transport gap region, with energy gaps ranging between ~ 6 meV and ~ 200 meV at zero magnetic field. In addition, the tunability of the emerging energy gaps by an applied magnetic field was examined [5, 6]. It was shown that the apparent size of energy gaps, estimated in all employed methods, decreases upon applying a magnetic field. This was further demonstrated in gate-bias spectroscopy measurements. Overall, the investigated graphene antidot lattices showed transport properties not sufficient for real transistor applications. Besides the reduction of (edge) disorder, also the neck width of the graphene antidot lattices should be further reduced, which would consequently increase the magnitude of the induced energy gaps and eventually enable real transistor action at room temperature.

As an alternative technique for band structure engineering of graphene, devices with electrostatically defined and gate-tunable two-dimensional superlattices with square and hexagonal lattice geometry and lattice constants of $a = 40$ nm were investigated, realized by the combination of uniform and patterned few-layer graphene gates [7, 13]. These superlattice devices exhibited pronounced band structure modifications, as evident from the emergence of satellite Dirac peaks in transport measurements at positions corresponding to filling up newly generated minibands. Furthermore, in combination with a magnetic field, signatures of the Hofstadter butterfly energy spectrum [14] were resolved in magnetotransport measurements including the manifestation of a non-trivial quantum Hall response due to superlattice-induced minigaps in agreement with the theoretical prediction by Thouless *et al.* [180]. The experimental results were also reproduced and explained in (magneto)transport simulations and miniband structure calculations [13, 269].

Moreover, band conductivity oscillations (so-called Brown-Zak oscillations [15]) were examined in the artificial superlattices whose origin lie in extended minibands in the magnetic band structure given by the Hofstadter butterfly. Due to the larger lattice constant of $a = 40$ nm compared to moiré superlattices in graphene/hexagonal boron nitride heterostructures with maximum lattice constants of ~ 14 nm [8–10], and due to the possibility of tuning the modulation strength by an applied gate voltage, further insight into these quantum oscillations was gained. In particular, their modulation by Weiss oscillations [161] was observed, originating from the occurrence of flat bands in the superlattice-induced magnetic band structure. In a device with an artificial hexagonal superlattice with a lattice constant of $a = 40$ nm in combination with a moiré superlattice with a lattice constant of ~ 14 nm, the interplay between these two superstructures was investigated. Besides features originating solely from one of the two superlattices, also gate-tunable features corresponding to a third superstructure with unit cell area of about twice the size of the moiré superlattice appeared. In addition, two types of band conductivity oscillations with different periodicity corresponding to the two main superstructures were identified.

Overall, the modification of the electronic band structure of graphene by means of gate-defined two-dimensional superlattices with square and hexagonal lattice geometry was successfully demonstrated, which now paves the way for more advanced lattice geometries. Fig. 5.1 (a)-(c) show other possible lattice geometries like the kagome, the distorted honeycomb, and the Lieb lattice, which display interesting features like additional band-crossing points or flat bands in the electronic band structure [284, 285]. These more advanced lattice geometries could provide the possibility to study e.g. strongly correlated electron physics [286, 287] (similar to the situation in magic-angle twisted bilayer graphene [117]) in electrostatically defined and gate-tunable superlattices. In this regard, in order to study more subtle effects in the superlattice devices, the charge carrier mobility should be further increased. This could be realized by using an additional graphite layer as a back gate, which would additionally screen trapped charges in the SiO_2 substrate and enhance the quality of the devices by reducing charge carrier density inhomogeneities in graphene [98], as depicted in Fig. 5.1 (d). Fig. 5.1 (e) illustrates a possible sample design with an additional graphite back gate. Moreover, placing the patterned few-layer graphene gates on top of the encapsulated graphene layer would allow more flexible use of the patterned gates. It would also make it possible to examine the gates and check for their integrity e.g. after carrying out transport measurements. And, if necessary, the patterned top gates could be simply removed by reactive ion etching with oxygen plasma, leaving the heterostructure below intact. Furthermore, defining the Hall bar geometry by etching trenches into the stack and filling them up with e.g. aluminium oxide would allow to avoid exposing the edges of graphene to the environment, and the flat surface of the whole stack could be used as a substrate for patterned top gates.

In conclusion, the present work provides the basis for the fabrication of gate-defined and gate-tunable two-dimensional superlattices in graphene. These superlattices allow to modify the electronic band structure of graphene, which was successfully demonstrated in transport measurements [13]. The topic has great potential for studying fascinating new physics in more advanced superlattice geometries and will be continued in a subsequent PhD thesis [288].

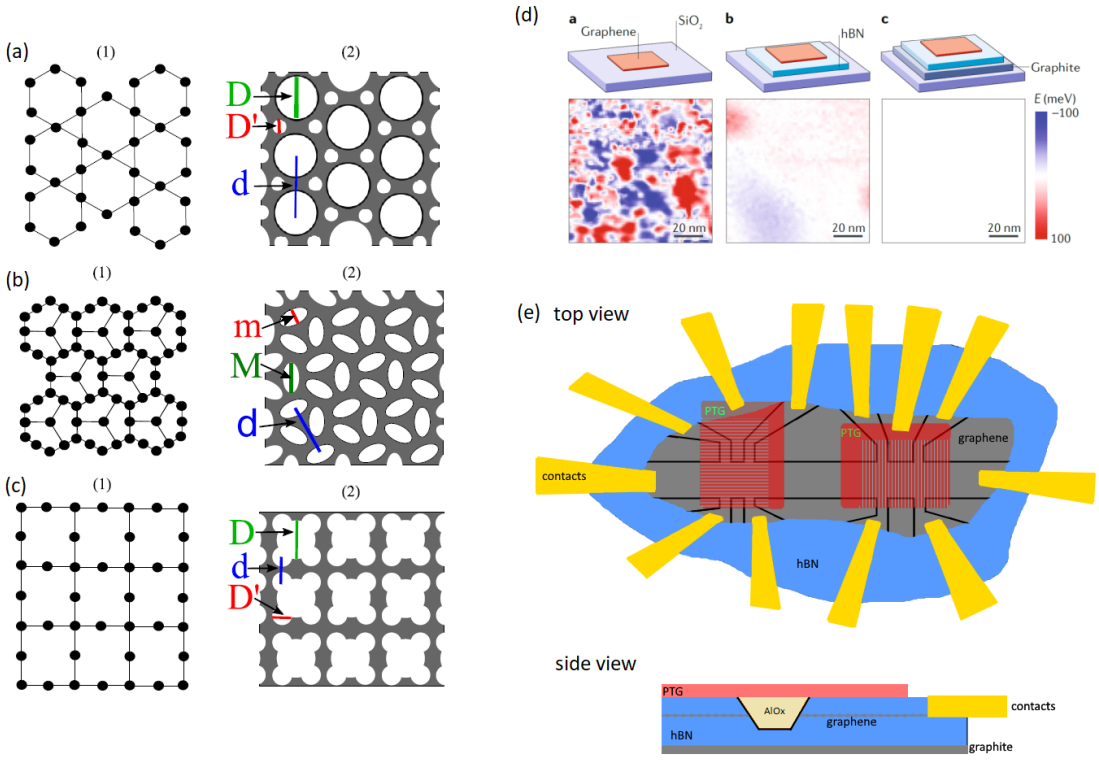

Figure 5.1: **(a)**-**(c)** More advanced superlattice geometries. Left images display the original atomic lattice and the right images show the corresponding lithographically defined lattice geometry. Adapted from [284]. **(a)** Kagome lattice. **(b)** Distorted honeycomb lattice. **(c)** Lieb lattice. **(d)** Potential landscape across a graphene layer. By using a graphite layer below graphene, charge carrier density inhomogeneities can be further reduced due to screening of trapped charges in the SiO_2 substrate, which enhances the charge carrier mobility. [98] **(e)** Possible sample design for patterned top gates (PTGs) in combination with a uniform graphite back gate. The Hall bar is defined by etching trenches into the stack which are consecutively filled up with e.g. aluminium oxide (AlOx). Top view: for more clarity, only the PTGs (here in the case of one-dimensional superlattices), the upper hexagonal boron nitride layer, and the monolayer graphene are displayed. Side view: All layers are shown.

APPENDIX A

PROCESS DOCUMENTATION

- Exfoliation of graphene and hBN
  - substrate: Si/SiO_2 chips with 90 nm SiO_2 and p^{++} doped Si
  - cleaning of substrate: (a) ultrasonic cleaning in acetone (b) isopropyl alcohol (c) blow-dry with nitrogen (d) oxygen plasma: 5 minutes, $1 - 2$ mbar O_2, 50% power
  - tape: Nitto wafer grinding tape (Nitto Denko Corp., ELP BT - 150ECM)
  - natural graphite: flaggy flakes
  - hBN: high-quality hBN crystals (provided by Kenji Watanabe and Takashi Taniguchi: National Institute for Materials Science, Japan)
  - use mechanical exfoliation technique
  - check for suitable flakes by means of an optical microscope and/or atomic force microscope (AFM)
- Van der Waals stacking process
  - prepare and clean microscope glass slide: (a) isopropyl alcohol (b) blow-dry with nitrogen
  - prepare PDMS (polydimethylsiloxane; Dow Corning, Sylgard 184): mixing of elastomer and curing agent (10:1), remove air bubbles by ultrasonic treatment
  - use pipette and place single drop of PDMS onto glass slide
  - bake PDMS on hot plate: 5 min at 150 °C
  - prepare PC (polycarbonate; Aldrich, Goodfellow, CT306310) layer: dissolve PC in chloroform (3%)
  - use two glass slides to prepare thin layer of PC: use pipette to cover one glass slide with PC, gently press the second glass slide onto the first one and immediately move it across the first one in order to produce a thin film of PC on the first glass slide
  - bake PC on hot plate: 20 s at 150 °C
  - use piece of tape with hole to pick up PC layer in order to obtain a suspended PC layer

  - place suspended PC layer across PDMS drop and fix everything with tape
  - use stacking setup and van der Waals stacking process to produce graphene/hBN heterostructures
  - remove PC in chloroform or oxygen plasma and check stack by means of an AFM

- Fabrication of Hall bar
  - spin coating of resist: PMMA 950k 5% (dissolved in anisole) [two-step spin coating: (a) 3000 rpm, accel.: 2000 rpm/s, time: 5 s (b) 6000 rpm, accel.: 4000 rpm/s, time: 30 s]
  - bake sample on hot plate: 10 min at 150 °C
  - electron beam lithography (EBL) with eDraw/eLitho-files (Nanonic): acceleration voltage: 30 kV, dose: 280 μC/cm^2, aperture: 30 μm, working distance: 5 mm, line spacing: 10 nm
  - develop resist: (a) 90 s in MIBK (b) 40 s in isopropyl alcohol (c) blow-dry with nitrogen
  - reactive ion etching (RIE)
  - non-selective etching step: CHF_3 (40 sccm) + O_2 (6 sccm), pressure: 55 mTorr, power: 35 W (+ cleaning and preconditioning of chamber) $\rightarrow$ etch rate of hBN $\sim$ 0.8 nm/s
  - selective etching step: (a) cleaning of exposed sample areas: O_2 (20 sccm), pressure: 30 mTorr, power: 20 W, time: 90 s (+ cleaning and preconditioning of chamber) (b) etching of hBN: SF_6 (3 sccm), pressure: 50 mTorr, power: 10 W, time: 30 s (+ cleaning and preconditioning of chamber)
  - remove resist: (a) acetone (b) isopropyl alcohol (c) blow-dry with nitrogen
  - if necessary clean sample and/or etch graphene by RIE: O_2 (20 sccm), pressure: 30 mTorr, power: 20 W, time: 60 s (+ cleaning and preconditioning of chamber)

- Fabrication of antidots
  - spin coating of resist: CSAR 4% (dissolved in anisole) [one-step spin coating: 4000 rpm, accel.: 1000 rpm/s, time: 35 s]
  - bake sample on hot plate: 10 min at 150 °C
  - EBL: acceleration voltage: 30 kV, dose: $\sim$ 0.5 fC (for lattice constant $a = 40$ nm and a patterned region with size of about 5×5 μm^2) or $\sim$ 1 fC (for lattice constant $a = 50$ nm and a patterned region with size of about 5×5 μm^2), aperture: 30 μm, working distance: 3.5 mm
  - develop resist: (a) 30 s in AR 600/546 at $\sim$ 10 °C (b) 20 s in H_2O (c) 20 s in isopropyl alcohol (c) blow-dry with nitrogen
  - RIE etching step: CHF_3 (40 sccm) + O_2 (6 sccm), pressure: 55 mTorr, power: 60 W (+ cleaning and preconditioning of chamber) $\rightarrow$ etch rate of hBN $\sim$ 1.1 nm/s
  - cleaning of contact areas by RIE: O_2 (20 sccm), pressure: 30 mTorr, power: 20 W, time: 30 s (+ cleaning and preconditioning of chamber)
  - remove resist: (a) AR 600/71 + syringe (b) H_2O (c) isopropyl alcohol (c) blow-dry with nitrogen

  - cleaning of sample by RIE: O_2 (20 sccm), pressure: 30 mTorr, power: 20 W, time: 60 s (+ cleaning and preconditioning of chamber)

- Fabrication of patterned few-layer graphene gates
  - spin coating of resist: PMMA 950k 2% (dissolved in anisole) [two-step spin coating: (a) 3000 rpm, accel.: 2000 rpm/s, time: 5 s (b) 6000 rpm, accel.: 4000 rpm/s, time: 30 s]
  - bake sample on hot plate: 10 min at 150 °C
  - EBL: acceleration voltage: 30 kV, dose: $\sim 1.4 - 1.8$ fC (for a lattice constant of about $a = 40$ nm and a patterned region with size of about 5×5 μm^2), aperture: 30 μm, working distance: 3.5 mm
  - develop resist: (a) 60 s in isopropyl alcohol : H_2O (7:3) at ~ 10 °C (b) blow-dry with nitrogen
  - RIE etching step: O_2 (100 sccm), pressure: 30 mTorr, power: 50 W, time: ~ 16 s (+ cleaning and preconditioning of chamber)
  - remove resist: (a) Remover PG at 60 °C for $t \sim 20$ h (b) isopropyl alcohol (c) H_2O (c) blow-dry with nitrogen
  - cleaning of sample in annealing oven: 400 °C in vacuum (~ 10 mbar) for $t \sim 2$ h
  - check patterned gates by means of an AFM

- Fabrication of contacts
  - spin coating of resist: PMMA 200k 9% (dissolved in anisole) [two-step spin coating: (a) 3000 rpm, accel.: 2000 rpm/s, time: 5 s (b) 6000 rpm, accel.: 4000 rpm/s, time: 30 s]
  - bake sample on hot plate: 10 min at 150 °C
  - spin coating of second resist: PMMA 950k 2% (dissolved in anisole) [two-step spin coating: (a) 3000 rpm, accel.: 2000 rpm/s, time: 5 s (b) 6000 rpm, accel.: 4000 rpm/s, time: 30 s]
  - bake sample on hot plate: 10 min at 150 °C
  - EBL fine wiring: acceleration voltage: 30 kV, dose: 435 μC/cm^2, aperture: 30 μm, working distance: 5 mm, line spacing: 10 nm
  - EBL coarse wiring: acceleration voltage: 30 kV, dose: 435 μC/cm^2, aperture: 30 μm, working distance: 5 mm, line spacing: 15 nm
  - develop resist: (a) 40 s in MIBK (b) 20 s in isopropyl alcohol (c) blow-dry with nitrogen
  - RIE etching step: CHF_3 (40 sccm) + O_2 (6 sccm), pressure: 55 mTorr, power: 35 W (+ cleaning and preconditioning of chamber) $\rightarrow$ etch rate of hBN ~ 0.8 nm/s
  - cleaning of contact areas by RIE: O_2 (20 sccm), pressure: 30 mTorr, power: 20 W, time: 30 s (+ cleaning and preconditioning of chamber)
  - evaporation of Cr(5 nm)/Au(80 nm)
  - lift-off: (a) acetone at 60 °C for $t > 1$ h + syringe (b) isopropyl alcohol (c) blow-dry with nitrogen

- final chips are glued into a chip carrier by two-component epoxy adhesive
- contact pads on the sample are connected to electrodes on the chip carrier by ultrasonic wire bonding of aluminium wires

APPENDIX B

ADDITIONAL FABRICATION TOOLS

Pick-Up and Transfer of Patterned Few-Layer Graphene

The following technique provides a way to pick up and transfer patterned few-layer graphene flakes. This allows flexible implementation of patterned gates at arbitrary layer positions during fabrication of van der Waals heterostructures. Fig. B.1 shows one possible transfer technique. First, a hBN flake is picked up by using a PDMS/PC polymer stamp. The polymer stamp with the hBN flake is then brought into contact with a patterned few-layer graphene (with a square antidot lattice with lattice constant $a = 45$ nm) on a Si/SiO_2 chip and the temperature is increased to about $150-160\,^{\circ}C$. The PC layer softens and encloses the target flakes. Subsequently, the target chip is cooled down to about $70\,^{\circ}C$ and the PC layer hardens again. The polymer stamp is removed from the target chip and the few-layer graphene is picked up and can be transferred. In order to examine the antidot pattern in the few-layer graphene, the top hBN layer is removed by RIE with SF_6. Fig. B.1 (l) displays an AFM image of the antidot lattice which exhibits no severe damage after the transfer process. It is also possible to directly pick up patterned few-layer graphene layers without additional hBN layers, but this causes more easily damage to the few-layer graphene flake. As an alternative fabrication process, also pristine few-layer graphene flakes can be picked up and transferred, e.g. onto a hBN flake, as shown in Fig. B.2. Then, the transferred few-layer graphene flake is patterned into the desired geometry (here: a square antidot lattice with lattice constant $a = 45$ nm). If necessary, the patterned flake can be removed with a gentle oxygen plasma etching step which does not affect the hBN layer. After successful fabrication it is possible to transfer additional 2D materials on top of the patterned few-layer graphene flake. Furthermore, one can enhance the stability of the patterned layer during the transfer procedure by using an additional hBN layer below the patterned flakes (see Fig. B.2). Then, the pick-up can be done directly by a PDMS/PC polymer stamp with the method described above. In addition, the hBN/patterned graphite stack can be also picked up by a second hBN layer (see Fig. B.2). Again, in order to check the patterned area after pick-up and transfer, the top hBN layer is removed by RIE with SF_6 and the antidot lattice is examined. Fig. B.2 (o) shows an AFM image which exhibits no severe damage to the patterned few-layer graphene flake and the antidot lattice after the transfer processes.

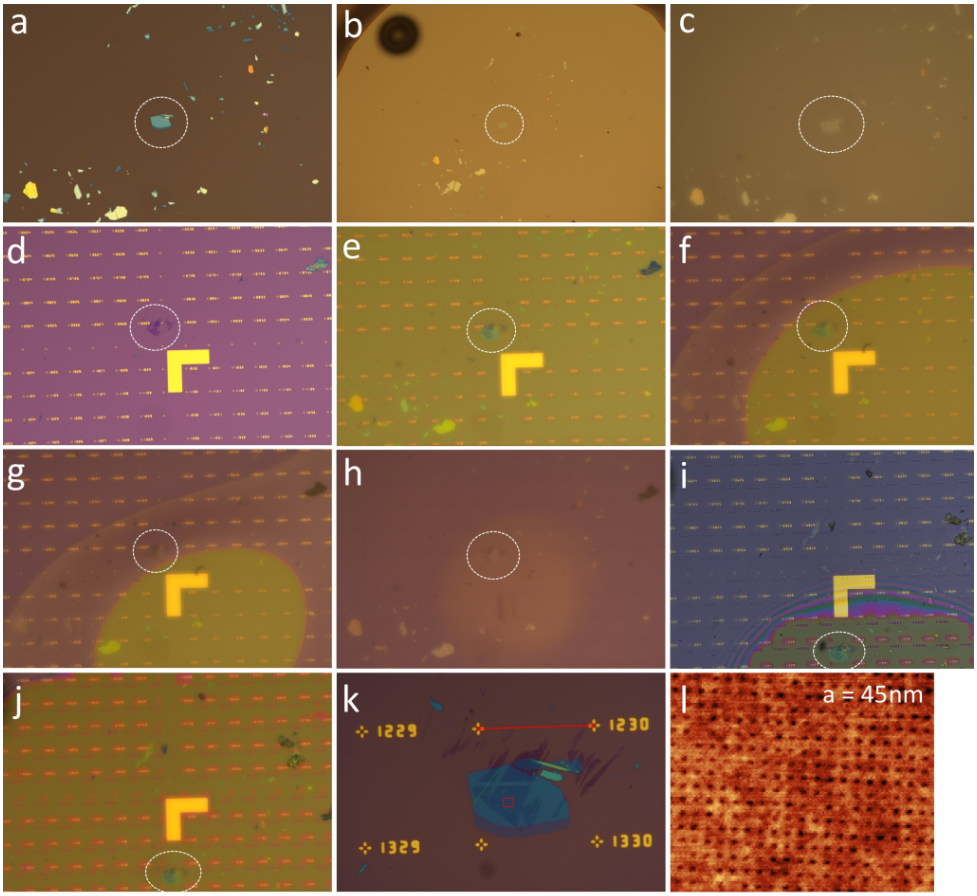

Figure B.1: **(a)** A hBN flake on a Si/SiO_2 chip. **(b)** A PDMS/PC polymer stamp is brought into contact with the hBN flake. **(c)** Pick-up of the hBN flake. **(d)** A patterned few-layer graphene flake on a Si/SiO_2 chip with Cr/Au coordinate system. **(e)** The picked-up hBN flake is brought into contact with the patterned few-layer graphene flake and the temperature is increased to about $150 - 160\,°C$. **(f)** Then, the temperature is decreased to about $70\,°C$ and the polymer stamp is retracted. **(g)** Pick-up of the patterned few-layer graphene flake. **(h)** The hBN flake and the picked-up patterned few-layer graphene on the polymer stamp. **(i)** Transfer of the picked-up materials to a different position on the chip. **(j)** After contact, the temperature is increased to about $180\,°C$. The PC layer with the 2D materials melts onto the chip. **(k)** The hBN/patterned few-layer graphene stack on the chip after removal of the PC layer with chloroform. The red line corresponds to a distance of 50 μm. The red box on the few-layer graphene flake highlights the position of the patterned area. **(l)** After removal of the top hBN layer: AFM image of the antidot lattice with lattice constant $a = 45$ nm in the few-layer graphene flake. [13]

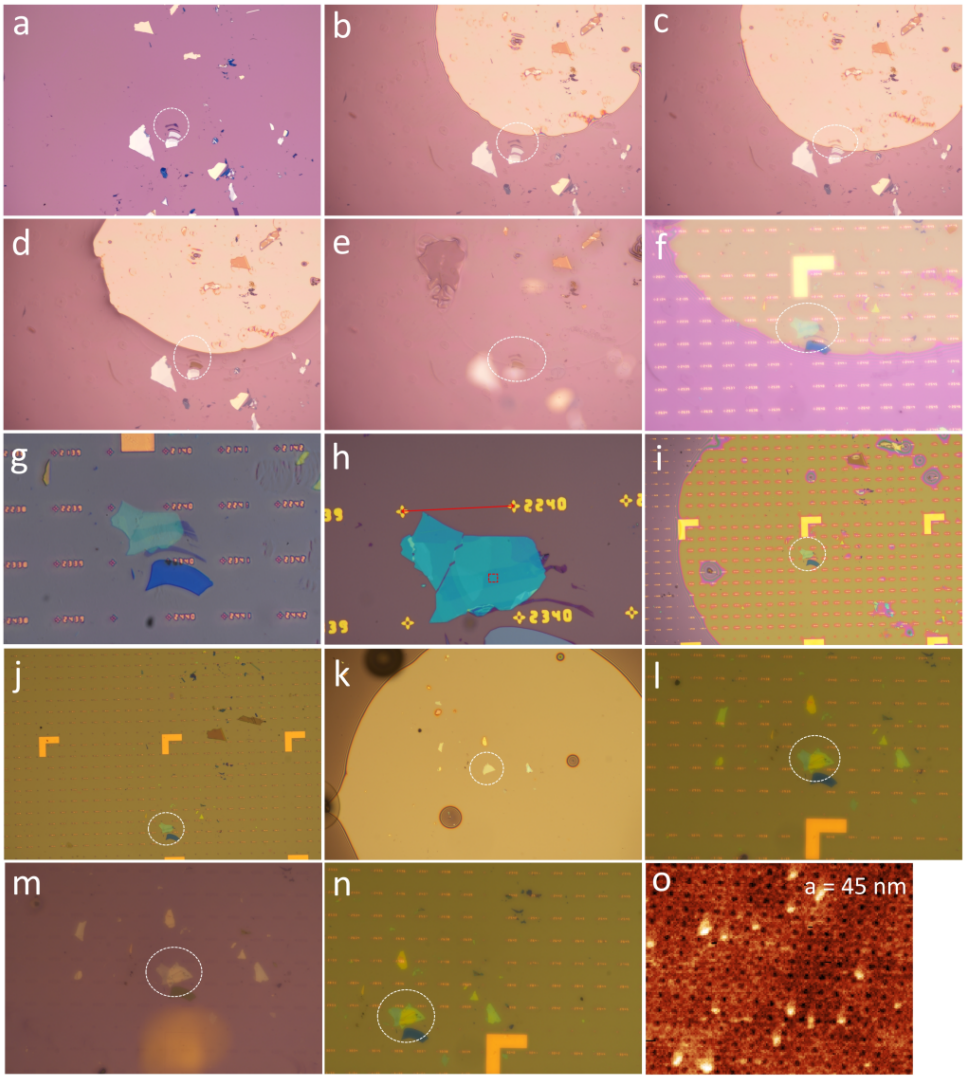

Figure B.2: **(a)** A few-layer graphene flake on a Si/SiO_2 chip. **(b)** A PDMS/PC polymer stamp is brought into contact with the chip. **(c)** The polymer covers the few-layer graphene flake. **(d)** The polymer stamp is retracted and the few-layer graphene flake is picked up. **(e)** The picked-up few-layer graphene on the polymer stamp. **(f)** Transfer of the few-layer graphene flake onto a hBN flake on a Si/SiO_2 chip with Cr/Au coordinate system. **(g)** The few-layer graphene flake on the hBN flake after the transfer step. **(h)** After removal of the PC layer. The few-layer graphene flake is patterned by EBL and RIE. The red box highlights the position of the patterned region. The red line corresponds to a distance of 50 μm. **(i)** A polymer stamp is brought into contact with the hBN/patterned few-layer graphene stack and the temperature is increased to about $150 - 160\,°C$. Subsequently, the temperature is decreased to about $70\,°C$ and the polymer stamp is retracted. The hBN/patterned few-layer graphene stack is picked up. **(j)** After transfer of the stack to a different position on the chip. **(k)** Pick-up of a second hBN layer by using a PDMS/PC polymer stamp. **(l)** The second hBN layer is brought into contact with the hBN/patterned few-layer graphene stack and the temperature is increased to about $150 - 160\,°C$. Subsequently, the temperature is decreased to about $70\,°C$ again and the polymer stamp is retracted. **(m)** The hBN/patterned few-layer graphene/hBN stack is picked up. **(n)** After transfer of the hBN/patterned few-layer graphene/hBN stack. **(o)** After removal of the top hBN layer: AFM image of the square antidot lattice with lattice constant $a = 45$ nm in the few-layer graphene. [13]

Precise Etching of hBN Dielectrics

The mechanical exfoliation of sufficiently thin and large hBN flakes, used as the dielectric material in the superlattice devices with patterned few-layer graphene gates, is difficult and time consuming since the yield of suitable flakes is usually quite low. As a solution, one could try to etch thicker flakes down to the desired thickness. In literature, one can find different recipes for the precise etching of hBN by RIE [289–291]. Fig. B.3 shows one possible RIE process in argon plasma with an etch rate of about 1.8 Å/ min. Since the SiO_2 substrate was also etched, the hBN flake was transferred onto another chip after the etching process in order to determine the etching rate. The used process parameters were: Ar (100 sccm), pressure: 200 mTorr, power: 40 W. The surface roughness after etching was in a tolerable range (roughness average: $ra \sim 130$ pm; root mean square: $rms \sim 170$ pm) and can be probably further optimized. The possibility to precisely etch hBN flakes would represent a helpful tool for easier and more advanced device fabrication − not only in view of the preparation of hBN dielectrics, but also for the fabrication of e.g. hBN tunnel barriers [292, 293].

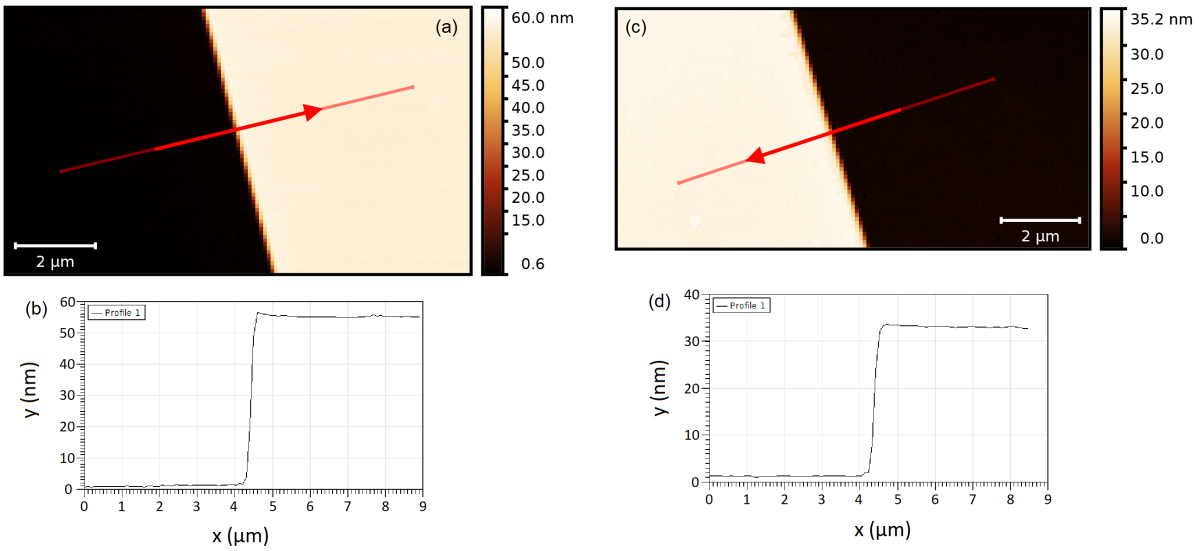

Figure B.3: **(a)** AFM topography image of a hBN flake prior to etching with a thickness of about $d \sim 54$ nm. **(b)** Line profile along the red line in (a). **(c)** AFM topography image of the hBN flake in (a) after 2 h etching by RIE in argon plasma. The thickness is about $d \sim 32$ nm. **(d)** Line profile along the red line in (c).

APPENDIX C

PYTHON CODE: HOFSTADTER BUTTERFLY

```
import math
import numpy
import matplotlib.pyplot as plt
import sympy
from sympy import var, Interval, solveset, S

pi = math.pi
pi2 = math.pi * 2.0
energy = var('energy')

A = numpy.array
listalpha = []
listnu = []
listq = []
alphaarray = []
nuarray = []
qarray = []
alphalist = []
resultlist = []
ymin = []
ymax = []
dataarray1 = []
dataarray2 = []
alphadata = []
edata = []
alphafinal = []

k = int
p = int
q = int
alpha = float
nu = float

pmax = 10
qmax = 10

#define function
def f(energy,k,alpha,nu):
        X = (energy - 2.0 * math.cos(pi2 * k * alpha - nu))
        return X

#create array with all alpha
for p in numpy.arange(0, pmax, 1):
        for q in numpy.arange(1, qmax, 1):

                alpha = p / q
                nu = pi / (2 * q)

                #jump to next q if alpha already in list
                if alpha in alphaarray:
                        continue

                alphaarray.append(alpha)
                nuarray.append(nu)
                qarray.append(q)

#use only alpha in interval [0,1]
a = len(alphaarray)
for i in numpy.arange(0, a):
        if alphaarray[i] in Interval(0,1):
```

```
                listalpha.append(alphaarray[i])
                listnu.append(nuarray[i])
                listq.append(qarray[i])
                continue

#calculate energy values for all alpha and write results in list
for a in numpy.arange(0, len(listalpha)):

        print (round(a * 100 / len(listalpha), 2), "%")

        A = numpy.array([[f(energy,0,listalpha[a],listnu[a]), -1], [1, 0]])

        for k in numpy.arange(1, listq[a], 1):
                B = numpy.array([[f(energy,k,listalpha[a],listnu[a]), -1], [1, 0]])
                A = numpy.dot(A,B)
                for i in numpy.arange(0,2):
                        for j in numpy.arange(0,2):
                                A[i][j]=sympy.sympify(sympy.expand(A[i][j]))

        abstrace = abs(numpy.trace(A))
        result = solveset(abstrace<=4, energy, domain=S.Reals)

        #extract intervals for every alpha and write in resultlist
        if a in numpy.arange(0,3):
                resultargs = list(result.args)
                alphalist.append(listalpha[a])
                resultlist.append((resultargs[0], resultargs[1]))
        else:
                resultargs = list(result.args)
                for i in numpy.arange(0, len(resultargs)):
                        if type(resultargs[i]) is Interval:
                                nums = (resultargs[i].left, resultargs[i].right)
                                alphalist.append(listalpha[a])
                                resultlist.append(list(nums))
                        else:
                                alphalist.append(listalpha[a])
                                resultlist.append(list(resultargs[i]))

#extract for every interval the left (ymin) and right (ymax) boundary
for i in numpy.arange(0, len(resultlist)):
        t = 0
        #in case of set of energy values
        if len(resultlist[i]) > 2:
                for a in numpy.arange(0,len(resultlist[i])):
                        ymin.append(resultlist[i][a])
                        ymax.append(resultlist[i][a])
                        alphafinal.append(alphalist[i])
        #in case of intervals of energy
        if len(resultlist[i]) == 2:
                ymin.append(resultlist[i][0])
                ymax.append(resultlist[i][1])
                alphafinal.append(alphalist[i])
        #in case of single energy value
        if len(resultlist[i]) == 1:
                ymin.append(resultlist[i][0])
                ymax.append(resultlist[i][0])
                alphafinal.append(alphalist[i])

#write data in txt file
#datafile1
dataarray1 = numpy.column_stack((alphafinal, ymin, ymax))
numpy.savetxt('data1.txt', dataarray1)

#datafile2
for i in numpy.arange(0, len(alphafinal)):
        alphadata.append(alphafinal[i])
        alphadata.append(alphafinal[i])
        edata.append(ymin[i])
        edata.append(ymax[i])

dataarray2 = numpy.column_stack((alphadata, edata))
numpy.savetxt('data2.txt', dataarray2)

#plot butterfly
for i in numpy.arange(0, len(alphafinal)):
        plt.xlim(-0.1, 1.1)
        plt.ylim(-4, 4)
        #if interval approximately single value, use scatter plot
        if round(ymin[i], 2) == round(ymax[i], 2):
                plt.scatter(alphafinal[i], (ymin[i]+ymax[i])/2, c = "black", s = 0.05)
        else:
                plt.axvline(alphafinal[i], (ymin[i]+4)/8, (ymax[i]+4)/8, linewidth = 0.5, color = "black")

#save as png-file
plt.savefig('HBF.png', dpi = 600)
```

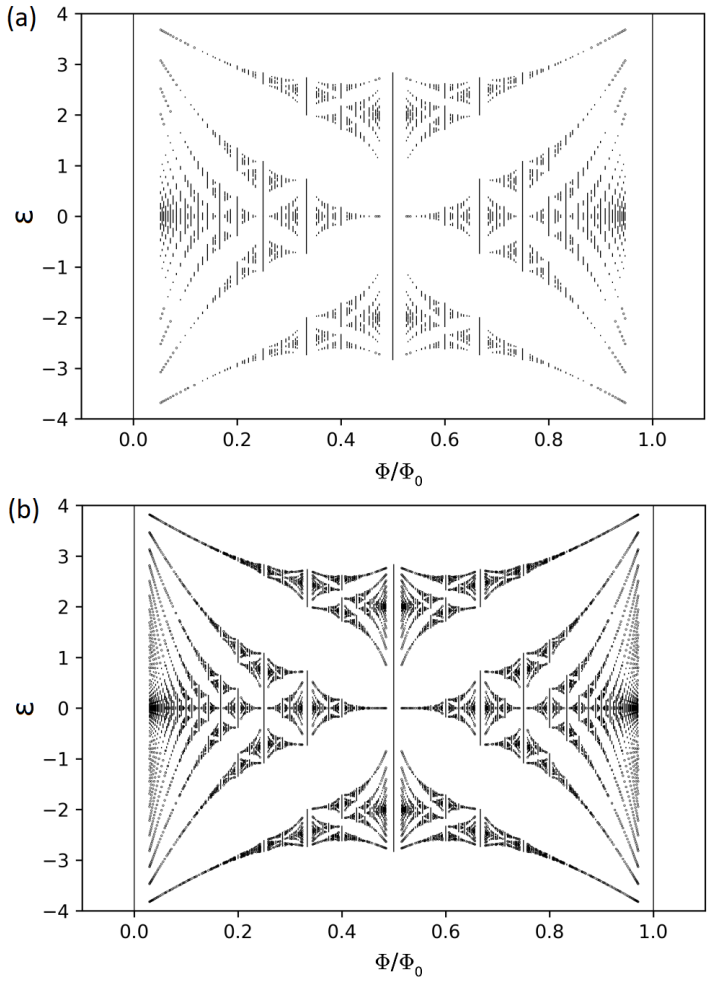

Figure C.1: Calculated Hofstadter butterfly with **(a)** $p_{max} = q_{max} = 20$ **(b)** $p_{max} = q_{max} = 35$.

BIBLIOGRAPHY

[1] P. R. Wallace, *The Band Theory of Graphite*, Phys. Rev. **71**, 622 (1947).

[2] K. S. Novoselov, A. K. Geim, S. Morozov, D. Jiang, M. Katsnelson, I. Grigorieva, S. V. Dubonos, and A. Firsov, *Two-Dimensional Gas of Massless Dirac Fermions in Graphene*, Nature **438**, 197 (2005).

[3] A. Sandner, T. Preis, C. Schell, P. Giudici, K. Watanabe, T. Taniguchi, D. Weiss, and J. Eroms, *Ballistic Transport in Graphene Antidot Lattices*, Nano Letters **15**, 8402 (2015).

[4] T. Pedersen, C. Flindt, J. Pedersen, N. Mortensen, A.-P. Jauho, and K. Pedersen, *Graphene Antidot Lattices: Designed Defects and Spin Qubits*, Physical Review Letters **100**, 136804 (2008).

[5] J. Pedersen and T. Pedersen, *Hofstadter butterflies and magnetically induced band gap quenching in graphene antidot lattices*, Physical Review B **87**, 235404 (2013).

[6] B. S. Jessen, L. Gammelgaard, M. R. Thomsen, D. M. A. Mackenzie, J. D. Thomsen, J. M. Caridad, E. Duegaard, K. Watanabe, T. Taniguchi, T. J. Booth, T. G. Pedersen, A.-P. Jauho, and P. Bøggild, *Lithographic band structure engineering of graphene*, Nature Nanotechnology **14**, 340 (2019).

[7] M. Drienovsky, A. Sandner, C. Baumgartner, M.-H. Liu, T. Taniguchi, K. Watanabe, K. Richter, D. Weiss, and J. Eroms, "Few-layer graphene patterned bottom gates for van der Waals heterostructures." arXiv:1703.05631 [cond-mat.mes-hall], (2017).

[8] B. Hunt, J. D. Sanchez-Yamagishi, A. F. Young, M. Yankowitz, B. J. LeRoy, K. Watanabe, T. Taniguchi, P. Moon, M. Koshino, P. Jarillo-Herrero, and R. C. Ashoori, *Massive Dirac Fermions and Hofstadter Butterfly in a van der Waals Heterostructure*, Science **340**, 1427 (2013).

[9] C. R. Dean, L. Wang, P. Maher, C. Forsythe, F. Ghahari, Y. Gao, J. Katoch, M. Ishigami, P. Moon, M. Koshino, T. Taniguchi, K. Watanabe, K. L. Shepard, J. Hone, and P. Kim, *Hofstadter's butterfly and the fractal quantum Hall effect in moiré superlattices*, Nature **497**, 598 (2013).

[10] L. A. Ponomarenko, R. V. Gorbachev, G. L. Yu, D. C. Elias, R. Jalil, A. A. Patel, A. Mishchenko, A. S. Mayorov, C. R. Woods, J. R. Wallbank, M. Mucha-Kruczynski, B. A. Piot, M. Potemski, I. V. Grigorieva, K. S. Novoselov, F. Guinea, V. I. Fal'ko, and A. K. Geim, *Cloning of Dirac fermions in graphene superlattices*, Nature **497**, 594 (2013).

[11] C. Forsythe, X. Zhou, K. Watanabe, T. Taniguchi, A. Pasupathy, P. Moon, M. Koshino, P. Kim, and C. R. Dean, *Band structure engineering of 2D materials using patterned dielectric superlattices*, Nature Nanotechnology **13**, 566 (2018).

[12] M. Drienovsky, J. Joachimsmeyer, A. Sandner, M.-H. Liu, T. Taniguchi, K. Watanabe, K. Richter, D. Weiss, and J. Eroms, *Commensurability Oscillations in One-Dimensional Graphene Superlattices*, Physical Review Letters **121**, 026806 (2018).

[13] R. Huber, M.-H. Liu, S.-C. Chen, M. Drienovsky, A. Sandner, K. Watanabe, T. Taniguchi, K. Richter, D. Weiss, and J. Eroms, *Gate-Tunable Two-Dimensional Superlattices in Graphene*, Nano Letters **20**, 8046 (2020).

[14] D. R. Hofstadter, *Energy levels and wave functions of Bloch electrons in rational and irrational magnetic fields*, Physical Review B **14**, 2239 (1976).

[15] R. Krishna Kumar, X. Chen, G. H. Auton, A. Mishchenko, D. A. Bandurin, S. V. Morozov, Y. Cao, E. Khestanova, M. Ben Shalom, A. V. Kretinin, K. S. Novoselov, L. Eaves, I. V. Grigorieva, L. A. Ponomarenko, V. I. Fal'ko, and A. K. Geim, *High-temperature quantum oscillations caused by recurring Bloch states in graphene superlattices*, Science **357**, 181 (2017).

[16] A. K. Geim and K. S. Novoselov, *The Rise of Graphene*, Nature Materials **6**, 183 (2007).

[17] A. K. Geim and A. H. MacDonald, *Graphene: Exploring carbon flatland*, Physics Today **60**, 35 (2007).

[18] M. Katsnelson, *Graphene: Carbon in Two Dimensions*, Materials Today **10**, 20 (2007).

[19] A. K. Geim, *Graphene: Status and Prospects*, Science **324**, 1530 (2009).

[20] M. Aliofkhazraei, N. Ali, W.I. Milne, C.S. Ozkan, S. Mitura, and J.L. Gervasoni, *Graphene Science Handbook, Six-Volume Set.* Taylor & Francis, (2016).

[21] A. H. Castro Neto, F. Guinea, N. M. R. Peres, K. S. Novoselov, and A. K. Geim, *The electronic properties of graphene*, Rev. Mod. Phys. **81**, 109 (2009).

[22] S. Das Sarma, S. Adam, E. H. Hwang, and E. Rossi, *Electronic transport in two-dimensional graphene*, Rev. Mod. Phys. **83**, 407 (2011).

[23] M. Lemme, *Current Status of Graphene Transistors*, Solid State Phenomena **156-158**, 499 (2009).

[24] S. Reich, J. Maultzsch, C. Thomsen, and P. Ordejón, *Tight-binding description of graphene*, Physical Review B **66**, 035412 (2002).

[25] T. Ihn, *Semiconductor Nanostructures Quantum States and Electronic Transport.* Oxford University Press, (2010).

[26] M. Goerbig; G. Montambaux, *Dirac Fermions in Condensed Matter and Beyond*, in *Dirac Matter*, B. Duplantier, V. Rivasseau, and J.-N. Fuchs, eds. Springer International Publishing, (2017).

[27] L.-A. Wu and M. Guidry, *The Ground State of Monolayer Graphene in a Strong Magnetic Field*, Scientific Reports **6**, 22423 (2015).

[28] S.-Y. Li, Y.-N. Ren, Y.-W. Liu, M.-X. Chen, H. Jiang, and L. He, "Detecting degeneracy and subtle broken-symmetry states of graphene at nanoscale." arXiv:1806.08882 [cond-mat.mes-hall], (2018).

[29] F. Chiappini, S. Wiedmann, K. S. Novoselov, A. Mishchenko, A. K. Geim, J. C. Maan, and U. Zeitler, *Lifting of the Landau level degeneracy in graphene devices in a tilted magnetic field*, Physical Review B **92**, 201412 (2015).

[30] A. F. Young, C. R. Dean, L. Wang, H. Ren, P. Cadden-Zimansky, K. Watanabe, T. Taniguchi, J. Hone, K. L. Shepard, and P. Kim, *Spin and valley quantum Hall ferromagnetism in graphene*, Nature Physics **8**, 550 (2012).

[31] Y. Barlas, K. Yang, and A. H. MacDonald, *Quantum Hall effects in graphene-based two-dimensional electron systems*, Nanotechnology **23**, 052001 (2012).

[32] B. Roy, M. Kennett, and S. Das Sarma, *Chiral Symmetry Breaking and the Quantum Hall Effect in Monolayer Graphene*, Physical Review B **90**, 201409 (2014).

[33] L. Du, T. Hasan, A. Castellanos-Gomez, G.-B. Liu, Y. Yao, C. N. Lau, and Z. Sun, "Engineering symmetry breaking in two-dimensional layered materials." arXiv:2011.09255 [cond-mat.mes-hall], (2020).

[34] V. Ariel and A. Natan, "Electron Effective Mass in Graphene." arXiv:1206.6100 [physics.gen-ph], (2012).

[35] Y. Zhang, Y.-W. Tan, H. L. Stormer, and P. Kim, *Experimental observation of the quantum Hall effect and Berry's phase in graphene*, Nature **438**, 201 (2005).

[36] M. Katsnelson, K. Novoselov, and A. K. Geim, *Chiral tunneling and the Klein paradox in graphene*, Nature Physics **2**, 620 (2006).

[37] D. Cooper, B. D'Anjou, N. Ghattamaneni, B. Harack, M. Hilke, A. Horth, N. Majlis, M. Massicotte, L. Vandsburger, E. Whiteway, and V. Yu, *Experimental Review of Graphene*, ISRN Condens. Matter Phys. **2012**, 501686 (2011).

[38] N. Ashcroft, N. Mermin, and D. Wei, *Solid State Physics: Revised Edition.* Cengage Learning Asia, (2016).

[39] C. W. J. Beenakker and H. Houten, *Quantum Transport in Semiconductor Nanostructures*, Solid State Phys. **44**, 1 (1991).

[40] R. Gross and A. Marx, *Festkörperphysik.* De Gruyter Oldenbourg, (2014).

[41] S. Datta, *Electronic Transport in Mesoscopic Systems.* Cambridge Studies in Semiconductor Physics and Microelectronic Engineering. Cambridge University Press, (1995).

[42] D. Tong, "Lectures on the Quantum Hall Effect." arXiv:1606.06687 [hep-th], (2016).

[43] D. Weiss, *Kommensurabilitätseffekte in lateralen Übergittern*, Habilitation thesis, Max Planck Institute for Solid State Research, Stuttgart (1992).

[44] K. I. Bolotin, *9 - Electronic transport in graphene: towards high mobility*, in *Graphene*, V. Skákalová and A. B. Kaiser, eds. Woodhead Publishing, (2014).

[45] E. Hwang and S. Das Sarma, *Acoustic phonon scattering limited carrier mobility in two-dimensional extrinsic graphene*, Physical Review B **77**, 115449 (2008).

[46] S. Morozov, K. Novoselov, M. Katsnelson, F. Schedin, D. Cunha Elias, J. Jaszczak, and A. K. Geim, *Giant Intrinsic Carrier Mobilities in Graphene and Its Bilayer*, Physical Review Letters **100**, 016602 (2008).

[47] K. Bolotin, K. J. Sikes, Z. Jiang, M. Klima, G. Fudenberg, J. Hone, P. Kim, and H. L. Stormer, *Ultrahigh Electron Mobility in Suspended Graphene*, Solid State Communications **146**, 351 (2008).

[48] X. Du, I. Skachko, A. Barker, and E. Y. Andrei, *Approaching ballistic transport in suspended graphene.*, Nature Nanotechnology **3**, 491 (2008).

[49] C. R. Dean, A. Young, I. Meric, C. Lee, L. Wang, S. Sorgenfrei, K. Watanabe, T. Taniguchi, P. Kim, K. Shepard, and J. Hone, *Boron Nitride Substrates for High-Quality Graphene Electronics*, Nature Nanotechnology **5**, 722 (2010).

[50] L. Wang, I. Meric, P. Y. Huang, Q. Gao, Y. Gao, H. Tran, T. Taniguchi, K. Watanabe, L. M. Campos, D. A. Muller, J. Guo, P. Kim, J. Hone, K. L. Shepard, and C. R. Dean, *One-Dimensional Electrical Contact to a Two-Dimensional Material*, Science **342**, 614 (2013).

[51] S. Fratini and F. Guinea, *Substrate limited electron dynamics in graphene*, Physical Review B **77**, 195415 (2007).

[52] J.-H. Chen, C. Jang, S. Xiao, M. Ishigami, and M. Fuhrer, *Intrinsic and extrinsic performance limits of graphene devices on SiO_2*, Nature Nanotechnology **3**, 206 (2008).

[53] J. Schiefele, F. Sols, and F. Guinea, *Temperature dependence of the conductivity of graphene on boron nitride*, Physical Review B **85**, 195420 (2012).

[54] L. Banszerus, T. Sohier, A. Epping, F. Winkler, F. Libisch, F. Haupt, K. Watanabe, T. Taniguchi, K. Müller-Caspary, N. Marzari, F. Mauri, B. Beschoten, and C. Stampfer, "Extraordinary high room-temperature carrier mobility in graphene-WSe_2 heterostructures." arXiv:1909.09523 [cond-mat.mes-hall], (2019).

[55] T. Stauber, N. M. R. Peres, and F. Guinea, *Electronic transport in graphene: A semiclassical approach including midgap states*, Physical Review B **76**, 205423 (2007).

[56] V. M. Galitski, S. Adam, and S. Das Sarma, *Statistics of random voltage fluctuations and the low-density residual conductivity of graphene*, Physical Review B **76**, 245405 (2007).

[57] J. Martin, N. Akerman, G. Ulbricht, T. Lohmann, J. Smet, K. von Klitzing, and A. Yacoby, *Observation of Electron-Hole Puddles in Graphene Using a Scanning Single Electron Transistor*, Nature Physics **4**, 144 (2007).

[58] J. Xue, J. Sanchez-Yamagishi, D. Bulmash, P. Jacquod, A. Deshpande, K. Watanabe, T. Taniguchi, P. Jarillo-Herrero, and B. LeRoy, *Scanning tunnelling microscopy and spectroscopy of ultra-flat graphene on hexagonal boron nitride*, Nature Materials **10**, 282 (2011).

[59] S. Adam, E. H. Hwang, V. M. Galitski, and S. Das Sarma, *A self-consistent theory for graphene transport*, Proceedings of the National Academy of Sciences **104**, 18392 (2007).

[60] S. Adam, E. H. Hwang, and S. Das Sarma, *Scattering mechanisms and Boltzmann transport in graphene*, Physica E: Low-dimensional Systems and Nanostructures **40**, 1022 (2007).

[61] S. Adam, E. H. Hwang, E. Rossi, and S. Das Sarma, *Theory of charged impurity scattering in two-dimensional graphene*, Solid State Communications **149**, 1072 (2009).

[62] Y.-W. Tan, Y. Zhang, K. Bolotin, Y. Zhao, S. Adam, E. H. Hwang, S. Das Sarma, H. L. Stormer, and P. Kim, *Measurement of Scattering Rate and Minimum Conductivity in Graphene*, Physical Review Letters **99**, 246803 (2007).

[63] H. van Houten, B. J. van Wees, and C. W. J. Beenakker, *Quantum and Classical Ballistic Transport in Constricted Two-Dimensional Electron Gases*, in *Physics and Technology of Submicron Structures*, H. Heinrich, G. Bauer, and F. Kuchar, eds. Springer, (1988).

[64] R. Waser, ed., *Nanotechnology. Volume 3: Information Technology I.* Wiley-VCH, (2008).

[65] B. Terrés, L. Chizhova, F. Libisch, J. Peiro, D. Jörger, S. Engels, A. Girschik, K. Watanabe, T. Taniguchi, S. Rotkin, J. Burgdörfer, and C. Stampfer, *Size quantization of Dirac fermions in graphene constrictions*, Nature Communications **7**, 11528 (2016).

[66] E. McCann, K. Kechedzhi, V. I. Fal'ko, H. Suzuura, T. Ando, and B. L. Altshuler, *Weak-Localization Magnetoresistance and Valley Symmetry in Graphene*, Physical Review Letters **97**, 146805 (2006).

[67] M. Y. Kharitonov and K. B. Efetov, *Universal conductance fluctuations in graphene*, Physical Review B **78**, 033404 (2008).

[68] S. Somanchi, B. Terrés, J. Peiro, M. Staggenborg, K. Watanabe, T. Taniguchi, B. Beschoten, and C. Stampfer, *From Diffusive to Ballistic Transport in Etched Graphene Constrictions and Nanoribbons*, Annalen der Physik **529**, 1700082 (2017).

[69] P. Kun, B. Fülöp, G. Dobrik, P. Nemes-Incze, I. E. Lukács, S. Csonka, C. Hwang, and L. Tapasztó, *Robust quantum point contact operation of narrow graphene constrictions patterned by AFM cleavage lithography*, npj 2D Materials and Applications **4**, 43 (2020).

[70] R. Krishna Kumar, D. Bandurin, F. Pellegrino, Y. Cao, A. Principi, H. Guo, G. Auton, M. Ben Shalom, L. Ponomarenko, G. Falkovich, I. Grigorieva, L. Levitov, M. Polini, and A. K. Geim, *Super-ballistic flow of viscous electron fluid through graphene constrictions*, Nature Physics **13**, 1182 (2017).

[71] B. Narozhny, I. Gornyi, A. Mirlin, and J. Schmalian, *Hydrodynamic Approach to Electronic Transport in Graphene*, Annalen der Physik **529**, 1700043 (2017).

[72] K. S. Novoselov, A. K. Geim, S. V. Morozov, D. Jiang, Y. Zhang, S. V. Dubonos, I. V. Grigorieva, and A. A. Firsov, *Electric Field Effect in Atomically Thin Carbon Films*, Science **306**, 666 (2004).

[73] M. Goerbig, "Quantum Hall Effects." arXiv:0909.1998 [cond-mat.mes-hall], (2009).

[74] M.-H. Liu, *Theory of carrier density in multigated doped graphene sheets with quantum correction*, Physical Review B **87**, 125427 (2013).

[75] M. Katsnelson, *Zitterbewegung, chirality, and minimal conductivity in graphene*, The European Physical Journal B **51**, 157 (2006).

[76] J. Tworzydło, B. Trauzettel, M. Titov, A. Rycerz, and C. W. J. Beenakker, *Sub-Poissonian Shot Noise in Graphene*, Physical Review Letters **96**, 246802 (2006).

[77] Y. Sui, T. Low, M. Lundstrom, and J. Appenzeller, *Signatures of Disorder in the Minimum Conductivity of Graphene*, Nano Letters **11**, 1319 (2011).

[78] K. Ziegler, *Minimal conductivity of graphene: Nonuniversal values from the Kubo formula*, Physical Review B **75**, 233407 (2007).

[79] K. von Klitzing, G. Dorda, and M. Pepper, *New Method for High-Accuracy Determination of the Fine-Structure Constant Based on Quantized Hall Resistance*, Physical Review Letters **45**, 494 (1980).

[80] K. von Klitzing, *The quantized Hall effect*, Rev. Mod. Phys. **58**, 519 (1986).

[81] B. Douçot, V. Pasquier, B. Duplantier, and V. Rivasseau, eds., *The Quantum Hall Effect*. Birkhäuser, (2005).

[82] M. Goerbig, *Electronic Properties of Graphene in a Strong Magnetic Field*, Reviews of Modern Physics **83**, 1193 (2010).

[83] K. S. Novoselov, Z. Jiang, Y. Zhang, S. V. Morozov, H. L. Stormer, U. Zeitler, J. C. Maan, G. S. Boebinger, P. Kim, and A. K. Geim, *Room-Temperature Quantum Hall Effect in Graphene*, Science **315**, 1379 (2007).

[84] A. Matulis and F. Peeters, *Appearance of enhanced Weiss oscillations in graphene: Theory*, Physical Review B **75**, 125429 (2007).

[85] M. Goerbig, *The quantum Hall effect in graphene – a theoretical perspective*, Comptes Rendus Physique **12**, 369 (2011).

[86] F. Fei, S. Zhang, M. Zhang, S. A. Shah, F. Song, X. Wang, and B. Wang, *The Material Efforts for Quantized Hall Devices Based on Topological Insulators*, Advanced Materials **32**, 1904593 (2019).

[87] B. Jeckelmann and B. Jeanneret, *The quantum Hall effect as an electrical resistance standard*, Rep. Prog. Phys **64**, 1603 (2001).

[88] P. Kühne, V. Darakchieva, and M. Schubert, "Landau Level optical Hall effect spectroscopy on two- and three-dimensional layered materials with graphene and graphite as examples." arXiv:1705.08398 [cond-mat.mtrl-sci], (2017).

[89] T. J. B. M. Janssen, A. Tzalenchuk, S. Lara-Avila, S. Kubatkin, and V. I. Fal'ko, *Quantum resistance metrology using graphene*, Reports on Progress in Physics **76**, 104501 (2013).

[90] T. Ando, A. B. Fowler, and F. Stern, *Electronic properties of two-dimensional systems*, Rev. Mod. Phys. **54**, 437 (1982).

[91] B. I. Halperin, *Quantized Hall conductance, current-carrying edge states, and the existence of extended states in a two-dimensional disordered potential*, Physical Review B **25**, 2185 (1982).

[92] M. Büttiker, *Absence of backscattering in the quantum Hall effect in multiprobe conductors*, Physical Review B **38**, 9375 (1988).

[93] D. K. Ferry, *The quantum Hall effect*, in *Transport in Semiconductor Mesoscopic Devices*, 2053-2563. IOP Publishing, (2015).

[94] V. Morandi and L. Ottaviano, eds., *GraphITA. Carbon Nanostructures*. Springer, (2017).

[95] J. W. Rhim and K. Park, *Self-similar occurrence of massless Dirac particles in graphene under magnetic field*, Physical Review B **86**, 235411 (2012).

[96] S. Sarkar, K. R. Amin, R. Modak, A. Singh, S. Mukerjee, and A. Bid, *Role of different scattering mechanisms on the temperature dependence of transport in graphene.*, Scientific Reports **5**, 16772 (2015).

[97] W. Zhu, V. Perebeinos, M. Freitag, and P. Avouris, *Carrier scattering, mobilities, and electrostatic potential in monolayer, bilayer, and trilayer graphene*, Physical Review B **80**, 235402 (2009).

[98] M. Yankowitz, Q. Ma, P. Jarillo-Herrero, and B. LeRoy, *van der Waals heterostructures combining graphene and hexagonal boron nitride*, Nature Reviews Physics **1**, 112 (2019).

[99] K. K. Kim, S. M. Kim, and Y. H. Lee, *A new horizon for hexagonal boron nitride film*, Journal of the Korean Physical Society **64**, 1605 (2014).

[100] R. Decker, Y. Wang, V. Brar, W. Regan, H.-Z. Tsai, Q. Wu, W. Gannett, A. Zettl, and M. Crommie, *Local Electronic Properties of Graphene on a BN Substrate via Scanning Tunneling Microscopy*, Nano Letters **11**, 2291 (2011).

[101] R. T. Weitz and A. Yacoby, *Graphene rests easy*, Nature Nanotechnology **5**, 699 (2010).

[102] J. Wang, F. Ma, and M. Sun, *Graphene, hexagonal boron nitride, and heterostructure: properties and applications*, RSC Advances **7**, 16801 (2017).

[103] K. Nagashio, T. Yamashita, T. Nishimura, K. Kita, and A. Toriumi, *Electrical transport properties of graphene on SiO_2 with specific surface structures*, Journal of Applied Physics **110**, 024513 (2011).

[104] A. S. Mayorov, R. V. Gorbachev, S. V. Morozov, L. Britnell, R. Jalil, L. A. Ponomarenko, P. Blake, K. S. Novoselov, K. Watanabe, T. Taniguchi, and A. K. Geim, *Micrometer-Scale Ballistic Transport in Encapsulated Graphene at Room Temperature*, Nano Letters **11**, 2396 (2011).

[105] D. Purdie, N. Pugno, T. Taniguchi, K. Watanabe, A. Ferrari, and A. Lombardo, *Cleaning Interfaces in Layered Materials Heterostructures*, Nature Communications **9**, 5387 (2018).

[106] L. Banszerus, M. Schmitz, S. Engels, M. Goldsche, K. Watanabe, T. Taniguchi, B. Beschoten, and C. Stampfer, *Ballistic Transport Exceeding 28 μm in CVD Grown Graphene*, Nano Letters **16**, 1387 (2016).

[107] A. K. Geim and I. Grigorieva, *Van der Waals heterostructures*, Nature **499**, 419 (2013).

[108] R. Frisenda, Y. Niu, P. Gant, M. Muñoz, and A. Castellanos-Gomez, *Naturally occurring van der Waals materials*, npj 2D Materials and Applications **4**, 38 (2020).

[109] V. Sangwan and M. Hersam, *Electronic Transport in Two-Dimensional Materials*, Annual Review of Physical Chemistry **69**, 299 (2018).

[110] T. S. Ghiasi, A. A. Kaverzin, P. J. Blah, and B. J. van Wees, *Charge-to-Spin Conversion by the Rashba-Edelstein Effect in Two-Dimensional van der Waals Heterostructures up to Room Temperature*, Nano Letters **19**, 5959 (2019).

[111] S. Omar and B. J. van Wees, *Spin transport in high-mobility graphene on WS_2 substrate with electric-field tunable proximity spin-orbit interaction*, Physical Review B **97**, 045414 (2018).

[112] T. Völkl, T. Rockinger, M. Drienovsky, K. Watanabe, T. Taniguchi, D. Weiss, and J. Eroms, *Magnetotransport in heterostructures of transition metal dichalcogenides and graphene*, Physical Review B **96**, 125405 (2017).

[113] Z. Wang, D.-K. Ki, J. Y. Khoo, D. Mauro, H. Berger, L. S. Levitov, and A. F. Morpurgo, *Origin and Magnitude of 'Designer' Spin-Orbit Interaction in Graphene on Semiconducting Transition Metal Dichalcogenides*, Physical Review X **6**, 041020 (2016).

[114] K. Bogdan, A. W. Cummings, K. Zollner, M. Vila, D. Khokhriakov, A. M. Hoque, A. Dankert, P. Svedlindh, J. Fabian, S. Roche, and S. P. Dash, *Magnetic proximity in a van der Waals heterostructure of magnetic insulator and graphene*, 2D Materials **7**, 015026 (2019).

[115] M.-C. Wang, C.-C. Huang, C.-H. Cheung, C.-Y. Chen, S. G. Tan, T.-W. Huang, Y. Zhao, Y. Zhao, G. Wu, Y.-P. Feng, H.-C. Wu, and C.-R. Chang, *Prospects and Opportunities of 2D van der Waals Magnetic Systems*, Annalen der Physik **532**, 1900452 (2020).

[116] Y. Cao, V. Fatemi, A. Demir, S. Fang, S. L. Tomarken, J. Y. Luo, J. D. Sanchez-Yamagishi, K. Watanabe, T. Taniguchi, E. Kaxiras, R. C. Ashoori, and P. Jarillo-Herrero, *Correlated insulator behaviour at half-filling in magic-angle graphene superlattices*, Nature **556**, 80 (2018).

[117] Y. Cao, V. Fatemi, S. Fang, K. Watanabe, T. Taniguchi, E. Kaxiras, and P. Jarillo-Herrero, *Unconventional superconductivity in magic-angle graphene superlattices*, Nature **556**, 43 (2018).

[118] A. L. Sharpe, E. J. Fox, A. W. Barnard, J. Finney, K. Watanabe, T. Taniguchi, M. A. Kastner, and D. Goldhaber-Gordon, *Emergent ferromagnetism near three-quarters filling in twisted bilayer graphene*, Science **365**, 605 (2019).

[119] A. Ferrari, F. Bonaccorso, V. Fal'ko, K. Novoselov, S. Roche, P. Bøggild, S. Borini, F. Koppens, V. Palermo, N. Pugno, J. Garrido, R. Sordan, A. Bianco, L. Ballerini, M. Prato, E. Lidorikis, J. Kivioja, C. Marinelli, T. Ryhänen, and J. Kinaret, *Science and Technology Roadmap for Graphene, Related Two-Dimensional Crystals, and Hybrid Systems*, Nanoscale **7**, 4598 (2014).

[120] N. Briggs, S. Subramanian, Z. Lin, X. Li, X. Zhang, K. Zhang, K. Xiao, D. Geohegan, R. Wallace, L.-Q. Chen, M. Terrones, A. Ebrahimi, S. Das, J. Redwing, C. Hinkle, K. Momeni, A. van Duin, V. Crespi, S. Kar, and J. A. Robinson, *A roadmap for electronic grade 2D materials*, 2D Materials **6**, 022001 (2019).

[121] S. Pezzini, V. Mišeikis, S. Pace, F. Rossella, K. Watanabe, T. Taniguchi, and C. Coletti, *High-quality electrical transport using scalable CVD graphene*, 2D Materials **7**, 041003 (2020).

[122] W. Yang, G. Chen, Z. Shi, C. Liu, L. Zhang, G. Xie, M. Cheng, D. Wang, R. Yang, D.-X. Shi, K. Watanabe, T. Taniguchi, Y. Yao, Y. Zhang, and G. Zhang, *Epitaxial growth of single-domain graphene on hexagonal boron nitride*, Nature Materials **12**, 792 (2013).

[123] Y. Qian, H. Van Ngoc, and D. J. Kang, *Growth of Graphene/h-BN Heterostructures on Recyclable Pt Foils by One-Batch Chemical Vapor Deposition*, Scientific Reports **7**, 17083 (2017).

[124] A. Davies, J. Albar, A. Summerfield, J. Thomas, T. Cheng, V. Korolkov, E. Stapleton, J. Wrigley, N. Goodey, C. Mellor, A. Khlobystov, K. Watanabe, T. Taniguchi, T. Foxon, L. Eaves, S. Novikov, and P. Beton, *Lattice-Matched Epitaxial Graphene Grown on Boron Nitride*, Nano Letters **18**, 498 (2017).

[125] H. Wang, F. Liu, Z. Fang, W. Zhou, and Z. Liu, *Two-dimensional heterostructures: Fabrication, characterization, and application*, Nanoscale **6**, 12250 (2014).

[126] A. Zavabeti, A. Jannat, L. Zhong, A. A. Haidry, Z. Yao, and J. Z. Ou, *Two-Dimensional Materials in Large-Areas: Synthesis, Properties and Applications*, Nano-Micro Letters **12**, 66 (2020).

[127] S. Das, J. A. Robinson, M. Dubey, H. Terrones, and M. Terrones, *Beyond Graphene: Progress in Novel Two-Dimensional Materials and van der Waals Solids*, Annual Review of Materials Research **45**, 1 (2015).

[128] D. Geng and H. Y. Yang, *Recent Advances in Growth of Novel 2D Materials: Beyond Graphene and Transition Metal Dichalcogenides*, Advanced Materials **30**, 1800865 (2018).

[129] I. V. Sankar, J. Jeon, S. K. Jang, J. H. Cho, E. Hwang, and S. Lee, *Heterogeneous Integration of 2D Materials: Recent Advances in Fabrication and Functional Device Applications*, Nano **14**, 1930009 (2019).

[130] K. Khan, A. K. Tareen, M. Aslam, R. Wang, Y. Zhang, A. Mahmood, Z. Ouyang, H. Zhang, and Z. Guo, *Recent developments in emerging two-dimensional materials and their applications*, J. Mater. Chem. C **8**, 387 (2020).

[131] M. G. Stanford, P. D. Rack, and D. Jariwala, *Emerging nanofabrication and quantum confinement techniques for 2D materials beyond graphene*, npj 2D Materials and Applications **2**, 20 (2018).

[132] N.-C. Yeh, C.-C. Hsu, J. Bagley, and W.-S. Tseng, *Single-step growth of graphene and graphene-based nanostructures by plasma-enhanced chemical vapor deposition*, Nanotechnology **30**, 162001 (2019).

[133] F. Bonaccorso, Z. Sun, T. Hasan, and A. C. Ferrari, *Graphene photonics and optoelectronics*, Nature Photonics **4**, 611 (2010).

[134] J. Cheng, C. Wang, X. Zou, and L. Liao, *Recent Advances in Optoelectronic Devices Based on 2D Materials and Their Heterostructures*, Advanced Optical Materials **7**, 1800441 (2019).

[135] B. H. Nguyen and V. H. Nguyen, *Advances in graphene-based optoelectronics, plasmonics and photonics*, Advances in Natural Sciences: Nanoscience and Nanotechnology **7**, 013002 (2016).

[136] W. Han, R. K. Kawakami, M. Gmitra, and J. Fabian, *Graphene spintronics*, Nature Nanotechnology **9**, 794 (2014).

[137] N. Kheirabadi, A. Shafiekhani, and M. Fathipour, *Review on graphene spintronic, new land for discovery*, Superlattices and Microstructures **74**, 123 (2014).

[138] A. Avsar, H. Ochoa, F. Guinea, B. Ozyilmaz, B.J. van Wees, and I.J. Vera-Marun, "Colloquium: Spintronics in graphene and other two-dimensional materials." arXiv:1909.09188 [cond-mat.mes-hall], (2019).

[139] J. R. Schaibley, H. Yu, G. Clark, P. Rivera, J. S. Ross, K. L. Seyler, W. Yao, and X. Xu, *Valleytronics in 2D materials*, Nature Reviews Materials **1**, 16055 (2016).

[140] J. H. J. Martiny, K. Kaasbjerg, and A.-P. Jauho, *Tunable valley Hall effect in gate-defined graphene superlattices*, Physical Review B **100**, 155414 (2019).

[141] C. Si, Z. Sun, and F. Liu, *Strain engineering of graphene: a review*, Nanoscale **8**, 3207 (2016).

[142] Z. Peng, X. Chen, Y. Fan, D. J. Srolovitz, and D. Lei, *Strain engineering of 2D semiconductors and graphene: from strain fields to band-structure tuning and photonic applications*, Light: Science & Applications **9**, 190 (2020).

[143] S. Carr, D. Massatt, S. Fang, P. Cazeaux, M. Luskin, and E. Kaxiras, *Twistronics: Manipulating the electronic properties of two-dimensional layered structures through their twist angle*, Physical Review B **95**, 075420 (2017).

[144] Y.-N. Ren, Y. Zhang, Y.-W. Liu, and L. He, "Twistronics in graphene-based van der Waals structures." arXiv:2008.09769 [cond-mat.mtrl-sci], (2020).

[145] Y. Yang, J. Li, J. Yin, S. Xu, C. Mullan, T. Taniguchi, K. Watanabe, A. K. Geim, K. S. Novoselov, and A. Mishchenko, *In situ manipulation of van der Waals heterostructures for twistronics*, Science Advances **6**, eabd3655 (2020).

[146] E. Y. Andrei and A. H. MacDonald, *Graphene bilayers with a twist*, Nature Materials **19**, 1265 (2020).

[147] Z. Hennighausen and S. Kar, "Twistronics: A turning point in 2D quantum materials." arXiv:2101.04501 [cond-mat.mes-hall], (2021).

[148] L. Esaki and R. Tsu, *Superlattice and Negative Differential Conductivity in Semiconductors*, IBM Journal of Research and Development **14**, 61 (1970).

[149] J. M. Chamberlain, L. Eaves, and J. C. Portal, eds., *Electronic Properties of Multilayers and Low-Dimensional Semiconductor Structures*. Springer, (1990).

[150] M. Killi, S. Wu, and A. Paramekanti, *Graphene: Kinks, Superlattices, Landau levels, and Magnetotransport*, International Journal of Modern Physics B **26**, 1242007 (2012).

[151] C.-H. Park, L. Yang, Y.-W. Son, M. L. Cohen, and S. G. Louie, *New Generation of Massless Dirac Fermions in Graphene under External Periodic Potentials*, Physical Review Letters **101**, 126804 (2008).

[152] Y. Li, S. Dietrich, C. Forsythe, T. Taniguchi, K. Watanabe, and P. Moon, "Anisotropic band flattening in graphene with 1D superlattices." arXiv:2006.08868 [cond-mat.mes-hall], (2020).

[153] C.-H. Park, L. Yang, Y.-W. Son, M. L. Cohen, and S. G. Louie, *Anisotropic behaviours of massless Dirac fermions in graphene under periodic potentials*, Nature Physics **4**, 213 (2008).

[154] C.-H. Park, Y.-W. Son, L. Yang, M. L. Cohen, and S. G. Louie, *Landau Levels and Quantum Hall Effect in Graphene Superlattices*, Physical Review Letters **103**, 046808 (2009).

[155] W.-H. Kang, S.-C. Chen, and M.-H. Liu, *Cloning of zero modes in one-dimensional graphene superlattices*, Physical Review B **102**, 195432 (2020).

[156] M. Yankowitz, J. Xue, D. Cormode, J. D. Sanchez-Yamagishi, K. Watanabe, T. Taniguchi, P. Jarillo-Herrero, P. Jacquod, and B. J. LeRoy, *Emergence of superlattice Dirac points in graphene on hexagonal boron nitride*, Nature Physics **8**, 382 (2012).

[157] Y. Du, N. Xu, X. Lin, and A.-P. Jauho, "Moiré effects in graphene–hBN heterostructures." arXiv:2011.13014 [cond-mat.mes-hall], (2020).

[158] M. Drienovsky, *Übergittereffekte in eindimensional moduliertem Graphen*. PhD thesis, University of Regensburg, (2018).

[159] A. Sandner, *High-mobility graphene in 2D periodic potentials*. PhD thesis, University of Regensburg, (2017).

[160] C. Forsythe, *Fractal Hofstadter Band Structure in Patterned Dielectric Superlattice Graphene Systems*. PhD thesis, Columbia University in the City of New York, New York City, (2017).

[161] D. Weiss, K. von Klitzing, K. Ploog, and G. Weimann, *Magnetoresistance Oscillations in a Two-Dimensional Electron Gas Induced by a Submicrometer Periodic Potential*, Europhysics Letters **8**, 179 (1989).

[162] R. Winkler, J. Kotthaus, and K. Ploog, *Landau band conductivity in a two-dimensional electron system modulated by an artificial one-dimensional superlattice potential*, Physical Review Letters **62**, 1177 (1989).

[163] D. Weiss, K. von Klitzing, K. Ploog, and G. Weimann, *Landau level broadening and Van Hove singularities in lateral surface superlattices*, Surface Science **229**, 88 (1990).

[164] M. Tahir, K. Sabeeh, and A. MacKinnon, *Weiss oscillations in the electronic structure of modulated graphene*, Journal of Physics: Condensed Matter **19**, 406226 (2007).

[165] S. Janecek, M. Aichinger, and E. R. Hernández, *Two-dimensional Bloch electrons in perpendicular magnetic fields: An exact calculation of the Hofstadter butterfly spectrum*, Physical Review B **87**, 235429 (2013).

[166] D. Langbein, *The Tight-Binding and the Nearly-Free-Electron Approach to Lattice Electrons in External Magnetic Fields*, Phys. Rev. **180**, 633 (1969).

[167] G. H. Wannier, *A Result Not Dependent on Rationality for Bloch Electrons in a Magnetic Field*, physica status solidi (b) **88**, 757 (1978).

[168] M. C. Geisler, *The Hofstadter Butterfly and Quantum Interferences in Modulated 2-Dimensional Electron Systems*. PhD thesis, Max Planck Institute for Solid State Research, Stuttgart, (2005).

[169] U. Rössler and M. Suhrke, *Bloch electrons in a magnetic field: Hofstadter's butterfly*, Advances in Solid State Physics **40**, 35 (2000).

[170] F. H. Claro and G. H. Wannier, *Magnetic subband structure of electrons in hexagonal lattices*, Physical Review B **19**, 6068 (1979).

[171] A. H. MacDonald, *Landau-level subband structure of electrons on a square lattice*, Physical Review B **28**, 6713 (1983).

[172] D. Pfannkuche and R. R. Gerhardts, *Theory of magnetotransport in two-dimensional electron systems subjected to weak two-dimensional superlattice potentials*, Physical Review B **46**, 12606 (1992).

[173] P. G. Harper, *The General Motion of Conduction Electrons in a Uniform Magnetic Field, with Application to the Diamagnetism of Metals*, Proceedings of the Physical Society. Section A **68**, 879 (1955).

[174] M.-N. Steffen, *Hofstadter Butterfly in Graphene*, Bachelor thesis, University of Hamburg (2020).

[175] M.C. Geisler, J.H. Smet, V. Umansky, K. von Klitzing, B. Naundorf, R. Ketzmerick, and H. Schweizer, *Detection of a Landau Band-Coupling-Induced Rearrangement of the Hofstadter Butterfly*, Physical Review Letters **92**, 256801 (2004).

[176] J. Eroms, *University of Regensburg, Regensburg, Germany*, personal communication (2020).

[177] C. Albrecht, K. von Klitzing, H. Schweizer, J. Smet, V. Umansky, and D. Weiss, *Evidence of Hofstadter's Fractal Energy Spectrum in the Quantized Hall Conductance*, Physical Review Letters **86**, 147 (2001).

[178] G. G. Naumis, *Topological map of the Hofstadter butterfly: Fine structure of Chern numbers and Van Hove singularities*, Physics Letters A **380**, 1772 (2016).

[179] I. I. Satija and D. R. Hofstadter, *Butterfly in the quantum world the story of the most fascinating quantum fractal.* IOP Concise Physics, (2016).

[180] D. J. Thouless, M. Kohmoto, M. P. Nightingale, and M. den Nijs, *Quantized Hall Conductance in a Two-Dimensional Periodic Potential*, Physical Review Letters **49**, 405 (1982).

[181] Y.-S. Wu and D. Thouless, *Quantized Hall conductance as a topological invariant*, Physical Review B **31**, 3372 (1985).

[182] H. Aoki and T. Ando, *Universality of quantum Hall effect: Topological invariant and observable*, Physical Review Letters **57**, 3093 (1986).

[183] P. Streda, *Quantised Hall effect in a two-dimensional periodic potential*, Journal of Physics C: Solid State Physics **15**, L1299 (1982).

[184] I. I. Satija, *A tale of two fractals: The Hofstadter butterfly and the integral Apollonian gaskets*, The European Physical Journal Special Topics **225**, 2533 (2016).

[185] B. Huckestein and R.N. Bhatt, *Influence of a periodic potential on the integer quantum Hall effect*, Surface Science **305**, 438 (1994).

[186] R. R. Gerhardts, D. Weiss, and U. Wulf, *Magnetoresistance oscillations in a grid potential: Indication of a Hofstadter-type energy spectrum*, Physical Review B **43**, 5192 (1991).

[187] K. Ensslin and T. Schlösser, *Experimental observation of an artificial band structure in lateral superlattices*, Physica Scripta **T69**, 26 (1997).

[188] D. Weiss, A. Menschig, K. von Klitzing, and G. Weimann, *Magnetoresistance in a grid-type lateral superlattice: the role of disorder*, Surface Science **263**, 314 (1992).

[189] E. Brown, *Bloch Electrons in a Uniform Magnetic Field*, Phys. Rev. **133**, A1038 (1964).

[190] J. Zak, *Magnetic Translation Group*, Phys. Rev. **134**, A1602 (1964).

[191] R. Krishna Kumar, A. Mishchenko, X. Chen, S. Pezzini, G. H. Auton, L. A. Ponomarenko, U. Zeitler, L. Eaves, V. I. Fal'ko, and A. K. Geim, *High-order fractal states in graphene superlattices*, Proceedings of the National Academy of Sciences **115**, 5135 (2018).

[192] Y. Zhang, T.-T. Tang, C. Girit, Z. Hao, M. C. Martin, A. Zettl, M. F. Crommie, Y. R. Shen, and F. Wang, *Direct observation of a widely tunable bandgap in bilayer graphene*, Nature **459**, 820 (2009).

[193] R. Skomski, P. A. Dowben, M. Sky Driver, and Jeffry A. Kelber, *Sublattice-induced symmetry breaking and band-gap formation in graphene*, Mater. Horiz. **1**, 563 (2014).

[194] E. Cappelluti, L. Benfatto, M. Papagno, D. Pacilè, P. M. Sheverdyaeva, and P. Moras, *Massless Dirac cones in graphene: Experiments and theory*, Annalen der Physik **526**, 387 (2014).

[195] S. Zhou, G.-H. Gweon, A. Fedorov, P. First, W. Heer, D.-H. Lee, F. Guinea, A. Castro Neto, and A. Lanzara, *Substrate-induced bandgap opening in epitaxial graphene*, Nature Materials **6**, 770 (2007).

[196] E. Wang, X. Lu, S. Ding, W. Yao, M. Yan, G. Wan, K. Deng, S. Wang, G. Chen, L. Ma, J. Jung, A. V. Fedorov, Y. Zhang, G. Zhang, and S. Zhou, *Gaps induced by inversion symmetry breaking and second-generation Dirac cones in graphene/hexagonal boron nitride*, Nature Physics **12**, 1111 (2016).

[197] J. G. Pedersen and T. G. Pedersen, *Band gaps in graphene via periodic electrostatic gating*, Physical Review B **85**, 235432 (2012).

[198] F. Molitor, J. Güttinger, C. Stampfer, S. Dröscher, A. Jacobsen, T. Ihn, and K. Ensslin, *Electronic properties of graphene nanostructures*, Journal of Physics: Condensed Matter **23**, 243201 (2011).

[199] L. A. Ponomarenko, F. Schedin, M. I. Katsnelson, R. Yang, E. W. Hill, K. S. Novoselov, and A. K. Geim, *Chaotic Dirac Billiard in Graphene Quantum Dots*, Science **320**, 356 (2008).

[200] M. Han, B. Ozyilmaz, Y. Zhang, and P. Kim, *Energy Band-Gap Engineering of Graphene Nanoribbons*, Physical Review Letters **98**, 206805 (2007).

[201] S. Dutta and S. K. Pati, *Novel properties of graphene nanoribbons: a review*, J. Mater. Chem. **20**, 8207 (2010).

[202] H. Shen, Y. Shi, and X. Wang, *Synthesis, charge transport and device applications of graphene nanoribbons*, Synthetic Metals **210**, 109 (2015).

[203] C. Tegenkamp, J. Aprojanz, and J. Baringhaus, *Electronic transport in graphene nanoribbons*, in *Graphene Nanoribbons*. IOP Publishing, (2019).

[204] M. Kim, N. Safron, E. Han, M. Arnold, and P. Gopalan, *Fabrication and Characterization of Large-Area, Semiconducting Nanoperforated Graphene Materials*, Nano Letters **10**, 1125 (2010).

[205] J. Yang, M. Ma, L. Laiquan, Y. Zhang, W. Huang, and X. Dong, *Graphene nanomesh: New versatile materials*, Nanoscale **6**, 13301 (2014).

[206] J. A. Fürst, J. G. Pedersen, C. Flindt, N. A. Mortensen, M. Brandbyge, T. G. Pedersen, and A.-P. Jauho, *Electronic properties of graphene antidot lattices*, New Journal of Physics **11**, 095020 (2009).

[207] S. Brun, M. Thomsen, and T. Pedersen, *Electronic and optical properties of graphene antidot lattices: Comparison of Dirac and tight-binding models*, Journal of Physics: Condensed Matter **26**, 265301 (2014).

[208] T. Pedersen and J. Pedersen, *Transport in graphene antidot barriers and tunneling devices*, Journal of Applied Physics **112**, 113715 (2012).

[209] R. Pedersen and T. G. Pedersen, *Quasiparticle properties of graphene antidot lattices*, Physical Review B **80**, 113404 (2009).

[210] F. Ouyang, S. Peng, Z. Liu, and Z. Liu, *Bandgap Opening in Graphene Antidot Lattices: The Missing Half*, ACS Nano **5**, 4023 (2011).

[211] M. Corso, E. Carbonell-Sanromà, and D. G. de Oteyza, *Bottom-Up Fabrication of Atomically Precise Graphene Nanoribbons*, in *On-Surface Synthesis II*, D. G. de Oteyza and C. Rogero, eds. Springer International Publishing, Cham, (2018).

[212] J. Pan, T. Zhang, H. Zhang, B. Zhang, Z. Dong, and P. Sheng, *Berry Curvature and Nonlocal Transport Characteristics of Antidot Graphene*, Physical Review X **7**, 031043 (2017).

[213] V. H. Nguyen, M. C. Nguyen, H.-V. Nguyen, and P. Dollfus, *Disorder effects on electronic bandgap and transport in graphene-nanomesh-based structures*, Journal of Applied Physics **113**, 013702 (2013).

[214] S. Power and A.-P. Jauho, *Electronic transport in disordered graphene antidot lattice devices*, Physical Review B **90**, 115408 (2014).

[215] Z. Fan, A. Uppstu, and A. Harju, *Electronic and transport properties in geometrically disordered graphene antidot lattices*, Physical Review B **91**, 125434 (2014).

[216] D. Querlioz, Y. Apertet, A. Valentin, K. Huet, A. Bournel, S. Galdin-Retailleau, and P. Dollfus, *Suppression of the orientation effects on bandgap in graphene nanoribbons in the presence of edge disorder*, Applied Physics Letters **92**, 042108 (2008).

[217] S. Yuan, R. Roldán, A.P. Jauho, and M. Katsnelson, *Electronic Properties of Disordered Graphene Antidot Lattices*, Physical Review B **87**, 085430 (2013).

[218] H. Jippo, M. Ohfuchi, and C. Kaneta, *Theoretical study on electron transport properties of graphene sheets with two- and one-dimensional periodic nanoholes*, Physical Review B **84**, 075467 (2011).

[219] X. Liang, Y.-S. Jung, S. Wu, A. Ismach, D. L. Olynick, S. Cabrini, and J. Bokor, *Formation of Bandgap and Subbands in Graphene Nanomeshes with Sub-10 nm Ribbon Width Fabricated via Nanoimprint Lithography*, Nano Letters **10**, 2454 (2010).

[220] X. Li, X. Wang, L. Zhang, S. Lee, and H. Dai, *Chemically Derived, Ultrasmooth Graphene Nanoribbon Semiconductors*, Science **319**, 1229 (2008).

[221] C. Berger, Z. Song, X. Li, X. Wu, N. Brown, C. Naud, D. Mayou, T. Li, J. Hass, A. N. Marchenkov, E. H. Conrad, P. N. First, and W. A. de Heer, *Electronic Confinement and Coherence in Patterned Epitaxial Graphene*, Science **312**, 1191 (2006).

[222] Y.-W. Son, M. Cohen, and S. Louie, *Energy Gaps in Graphene Nanoribbons*, Physical Review Letters **97**, 216803 (2006).

[223] K. Nakada, M. Fujita, G. Dresselhaus, and M. S. Dresselhaus, *Edge state in graphene ribbons: Nanometer size effect and edge shape dependence*, Physical Review B **54**, 17954 (1996).

[224] V. Barone, O. Hod, and G. E. Scuseria, *Electronic Structure and Stability of Semiconducting Graphene Nanoribbons*, Nano Letters **6**, 2748 (2006).

[225] J. Eroms and D. Weiss, *Weak localization and transport gap in graphene antidot lattices*, New Journal of Physics **11**, 095021 (2009).

[226] P. Gallagher, K. Todd, and D. Goldhaber-Gordon, *Disorder-induced gap behavior in graphene nanoribbons*, Physical Review B **81**, 115409 (2009).

[227] F. Molitor, A. Jacobsen, C. Stampfer, J. Güttinger, T. Ihn, and K. Ensslin, *Transport gap in side-gated graphene constrictions*, Physical Review B **79**, 075426 (2009).

[228] F. Molitor, C. Stampfer, J. Güttinger, A. Jacobsen, T. Ihn, and K. Ensslin, *Energy and transport gaps in etched graphene nanoribbons*, Semiconductor Science and Technology **25**, 034002 (2010).

[229] D. Bischoff, A. Varlet, P. Simonet, M. Eich, H. Overweg, T. Ihn, and K. Ensslin, *Localized charge carriers in graphene nanodevices*, Applied Physics Reviews **2**, 031301 (2015).

[230] C. Stampfer, J. Güttinger, S. Hellmüller, F. Molitor, K. Ensslin, and T. Ihn, *Energy Gaps in Etched Graphene Nanoribbons*, Physical Review Letters **102**, 056403 (2009).

[231] A. Epping, C. Volk, F. Buckstegge, K. Watanabe, T. Taniguchi, and C. Stampfer, *Insulating State in Low-Disorder Graphene Nanoribbons*, physica status solidi (b) **256**, 1900269 (2019).

[232] E. Peters, A. Giesbers, and M. Burghard, *Variable range hopping in graphene antidot lattices*, Physica Status Solidi B Basic Research **249**, 2522 (2012).

[233] A. Giesbers, E. Peters, M. Burghard, and K. Kern, *Charge transport gap in graphene antidot lattices*, Physical Review B **86**, 045445 (2012).

[234] F. Sols, F. Guinea, and A. H. Castro Neto, *Coulomb Blockade in Graphene Nanoribbons*, Physical Review Letters **99**, 166803 (2007).

[235] D. Bischoff, T. Krähenmann, S. Dröscher, M. A. Gruner, C. Barraud, T. Ihn, and K. Ensslin, *Reactive-ion-etched graphene nanoribbons on a hexagonal boron nitride substrate*, Applied Physics Letters **101**, 203103 (2012).

[236] J. Bai, R. Cheng, F. Xiu, L. Liao, M. Wang, A. Shailos, K. L. Wang, Y. Huang, and X. Duan, *Very large magnetoresistance in graphene nanoribbons*, Nature Nanotechnology **5**, 655 (2010).

[237] M. Evaldsson, I. V. Zozoulenko, H. Xu, and T. Heinzel, *Edge-disorder-induced Anderson localization and conduction gap in graphene nanoribbons*, Physical Review B **78**, 161407(R) (2008).

[238] E. R. Mucciolo, A. H. Castro Neto, and C. H. Lewenkopf, *Conductance quantization and transport gaps in disordered graphene nanoribbons*, Physical Review B **79**, 075407 (2009).

[239] M. Y. Han, *Electronic Transport in Graphene Nanoribbons*. PhD thesis, Columbia University in the City of New York, New York City, (2010).

[240] D. Bischoff, F. Libisch, J. Burgdörfer, T. Ihn, and K. Ensslin, *Characterizing wave functions in graphene nanodevices: Electronic transport through ultrashort graphene constrictions on a boron nitride substrate*, Physical Review B **90**, 115405 (2014).

[241] L. Chen, L. He, H. S. Wang, H. Wang, S. Tang, C. Cong, H. Xie, L. Li, H. Xia, T. li, Ti. Wu, D. Zhang, L. Deng, T. Yu, X. Xie, and M. Jiang, *Oriented Graphene Nanoribbons Embedded in Hexagonal Boron Nitride Trenches*, Nature Communications **8**, 14703 (2017).

[242] H. S. Wang, L. Chen, K. Elibol, L. He, H. Wang, C. Chen, C. Jiang, C. Li, T. Wu, C. X. Cong, T. J. Pennycook, G. Argentero, D. Zhang, K. Watanabe, T. Taniguchi, W. Wei, Q. Yuan, J. C. Meyer, and X. Xie, *Towards chirality control of graphene nanoribbons embedded in hexagonal boron nitride*, Nature Materials https://doi.org/10.1038/s41563–020–00806–2 (2020).

[243] H. Karakachian, T. T. N. Nguyen, J. Aprojanz, A. A. Zakharov, R. Yakimova, P. Rosenzweig, C. M. Polley, T. Balasubramanian, C. Tegenkamp, S. R. Power, and U. Starke, *One-dimensional confinement and width-dependent bandgap formation in epitaxial graphene nanoribbons*, Nature Communications **11**, 6380 (2020).

[244] M. Thomsen, S. Power, A.-P. Jauho, and T. Pedersen, *Magnetic edge states and magnetotransport in graphene antidot barriers*, Physical Review B **94**, 045438 (2016).

[245] D. Weiss, K. Richter, E. Vasiliadou, and G. Lütjering, *Magnetotransport in antidot arrays*, Surface Science **305**, 408 (1994).

[246] D. Weiss, G. Lütjereng, and K. Richter, *Chaotic electron motion in macroscopic and mesoscopic antidot lattices*, Chaos, Solitons & Fractals **8**, 1337 (1997).

[247] D. Weiss, K. Richter, and J. Eroms, *Classical and Quantum Transport in Antidot Arrays*, in *Electron Transport in Quantum Dots*. Springer, (2003).

[248] D. Weiss, M. Roukes, A. Menschig, and P. Grambow, *Electron Transport Through an 'Anti' Dot Array*, in *Nanostructures and Mesoscopic Systems: proceedings of the International Symposium, Santa Fe, New Mexico, May 20 - 24, 1991*, Wiley P. K., ed. Academic Press, (1992).

[249] R. Fleischmann, T. Geisel, and R. Ketzmerick, *Magnetoresistance due to chaos and nonlinear resonances in lateral surface superlattices*, Physical Review Letters **68**, 1367 (1992).

[250] T. Shen, Y. Q. Wu, M. A. Capano, L. P. Rokhinson, L. W. Engel, and P. D. Ye, *Magnetoconductance oscillations in graphene antidot arrays*, Applied Physics Letters **93**, 122102 (2008).

[251] D. Weiss, K. Richter, A. Menschig, R. Bergmann, H. Schweizer, K. von Klitzing, and G. Weimann, *Quantized periodic orbits in large antidot arrays*, Physical Review Letters **70**, 4118 (1993).

[252] H. Silberbauer and U. Rössler, *Quantum study of magnetotransport in antidot superlattices*, Physical Review B **50**, 11911 (1994).

[253] D. Weiss, M. Roukes, A. Menschig, P Grambow, K. von Klitzing, and G. Weimann, *Electron pinball and commensurate orbits in a periodic array of scatterers*, Physical Review Letters **66**, 2790 (1991).

[254] R. Yagi, R. Sakakibara, R. Ebisuoka, J. Onishi, K. Watanabe, T. Taniguchi, and Y. Iye, *Ballistic transport in graphene antidot lattices*, Physical Review B **92**, 195406 (2015).

[255] G. Datseris, T. Geisel, and R. Fleischmann, *Robustness of ballistic transport features in antidot superlattices*, New Journal of Physics **21**, 043051 (2017).

[256] T. Ando, S. Uryu, T. Nakanishi, and S. Ishizaka, *Theory of quantum transport in mesoscopic systems: antidot lattices*, in *Physics and Applications of Semiconductor Quantum Structures*. CRC Press, (2001).

[257] M. Marocko, *Beseitigung von Verunreinigungen in van-der-Waals-Heterostrukturen*, Bachelor thesis, University of Regensburg (2018).

[258] A.-T. Nguyen, *Reaktives Ionenätzen von Bornitrid*, Bachelor thesis, University of Regensburg (2015).

[259] J. Sahliger, *Reaktives Ionenätzen von Bornitrid und Graphit*, Bachelor thesis, University of Regensburg (2015).

[260] F. Pizzocchero, L. Gammelgaard, B. Jessen, J. Caridad, L. Wang, J. Hone, P. Bøggild, and T. Booth, *The hot pick-up technique for batch assembly of van der Waals heterostructures*, Nature Communications **7**, 11894 (2016).

[261] J. Amann, *Reaktives Ionen-Ätzen von Bornitrid mit Schwefelhexafluorid*, Bachelor thesis, University of Regensburg (2017).

[262] S. Thoms and D. S. Macintyre, *Investigation of CSAR 62, a new resist for electron beam lithography*, Journal of Vacuum Science & Technology B **32**, 06FJ01 (2014).

[263] A. S. Gangnaik, Y. M. Georgiev, and J. D. Holmes, *New Generation Electron Beam Resists: A Review*, Chem. Mater. **29**, 1898 (2017).

[264] M. Schirmer, B. Büttner, F. Syrowatka, G. Schmidt, T. Köpnick, and C. Kaiser, *Chemical Semi-Amplified Positive E-Beam Resist CSAR 62 for Highest Resolution*, Proc. SPIE **8886**, 29th European Mask and Lithography Conference (2013).

[265] T. Greibe, T. Anhøj, L. Johansen, and A. Han, *Quality control of JEOL JBX-9500FSZ e-beam lithography system in a multi-user laboratory*, Microelectronic Engineering **155**, 25 (2016).

[266] S. Yasin, D. G. Hasko, and H. Ahmed, *Comparison of MIBK/IPA and water/IPA as PMMA developers for electron beam nanolithography*, Microelectronic Engineering **61-62**, 745 (2002).

[267] W. W. Hu, K. Sarveswaran, M. Lieberman, and G. H. Bernstein, *Sub-10 nm electron beam lithography using cold development of poly(methylmethacrylate)*, Journal of Vacuum Science & Technology B: Microelectronics and Nanometer Structures Processing, Measurement, and Phenomena **22**, 1711 (2004).

[268] L. E. Ocola and A. Stein, *Effect of cold development on improvement in electron-beam nanopatterning resolution and line roughness*, Journal of Vacuum Science & Technology B: Microelectronics and Nanometer Structures Processing, Measurement, and Phenomena **24**, 3061 (2006).

[269] M.-H. Liu and S.-C. Chen, *National Cheng Kung University, Tainan, Taiwan*, personal communication (2020).

[270] S. Reinhardt, C. Butschkow, S. Geissler, A. Dirnaichner, F. Olbrich, C. E. Lane, D. Schröer, and A. K. Hüttel, *Lab::Measurement–A portable and extensible framework for controlling lab equipment and conducting measurements*, Computer Physics Communications **234**, 216 (2019).

[271] A. Einwanger, *Spin-Injection into GaAs using ferromagnetic (Ga,Mn)As contacts*. PhD thesis, University of Regensburg, (2012).

[272] M. Y. Han, J. C. Brant, and P. Kim, *Electron Transport in Disordered Graphene Nanoribbons*, Physical Review Letters **104**, 056801 (2010).

[273] T. Shimizu, J. Haruyama, D. C. Marcano, D. V. Kosinkin, J. M. Tour, K. Hirose, and K. Suenaga, *Large intrinsic energy bandgaps in annealed nanotube-derived graphene nanoribbons*, Nature Nanotechnology **6**, 45 (2011).

[274] S. Das Sarma and E. H. Hwang, *Two-dimensional metal-insulator transition as a strong localization induced crossover phenomenon*, Physical Review B **89**, 235423 (2014).

[275] B. Obradovic, R. Kotlyar, F. Heinz, P. Matagne, T. Rakshit, M. D. Giles, M. A. Stettler, and D. E. Nikonov, *Analysis of graphene nanoribbons as a channel material for field-effect transistors*, Applied Physics Letters **88**, 142102 (2006).

[276] J. Wang, R. Zhao, M. Yang, Z. Liu, and Z. Liu, *Inverse relationship between carrier mobility and bandgap in graphene*, The Journal of Chemical Physics **138**, 084701 (2013).

[277] G. Mihajlović, J. E. Pearson, M. A. Garcia, S. D. Bader, and A. Hoffmann, *Negative Nonlocal Resistance in Mesoscopic Gold Hall Bars: Absence of the Giant Spin Hall Effect*, Physical Review Letters **103**, 166601 (2009).

[278] D. Xiao, M.-C. Chang, and Q. Niu, *Berry phase effects on electronic properties*, Rev. Mod. Phys. **82**, 1959 (2010).

[279] R. V. Gorbachev, J. C. W. Song, G. L. Yu, A. V. Kretinin, F. Withers, Y. Cao, A. Mishchenko, I. V. Grigorieva, K. S. Novoselov, L. S. Levitov, and A. K. Geim, *Detecting topological currents in graphene superlattices*, Science **346**, 448 (2014).

[280] Y. Li, M. Amado, T. Hyart, G. P. Mazur, and J. W. A. Robinson, *Topological valley currents via ballistic edge modes in graphene superlattices near the primary Dirac point*, Communications Physics **3**, 224 (2020).

[281] F. Claro, *Spectrum of Tight Binding Electrons in a Square Lattice with Magnetic Field*, physica status solidi (b) **104**, K31 (1981).

[282] D. Springsguth, R. Ketzmerick, and T. Geisel, *Hall conductance of Bloch electrons in a magnetic field*, Physical Review B **56**, 2036 (1997).

[283] L. Wang, S. Zihlmann, M.-H. Liu, P. Makk, K. Watanabe, T. Taniguchi, A. Baumgartner, and C. Schönenberger, *New Generation of Moiré Superlattices in Doubly Aligned hBN/Graphene/hBN Heterostructures*, Nano Letters **19**, 2371 (2019).

[284] A. Tadjine, G. Allan, and C. Delerue, *From lattice Hamiltonians to tunable band structures by lithographic design*, Physical Review B **94**, 075441 (2016).

[285] K.-E. Huhtinen, M. Tylutki, P. Kumar, T. I. Vanhala, S. Peotta, and P. Törmä, *Spin-imbalanced pairing and Fermi surface deformation in flat bands*, Physical Review B **97**, 214503 (2018).

[286] L. Balents, C. R. Dean, D. K. Efetov, and A. F. Young, *Superconductivity and strong correlations in moiré flat bands*, Nature Physics **16**, 725 (2020).

[287] A. Skurativska, S. S. Tsirkin, F. D. Natterer, T. Neupert, and M. H. Fischer, "Flat bands with fragile topology through superlattice engineering on single-layer graphene." arXiv:2101.08273 [cond-mat.mes-hall], (2021).

[288] J. Amann, *ongoing PhD thesis*, University of Regensburg (2020).

[289] H. Park, G. H. Shin, K. J. Lee, and S.-Y. Choi, *Atomic-scale etching of hexagonal boron nitride for device integration based on two-dimensional materials*, Nanoscale **10**, 15205 (2018).

[290] Z. Ma, C. C. Prawoto, Z. Ahmed, Y. Xiao, L. Zhang, C. Zhou, and M. Chan, *Control of Hexagonal Boron Nitride Dielectric Thickness by Single Layer Etching*, Journal of Materials Chemistry C **7**, 6273 (2019).

[291] T. Vogl, M. Doherty, B. Buchler, Y. Lu, and P. K. Lam, *Atomic localization of quantum emitters in multilayer hexagonal boron nitride*, Nanoscale **11**, 14362 (2019).

[292] L. Britnell, Ro. V. Gorbachev, R. Jalil, B. D. Belle, F. Schedin, M. I. Katsnelson, L. Eaves, S. V. Morozov, A. S. Mayorov, N. M. R. Peres, A. H. Castro Neto, J. Leist, A. K. Geim, L. A. Ponomarenko, and K. S. Novoselov, *Electron Tunneling through Ultrathin Boron Nitride Crystalline Barriers*, Nano Letters **12**, 1707 (2012).

[293] M. Gurram, S. Omar, and B. J. van Wees, *Electrical spin injection, transport, and detection in graphene-hexagonal boron nitride van der Waals heterostructures: progress and perspectives*, 2D Materials **5**, 032004 (2018).

DANKSAGUNG

Ein herzliches Dankeschön an alle, die zum Gelingen dieser Arbeit beigetragen haben!

Vielen lieben Dank

- an PD Dr. Jonathan Eroms und Prof. Dr. Dieter Weiss, die es mir ermöglicht haben an diesem faszinierenden und interessanten Thema zu arbeiten.

- an PD Dr. Jonathan Eroms für die hervorragende Betreuung, die Unterstützung und neuen Anregungen während der Bearbeitung dieses Themas, und die stets kompetente Hilfe bei Fragen und Problemen aller Art.

- an Prof. Dr. Dieter Weiss für die wegweisenden Diskussionen und das durchgehende Interesse am Fortschritt meiner Arbeit.

- an Prof. Dr. Ming-Hao Liu, Dr. Szu-Chao Chen, und Prof. Dr. Klaus Richter für die außerordentlich produktive Zusammenarbeit, die in einer gemeinsamen Publikation gipfelte.

- an Prof. Dr. Daniela Pfannkuche und Max-Niklas Steffen für die fruchtvolle Zusammenarbeit und die hilfreichen und weiterführenden Diskussionen.

- an Dr. Martin Drienovsky und Dr. Andreas Sandner, die mir noch einiges an Tipps und Tricks mit auf den Weg gaben.

- an meine hilfreichen Korrekturleser Jonathan Eroms, Tobias Völkl, Tobias Preis, Elisabeth Richter, Hubert Maier, Julia Amann, Albert Koop, und Marina Marocko. Danke, dass ihr euch die Zeit genommen habt!

- an meine Bachelorstudenten Simon Wagner, Linus Fresz, Marina Marocko und meinen Masterstudenten Thomas Lorenz für die produktive Zusammenarbeit und den daraus gewonnenen Erkenntnissen.

- an alle Mitglieder des Lehrstuhls Weiss und der Graphen-Arbeitsgruppe für die Schaffung einer angenehmen und kollegialen Arbeitsatmosphäre und für die ein oder andere zerstreuende Aktivität während und außerhalb der Arbeit.

- an Claudia Moser und Elke Haushalter für die stets freundliche Unterstützung in allen organisatorischen und bürokratischen Belangen.

- an Cornelia Linz, Uli Gürster, Daniel Pahl, Thomas Haller, und Michael Weigl für die Hilfe und Unterstützung bei technischen Fragen und Problemen aller Art.

- an Kutschi, Hupfi, Andi, Tobi, Stefan, und Mo für die ein oder andere ausgelassene Festivität als Ausgleich zum Uni-Alltag.

- an meine Bürokolleginnen und -kollegen für das durchgehend harmonische Arbeitsklima und die Gespräche über Physik und andere (mal mehr und mal weniger ernsthafte) Themen. Insbesondere sei hier die glorreiche Büro-Gang mit Eli und Hubert hervorgehoben, mit der immer für gute Laune gesorgt war.

- an die Cafeten-Gang (insbesondere Julia, Stefan, Eli, Tobi, Simon, Franz, Hubert, und Marina) mit denen ich viele kurzweilige Pausen und einiges an (kalten) Kaffee genießen konnte.

- an meine Freunde für alle außeruniversitären Aktivitäten und die nötige Ablenkung von der Arbeit.

- an meine Familie und Angehörigen für die stets liebevolle Unterstützung.